

**Next-Gen Thermal Management for Electronics in Space – Asymmetric Sawtooth and  
Cavity-Enhanced Nucleation-Driven Transport (ASCENT)**

by

Karthekeyan Sridhar

A dissertation submitted to the Graduate Faculty of  
Auburn University  
in partial fulfillment of the  
requirements for the Degree of  
Doctor of Philosophy

Auburn, Alabama  
December 9, 2023

Keywords: Nucleate boiling, Microgravity, Microstructure, Enhanced boiling, Liquid layer

Copyright 2023 by Karthekeyan Sridhar

Approved by

Sushil H. Bhavnani, Professor, Mechanical Engineering  
Roy W. Knight, Associate Professor, Mechanical Engineering  
Nicholas Tsolas, Assistant Professor, Mechanical Engineering  
Nedret Billor, Professor, Mathematics and Statistics  
Allan David, Associate Professor, Chemical Engineering

## Abstract

Nucleate pool boiling in microgravity is characterized by stagnant vapor bubble dynamics, leading to early dryout of the heated surface compared to terrestrial conditions. The Asymmetric Sawtooth and Cavity-Enhanced Nucleation-driven Transport (ASCENT) investigation studied an engineered microstructure in a nucleate pool boiling setup aboard the International Space Station (ISS) from November 2022-January 2023 to address this longstanding problem. The experiment was housed in the Microgravity Science Glovebox (MSG) and used degassed FC-72 as the test liquid. The engineered microstructure consisted of repeating mm-sized  $60^{\circ}$ - $30^{\circ}$  sawtooth structures located within a hermetically sealed square ampoule as the test chamber. Experimental investigations were conducted to explore a range of input heat fluxes, ranging from 0.5 to 2.3 W/cm<sup>2</sup>. The resulting vapor dynamics and heat transfer were compared against a flat baseline surface. Both surfaces contained 250  $\mu$ m square cavities spaced 1-mm apart.

The constrained dimensions of the 8-mm square chamber severely influenced vapor bubble dynamics across the heated surface. The presence of a liquid layer beneath vapor slugs on the microstructure was observed, in contrast to the baseline surface, where no liquid layer was visually detected. The transient heat transfer coefficient from the microstructure was higher than the baseline surface as the vapor bubbles grew larger at constant heat flux due to liquid film access provided by the asymmetric ridges of the microstructure. A significant increase in the heat transfer coefficient was observed at 1.8 W/cm<sup>2</sup>, potentially due to vigorous nucleation in the observed liquid pockets along the microstructure, increasing the heat transfer coefficient from 2900 to 6200 W/m<sup>2</sup>K. Nucleation was observed at heat fluxes as low as 0.3 W/cm<sup>2</sup> from the engineered cavities, and a quasi-steady heat transfer coefficient of 2200 W/m<sup>2</sup>K was obtained at 2.3 W/cm<sup>2</sup> from the microstructured surface. The quasi-steady analysis also indicated that both surfaces performed

similarly in microgravity and terrestrial gravity in the same experimental setup. The results demonstrate that the liquid film dynamics underneath vapor slugs influence heat transfer to a large extent in microgravity conditions.

Another surface was fabricated using wire electric discharge machining, with hammerhead slots (250  $\mu\text{m}$  mouth) featuring on every third sawtooth (4.5 mm apart). The slots acted as engineered nucleation sites, ejecting vapor at an angle perpendicular to the long slope of the microstructure. Vapor bubbles nucleated from the engineered sites at heat fluxes as low as 0.8  $\text{W}/\text{cm}^2$ , and the number of active slots increased as the heat input increased. The departure frequency also increased with increasing heat flux; each slot consisted of multiple nucleation sites. Vapor slugs moved toward the pressure relief membrane in the sealed ampoule at velocities as high as 20.4 mm/s and interacted with liquid pockets between the crest and trough of the microstructure. Individual slug departures increased the cold zone temperature by 19°C at 2.4  $\text{W}/\text{cm}^2$ . The observed vapor bubble ejection from the surface and slug mobility suggests that the surface enhancement can facilitate vapor mobility and heat transfer enhancement in reduced gravity environments.

Similar to the microgravity environments, stagnant vapor growth on a downward-facing flat surface leads to increased surface temperature and dryout at relatively low heat fluxes. The current study investigated the 60°-30° asymmetric sawtooth microstructure to mechanistically improve outcomes in adverse gravity by mobilizing vapor due to a pressure difference between the crest and trough of the surface enhancement following the Young-Laplace relationship. Bubble dynamics were experimentally investigated in an 8-mm square borosilicate glass tube and visualized using a high-speed camera to measure vapor bubble morphology and velocity in the FC-72 dielectric liquid. The vapor bubble's shape changed based on how many sawteeth it covered.

This change manifested as a decrease in the curvature ratio between the crest and trough of the microstructure. The pattern of vapor slugs nucleating from intended engineered sites, coalescing to form larger slugs that slid across the microstructure, was repeated at different frequencies at different heat fluxes. The microstructure supported increased vapor volume at higher heat fluxes, suggesting that a passive and self-regulating thermal management solution for adverse gravity applications was feasible. The study proposed an empirical model to recognize the dominant forces driving the observed motion in an adverse gravity configuration. The interplay between the pressure differential force and the buoyancy force was analyzed at different liquid film thicknesses, and the force balance was compared with a 75°-15° sawtooth structure. For a vapor slug spanning four sawteeth, the 75°-15° structure supported a 54% increase in the feasible liquid film thickness range due to the increased long slope area. The outcomes and analysis allow for the creation of numerical frameworks for the microstructure. These models can be based on quantitative image processing, serving as a reference point for future development.

ASCENT investigated the effects of a surface microstructure on boiling in microgravity and terrestrial adverse gravity using degassed FC-72. The results showed that liquid film dynamics played a crucial role in heat transfer, with the microstructure producing a higher transfer coefficient than the baseline surface in microgravity. The microstructured surface offers the promise of enhanced thermal management solutions for electronics in suppressed buoyancy conditions without the complexity of flow loops while maintaining the versatility of being design-inclusive for silicon devices or a bolt-on solution on existing components.



## **Acknowledgements**

To my committee members Dr. Sushil H. Bhavnani, Dr. Roy W. Knight, Dr. Nicholas Tsolas, and Dr. Nedret Billor, thank you for reviewing this dissertation and serving on my committee.

I am deeply grateful to my advisor, Sushil Bhavnani, for his patient guidance, unwavering dedication, and passion for my research. His exceptional qualities as a great human being and mentor have been an invaluable inspiration throughout my dissertation journey. I am incredibly fortunate to have been his student, and this dissertation would not have been possible without him.

I am immensely thankful to Dr. Vinod Narayanan from the University of California, Davis, for being an integral part of our project and reviewing my manuscripts; your guidance and support have been crucial.

I express my gratitude to Heidi Parris, the NASA Associate Program Scientist for International Space Station Operations, Shawn Stephens, the Operations Project Manager for International Space Station, and Rachel Ormsby, the Project Manager at Redwire Space, for their valuable contributions to ASCENT. Additionally, I extend my appreciation to Tony Hammond at Redwire Space for his assistance in data collection for ASCENT.

Thanks to my Auburn friend, Aaron Smith, for his support as a friend and colleague.

Finally, I would like to thank my parents and my sister for their confidence, support, and love, without whom this work would not have been possible.

# Table of Contents

Abstract.....	ii
Acknowledgements.....	v
List of Figures.....	ix
List of Tables.....	xviii
NOMENCLATURE.....	xix
CHAPTER 1 INTRODUCTION.....	1
1.1 Objectives of the study.....	3
1.2 Bubble dynamics from downward-facing surfaces.....	4
1.3 Bubble dynamics in microgravity experiments.....	11
1.4 Prior efforts from the sawtoothed surface.....	19
1.5 Summary.....	23
CHAPTER 2 Test Surfaces.....	25
1.1 Test surface fabrication – Auburn University.....	25
1.2 Test surface geometry – Auburn University.....	27
1.3 Titanium (Ti-6Al-4V) test surface polishing and test.....	28
1.4 Other attempts to polish Ti-6Al-4V surfaces.....	31
1.5 Test surface geometry – University of California, Davis.....	32
1.6 Test surface shipped to implementation partner – Redwire Techshot.....	33
CHAPTER 3 TERRESTRIAL EXPERIMENTS.....	36
3.1 Terrestrial Experiments at Auburn University.....	36
3.1.1 Experimental Setup.....	36
3.1.2 Image Processing.....	37
3.1.3 Experimental Results and Discussion.....	41
3.1.3.1 Comparison of Baseline and Microstructured Surface.....	41
3.1.3.2 Quantifying Vapor Mobility Across the Microstructure at Different Fluxes..	42
3.1.3.3 Force Balance Model from the Microstructure.....	44

3.1.3.4	Force Balance Model Analysis and Discussion .....	51
3.2	Summary of the Auburn University Experiments.....	59
3.3	ASCENT – Organizational Chart.....	60
3.4	Transfer of Information from the Science Team to the NASA Implementation Partner61	
3.4.1	Test surface fabrication .....	62
3.4.2	Borosilicate glass ampoule/ test chamber manufacturing.....	62
3.4.3	Filling and charging of the fabricated ampoule .....	63
3.4.4	Degassing the dielectric liquid FC-72.....	63
3.4.5	Leak checking .....	63
3.4.6	Characterization of each ground ampoule.....	63
3.4.7	Resistance heater coating in the square ampoule .....	64
3.4.8	Copper coating along the circular section of the ampoule .....	64
3.4.9	Placement of thermocouples .....	65
3.4.10	Pressure relief membrane material.....	66
3.4.11	Pressure relief testing .....	66
3.4.12	Thermal interface material .....	67
3.4.13	Thermal interface bonding with constant pressure .....	67
3.4.14	Candidate high-speed camera tests .....	67
3.5	Terrestrial Experiments at Redwire Techshot.....	72
3.5.1	PFMI Furnace and the ASCENT Ampoule.....	73
3.5.2	Development Test 1 – Ground Furnace .....	79
3.5.3	Development Test 2 – Ground Furnace .....	81
3.5.4	Checkout Runs in Ground Furnace .....	84
3.5.5	Pre-flight Science Tests – Flight Furnace .....	86
3.5.6	Challenges with the FLT #4 ampoule .....	87
3.5.7	Challenges with the FLT #1 Ampoule .....	88
3.5.8	Pre-flight test results.....	89
3.5.9	Summary .....	94
CHAPTER 4	MICROGRAVITY EXPERIMENTS .....	95
4.1	Preparation for launch .....	95
4.2	Experimental anomalies .....	96

4.3	Experimental procedure .....	97
4.4	Data reduction .....	100
4.5	Experimental Results and Discussion .....	102
4.5.1	Raw data and analysis approach.....	102
4.5.2	Nucleation from the liquid film.....	106
4.5.3	Transient heat transfer analysis .....	110
4.5.4	Quasi-steady analysis .....	112
4.5.5	Nucleation from the engineered cavities.....	119
4.5.6	Vapor mobility across the microstructure .....	122
4.5.7	Vapor bubble dynamics from FLT3 Ampoule.....	126
4.5.8	Summary .....	133
CHAPTER 5	CONCLUSIONS AND RECOMMENDATIONS .....	134
5.1	Terrestrial downward-facing experiments .....	135
5.2	Microgravity experiments .....	135
5.3	Recommendations .....	137
REFERENCES	.....	139
APPENDIX A:	THERMOPHYSICAL PROPERTIES OF FC-72 .....	152
APPENDIX B:	SAMPLE MODEL CALCULATIONS .....	153
APPENDIX C:	UNCERTAINTY ANALYSIS.....	156
Experimental Uncertainty for the Microgravity Experiments	.....	156
APPENDIX D:	SCIENCE VERIFICATION DOCUMENT .....	158
Science Verification Checklist.....	.....	158
ASCENT Success Criteria .....	.....	158
Sample Flight Ampoule Processing Protocol .....	.....	158
Flight Ampoule Thermocouple Calibration Data .....	.....	158

## List of Figures

Figure 1.1(a) The increase in the maximum chip power and transistor counts from 2000-2020 (b) The causes of failure in electronic equipment [4].....	2
Figure 1.2 The change in vapor bubble dynamics near CHF at different orientations [7]. .....	5
Figure 1.3 The illustration of boiling behavior on an inclined downward-facing surface (a) compared with a downward-facing surface (b) [5].....	6
Figure 1.4 The difference in boiling behavior between a plain surface and a honeycomb surface at a low heat flux and near-CHF. (a) bare, heat flux = 0.02 MW/m <sup>2</sup> , (b) honeycomb, heat flux = 0.02 MW/m <sup>2</sup> , (c) bare, heat flux = 0.25 MW/m <sup>2</sup> (near CHF), (d) honeycomb, heat flux = 0.42 MW/m <sup>2</sup> (near CHF) [13].....	7
Figure 1.5 (a) The mean absolute error of different models and correlations at various orientation angles are illustrated. (b)The mean average errors of the overall models and correlations when the downward-facing is included [28]. .....	9
Figure 1.6 The side (top) and front (bottom) angles of the vapor slug in the downward-facing orientation at different heat fluxes. The scale bar indicates 10 mm, and the number indicates the heat flux in kW/m <sup>2</sup> [29].....	11
Figure 1.7 Sequences of images showing bubble nucleation and growth on the surface of the heater with smaller bubbles coalescing to form one large, central bubble in microgravity [52]. .....	14
Figure 1.8 The change in boiling behavior from terrestrial gravity (t<0s) and the vapor behavior in short-term microgravity (t> 0 s) near the critical heat flux [53]. .....	15
Figure 1.9 The effect of metal foam wettability on the number of generated vapor bubbles under short-term microgravity (drop-tower experiment) [60]. .....	17
Figure 1.10 Bubble detachment under the influence of an electric field at an electrode distance of 6 mm and an electrode voltage of 15 kV [67]. .....	18

Figure 1.11 Collage of images detailing the net axial component of velocity from vapor bubble generated on the long slope of the symmetric sawtooth microstructure. Image (g) denotes a unit cell of influence directing liquid motion around the vapor bubble [34]. ..... 20

Figure 1.12 Bubble dynamics in FC-72 along the sawtooth microstructure under microgravity during the parabolic flight experiments at a)  $q=0.5 \text{ W/cm}^2$  b)  $q= 1.4 \text{ W/cm}^2$  [72]..... 21

Figure 1.13 Video sequence recorded during a flash test (left) and a cross-sectional schematic of the bubble (right) indicating the hypothesized bubble shape and corresponding liquid layer thicknesses between the slug and the top and bottom walls [70]. ..... 22

Figure 2.1 A schematic of the laser powder bed fusion process [1] ..... 26

Figure 2.2 The fabricated titanium test surfaces (Ti-6Al-4V) on the baseplate ..... 27

Figure 2.3 (a) The asymmetric sawtooth microstructure (pitch = 1mm) with 250  $\mu\text{m}$  cavities on the long slope. (b) The baseline surface contains the 250  $\mu\text{m}$  cavities spaced 1-mm apart on a flat profile..... 28

Figure 2.4 Depiction of spurious sites from an unpolished Ti-6Al-4V surface..... 29

Figure 2.5 The six test surfaces from Auburn University were machined to their final dimensions and polished before being shipped to Techshot..... 31

Figure 2.6 The detailed test surface dimensions of the 60°-30° slot test surface. The hammerhead slots are located on every third sawtooth. A picture of the fabricated surface is shown on top. ... 33

Figure 2.7 The final test surfaces shipped from Auburn University and the University of California, Davis. The vacuum-sealed packages from Auburn University are illustrated at the top, and the two wire EDM test surfaces from the University of California, Davis, are shown at the bottom. The Auburn University test surface with the trailing label "-F" indicates a flight surface, and "-G" denotes a ground surface..... 35

Figure 3.1 (a) The experimental setup with the downward-facing surface in the borosilicate glass ampoule for backlit high-speed imaging (b) Isometric view of 60°-30° sawtooth microstructure

with 250  $\mu\text{m}$  cavities 1-mm apart and (c) Side view of the repeating millimetric-scale microstructures..... 37

Figure 3.2 The process of generating a background subtracted image from the initial stack of raw high-speed images using maximum intensity Z-projection is illustrated ..... 38

Figure 3.3 The different image binarization algorithms were attempted on the background-subtracted image. The algorithms marked in red did not converge and were eliminated as candidates for further analysis. .... 39

Figure 3.4 The binarized image is inverted for the fill holes operation. A watershed mask with distance transform was used to separate connected vapor bubbles. .... 40

Figure 3.5 Comparison in total vapor area between the  $60^\circ\text{-}30^\circ$  sawtooth and the baseline surface with the same frame of view (13.4 x 6.7 mm). The asymmetric microstructure induced three cycles of vapor nucleation, growth, and slide-off, while the baseline surface produced stationary vapor slugs with relatively larger areas..... 42

Figure 3.6 Difference in total vapor area patterns at  $1.3 \text{ W/cm}^2$  and  $2.3 \text{ W/cm}^2$  for the  $60^\circ\text{-}30^\circ$  sawtooth with cavities spaced 1-mm apart. The high-speed imagery (1024x768, 1000fps) of the highs and lows at  $2.3 \text{ W/cm}^2$  are depicted on the right. .... 44

Figure 3.7 The ratio of the radius of curvature between the peak and crest of the asymmetric sawtooth in the vapor slug as a function of the characteristic length-scale of the vapor slug (number of sawtooth periods covered) captured in the Bond number. The velocity of the indicated slugs (shown on the right) increases with the length of vapor masses spanning more than three sawteeth. .... 45

Figure 3.8 Force balance on a vapor slug moving in the dielectric liquid (marked in yellow) denoting the dominant forces. The buoyancy forces and the pressure difference across the microstructure drive the vapor slug, while the drag and added mass forces limit the motion..... 46

Figure 3.9 The change in the drag coefficient as the vapor slug grows for the current study is illustrated, as given by Eq (5) ..... 49

Figure 3.10 The change in the net pressure different driver and the net force as the liquid film thickness changes from up to 110 microns for a slug spanning four sawteeth and a velocity of 26 mm/s. The inset image shows the liquid-vapor interface across a slug spanning four sawteeth, highlighting the growth in the liquid film from crest to trough..... 53

Figure 3.11 The difference in net force generated and the net pressure difference when the angle of asymmetric sawtooth changes from 30° to 15°. ..... 55

Figure 3.12 The net and differential pressure forces for the hypothetical 85°-5° sawtooth microstructure are compared against the 60-30 sawtooth microstructure. .... 57

Figure 3.13 Comparison of the net forces and the differential pressure forces for vapor slugs spanning across four, five, and six sawteeth..... 59

Figure 3.14 The flow of information between the different agencies involved in the ASCENT investigation..... 61

Figure 3.15 The unboxed components of the candidate USB 3.0 camera are shown..... 68

Figure 3.16 The lens setup at Auburn University for close-range high-speed imaging of the USB3.0 camera..... 69

Figure 3.17 The various framerate and exposures attempted in-house at Auburn University's terrestrial setup..... 70

Figure 3.18 The layout of the imaging system for the PFMI-ASCENT experiment is illustrated. The additional light bar backlights the high-speed camera imaging while the COHU camera captures a top view of the test surface. .... 75

Figure 3.19 a) The layout of the PFMI ASCENT ampoule is shown on the left. b) A fabricated sample ampoule assembly on the right indicates the cartridge head and the sputtered copper and nichrome coating. The nichrome coating is the resistive heater for the ASCENT experiment.... 77



Figure 3.20 The position of the surface, fluid, and cold zone thermocouples is illustrated in the PFMI layout. The cold zone thermocouples are centered radially and axially under the cold zone locations. .... 78

Figure 3.21 Challenges encountered during the first temperature-controlled ground test for ASCENT. The SUBSA/PFMI control interface is shown. .... 81

Figure 3.22 The boiling curve for the first cycle of the heat-flux controlled development test in the PFMI furnace is shown. .... 82

Figure 3.23 The boiling curve for the second cycle of the heat-flux controlled development test in the PFMI furnace is shown. .... 83

Figure 3.24 The narrow high-speed view at 1.4 W/cm<sup>2</sup> and 2.6 W/cm<sup>2</sup> is shown in (a) and (b) respectively. The wide high-speed view that covers almost the entire test surface at 1.2 W/cm<sup>2</sup> is shown in (c)..... 84

Figure 3.25 The pressure traces of three flight ampoules recorded during the checkout runs are shown. .... 86

Figure 3.26 The first cycle (a ramp-up followed by a ramp-down) at each cold zone temperature for the FLT2 ampoule. The test surface is 60-30 sawtooth geometry with cavities spaced 1-mm apart. The boiling curves are generated assuming constant pressure (1 atm) in the closed ampoule. .... 90

Figure 3.27 Consecutive cycles at the same cold zone temperature captured during the pre-flight tests for FLT2 at 40°C cold zone temperature. The boiling curves are generated assuming constant pressure (1 atm) in the closed ampoule..... 91

Figure 3.28 The first cycle of the FLT2, FLT1, and FLT3 ampoules at 20°C cold zone temperature is illustrated in the boiling curve. The boiling curves are generated assuming constant pressure (1 atm) in the closed ampoule. .... 93

Figure 3.29 The narrow high-speed (left) and the COHU camera (right) views for the FLT2 and FLT3 flight ampoules captured during the pre-flight science tests. .... 94

Figure 4.1 The re-filled flight ampoules for the ASCENT projects are illustrated. Five total flight ampoules were flown to the ISS: A calibration ampoule to verify the functioning of the PFMI furnace and four ampoules with test surfaces provided by the ASCENT science team. .... 96

Figure 4.2 An example run with the on-off cycles is illustrated. At the start of the test, the cold zones are at 20°C, and the sample and fluid temperatures are ambient. A dip in the surface temperature signifies the start of nucleation. As the slugs grow larger and traverse toward the pressure relief system, a temperature spike in the cold zone is recorded. After the heating is turned off, the temperatures gradually return to ambient conditions. The run illustrated here was recorded on 16th December 2022 at a heat flux of 0.8 W/cm<sup>2</sup> on the baseline surface. The markers in the plot are used to differentiate the different thermocouples. All times are in UTC. .... 99

Figure 4.3 The ISS flight plan indicating loss-of-signal period due to satellite handovers and line-of-sight constraints within the Tracking and Data Relay Satellite System. The orange and green bar indicate the availability of different feeds (video, voice, data etc). .... 100

Figure 4.4 The power supply is connected to a DC-DC converter which steps down the voltage and is controlled by a Eurotherm controller. The surface thermocouple provides feedback to the Eurotherm controller until the desired setpoint is reached. .... 101

Figure 4.5 The temperature traces at different heat fluxes for the flat baseline surface (left) and the 60°-30° microstructure (right). The period between 60 and 80 seconds) was used for the quasi-steady state analysis of the experimental runs from the average between these bounds. The markers in the plot are used to differentiate between the different heat fluxes. The inset image shows the increase in vapor area at ~95 seconds after the heating command was issued for different heat fluxes for the baseline surface. The total vapor area increases from 4.5 mm<sup>2</sup> at 0.5 W/cm<sup>2</sup> to 200 mm<sup>2</sup> at 1.2 W/cm<sup>2</sup>. .... 105

Figure 4.6 The dip in surface and fluid temperatures after the temperature was maintained steadily at 80 °C at 1.8 W/cm<sup>2</sup> (left). Though minor oscillations were observed at other heat fluxes at the setpoint, the magnitude of this decline was unprecedented. The corresponding jump in the time-dependent experimental heat transfer coefficient is illustrated on the right. .... 106

Figure 4.7 COHU camera capture at 142 seconds after the heating command was issued, capturing consistent, vigorous nucleation at multiple locations along the growing slug in  $\mu\text{g}$  (top). The collage of high-speed images on the bottom (numbered 1-8) depicts detailed nucleation from a spot along the liquid film. The nucleating vapor bubble coalesces into the large slug between frames 4 and 5 as the top of the vapor bubble collapses and creates undulations along the surface. The top left of the collage shows another vapor bubble emerging from the microlayer. Each frame is 1.11 milliseconds apart, and the frame of view is 15.20 mm x 8.44 mm at 900 fps. The schematic on the top right illustrates the location of the surface thermocouple along the test surface relative to the location of the nucleation spot and the vapor slug..... 109

Figure 4.8 Time-dependent heat transfer coefficient of the microstructure (blue) against the baseline (orange) at different heat fluxes: 0.7 W/cm<sup>2</sup> (left), 1.0 W/cm<sup>2</sup> (center), and 1.3 W/cm<sup>2</sup> (right). The start of vapor nucleation is annotated on the plots. The inset images for 0.7 W/cm<sup>2</sup> and 1 W/cm<sup>2</sup> show the narrow high-speed image captures for the baseline and the microstructure surfaces, respectively. The near-constant heat transfer coefficient observed for the microstructure at 1.0 W/cm<sup>2</sup> from 145 seconds is due to a constant temperature difference being maintained between the surface and fluid. The inset image for 1.3 W/cm<sup>2</sup> shows a vapor slug departing the frame of view after interacting with the fluid thermocouple (left) at 103 seconds. The error bars on the heat transfer coefficient are  $\pm 4.1\%$  of the derived experimental value, as explained in Appendix D..... 111

Figure 4.9 Slug dynamics for the baseline surface (left) and the microstructure (Right) at 1.3 W/cm<sup>2</sup> in microgravity. The vapor slug covers the frame of view (FOV) for the baseline surface, and no microlayer is visible between the vapor slug and the baseline surface. On the right, a growing slug was captured on the microstructure surface with clear visible liquid microlayer film across the crests of the asymmetric sawtooth. .... 112

Figure 4.10 Comparison of nucleate boiling data in previous microgravity studies compared with ASCENT's quasi-steady state data. Adapted from Warriar et al. [52]. .... 115

Figure 4.11 Comparison of ASCENT's derived quasi-steady heat transfer coefficients with other microgravity studies. Adapted from Warriar et al. [52]..... 117

Figure 4.12 Comparison of ASCENT  $\mu\text{g}$  (time-averaged) data with 1g steady-state data assuming constant pressure in the test ampoule..... 119

Figure 4.14 The increase in the number of active cavities with increasing heat flux for the flat test surface is illustrated in the figure. Beyond  $1 \text{ W/cm}^2$ , consistent and uniform nucleation was observed across the test surface. The inset image shows a representative high-speed capture at  $0.7 \text{ W/cm}^2$ . ..... 120

Figure 4.15 The COHU camera views of the  $60^\circ\text{-}30^\circ$  sawtooth structure at multiple heat fluxes in microgravity are illustrated in the figure. The number of triggered active engineered sites increases with input heat flux increment. .... 121

Figure 4.16 Comparison of vapor bubble dynamics from the flat baseline surface (left) and the  $60^\circ\text{-}30^\circ$  microstructure (right) at  $0.50 \text{ W/cm}^2$ . The  $250 \mu\text{m}$  square cavities produce consistent nucleation activity on both test surfaces, but vapor bubbles ride on the crests of the sawteeth at the departure diameter. .... 123

Figure 4.17 Comparison in vapor slug movement for the downward-facing surfaces at  $1.3 \text{ W/cm}^2$  is illustrated. The baseline surface produces stationary vapor slugs that cover the heated area, while the microstructure produces organized movement of vapor slugs..... 125

Figure 4.18 The number of active slots at different heat fluxes in microgravity is represented in the plot. .... 127

Figure 4.19 Preferential vapor ejection from a slot in microgravity at  $2.4 \text{ W/cm}^2$  is illustrated in the image sequence. A reference image depicting the location of the slot is appended for ease of viewing. The location of the slot is outlined in the following images to improve clarity. .... 128

Figure 4.20 The image sequence shows slug mobility across the sawtooth microstructure at a heat flux of  $2.4 \text{ W/cm}^2$ . The frames are spaced one second apart. Three slugs depart over six seconds by sliding across the microstructure. The side view of the COHU orientation is shown on the top right to improve clarity. .... 130

Figure 4.21 The change in cold zone temperature as vapor slugs move toward the pressure relief membrane is illustrated. The input heat flux is  $2.4 \text{ W/cm}^2$ ..... 131

Figure 4.22 Liquid pockets were observed between the crests and troughs of the microstructure beneath moving vapor slugs. The input heat flux is  $2.8 \text{ W/cm}^2$  for the depicted high-speed images.

..... 132

## List of Tables

Table 2.1 The test surface geometries and their intended configurations for the microgravity experiments .....	34
Table 3.1 Liquid film thicknesses calculated from the force balance model.....	50
Table 3.2 Extrapolation of the ratio of the radii of curvature and the slug velocity for an 85°-5° sawtooth microstructure from the obtained empirical results.....	56
Table 3.3 The raw frames per second from the camera interfacing software due to the default settings .....	71
Table 3.4 The description of each planned test for the ASCENT project .....	73
Table 4.1 The important pre-launch milestones for the ASCENT payload.....	95
Table 4.2 Test parameters for the ASCENT investigation .....	99
Table 4.3 Test parameters for the microgravity studies in Figure 4.10 .....	113
Table 4.4 Mobility diameters of the vapor bubbles on the 60°-30°sawtooth microstructure in microgravity .....	124
Table 4.5 Vapor bubble departure frequency ranges with varying heat flux for the slots.....	129
Table A.1 The thermophysical properties of FC-72 at 1 atm .....	152

# NOMENCLATURE

## Acronyms

ASCENT	Asymmetric Sawtooth and Cavity-Enhanced Nucleation-Driven Transport
CHF	Critical Heat Flux
CTE	Coefficient of Thermal Expansion
EDM	Electric Discharge Machining
ISS	International Space Station
MSG	Microgravity Science Glovebox
NPBX	Nucleate Pool Boiling eXperiment
ONB	Onset of Nucleate Boiling
TED	Thermoelectric Device
PFMI	Pore Formation and Mobility During Controlled Directional Solidification in a Microgravity Environment Investigation

## Symbols

A	area, m <sup>2</sup>
Bo	Bond number
C <sub>d</sub>	drag coefficient
C <sub>m</sub>	added mass coefficient

D	diameter, m
F	force, N
g	gravity, $\text{m/s}^2$
H	height, m
h	heat transfer coefficient, $\text{W/m}^2\text{K}$
I	supply current, A
k	thermal conductivity, $\text{W/mK}$
L	length, m
m, n	number of sawteeth
P	pressure, Pa
Q	power supplied to the heater, W
$q''$	heat flux, $\text{W/cm}^2$
R	radius, m
r	radius of curvature, m
T	temperature, $^{\circ}\text{C}$
V	velocity, m/s

### **Greek symbols**

$\Delta T_{\text{sub}}$	inlet subcooling, $^{\circ}\text{C}$
-------------------------	--------------------------------------



$\mu$	dynamic viscosity, $\text{Nsm}^{-2}$
$\nu$	kinematic viscosity, $\text{m}^2/\text{s}$
$\rho$	density, $\text{kg}/\text{m}^3$
$\sigma$	surface tension, $\text{N}/\text{m}$
$\theta$	saw tooth angle, degree

### **Subscripts**

l	liquid
sat	saturation
w	wall
v	vapor

# CHAPTER 1 INTRODUCTION

Two-phase electronic thermal management supports small form-factor devices with high-heat flux density, enabling the practical design of next-gen electronics. Phase-change solutions leverage consistent vapor removal from a heated surface to maintain device operating temperatures within design limits. Though buoyancy aids the effective removal of vapor bubbles in multiple surface orientations under terrestrial gravity, microgravity, and adverse gravity applications are limited by stationary vapor bubbles hindering effective heat transfer, leading to burnout of electronic devices.

As the space exploration industry also grows rapidly, thermal sciences are at a unique intersection with the ability to benefit both earth and space applications. Space provides the opportunity to study dominant heat transfer mechanisms without the interference of buoyancy forces. The leverage of this unique opportunity is amplified in two-phase systems, as the phase-change process is severely disrupted by the diminished Archimedean force. Dielectric fluids are a popular process fluid as they can be incorporated in immersion cooling systems, where heat can be taken away at the source rather than using a secondary solution like a heat sink or a cold plate.

For example, the Perseverance Rover launched in 2020 contains an array of electronic instruments for scientific research and exploration. It has nine engineering cameras, seven science cameras, and seven cameras for entry, descent, and landing – totaling twenty-three cameras [1]. It even contains Ingenuity, a helicopter, a soil sample collection system, and a robotic arm [2]. While these components enable revolutionary space exploration, they also burden the system's thermal dissipation requirements at both the component level and the functional range of the entire rover. The added challenges with these systems are that they are quite far away to depend on maintenance or corrective tools to ensure optimal operation. In addition, the components were designed to

perform nominally in the ambient extremes of the Mars environment with independent control zones for different hardware systems. The heat removal system of the rover is a mechanically pumped fluid loop with Freon 11 as the working fluid, with a series of passively-activated control valves to direct fluid flow to move heat as needed [3]. As the appetite for additional data from space and low earth orbits increases, multiple reliable and passive thermal management systems are essential to reliably operate silicon-based devices far away from Earth.

Moore’s law has enabled the development of an ecosystem that has led to the rapid increase in the number of transistors in chips and has helped build cost-optimized integrated circuits. An increase in the number of transistors has also driven an increase in the maximum chip power and a corresponding increase in the maximum chip heat flux, as shown in Figure 1.1(a). In addition, the majority of failures in electronic equipment are sourced from excessive device temperatures, as shown in Figure 1.1(b).

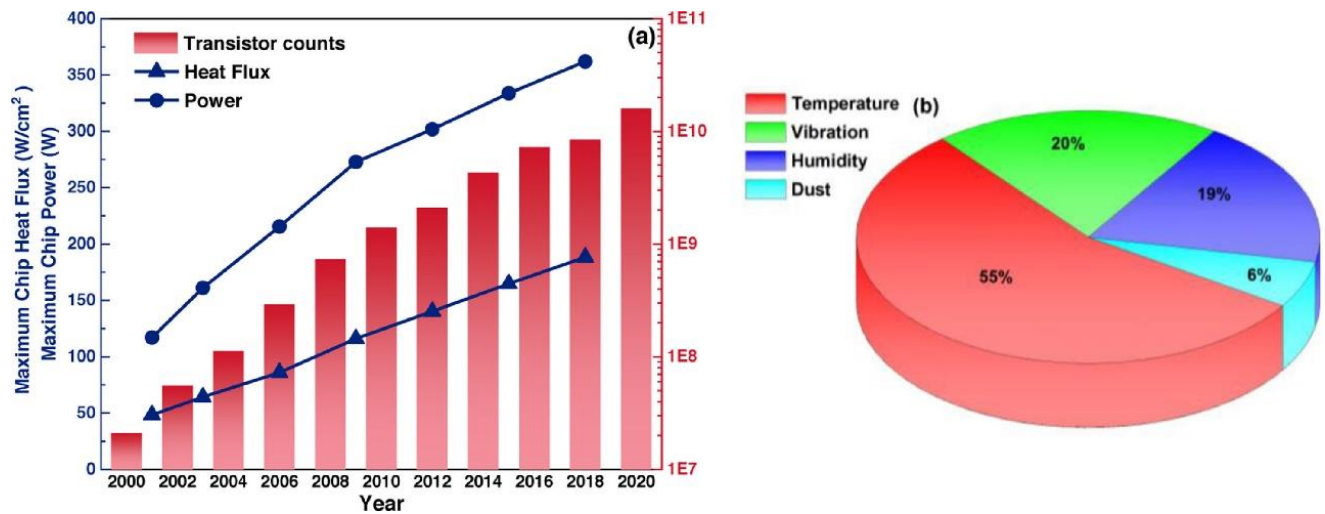


**Figure 1.1(a) The increase in the maximum chip power and transistor counts from 2000-2020 (b) The causes of failure in electronic equipment [4].**

## 1.1 Objectives of the study

The primary objectives of Asymmetric Sawtooth and Cavity-Enhanced Nucleation driven Transport (ASCENT) project are detailed below:

- (I) Verify lateral bubble motion observed in microgravity flight experiments aboard the ISS lab
- (II) Perform ground-based experiments and analysis to validate/ refine model and explore terrestrial applications; and
- (III) Validate and refine the steady state bubble motion model based on ISS and terrestrial data.

The long-term goal of this multi-stage project is to verify passive vapor bubble motion from the microstructure in different orientations terrestrially and in microgravity conditions. The exhaustive experimental results are expected to provide improved information on the near-wall behavior associate with the microstructure and enable numerical simulations of two-phase physics from the microstructure. Passive vapor mobility from electronic surfaces enables upgradation of in-flight hardware for future microgravity missions while enabling the development of pump-less flow loops for consumer hardware terrestrially.

The novel contributions of the research work are outlined below

1. Passive vapor mobility induced in microgravity conditions - enables upgradation of in-flight hardware for future microgravity missions while enabling the development of pump-less flow loops for consumer hardware and spacecraft systems terrestrially.

2. The sawtooth microstructure is expected to be a self-regulating thermal management technique which can increase the rate of heat dissipation with an increase in heat flux within a selected operating range for the given experimental conditions.
3. Mechanistic understanding of vapor bubble dynamics from the sawtooth microstructure in terrestrial upward-facing, downward-facing and in microgravity conditions.
4. Development and refinement of model to predict liquid film thickness to enable numerical simulation of two-phase physics from the sawtooth microstructure to explore the feasibility of varying sawtooth structures.

## **1.2 Bubble dynamics from downward-facing surfaces**

Vapor dynamics from a heated surface influences heat transfer extensively in two-phase heat transfer systems. A terrestrial downward-facing surface leads to stagnant vapor bubbles, and severely deteriorating heat transfer. Guo & El-Genk [5] observed that the quenching time for water along a downward-facing surface is six times that of the  $5^\circ$  inclination, with the critical heat flux significantly lower than other inclination angles. At the critical heat flux, boiling ceases to be an effective form of heat transfer as the heated surface dries out and leads to a rapid increase in temperatures. Dielectric liquids like HFE-7100 [6] and FC-72 [7]–[9] followed this trend at near atmospheric pressures, with a stable vapor film curbing the maximum input heat flux. The change in vapor bubble dynamics near CHF for saturated FC-72 in different orientations is illustrated in Figure 1.2. For PF-5060, El-Genk et al. [10] observed that downward-facing boiling stimulates Marangoni convection along the surface and hypothesized that the thin liquid film sets up a local surface tension gradient along the interface. The authors reasoned that the inertia of the rising liquid extended the vapor bubbles laterally, leading to the eventual release of the vapor mass along the sides by Marangoni convection, as shown in Figure 1.3. Later studies noted that variations in

dimensions [11] and the aspect ratio [12] of the downward-facing surface improved the critical heat flux limit by encouraging vapor motion across the downward-facing surface.

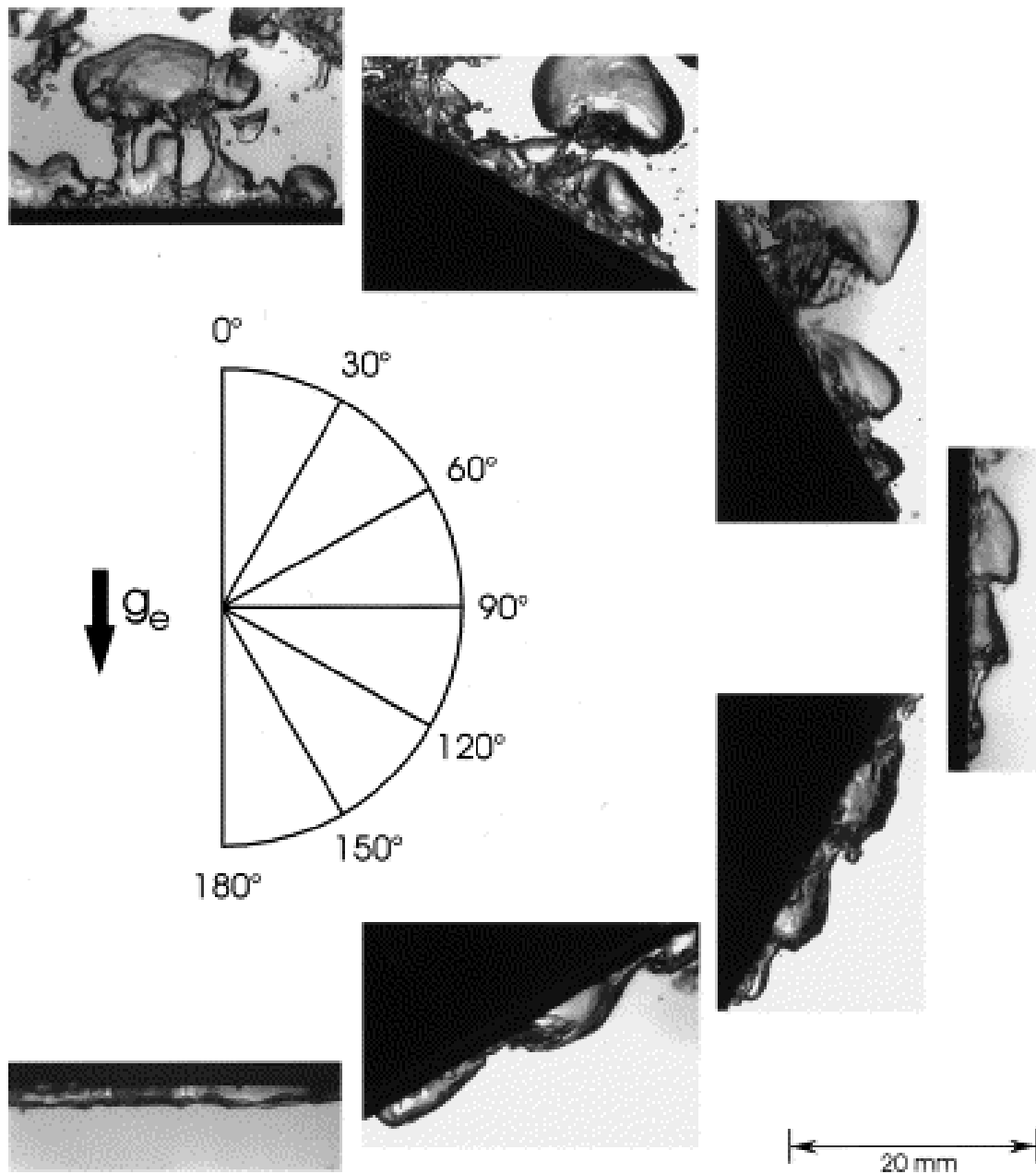
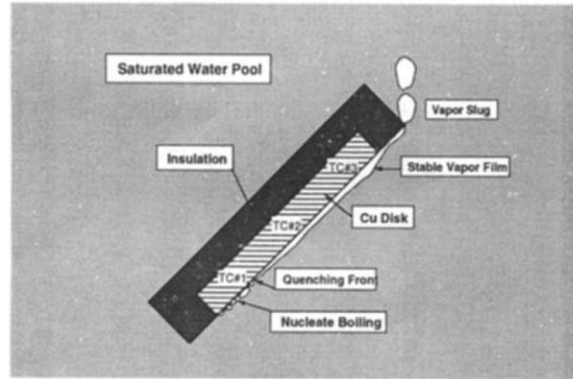
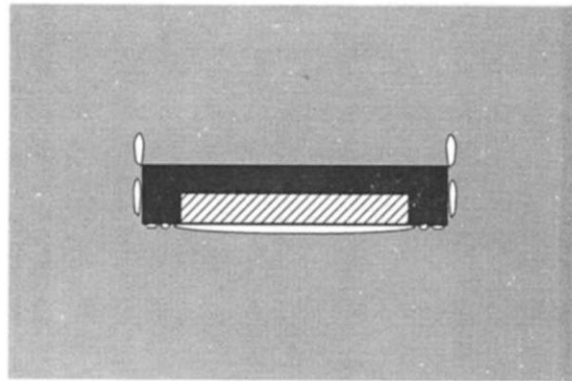


**Figure 1.2 The change in vapor bubble dynamics near CHF at different orientations [7].**



(a) Inclined position



(b) Downward Facing Position

**Figure 1.3 The illustration of boiling behavior on an inclined downward-facing surface (a) compared with a downward-facing surface (b) [5]**

The enhancement of downward-facing nucleate boiling has also been pursued by introducing surface enhancements like honeycomb structures [13], conical pin fin structures [14], and interconnected grooves [15] to rewet the heated surface. The difference in vapor dynamics between a plain and a honeycomb surface is illustrated in Figure 1.4. Recent studies have also achieved improvements by seeding nanofluids [16], [17], flow impingement [18], phase-separating wick [19], and surface-active ionic liquids [20]. Other creative pathways for vapor bubble removal in adverse gravity situations include surfactants [21] and acoustic streaming [22].

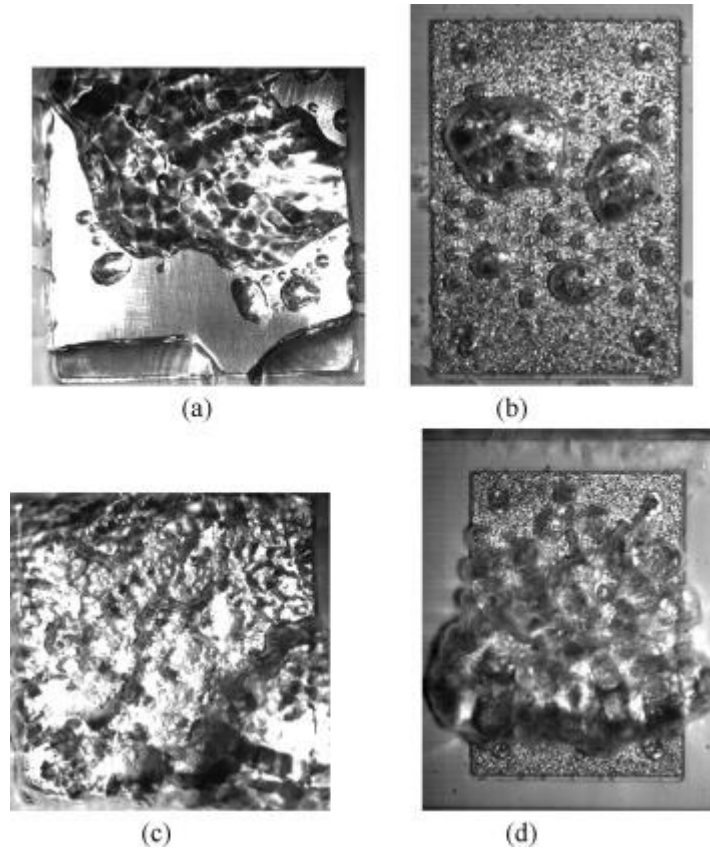
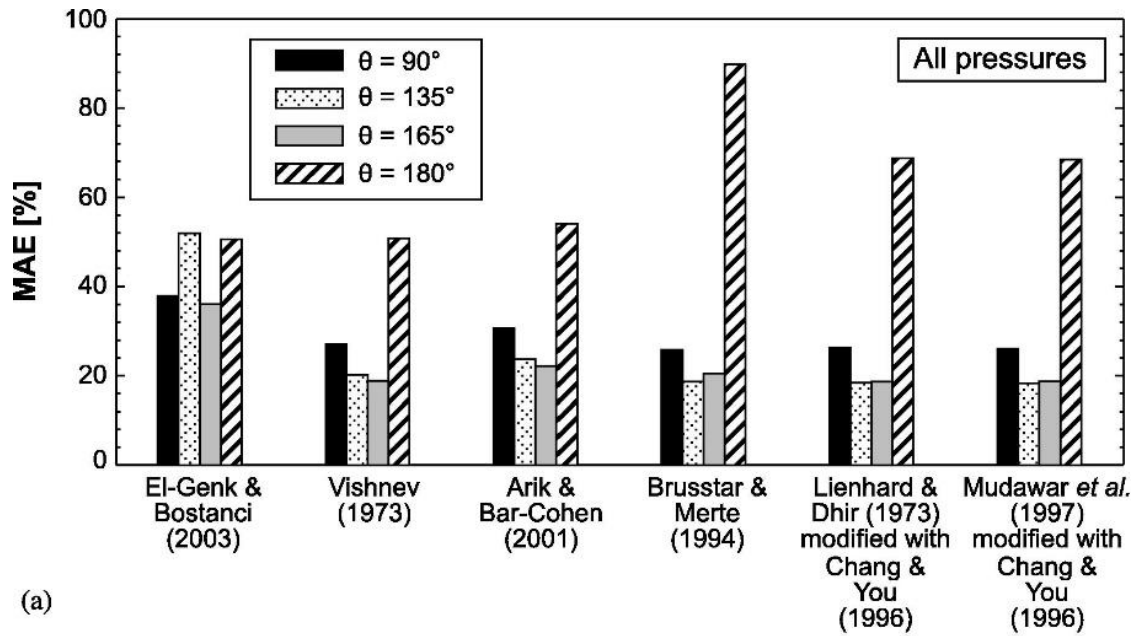


**Figure 1.4 The difference in boiling behavior between a plain surface and a honeycomb surface at a low heat flux and near-CHF. (a) bare, heat flux = 0.02 MW/m<sup>2</sup>, (b) honeycomb, heat flux = 0.02 MW/m<sup>2</sup>, (c) bare, heat flux = 0.25 MW/m<sup>2</sup> (near CHF), (d) honeycomb, heat flux = 0.42 MW/m<sup>2</sup> (near CHF) [13].**

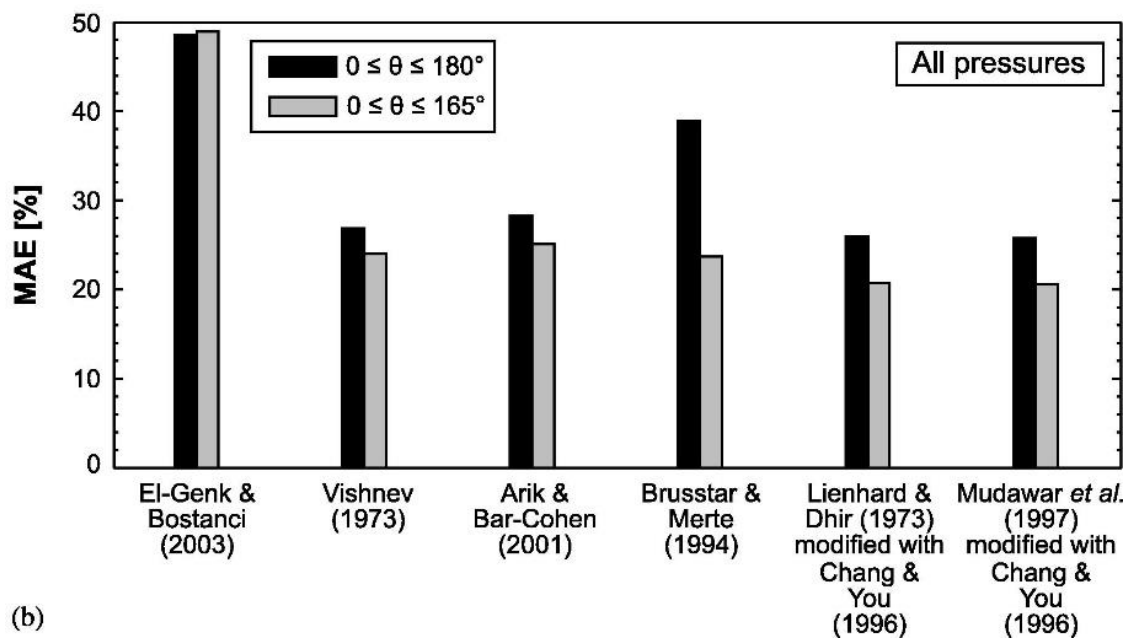
However, an incomplete understanding of the liquid-vapor interface near the wall leads to multiple CHF models [23]–[25] losing accuracy when the downward-facing/near-downward-facing orientation is included, as shown in Figure 1.5. Though the studies address the need to remove vapor from the surface for effective phase-change heat transfer, the methods are either actively managed or propose surface modifications and features that are infeasible for electronic surfaces in reduced gravity situations. While flow boiling studies [26], [27] hint at enticing advances, the



relative complexity of flow loops and the additional power demands are considerable roadblocks for scalable implementation. Passive, high-heat flux dissipation combining the advantages of flow and nucleate pool boiling offer attractive trade-offs.



(a)



(b)

Figure 1.5 (a) The mean absolute error of different models and correlations at various orientation angles are illustrated. (b) The mean average errors of the overall models and correlations when the downward-facing is included [28].

Terrestrial downward-facing surfaces can provide insight into the vapor bubble dynamics in microgravity, as buoyancy forces do not assist in the removal of vapor bubbles from the surface. A study conducted on the dynamics of the vapor slug in different orientations between  $120^\circ$  and  $170^\circ$  by Kim et al. [29] found that the translation speed of the sliding vapor slug was dependent on the size of the vapor slug and the orientation angle, as shown in Figure 1.6. A similar study with an inclined heater surface by Qiu and Dhir [30] led to the observation of a wedge-shaped liquid region between the vapor slug and the heated surface. The film thickness increased from the downstream side to the upstream side of the vapor slug. Similar dynamics observed in the lower part of a horizontal tube by Kim et al. [31] resulted in a force balance model to account for the dominant forces that contribute to the sliding motion. While buoyancy, quasi-steady drag, and added mass forces (from the motion of the surrounding liquid) were dominant, the authors argued that the wake generated from a previous bubble might contribute to the motion and factored this correction into their model. For a bubble sliding upward in a narrow rectangular channel, Ren et al. [32] found that the drag force due to the difference in velocity between the bubble and liquid drove the sliding motion for decreasing bubble sizes. The lack of clarity about the liquid-vapor interface for downward-facing surfaces, along with the dynamic phenomena associated with vapor motion for inclined surfaces, hamper the development of electronic cooling solutions for this orientation.

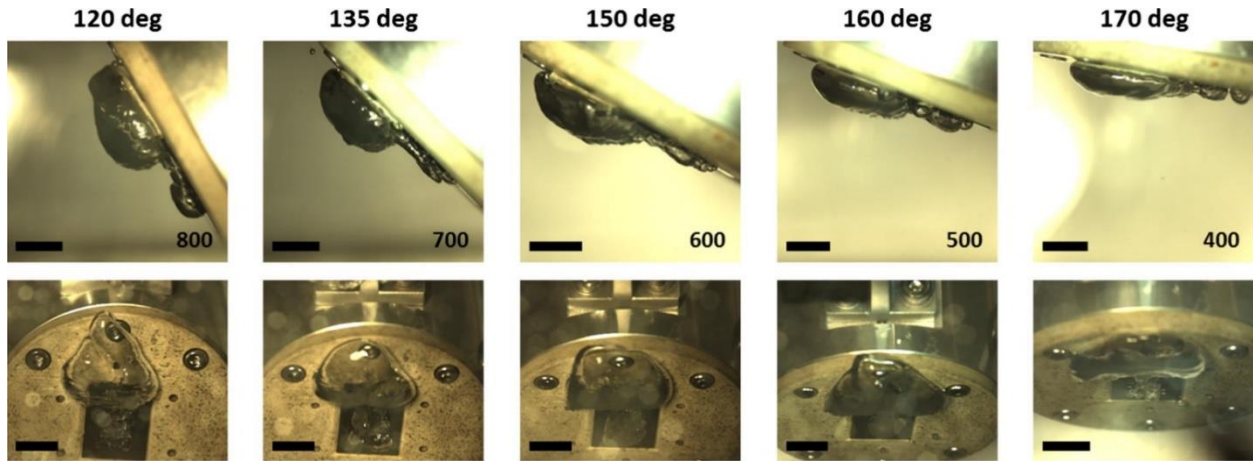


**Figure 1.6** The side (top) and front (bottom) angles of the vapor slug in the downward-facing orientation at different heat fluxes. The scale bar indicates 10 mm, and the number indicates the heat flux in  $\text{kW/m}^2$  [29].

A specific surface modification, an asymmetric sawtooth microstructure, has propelled liquid droplets in the Leidenfrost regime [33], directed vapor bubbles in the upward-facing surface in the nucleate boiling regime [34], and induced self-propelled sliding vapor in a parabolic flight experiment [35]. Successive studies by the group have also demonstrated predictable condensate mobility from the microstructure, suggesting its feasibility in a pumpless self-regulating phase-change thermal management system [36], [37]. The current study explores the microstructure for the adverse gravity surface orientation to move vapor across heated microelectronics surfaces.

### **1.3 Bubble dynamics in microgravity experiments**

Nucleate pool boiling is an effective heat transfer technique due to the heat dissipated by the phase-change process and vapor removal from the heated surface. Diminished gravity environments pose a considerable challenge in implementing heat dissipation on high-heat flux electronic surfaces, as the density differences do not drive the vapor away from a surface. Nucleate pool boiling in microgravity has been studied through parabolic flight experiments, drop towers, and experiments

aboard the International Space Station. In a review of the early attempts by researchers, Straub [38] summarized the results from drop tower experiments [39], [40], parabolic flight experiments and sounding rockets [41]–[44], and three Space Shuttle missions [45]–[47]. Multiple refrigerants like R113, R123, R134a, R11, and R12 were experimentally tested on various heater geometries, including platinum wires, small spherical heaters (thermistors), plates and tubes consisting of a quartz substrate with a thin gold film at different subcooled and saturated conditions. He proposed that the surface tension forces dominate in reduced gravity environments. The heat transfer mechanism is primarily governed by liquid-vapor interface dynamics arising from thermocapillary convection. Lee et al. [42], Ohta [43], and Oka et al. [44] observed a large bubble levitating over a flat heated surface and a thin liquid layer separating it from the wall. However, Zell et al. [41] observed a large bubble covering a large part of the heated surface and in contact with the wall. The author also noted that parabolic flight experiments suffered from gravity fluctuations, rendering fluid science investigations challenging to achieve. Straub [38] recommended extensive experimental studies in pristine microgravity environments like the International Space Station with different heater topologies like microstructures to further understand the complex mechanisms associated with the liquid-vapor phase change heat transfer.

Though heat transfer was found to be weakly dependent on microgravity, the clear consensus from these early studies pointed towards varying vapor bubble dynamics in reduced gravity environments. Using transparent film heaters in a parabolic flight campaign, Kubota et al. [48] visualized liquid-vapor behavior with degassed FC-72 in microgravity. They found that the sliding bubbles on the heater surface enhanced heat transfer coefficients in the short-term microgravity environment and that the direction and level of residual gravity severely influenced the liquid-vapor interface behavior. Controlled temperature tests with FC-72 on a microheater array (2 mm

x 2 mm to 7 mm x 7mm) with a transparent heater enabled imaging to visualize contact line underneath the bubbles in parabolic flights by Kim et al. [49] and Christopher and Kim [50]. With the same heater aboard the International Space Station in Perfluoro-n-hexane (3-M trade name – FC-72) [51], Raj et al. observed that the entire heater was covered by vapor at low subcooling. They also proposed a framework for predicting the wall heat flux at different vapor subcooling and heater sizes by using the ratio of the heater length to the capillary length scale. In surface tension-dominated boiling (SDB), the heat transfer was dependent on heater size, while in buoyancy-dominated boiling, the heat transfer was independent of the heater size. However, the lack of vapor bubble imagery from the side and bottom precludes in-depth discussion of further implications from the framework. While pointing out this shortcoming, Warriar et al. [12] used the same process fluid to study vapor generation from five cylindrical cavities ( $D \sim 16 \mu\text{m}$ ) located on a polished aluminum disc to study temperature-controlled nucleate boiling tests aboard the International Space Station. Similar to previous researchers, a large central bubble attached to the heater surface covered the entire heater at  $\Delta T_{\text{sub}}$  between 7.6 and 13.5° C, as shown in Figure 1.7. Nucleation was triggered by increasing the temperature of the nucleation site until incipience was recorded on the temperature trace. The boiling curve was then generated by increasing the temperature of the wafer in increments of 1-3°C every 2 minutes. The authors compared terrestrial data to microgravity from previous studies. They concluded that fluid confinement and heater size might be critical in hindering the extrapolation of experimental results between gravity levels. Most studies utilize a smooth surface to study nucleate pool boiling in microgravity, as seen in the section above.

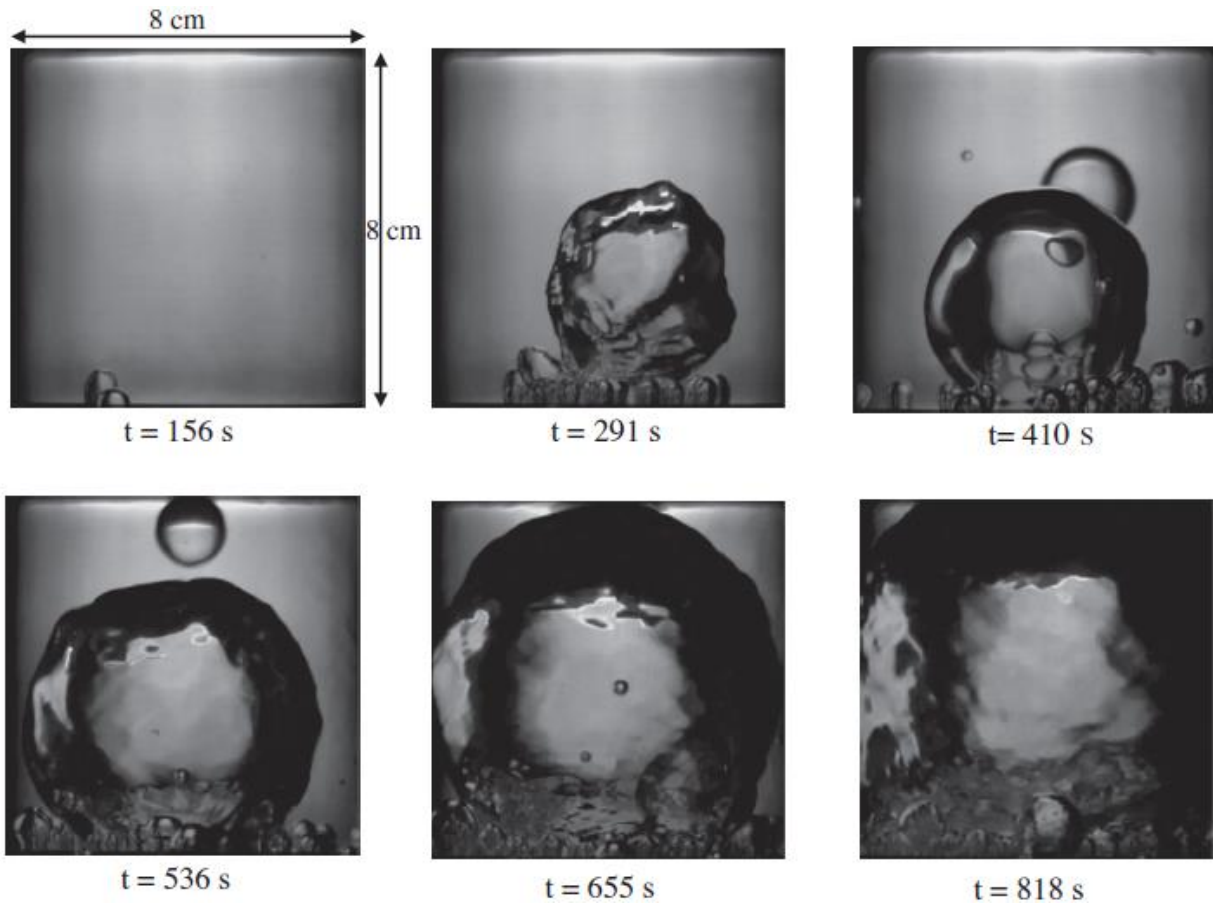


**Figure 1.7 Sequences of images showing bubble nucleation and growth on the surface of the heater with smaller bubbles coalescing to form one large, central bubble in microgravity [52].**

In highly subcooled ( $T_{\text{sub}}=40\text{ K}$ ) experiments conducted in the drop tower Beijing, Xue et al. [53] achieved steady-state boiling on a small ( $10\times 10\times 0.5\text{mm}^3$ ) silicon chip using FC-72. They observed vapor bubble growth and coalescence creating a large bubble and reasoned that the lack of quenching liquid at the base of the bubble created a local hotspot, as shown in Figure 1.8. At low subcooling, Ohta et al. [54] argued that the transition to eventual burnout is unavoidable even at low heat fluxes. However, a recent study by Kannengeiser et al. [55] attributed these differences

to pressure changes associated with the subcooling instead, noting that subcooling strongly influences bubble size. Such disagreements are common in short-term microgravity boiling studies, as noted in investigations by Zell et al. [41] and Lee et al. [42], who studied R-113 on a flat plate using a gold-coated heater but derived different boiling curves.

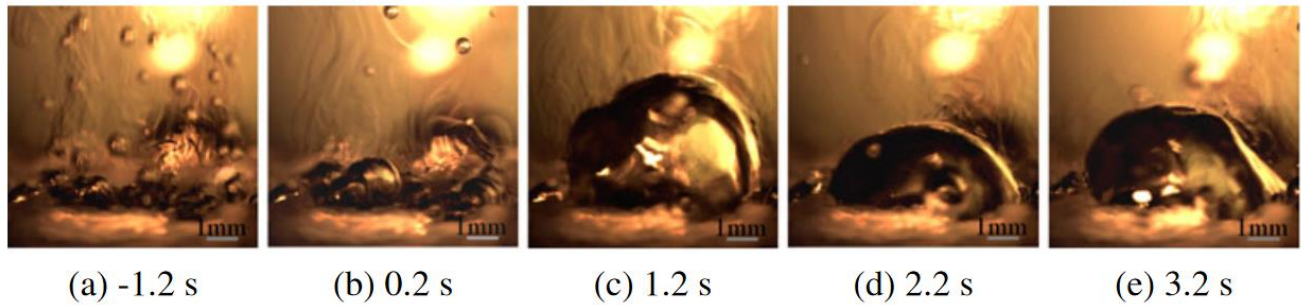


**Figure 1.8 The change in boiling behavior from terrestrial gravity ( $t < 0$ s) and the vapor behavior in short-term microgravity ( $t > 0$  s) near the critical heat flux [53].**

Various techniques have been attempted to detach the vapor from the nucleating surface in microgravity. In a follow-up study to their drop tower experiment using a smooth surface [53], Zhang et al. [56] noticed an enhancement with micro pin finned surfaces extending 60 or 120  $\mu\text{m}$  above the surface. The authors attributed the enhancement to improved thermocapillary flow from the quenching liquid across the increased surface area. Imposed electric fields enabled the departure of larger bubbles in the ARIEL experiment [57], substituting for the buoyancy forces in terrestrial gravity. Combining these techniques reportedly improved [58] both the near-wall and secondary mechanisms, delaying the critical heat flux. Similar detachment attempts have also been made by exaggerating the surface-tension gradients [59] between the test surface and the working fluid. Stagnating vapor is not unique to the microgravity environment as dielectric liquids like



HFE-7100 [6] and FC-72 [7]–[9] displayed a similar trend in terrestrial downward-facing surfaces, with a stable vapor film curbing the maximum input heat flux.

Limited studies investigate the effect of engineered microstructure or enhanced surface on pool boiling performance in microgravity conditions. Shi et al. [60] investigated the impact of a super-hydrophilic metal foam against a smooth brass surface utilizing a drop tower. Though steady-state boiling could not be achieved, the authors reported a 12.9% enhancement over untreated metal foam over 3.6 seconds. The difference was attributed to increased bubble departure frequencies from the metal foam structure. Similarly, Zhang et al. [61] reported enhanced heat transfer from the micro-pin-finned surface and attributed the difference to increased bubble departure frequency. Other studies also reported heat transfer enhancement in microgravity due to Marangoni flow induced by concentration gradient [62], electric force to substitute the weakened buoyancy force [63], [64], and oscillatory motion of the heated surface [65].

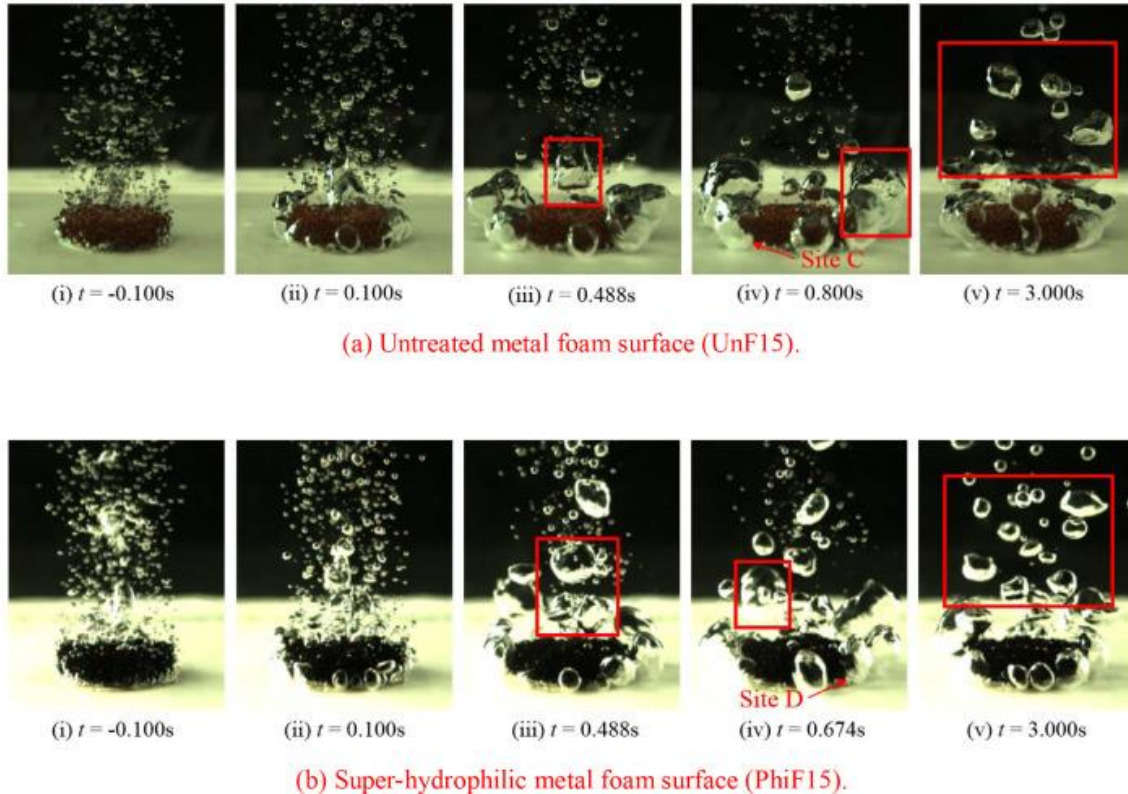


**Figure 1.9 The effect of metal foam wettability on the number of generated vapor bubbles under short-term microgravity (drop-tower experiment) [60].**

Engineered surfaces have produced predictable vapor germination sites in microgravity, following the trends seen in terrestrial gravity. Zhao et al. [66] observed an explosion of vapor at nucleation incipience in microgravity during the initial run with an  $\text{Al}_2\text{O}_3$  substrate. The authors observed that triggered cavities led to residual vapor in microbubbles, leading to lower wall superheats at incipience in subsequent runs. Vapor bubbles attached to the surface also suppressed nucleation from neighboring cavities in the dielectric liquid (FC-72).

Replacing the buoyancy force with a secondary force has aided vapor bubble departure in microgravity environments. The Reference mUltiscale Boiling Investigation (RUBI) [67] studied

a single bubble nucleating from an artificial nucleation site on a heated surface with FC-72 as the test liquid. An electrode above the nucleation site imposed an electrostatic field. No detachment occurred without an electric field, while bubbles consistently detached at varying electric fields, as shown in Figure 1.10. The electric field also reduced the bubble growth rate and the vapor bubble geometry at the detachment. Detachment of germinated vapor bubbles in microgravity in flow boiling has also been attempted. Ma and Chung [68] studied bubble nucleation, growth, and departure in microgravity at different flow rates. Bubble departure frequency increased with increasing flow rate, while bubble growth was inhibited from the nucleation site.

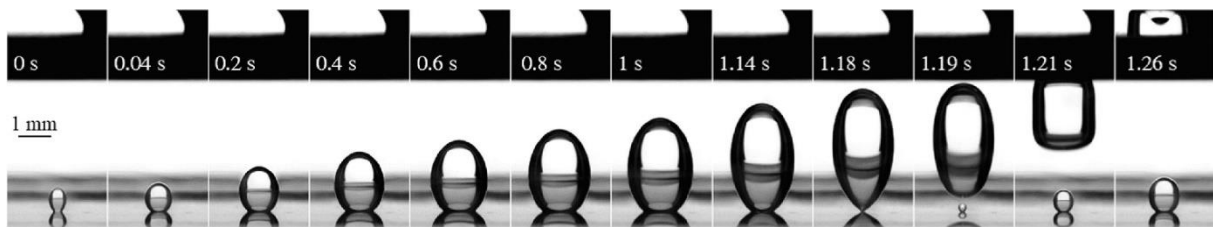


**Figure 1.10 Bubble detachment under the influence of an electric field at an electrode distance of 6 mm and an electrode voltage of 15 kV [67].**

Despite multiple studies espousing the difference in vapor dynamics between terrestrial gravity and microgravity, limited data exist on the liquid-vapor interface in microgravity conditions. Constant heat flux conditions are common in most engineering applications, and there is scarce data on boiling data in high-quality microgravity environments. While helpful in interpreting overall trends, short-term microgravity environments are unsuited for capturing the complex minutiae associated with heat transfer enhancement.

Prior microgravity experiments attest to the weak buoyancy forces inhibiting the nucleate boiling process due to growing vapor on the heated surface. The current study explores the feasibility of

periodic slots on repeating sawtooth structures on a titanium surface as a surface enhancement for reduced gravity environments. Passive vapor mobility and heat transfer enhancement from heated electronic surfaces can help build high heat-flux thermal management systems for microgravity applications. The reported sawtooth structure has also enabled preferential vapor motion in downward-facing heated surfaces [69], open-channel configuration [70], and a prior parabolic flight experiment [35].

#### **1.4 Prior efforts from the sawtoothed surface**

The present study details the efforts to utilize repeating asymmetric microstructure to induce passive vapor mobility in microgravity experiments aboard the International Space Station (ISS). The work draws inspiration from a study by Linke et al. [33], who demonstrated the passive motion of liquid droplets in the Leidenfrost regime by use of repeating millimetric-scale surface asymmetry in the form of  $60^\circ$ - $30^\circ$  ratchets. Kapsenberg et al. [71] added re-entrant cavities on the long slopes of the  $60^\circ$ - $30^\circ$  sawtooth profile and demonstrated liquid motion parallel to the surface due to bubble growth for a terrestrial upward-facing surface, as shown in Figure 1.11.

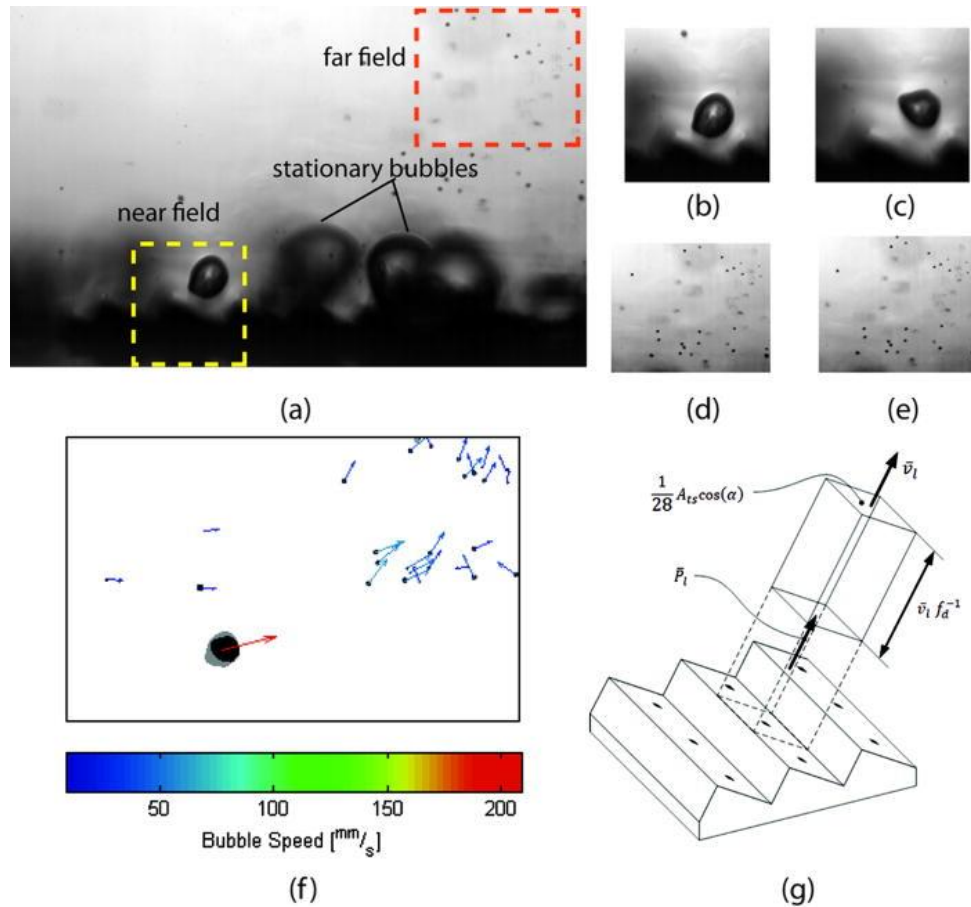


**Figure 1.11 Collage of images detailing the net axial component of velocity from vapor bubble generated on the long slope of the symmetric sawtooth microstructure. Image (g) denotes a unit cell of influence directing liquid motion around the vapor bubble [34].**

A parabolic flight experiment conducted with the sawtooth profile by Thiagarajan et al. [72] observed vapor bubbles sliding across the ratcheted microstructure in velocities up to 27.4 mm/s in microgravity flight experiments, as shown in Figure 1.12. The generated FC-72 vapor bubbles were also much larger than the bubbles observed in terrestrial gravity, similar to other microgravity experiments.

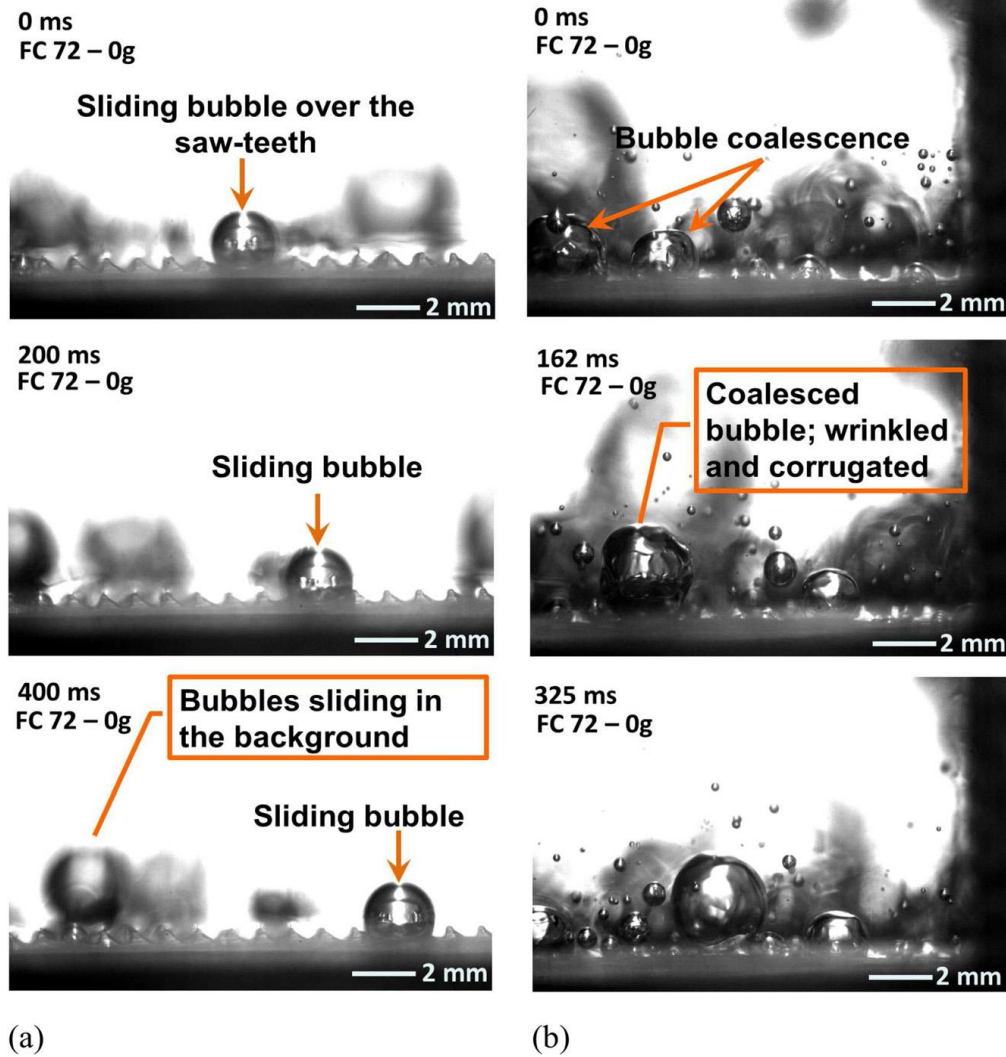


**Figure 1.12** Bubble dynamics in FC-72 along the sawtooth microstructure under microgravity during the parabolic flight experiments at a)  $q=0.5 \text{ W/cm}^2$  b)  $q= 1.4 \text{ W/cm}^2$  [72].

In continued efforts from this group, Bhavnani et al. [70] presented a slug transport model using high-speed images obtained from an open-ended channel configuration with the ratcheted microstructure on the top and bottom walls. A flash procedure (reduction in chamber pressure with no heat input) induced vapor slugs that demonstrated clear preferential motion towards the long

slope direction, as shown in Figure 1.13. The mechanistic Couette-Poiseuille flow model hypothesized that the driving force for the slug motion is due to the pressure difference between the crest and the trough of the sawtooth, which leads to a net pressure gradient in the direction of the long slope. The shear force between the channel walls imparted a retarding force to the vapor slug, and the liquid layer height on the walls was obtained from the estimated slug velocity. A similar model [72] was presented for the parabolic flight microgravity experiments, but both models require interfacial dynamics data to discuss the contribution of the dominant force to the vapor motion. Therefore, the vapor bubble dynamics of the ratcheted microstructure in adverse gravity conditions and microgravity conditions require further investigation.

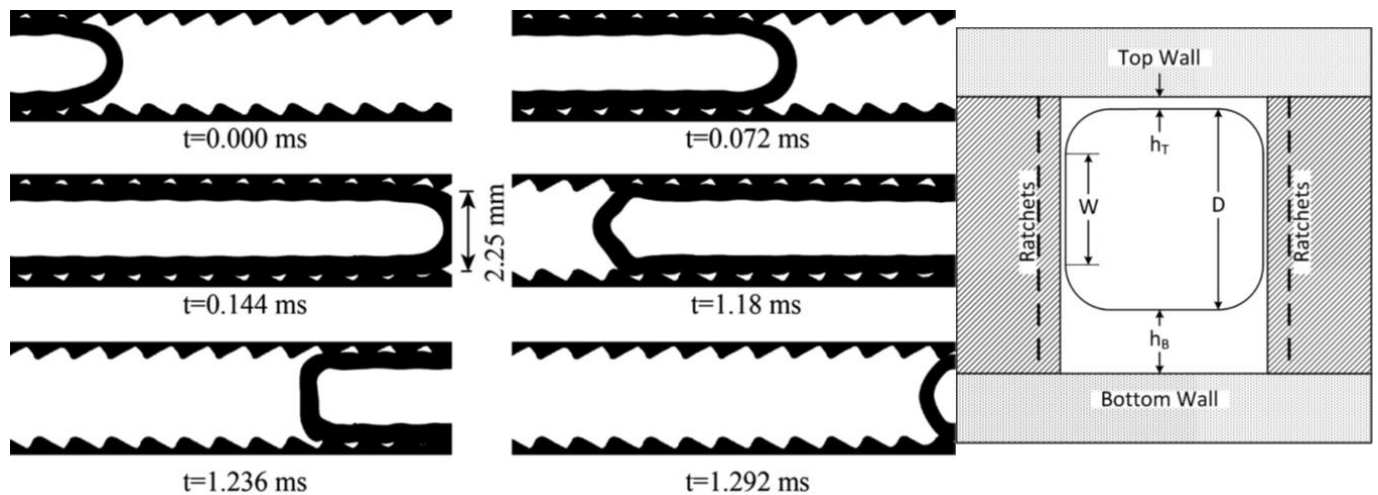


**Figure 1.13 Video sequence recorded during a flash test (left) and a cross-sectional schematic of the bubble (right) indicating the hypothesized bubble shape and corresponding liquid layer thicknesses between the slug and the top and bottom walls [70].**

While many short-term and long-term microgravity studies recognize the importance of removing vapor from the surface in nucleate pool boiling, the enhancements reported do not provide a

consistent framework for repeatable and reliable application in microelectronics thermal management. Vapor nucleation from artificial and engineered sites on a surface has also not been studied extensively in prior microgravity research. The current study aims to study vapor mobility in a long-term microgravity environment from an asymmetric sawtooth microstructure showing orderly vapor mobility in a terrestrial downward-facing surface [69] and vapor sliding motion in a parabolic flight experiment [72]. This experimental investigation was conducted aboard the International Space Station (ISS) in a constrained enclosure resembling form factors representative of high-heat flux electronic devices from November 2022 to January 2023. The results are compared against terrestrial downward-facing surfaces in the same enclosure to differentiate the vapor mobility from the proposed surface enhancement in varying gravitational levels.

### **1.5 Summary**

The consensus from the microgravity studies points to vapor stagnation over smooth, heated surfaces in microgravity conditions. A central large vapor bubble was produced due to bubble growth and coalescence, eventually leading to dryout in some investigations. This phenomenon was observed at different levels of microgravity through different investigation methods like drop towers, parabolic flight experiments, the space shuttle, and the International Space Station. Substituting the buoyancy force is crucial to improving heat transfer in reduced gravity situations. Many different forces have been explored to replace the buoyancy force and encourage vapor bubble motion, including imposed electrostatic fields, excessive surface tension gradients (Marangoni effects), and flow boiling at different flow rates. However, the passive and self-induced motion of vapor bubbles in microgravity environments can enable the development of pump-less cooling solutions for high-density electronic devices.



While limited studies have explored microstructure-based enhancement, the vapor bubble dynamics in short-term microgravity environments suffer from several transitory effects. Further, pool boiling characteristics in confined test chambers representative of high-heat flux electronics are not available to anticipate the vapor bubble dynamics in similar devices. Long-term experiments in high-quality microgravity environments on engineered structures are necessary to observe liquid-vapor dynamics without buoyancy forces.

Similarly, the downward-facing studies point to critical heat flux at lower heat fluxes due to vapor crowding along the heated surface. The buoyancy forces pin the vapor against the heated surface, leading to stationary vapor bubbles. The changes in length and aspect ratios of the heated surface have encouraged vapor departure along the sides through Marangoni convection. Heat transfer enhancement has also been pursued through engineered structures like fins, grooves, honeycomb structures, and interconnected structures to rewet the heated surface and prevent early dryout for the downward-facing surface. The consensus from the available studies points to the need for passive vapor removal combined with heat transfer enhancement to improve heat transfer outcomes in the adverse gravity orientation significantly.

The current work addresses the issues in two-phase heat transfer where vapor is not readily detached from the heated surface through the asymmetric sawtooth structure to influence vapor bubble dynamics and heat transfer.

## CHAPTER 2 Test Surfaces

### 1.1 Test surface fabrication – Auburn University

The test surfaces were fabricated using powder bed fusion, a metal additive manufacturing technique. Contrary to conventional processes, where planes and cylinders are the most straightforward geometrical entities to manufacture, additive manufacturing (AM) can produce virtually any geometrical structure. Powder bed fusion for metals is accomplished by additively fusing layers of metal powder to fabricate a part. After a layer of metal powder is deposited, a laser delivery system, supported by a scanner, focuses the laser beam onto a spot, as shown in Figure 2.1. A recoater blade disperses the metal powder from the delivery system, while a piston-mounted build platform is lowered to a level that matches the thickness of the slice that needs to be melted. The above process is repeated for all points on the build platform to complete a layer. An inert gas, like nitrogen or argon, is passed over the bed to prevent oxidation and clear any residual spatter from the previous layer [1].

The fabrication steps are repeated layer-by-layer to complete a part. Complex geometry, like a ratcheted microstructure with embedded cavities, can be manufactured using laser powder bed fusion. Various metals and their alloys can be fabricated by controlling the process parameters like layer thickness, spot size, powder bed temperature, laser power, and scanning speed. While powder-based additive manufacturing technologies can pose their own challenges and constraints for specific design features, the ability to obtain the complex microstructure in 'one step' for this study was prioritized to reduce the overall lead time of the multi-stage project.

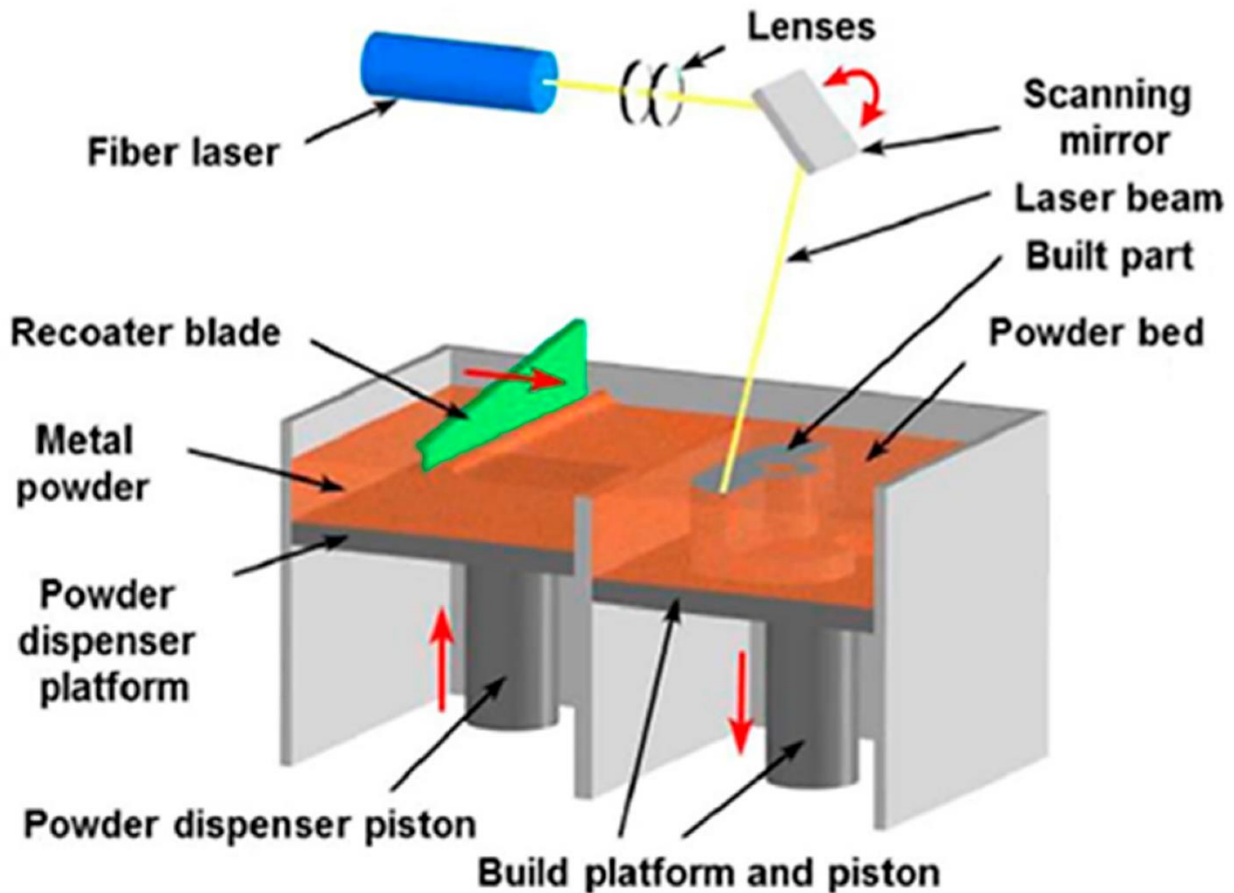


**Figure 2.1 A schematic of the laser powder bed fusion process [1]**

However, it should be noted that the microstructure of interest in this study can be manufactured in silicon for electronics thermal management. Research predecessors manufactured the asymmetric sawtooth microstructure using grayscale lithography, DRIE, anisotropic etching, and standard photolithography [2]. In addition to additive manufacturing, the microstructure can be manufactured through subtractive fabrication techniques like wire electric discharge machining. The versatility in fabricating the asymmetric sawtooth structure with different base materials and processes also expands the potential utility of the heat sink to be design-inclusive for silicon devices and function as a 'bolted-on solution' for electronic thermal management.

Stainless steel (SS 316-L) surfaces were fabricated for the terrestrial reference experiments. In contrast, titanium alloy (Ti-6Al-4V) test surfaces were used for the microgravity experiments due to the close coefficient of thermal expansion (CTE) match to borosilicate glass. A close CTE match to the glass ampoule was desired to allow multiple ways to bond the test surface to the borosilicate glass ampoule, reducing the thermal stresses at the test surface interface from differing expansion rates. The as-printed Ti-6Al-4V surfaces are shown in Figure 2.2.

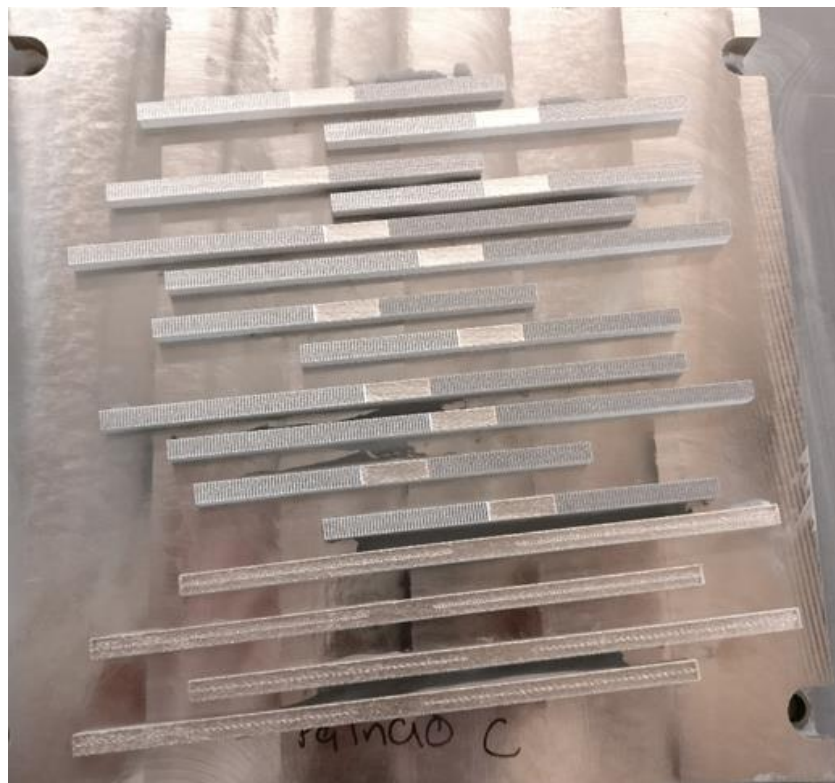


**Figure 2.2 The fabricated titanium test surfaces (Ti-6Al-4V) on the baseplate**

## **1.2 Test surface geometry – Auburn University**

The asymmetric sawtooth test surface consisted of repeating  $60^{\circ}$ - $30^{\circ}$  structures with a long and short slope.  $250\ \mu\text{m}$  cavities were located on each long slope, and the hollow feature was maintained to the depth of the test surface (2 mm), as shown in Figure 2.3a. The pitch of the

sawtooth structure was 1 mm. The baseline surface did not contain the repeating sawtooth structures. However, the 250  $\mu\text{m}$  cavities were spaced 1-mm apart, as shown in Figure 2.3b. The test surface dimensions were 80 mm x 6 mm x 2 mm (Lx W x H). An additional variation of the test surface for the microgravity experiments was the nucleation site density across the microstructure. A variation of the sawtooth test surface consisted of the 250  $\mu\text{m}$  square cavities on every other sawtooth.

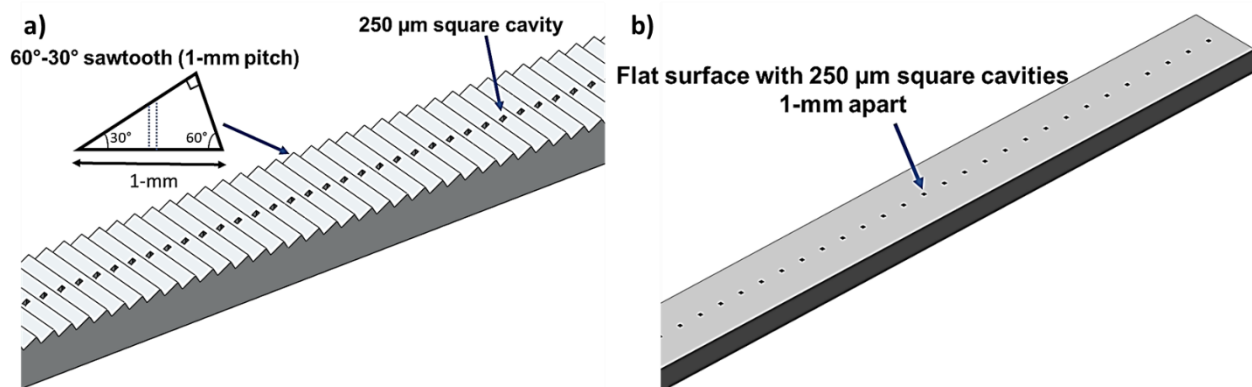


**Figure 2.3 (a) The asymmetric sawtooth microstructure (pitch = 1mm) with 250  $\mu\text{m}$  cavities on the long slope. (b) The baseline surface contains the 250  $\mu\text{m}$  cavities spaced 1-mm apart on a flat profile.**

### 1.3 Titanium (Ti-6Al-4V) test surface polishing and test

Titanium test surfaces manufactured using powder bed fusion were heat-treated to remove residual stresses from the additive manufacturing technique. As a result, oxidation layers develop across the surface, which worsens the surface finish of the metal and increases surface roughness. An increase in surface roughness leads to an increase in spurious sites from the test surface, as shown in Figure 2.4. Spurious sites are undesirable as they introduce additional nucleation sites for vapor, potentially impacting vapor motion induced by the microstructure. The ground experiments

described in the next section narrowed the pool of available test surfaces by experimental testing for spurious sites.

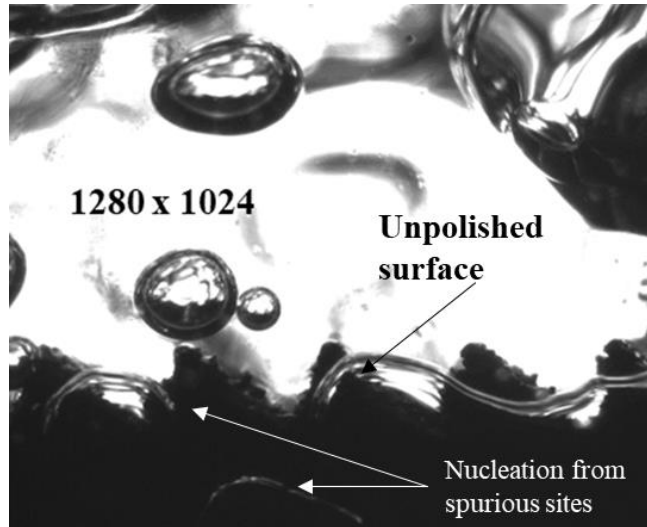


**Figure 2.4 Depiction of spurious sites from an unpolished Ti-6Al-4V surface**

The stainless steel surfaces were electropolished in-house for a smooth texture and mirror finish. Electropolishing is a method that takes off microscopic layers of material by passing an electrical current through the specimen while placed in an electrolyte solution. However, electropolishing of the titanium alloys in-house posed significant safety hazards.

Therefore, the titanium test surfaces were polished using a custom workflow developed for the ratcheted surface. The Dremel was maintained at ~10,000-15,000 rpm during this process, with the polish slurry regularly supplied. Constant brushing produced a thick black residue in the slurry, indicating that the oxide of the alloy was polishable. The polish was mostly a mix of petroleum distillates and aluminum oxide. The test surface was soaked in an isopropyl alcohol bath for cleaning, dried, and then cleaned with nylon bristles at ~20,000-30,000 rpm to remove residual surface impurities. This workflow introduced no macroscopic defects.

Before these test surfaces were shipped to Techshot, they were tested in the Auburn University terrestrial experimental setup. The experimental setup, designed to replicate the key features of the intended ISS hardware (the PFMI furnace), was utilized to observe the test surface for potential spurious sites. Terrestrial upward-facing tests were conducted to preempt potential spots of high surface roughness, creating unintended nucleation in the closed ampoule. During these tests, multiple sites produced spurious nucleation. Though these sites do not interfere extensively when buoyancy assists bubble departure, the absence of buoyancy forces increases the influence of secondary mechanisms. Therefore, spurious nucleation from unintended sites can influence the physics of the vapor bubbles sourced from the engineered sites, potentially muddying the microstructure-based physics.

The location of these spurious sites was recorded during these upward-facing tests. These locations were then polished using the workflow mentioned above. Successive tests were conducted to observe nucleation from these polished locations and record the location of other spurious sites. The cycle was repeated for each test surface until vapor nucleation was only observed from the intended nucleation sites, the engineered 250  $\mu\text{m}$  square cavities.

The described polishing and testing workflow also enabled the resolution of potential locations of high surface roughness that could otherwise be clouded in average surface roughness measurements. The final test surfaces are shown in Figure 2.5.

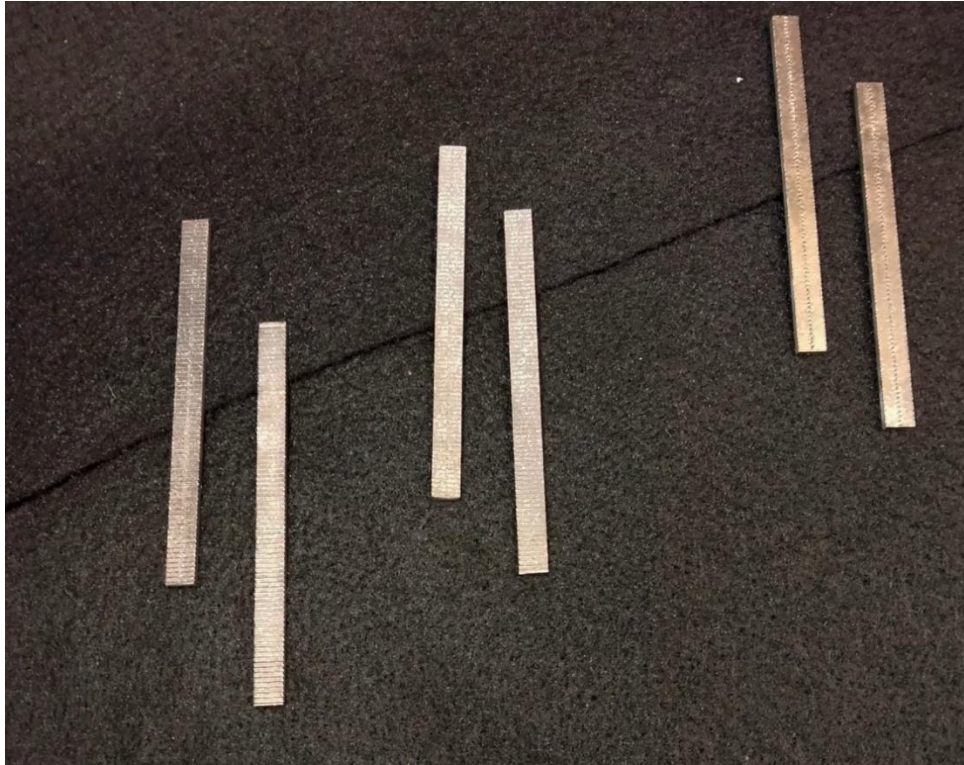


**Figure 2.5 The six test surfaces from Auburn University were machined to their final dimensions and polished before being shipped to Techshot.**

#### **1.4 Other attempts to polish Ti-6Al-4V surfaces**

Etching was attempted using Kroll's reagent on the titanium surfaces to improve the surface finish of as-printed test surfaces. Several attempts were made with varying hydrofluoric acid concentrations to remove oxidation from the as-printed titanium. However, the etch attempts were not successful due to the unique pattern of the microstructure.

As the peaks and valleys would selectively etch at different rates, the integrity of the microstructure could not be retained. Any changes to the microstructure's shallow or steep slope angle would unpredictably influence vapor bubble dynamics and severely detract from the possible



interpretation of the empirical results in reduced gravity. These problems persisted despite using different reagents, mainly focused on hydrofluoric acid (HF) concentration.

Due to the previous success with electropolishing stainless steel, an outside vendor was contacted to provide a sample finish of one of the test surfaces. However, the resulting surface finish was unfortunately poor, resulting in more spurious sites than the as-printed test surfaces. Due to these results, the custom polishing workflow was developed to prepare the test surfaces for the nucleate pool boiling experiments in microgravity.

### **1.5 Test surface geometry – University of California, Davis**

The two test surfaces from the University of California, Davis, were fabricated to explore the effects of vapor nucleation from a slot-based cavity extending across the test surface's width. The microstructure comprised  $60^{\circ}$ - $30^{\circ}$  sawtooth structures, and the pitch in the design shown in Figure 2.6 was 1.5 mm. Slot cavities with a reentrant design were located in every third ratchet on the shallow slope. The hammerhead slots were fabricated close to the base surface to match the resistance heater's surface temperature. The test surface was fabricated using wire electric discharge machining (EDM), and a section of the fabricated surface is illustrated on top in Figure 2.6.

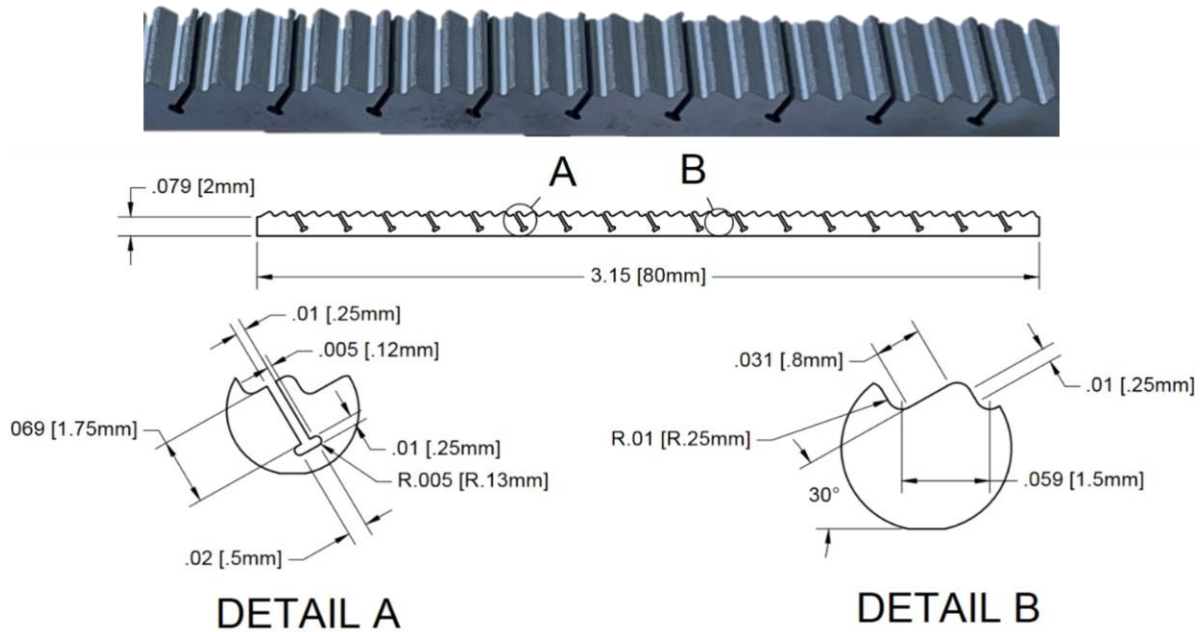


Figure 2.6 The detailed test surface dimensions of the 60°-30° slot test surface. The hammerhead slots are located on every third sawtooth. A picture of the fabricated surface is shown on top.

### 1.6 Test surface shipped to implementation partner – Redwire Techshot

A total of eight test surfaces were shipped to Techshot; six test surfaces from Auburn University and two test surfaces from the University of California, Davis. The test surfaces from Auburn were vacuum-sealed and shipped to Techshot at Greenville, Indiana. Each test surface variation was prepared in duplicate – intended for ground and flight tests, as shown in Table 2.1. The final shipped test surfaces to the NASA implementation partner, Redwire Techshot, are shown in Figure 2.7.

**Table 2.1 The test surface geometries and their intended configurations for the microgravity experiments**

<b>Test surfaces shipped to Techshot</b>	<b>Intended Configuration</b>
60°-30° sawtooth with cavities spaced 1-mm apart	Ground
60°-30° sawtooth with cavities spaced 1-mm apart	Flight
60°-30° sawtooth with cavities spaced 2-mm apart	Ground
60°-30° sawtooth with cavities spaced 2-mm apart	Flight
60°-30° sawtooth with slot cavities	Ground
60°-30° sawtooth with slot cavities	Flight
Baseline (cavities spaced 1-mm apart)	Ground
Baseline (cavities spaced 1-mm apart)	Flight



**Figure 2.7 The final test surfaces shipped from Auburn University and the University of California, Davis. The vacuum-sealed packages from Auburn University are illustrated at the top, and the two wire EDM test surfaces from the University of California, Davis, are shown at the bottom. The Auburn University test surface with the trailing label "-F" indicates a flight surface, and "-G" denotes a ground surface.**

## CHAPTER 3 TERRESTRIAL EXPERIMENTS

### 3.1 Terrestrial Experiments at Auburn University

This section describes the terrestrial downward-facing experiments conducted at Auburn University in an in-house fabricated experimental setup. Key features of the selected ISS hardware were reproduced for these in-lab experiments, with additional features added to encourage repeatable use. The described setup was custom-made to test upward-facing or downward-facing heated surfaces with high-speed imaging of the vapor bubble dynamics.

The obtained high-speed images were post-processed with a workflow developed to capture the differences between the baseline surface and microstructure surface. The change in vapor bubble dynamics across the microstructure with an increase in heat flux was also intended to be captured by this dedicated image-processing workflow. In addition to this transient analysis, the static vapor bubble morphology and a force balance analysis from the microstructure were also explored, as explained in this section.

#### 3.1.1 Experimental Setup

The millimetric-scale microstructure with 1-mm pitch was fabricated using metal additive manufacturing, with 250  $\mu\text{m}$  truncated square pyramidal cavities featured on every long slope of the microstructure, as illustrated in Figure 3.1 (b). The 60°-30° asymmetric sawtooth microstructure (80 mm (L) x 6 mm (W) X 2 mm (H)) was attached to the borosilicate glass tube (shown in Figure 3.1(a)), and a polyimide film heater was affixed to the outside of the tube for the constant heat-flux experiment using Kapton™ adhesive. The degassed FC-72 liquid was charged to the ampoule at a low (<0.05 psi) vacuum. A digital angle gauge leveled the glass ampoule at two locations on the square cross-section to an accuracy of  $\pm 0.1^\circ$ . The setup was supported by

pneumatic vibration isolating feet (Newport™ SLM-1A) to deter the impact of environmental noise on vapor mobility dynamics. Digital high-speed imaging was accomplished by a Phantom v310 camera equipped with an Infinity microscope lens. The subcooling for the results reported is 20K. Other details of the experimental setup are provided in a prior study [69].

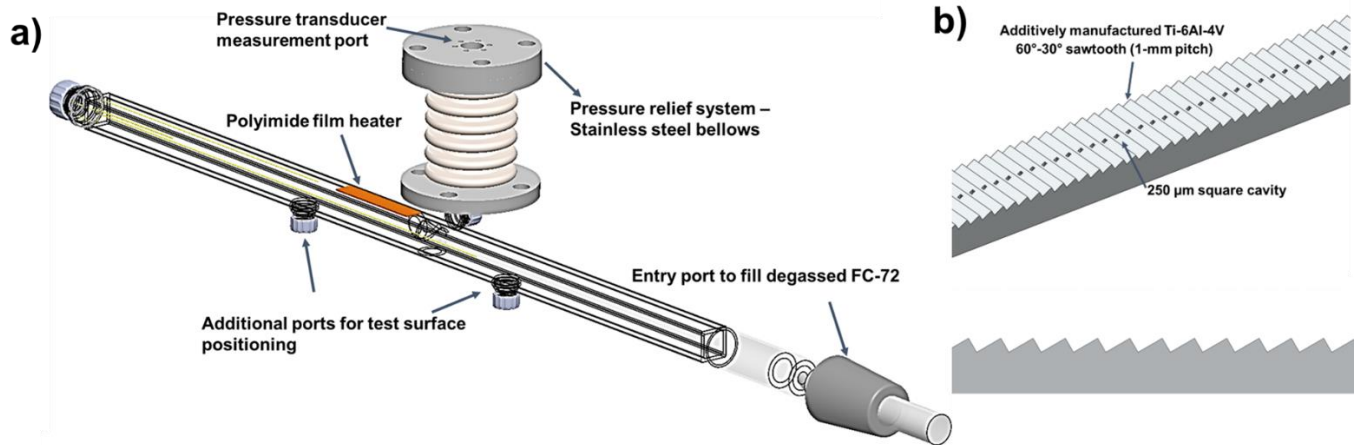


**Figure 3.1 (a) The experimental setup with the downward-facing surface in the borosilicate glass ampoule for backlit high-speed imaging (b) Isometric view of 60°-30° sawtooth microstructure with 250 μm cavities 1-mm apart and (c) Side view of the repeating millimetric-scale microstructures**

### 3.1.2 Image Processing

The obtained high-speed were post-processed in the open-source platform, ImageJ. A more comprehensive package of ImageJ with plugins and extensions loaded called Fiji was used to process the obtained high-speed images.

The obtained high-speed videos were converted from their native format (.cine) to a stack of numbered images(.tiff) for image processing using Fiji [73]. Typical background subtraction techniques like estimating the mean pixel intensity of the background cannot distinguish between the vapor mass and the test surface, especially for the downward-facing surface. As the vapor mass

interacts with the test surface dynamically in the adverse gravity orientation, a custom background image must be generated for each unique image stack. Maximum intensity projection analyzes the stack of 2D images to select the highest intensity pixel from each image to create the background image. For both orientations, the background image produced is the test surface dimensions for the imaging session, as shown in Figure 3.2.

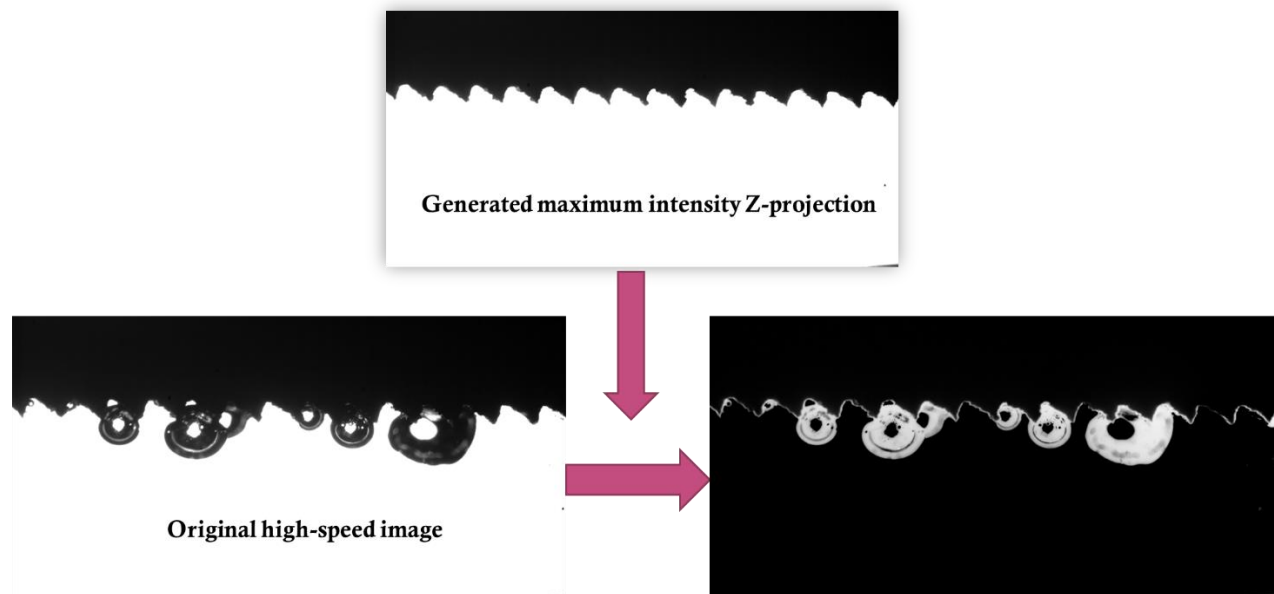


**Figure 3.2 The process of generating a background subtracted image from the initial stack of raw high-speed images using maximum intensity Z-projection is illustrated**

The background-subtracted image is binarized for further analysis. Multiple fuzzy thresholding algorithms are available natively in the image processing platform to convert the background-subtracted image, as illustrated in Figure 3.3. The algorithms highlighted in red did not converge and were eliminated as candidates for further analysis. Though most illustrated models picked up the edges of the bubble features, the algorithms processed the sections of vapor bubbles differently due to their adaptive thresholds.

Though the thresholds can be set manually for conversion, the automatic algorithms calculate the threshold without introducing user bias. Huang's fuzzy thresholding method, a popular imaging segmentation technique, was chosen as it can accurately segment images with dynamic lighting conditions and uneven topography.

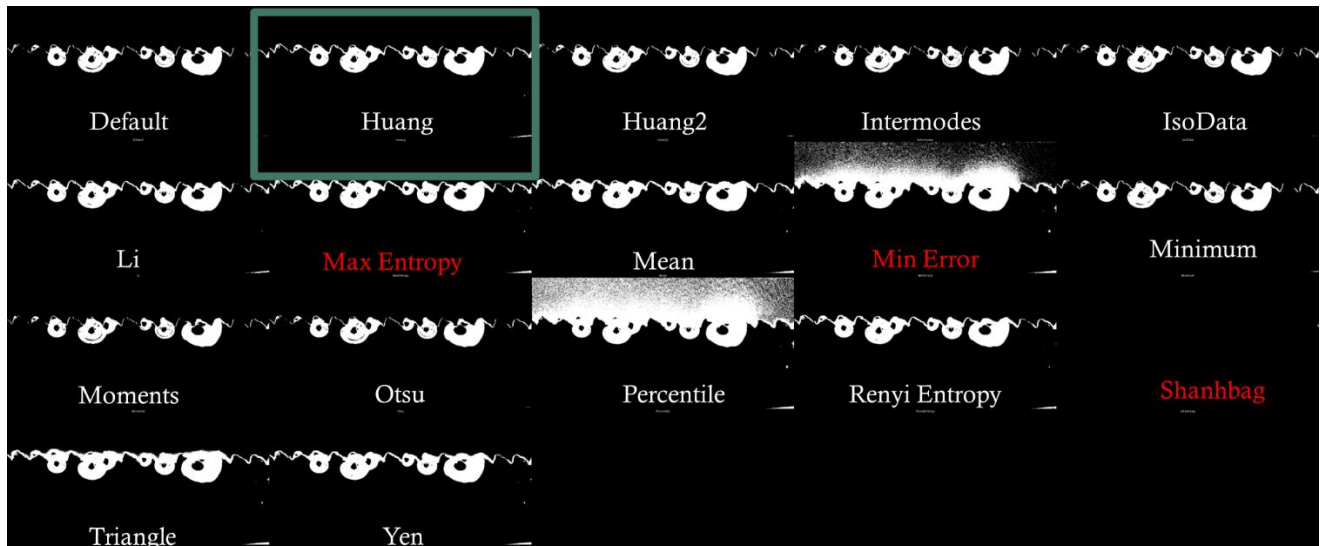


**Figure 3.3** The different image binarization algorithms were attempted on the background-subtracted image. The algorithms marked in red did not converge and were eliminated as candidates for further analysis.

The binarized image is inverted, filling holes to complete the vapor bubble features. The fill holes operation sometimes erroneously connects neighboring bubbles to create a single vapor mass. The watershed segmentation cuts apart the connections to distinguish neighboring vapor bubbles. For the downward-facing surface, the unique bubble morphology and slug growth with constant heat flux were analyzed with a dynamic watershed segmentation with distance transform[74] to scale the operation appropriately, as shown in Figure 3.4.



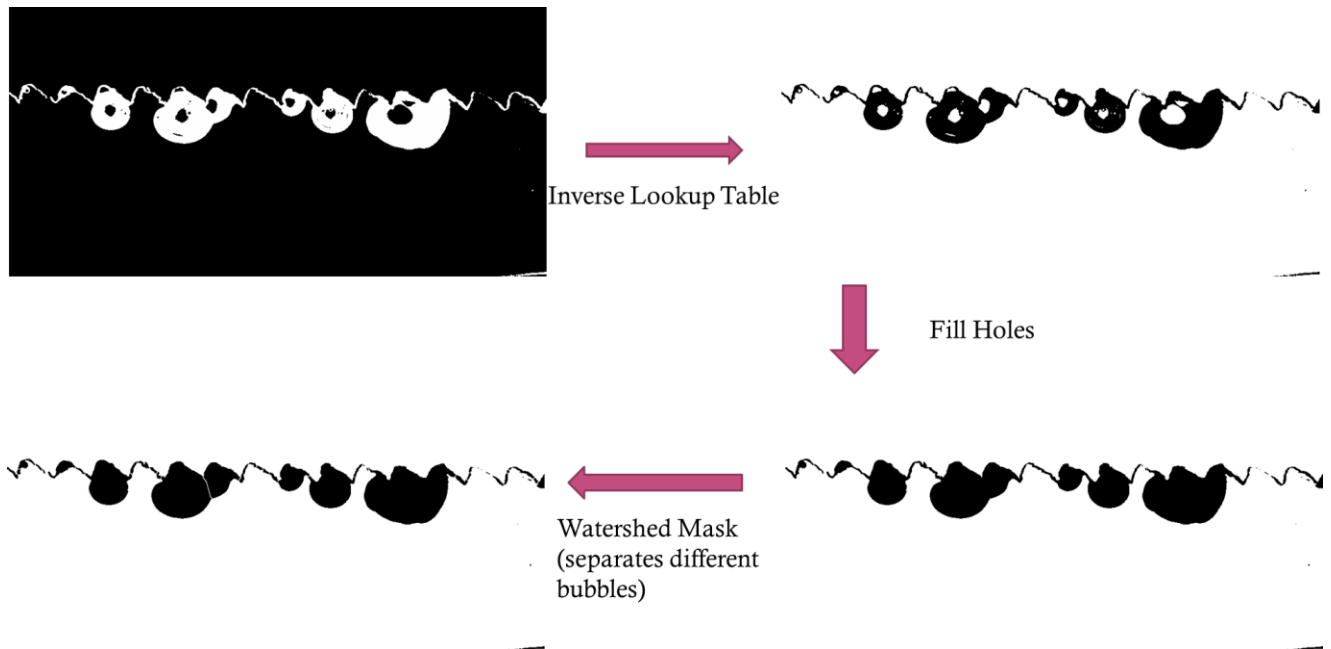


**Figure 3.4 The binarized image is inverted for the fill holes operation. A watershed mask with distance transform was used to separate connected vapor bubbles.**

Circularity and the size of the vapor bubbles were used to analyze each high-speed image. A minimum size and circularity of  $0.3 \text{ mm}^2$  and 0.1, respectively, were used to eliminate noise and undulations of light along the downward-facing surface. As this image processing workflow aims to adequately quantify the total vapor area in each frame within a high-speed image stack, the loss of resolution along the liquid-vapor interface by the imposed analysis constraints does not impact the results.

The processed images were input to the Trackmate plugin [75] to calculate the vapor masses' velocity. The threshold detector was used to isolate the vapor masses in the image, and a linear motion tracker (Linear Assignment Problem), well suited for Brownian motion, tracked the vapor slugs. The positions of the spots are then exported as .xml files for analysis and processing.

### **3.1.3 Experimental Results and Discussion**

#### **3.1.3.1 Comparison of Baseline and Microstructured Surface**

With the calibrated frame of view remaining constant, the flat surface (baseline) with 250  $\mu\text{m}$  cavities produced stationary vapor slugs that oscillated without preferential motion in any direction, as shown in Figure 3.5. The changes in total area were due to large vapor slugs sliding away from the plane of view, exceeding the width (6 mm) of the test surface at 1.3  $\text{W}/\text{cm}^2$ . At the same heat flux, the asymmetric microstructure depicted three repeating cycles of vapor nucleation, coalescence, and slide-off at 2.5 Hz. The peaks at this heat flux comprise multiple slugs spanning across two or three sawteeth (a "peak"), which then slide off in the direction of the long slope, significantly reducing the total vapor area (a "valley"). Nucleation from the square cavities recurs at the trailing edge of the departing slug at two or three sawteeth, explaining the low vapor volume at the valley.

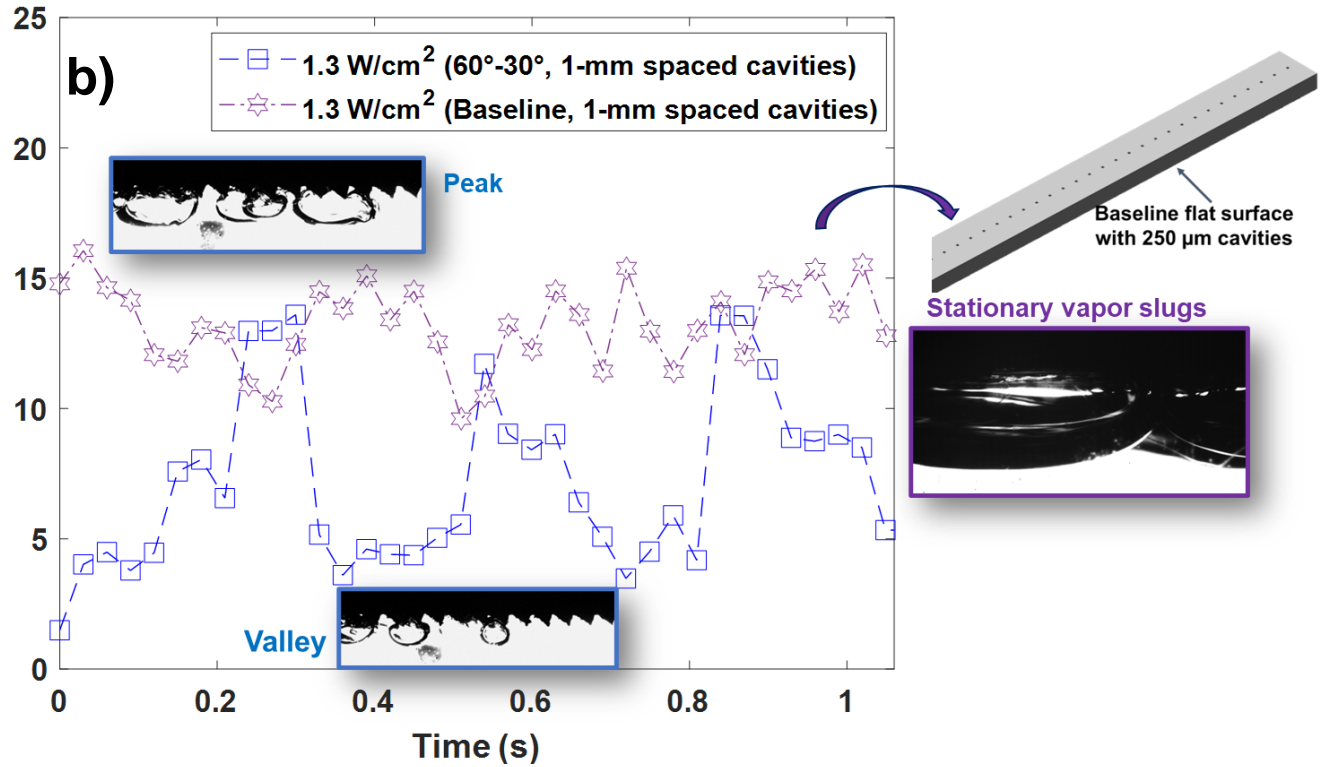


**Figure 3.5 Comparison in total vapor area between the 60°-30° sawtooth and the baseline surface with the same frame of view (13.4 x 6.7 mm). The asymmetric microstructure induced three cycles of vapor nucleation, growth, and slide-off, while the baseline surface produced stationary vapor slugs with relatively larger areas.**

### 3.1.3.2 Quantifying Vapor Mobility Across the Microstructure at Different Fluxes

An increase in the heat flux to 2.3 W/cm<sup>2</sup> revealed the higher vapor loads supported by the microstructure with a similar pattern, as shown in Figure 3.6. The cycles shift upwards due to the increased vapor nucleation, growth, and coalescence at this higher heat flux. At 3.33 Hz, four cycles of vapor nucleation, growth, coalescence, and slide-off were completed. Increased vapor production at the engineered cavities and rapid coalescence led to multiple vapor slugs spanning two to six sawteeth at the peaks (snapshots 1 (0.18 s), 3 (0.42 s), and 5 (0.69 s)) as depicted in Figure 3. Multiple vapor slugs extending across five or six sawteeth) depart the viewing frame

with fresh nucleation on the trailing edge, leading to the relative lows (snapshots 2 (0.24 s), 4 (0.63 s), and 6 (0.93 s)). The differences in the magnitude of these relative lows are explained by the length of the departing vapor slugs in their prior highs. From inset image 1, a vapor slug extending over five sawteeth departs the viewing frame leading to inset image 2. In the next 0.2 seconds, vapor nucleation and coalescence produce multiple vapor slugs and bubbles (inset image 3), which grow large enough to coalesce. This long slug, bridging across ten sawteeth, quickly departs the viewing frame leading to the subsequent valley (inset image 4). This is followed by rapid nucleation at all available cavities, leading to inset image 5. The length of the departing slugs in each frame corresponds to the arrow length in images 1, 3, and 5. The results indicate that vapor growth and coalescence are crucial in producing extended slugs that lead to vapor motion across the microstructure. The observed vapor mobility from the textured surface occurs in predictable cycles comprising peaks and valleys at different heat fluxes, enabling a passive, self-regulating thermal management system.

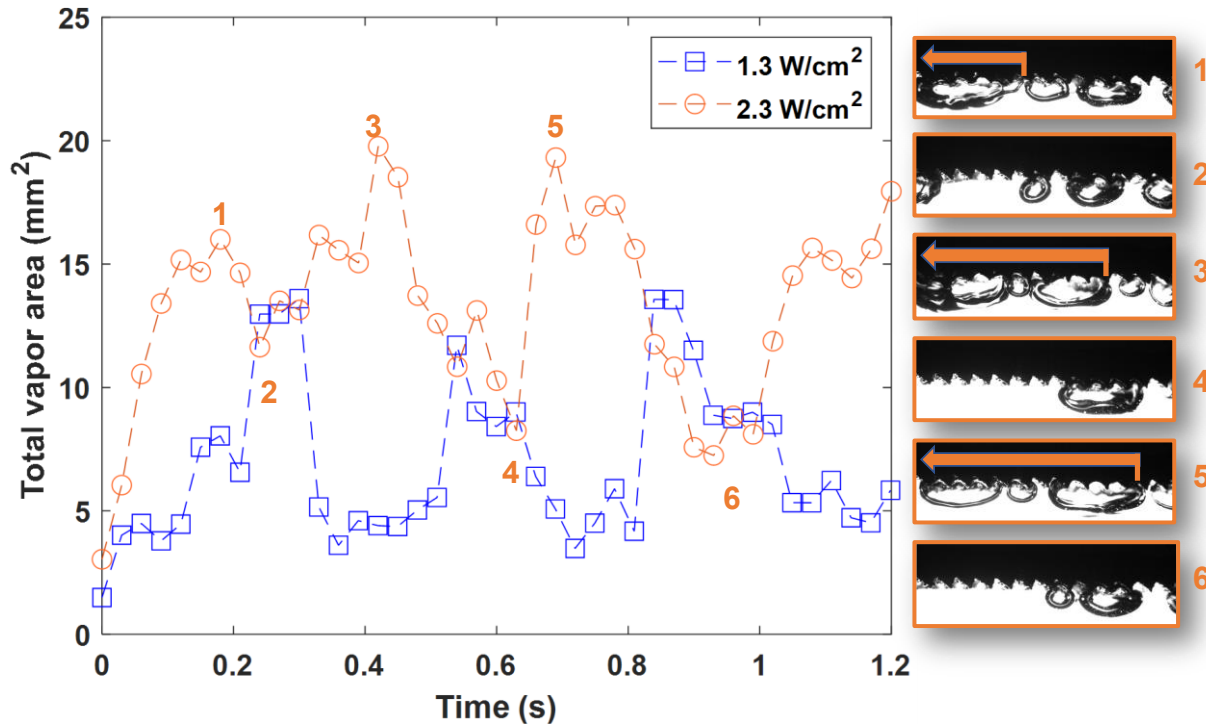


**Figure 3.6** Difference in total vapor area patterns at 1.3 W/cm<sup>2</sup> and 2.3 W/cm<sup>2</sup> for the 60°-30° sawtooth with cavities spaced 1-mm apart. The high-speed imagery (1024x768, 1000fps) of the highs and lows at 2.3 W/cm<sup>2</sup> are depicted on the right.

### 3.1.3.3 Force Balance Model from the Microstructure

The length scale of the slugs also influences vapor bubble morphology, as shown in Figure 3.7. The ratio of the concave radius of curvature at the peak to the convex radius of curvature at the crest potentially changes as the number of sawteeth covered by the slug increases. The change in vapor bubble morphology as it grows and interacts with the microstructure in the adverse gravity orientation can be represented as a force balance model. The driving motion from the asymmetric microstructure and the buoyancy forces acting along the microstructure oppose the drag motion and the added mass forces on the vapor slug.

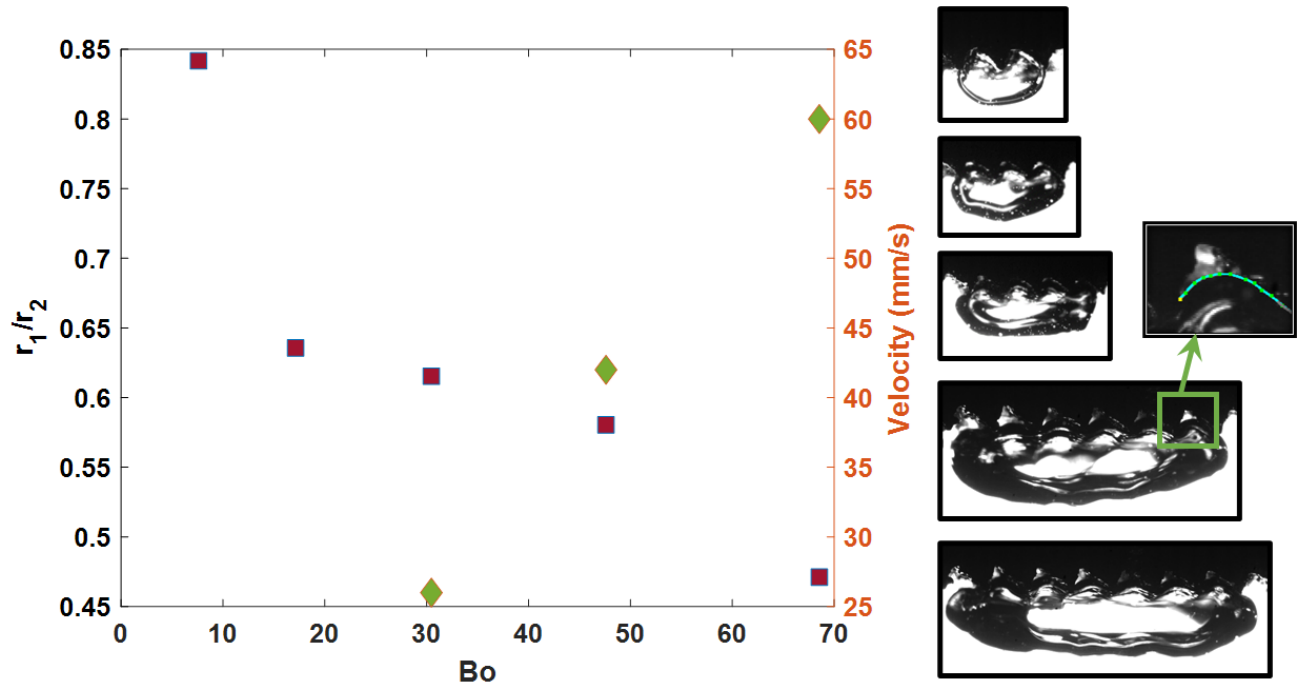


**Figure 3.7** The ratio of the radius of curvature between the peak and crest of the asymmetric sawtooth in the vapor slug as a function of the characteristic length-scale of the vapor slug (number of sawtooth periods covered) captured in the Bond number. The velocity of the indicated slugs (shown on the right) increases with the length of vapor masses spanning more than three sawteeth.

The complete slug motion model (shown in Figure 3.8) can be simplified to,

$$F_{\Delta P, tot} - F_d + F_{b1} - F_{b2} - F_{am} = 0 \quad 1$$

The current framework estimates a uniform liquid film thickness, though high-speed imagery indicates different liquid film thicknesses at the crest and trough of the sawtooth.  $F_{\Delta P, tot}$  is the driving force from the microstructure originating from pressure differences while  $F_{b1}$  and  $F_{b2}$  are the buoyancy forces acting on the vapor slug along the long and short slopes, respectively. The

drag force opposes the slug motion,  $F_d$ , and the added mass forces,  $F_{am}$ . Each of the stated forces is explained in the following section.

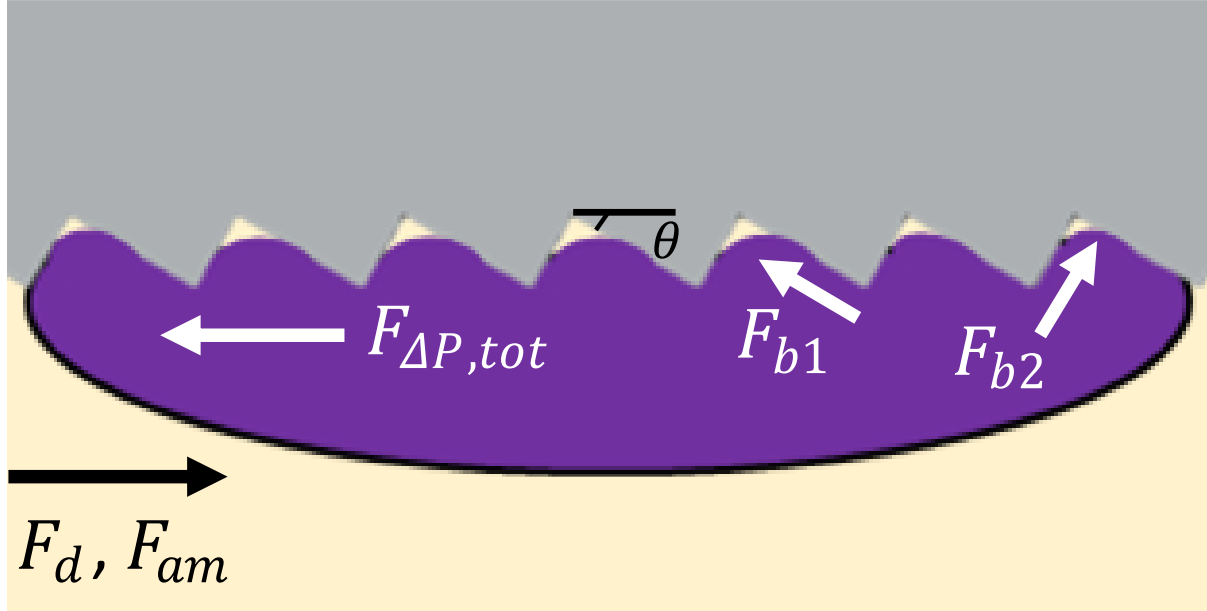


**Figure 3.8 Force balance on a vapor slug moving in the dielectric liquid (marked in yellow) denoting the dominant forces. The buoyancy forces and the pressure difference across the microstructure drive the vapor slug, while the drag and added mass forces limit the motion.**

A prior study in microgravity [35] with the same microstructure contributed to a semi-empirical force balance to determine the velocity of a moving vapor slug by measuring the liquid film thickness. The model hypothesizes that the primary driver of vapor motion across the sawteeth is the difference in pressure between the crest and trough of the sawtooth arising from the difference in radii of curvature at the two locations, as shown in Eq (2).

$$F_{\Delta P, tot} = \left\{ \begin{array}{l} m \left[ \left( \frac{\mu V}{H} + \frac{H}{2} \frac{\partial P}{\partial x} \right) LD \cos \theta \right]_{long\ slope} \\ -n \left[ \left( \frac{\mu V}{H} + \frac{H}{2} \frac{\partial P}{\partial x} \right) LD \sin \theta \right]_{short\ slope} \end{array} \right\} \quad 2$$

To determine the liquid film thickness ( $H$ ), the diameter of the bubble ( $D$ ), the number of sawteeth covered by the vapor mass ( $m$  and  $n$ ), the radii of curvature at the crest ( $r_1$ ) and trough ( $r_2$ ) which drives the pressure gradient ( $\partial P/\partial x$ ), and the velocity of the moving slug is required. The slug's diameter ( $D$ ) is the number of sawteeth covered by the slug for this force balance model. The liquid film thickness between the vapor mass and the sawtooth structure is difficult to determine empirically, as the film is typically tens of microns thick, and the vapor mass dynamically interacts with the sawtooth microstructure due to the adverse gravity orientation. The pressure gradient across the thin liquid film is derived from the Young-Laplace equation as a function of the difference in radii of curvature across the crest and trough of the sawtooth [35].  $\theta$  is the angle of the sawtooth ( $30^\circ$ ), and the fluid properties of saturated FC-72 at 1 atm are used in the model. Other vapor bubble measurements are empirically determined from high-speed images to assess the liquid film thickness.

Curvature analysis at the crests and trough was accomplished with the Kappa [76] plugin. The liquid-vapor interface was outlined with an initialization curve to produce an open B-Spline curve to fit against the data with a minimization algorithm.

Coalescing slugs were excluded from the analysis; therefore, the force due to coalescence was not considered in the force balance. The high-speed images indicate that the geometry of the slug changes as it merges and grows, and the effect of this geometry is encapsulated in the curvature ratio between the peak and crest.

Buoyancy forces acting along the long and short slopes of the microstructure were included in the analysis due to the magnitude of the Bond number, decomposed to its two-component forces.

$$F_{b1} = \rho_l g V_{half-ellipsoid} \cos \theta \left( \frac{L_{long\ slope}}{L_{long\ slope} + L_{short\ slope}} \right) \quad 3$$



$$F_{b2} = \rho_l g V_{half-ellipsoid} \sin \theta \left( \frac{L_{short\ slope}}{L_{long\ slope} + L_{short\ slope}} \right) \quad 4$$

where  $F_{b1}$  is the buoyancy force acting along the long slopes aiding the vapor bubble in the intended direction while  $F_{b2}$  is the limiting buoyancy force pushing the vapor bubble backward along the short slope.  $V_{half-ellipsoid}$  is the volume of the vapor slug approximated as a half-ellipsoid with the depth of the slug matching its height. The buoyancy forces push the vapor bubbles along the walls leading to a flattened vapor mass, enabling this simplification.  $\rho_l$  is the density of the dielectric liquid (FC-72) at the saturation temperature of 1 atm.

The drag force on the half-ellipsoid vapor bubble at  $\geq 20$  Bo number is estimated by comparing this pressure-driven mobility to the drag coefficient on a slightly inclined downward-facing surface ( $2^\circ$ ) as determined by Perron et al. [77],

$$C_d = 0.0683 * Bo^{0.450} \quad 5$$

where the Bond number is defined by,

$$Bo = \frac{g(\rho_l - \rho_v)D^2}{\sigma} \quad 6$$

The correlation is valid for  $Bo \leq 90$ , which falls in the range depicted in Figure 3.7. The change in drag coefficient with the Bond number for the current study is illustrated in Figure 3.9.

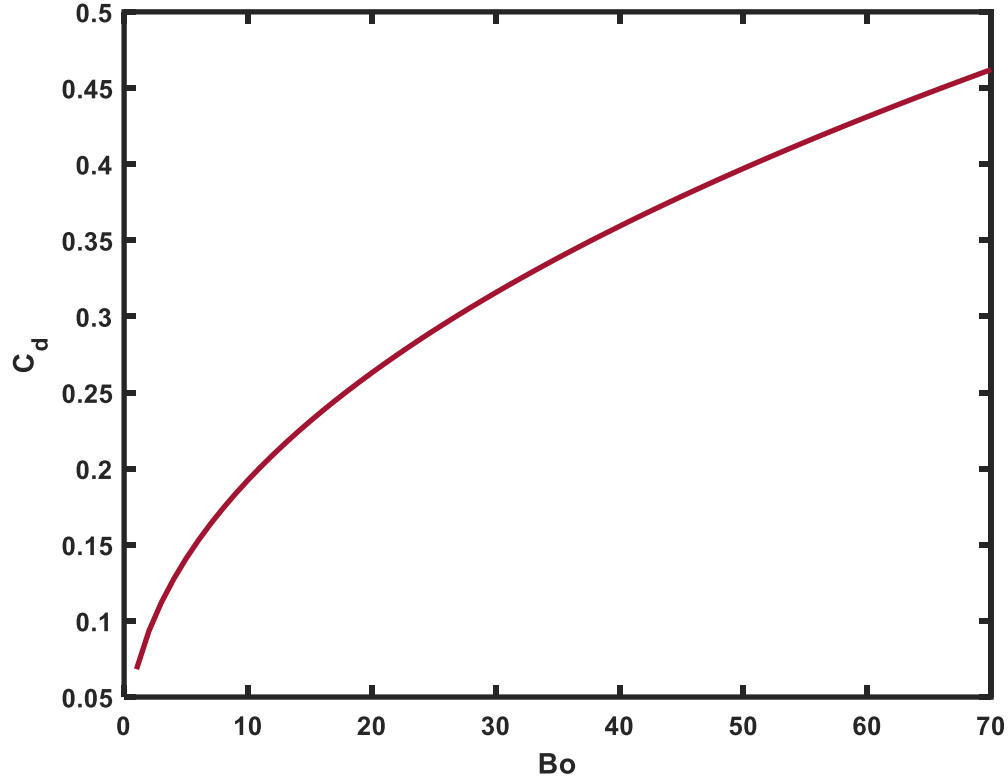


**Figure 3.9** The change in the drag coefficient as the vapor slug grows for the current study is illustrated, as given by Eq (5)

The drag force for the vapor slug is calculated by,

$$F_d = \frac{C_d A_{half-ellipsoid} \rho_l U^2}{2} \quad 7$$

where the area of the half-ellipsoid is defined as,

$$A_{half-ellipsoid} = \frac{1}{2} * \pi * D * height \quad 8$$

The added mass forces,  $F_{am}$ , represent the forces needed to move the liquid around the vapor mass as the microstructure propels them. This term accounts for the inertial effect of accelerating the surrounding fluid and the slug from rest. This transient effect hypothesizes that the acceleration of

the vapor bubble is the difference in average velocity over 20 ms for different length scales of the vapor bubble. The consistent motion was not observed for vapor slugs spanning three or lower sawteeth, so the slug is assumed to be at rest. For a spherical bubble or particle [78], the force is represented by,

$$F_{am(spherical)} = \frac{\pi}{6} D^3 [(\rho_l) C_m + \rho_v] \left( \frac{dU}{dt} \right) \quad 9$$

where  $C_m$  is the added mass coefficient. Though  $C_m$  changes with the geometry of the vapor bubble, a rigorous formulation of the coefficient for oblate spheroids or ellipsoids is not available. For a sphere,  $C_m = 1/2$  is well established [79] and is used in this force balance. Further, the volume of the sphere is switched to the volume of the half-ellipsoid. As  $\rho_l \gg \rho_v$ , the density of the vapor bubble is neglected. The results of the force balance are illustrated in Table 3.1.

**Table 3.1 Liquid film thicknesses calculated from the force balance model**

Sawteeth covered by the vapor slug - experimental	Height/Depth of the vapor bubble (m) - experimental	Velocity (m/s)- experimental	Acceleration (m/s <sup>2</sup> )- experimental	H (μm)- calculated
4	0.0010	0.026	1.3	93.5
5	0.0012	0.042	2.1	97.9
6	0.0015	0.060	3.0	90.5

Though the velocity increases with the number of sawteeth covered by the slug, the liquid film thickness for different vapor slugs is closely bunched together from this analysis of high-speed images. The dynamic change in liquid film thickness associated with the motion might play an

essential role in the sweeping movement of the vapor bubbles. In addition to the added mass forces, the change in vapor bubble morphology due to coalescence and growth may impact vapor bubble motion transiently.

This model formulation, derived from a combined Couette-Poiseuille flow formulation, predicts a uniform liquid film thickness underneath the moving vapor slug. However, the radii of curvature and the interface from the high speed indicate significant differences in the liquid film thickness from the crest to the trough.

#### **3.1.3.4 Force Balance Model Analysis and Discussion**

In addition to predicting liquid film thickness for the microstructure, this static formulation provides more insight into the interplay between the buoyancy force and the pressure differential driving force.

The change in net force and the net pressure difference across a slug spanning four sawteeth, moving at 26 mm/s, is shown in Figure 3.10. When the liquid film thickness is varied from upto 110  $\mu\text{m}$ , the net buoyancy force ( $F_{b1}-F_{b2}$ ), the drag force ( $F_d$ ), and the added mass forces ( $F_{am}$ ) are constant. For this case, the net buoyancy force is  $5.41 \times 10^{-5}$  N, the drag force is  $2.85 \times 10^{-6}$  N, and the added mass force is  $1.42 \times 10^{-5}$  N.

The high-speed images clearly show that the liquid film thickness changes from the crest to the trough, as shown in the inset image in Figure 3.10. Therefore, the x-axis in Figure 3.10 can also be substituted for the length along the sawtooth, from the crest to the trough, as the liquid film thickness increases along the sawtooth.

The interplay between the net buoyancy force ( $F_{b1}-F_{b2}$ ) and the net pressure difference driver ( $F_{\Delta P, \text{tot}}$ ) is illustrated by the shaded areas in Figure 3.10. The pressure difference between the long and

short slope aid in driving the vapor slug in the direction of the long slope up to 15  $\mu\text{m}$ . From 15  $\mu\text{m}$  to 94  $\mu\text{m}$ , the buoyancy forces along the angled microstructure drive the motion of the vapor slug. The net force becomes negative at higher liquid film thicknesses, and the vapor slug no longer moves.

Qualitatively, as the vapor slug grows, larger areas contact the microstructure within the thin liquid film range ( $\leq 15 \mu\text{m}$  for the example shown in Figure 3.10) and produce regions of high-net force, contributing to the increasing velocity with an increase in size. Though the model resolves in the buoyancy-driven range for the cases shown in Table 3.1, the results should be interpreted within the context of the multi-layered force balance propelling the slug in a predictable direction.

As the current model does not account for forces due to coalescence or nucleation, it is conceivable that there may be additional drivers for motion from the engineered microstructure.

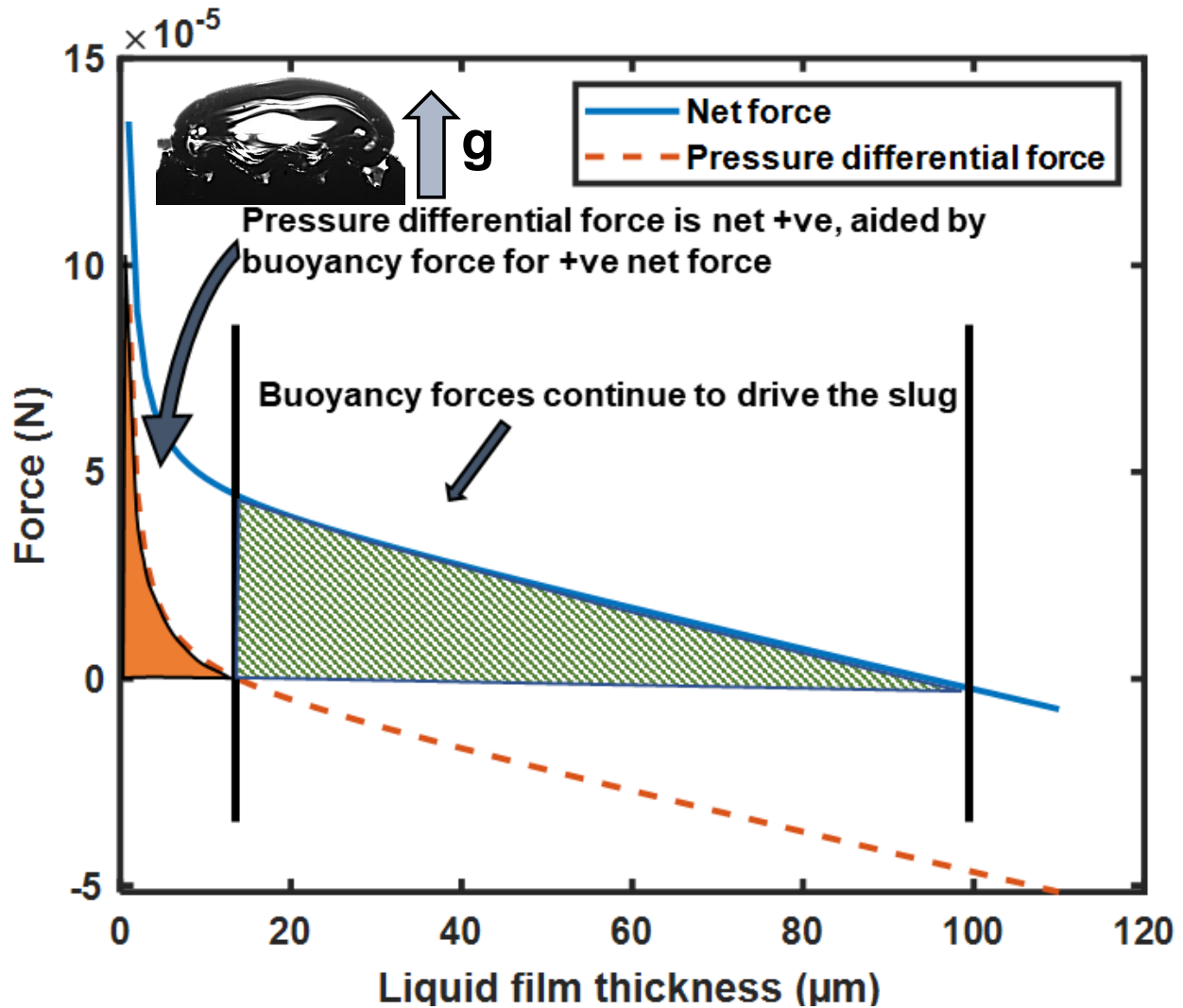


Figure 3.10 The change in the net pressure different driver and the net force as the liquid film thickness changes from up to 110 microns for a slug spanning four sawteeth and a velocity of 26 mm/s. The inset image shows the liquid-vapor interface across a slug spanning four sawteeth, highlighting the growth in the liquid film from crest to trough.

Figure 3.11 illustrates the comparison between  $\theta = 15^\circ$  and  $30^\circ$  for the analysis shown in the previous section.  $\theta = 15^\circ$  was selected for comparative analysis as a similar asymmetric sawtooth had chosen vapor motion in a previous study [69]. The change in the angle of the sawtooth also

changes the length of the long and short slopes, influencing eqs. (2), (3), and (4). The radii of curvature, the diameter, and the velocity of the slug were derived from a previous study by the group. A slug spanning four sawteeth, moving at 22 mm/s on a 75°-15° sawtooth structure with  $r_1=0.26$  mm and  $r_2=0.35$  mm, is compared against the 60°-30° sawtooth structure in Figure 3.11. For this case, the net buoyancy force is  $9.32 \times 10^{-5}$  N, the drag force is  $7.82 \times 10^{-7}$  N, and the added mass force is  $7.45 \times 10^{-6}$  N.

The lower  $\theta$  microstructure generates higher net force at low liquid film thickness due to a higher net pressure differential and buoyancy force from the sawtooth structure. However, the pressure difference drives the vapor slug for the vapor slug at a similar range ( $\leq 15$   $\mu\text{m}$ ) for both microstructure angles.

However, the plot's crossover points (when net force becomes negative) occur at different liquid film thicknesses. The 75°-15° sawtooth structure resolves at 145  $\mu\text{m}$  with the current model, while the 60°-30° sawtooth structure is predicted to have 94  $\mu\text{m}$  liquid film thickness. The additional vapor mobility region afforded by the 75°-15° microstructure arises from the difference in areas of the sawtooth structure between the two angles. An increase in the length of the long slope of the microstructure drives the buoyancy force,  $F_{b1}$ , higher. The length ratio is depicted in eqs. (3) and (4) favors the driving buoyancy force and reduce the adverse buoyancy force. This change enables the asymmetry to propel the vapor slug across thicker liquid films. The liquid film thickness predicted for the 75°-15° microstructure at 145  $\mu\text{m}$  also falls between the empirically measured range from the previous study from 74  $\mu\text{m}$  at the crest to 180  $\mu\text{m}$  at the trough, validating the force balance analysis. A higher radii ratio implies a lower curvature along the interface of the vapor slug as it interacts with the microstructure.

This force balance model can be applied to different microstructure morphology to predict vapor mobility, enabling robust heat transfer systems design.

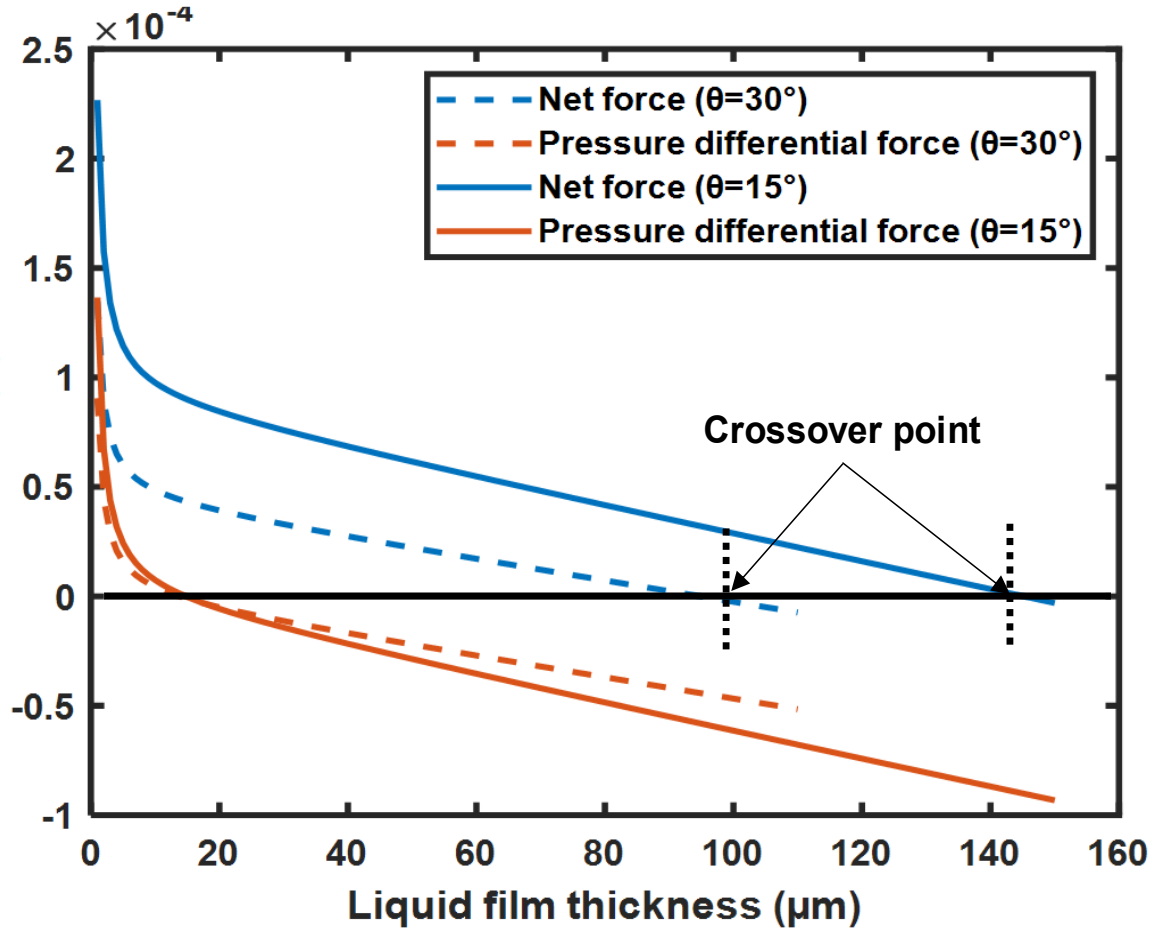


**Figure 3.11** The difference in net force generated and the net pressure difference when the angle of asymmetric sawtooth changes from  $30^\circ$  to  $15^\circ$ .

The results suggest that a reduction in the sawtooth angle can provide an increased range of feasible liquid film thickness to induce vapor mobility. A hypothetical scenario for an  $85^\circ$ - $5^\circ$  sawtooth microstructure is explored in the next section. The ratio of the radii of curvature and the velocity for a slug spanning across four sawteeth is extrapolated in Table 3.2.



**Table 3.2 Extrapolation of the ratio of the radii of curvature and the slug velocity for an 85°-5° sawtooth microstructure from the obtained empirical results**

<b>Theta (°)</b>	<b>r<sub>1</sub>/r<sub>2</sub></b>	<b>V (m/s)</b>
30	0.611	0.026
15	0.743	0.022
5	0.83	0.0193

The force generated for this hypothetical 85°-5° microstructure is compared against a 60°-30° sawtooth microstructure in Figure 3.12. The long and short slope lengths for this microstructure are calculated to be 0.996 and 0.0872 mm, respectively. As  $\theta$  decreases, diminishing or worse returns may be available as the increase in the length of the long slope approaches a constant. This saturation, combined with the minimal pressure differential force increase, leads to a similar or worse liquid film thickness range. For example, the plot predicts a liquid film thickness of 137  $\mu\text{m}$ , compared to the 145  $\mu\text{m}$  predicted for the 75°-15° sawtooth microstructure. In addition, manufacturing a lower sawteeth angle with a short slope length of 0.087 mm can be challenging. Modifying the sawtooth pitch, process fluid, and angles for different applications will help optimize this sawtooth structure for different adverse gravity orientations and heat transfer systems.

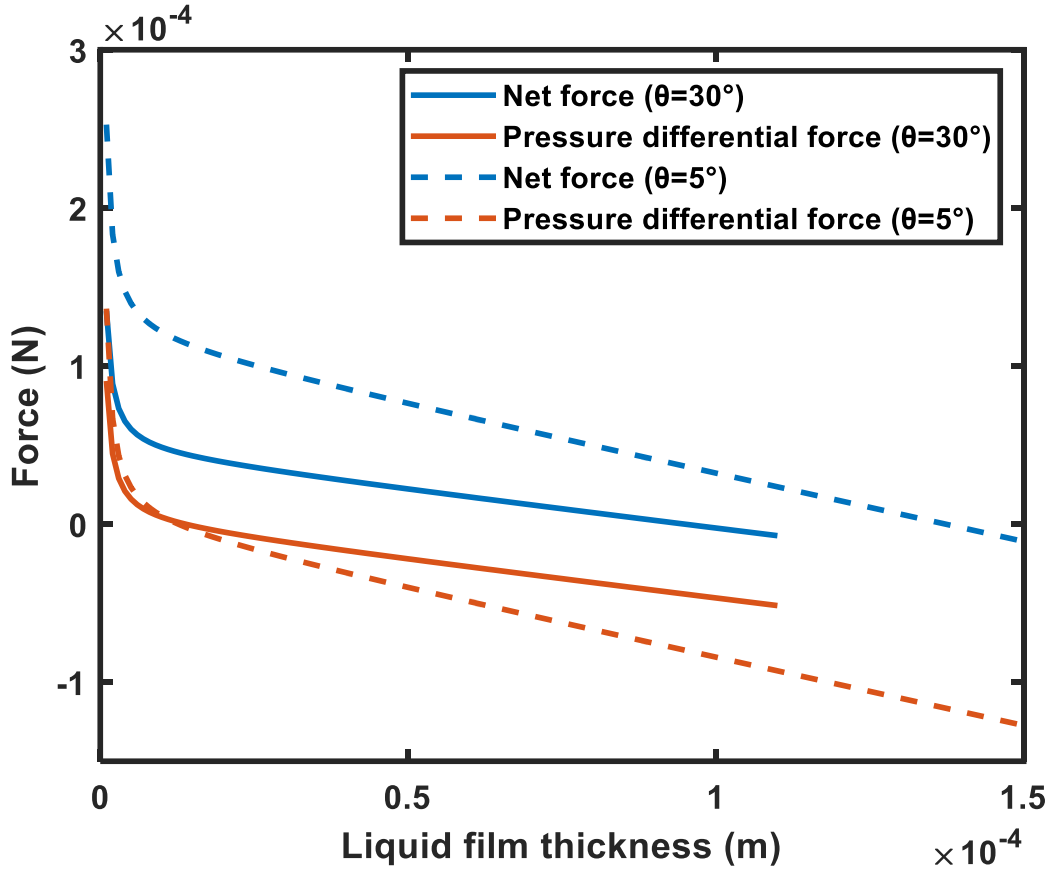


**Figure 3.12 The net and differential pressure forces for the hypothetical 85°-5° sawtooth microstructure are compared against the 60-30 sawtooth microstructure.**

Similarly, for a flat downward-facing, no curvature occurs at the crest and trough; therefore, no pressure differential force is generated. Similarly,  $\theta \rightarrow 0$  decomposes the buoyancy forces into a single vertical force with no horizontal components. A typical force balance for a downward-facing surface can be used without any drivers as a rationality check for the semi-empirical model.

$$\Delta P \propto \frac{1}{r_{(\text{crest,trough})}} ; r_{\text{crest,trough}} \rightarrow \infty, \Delta P \rightarrow 0$$

The change in the net force and the driving pressure differential force for slugs spanning four, five, and six sawteeth is illustrated in Figure 3.13. Higher pressure differential force is generated at low

liquid film thickness with an increase in size. However, it produces a negligible change in predicted liquid film thickness due to the interplay between driving and limiting forces.

The corresponding increases in added mass forces and drag force negates the increase in buoyancy forces.

For four sawteeth, the net buoyancy force is  $5.41 \times 10^{-5} \text{ N}$ , the drag force is  $2.85 \times 10^{-6} \text{ N}$ , and the added mass force is  $1.42 \times 10^{-5} \text{ N}$ .

For six sawteeth, the net buoyancy force is  $1.89 \times 10^{-4} \text{ N}$ , the drag force is  $2.1 \times 10^{-5} \text{ N}$ , and the added mass force is  $7.89 \times 10^{-5} \text{ N}$ .

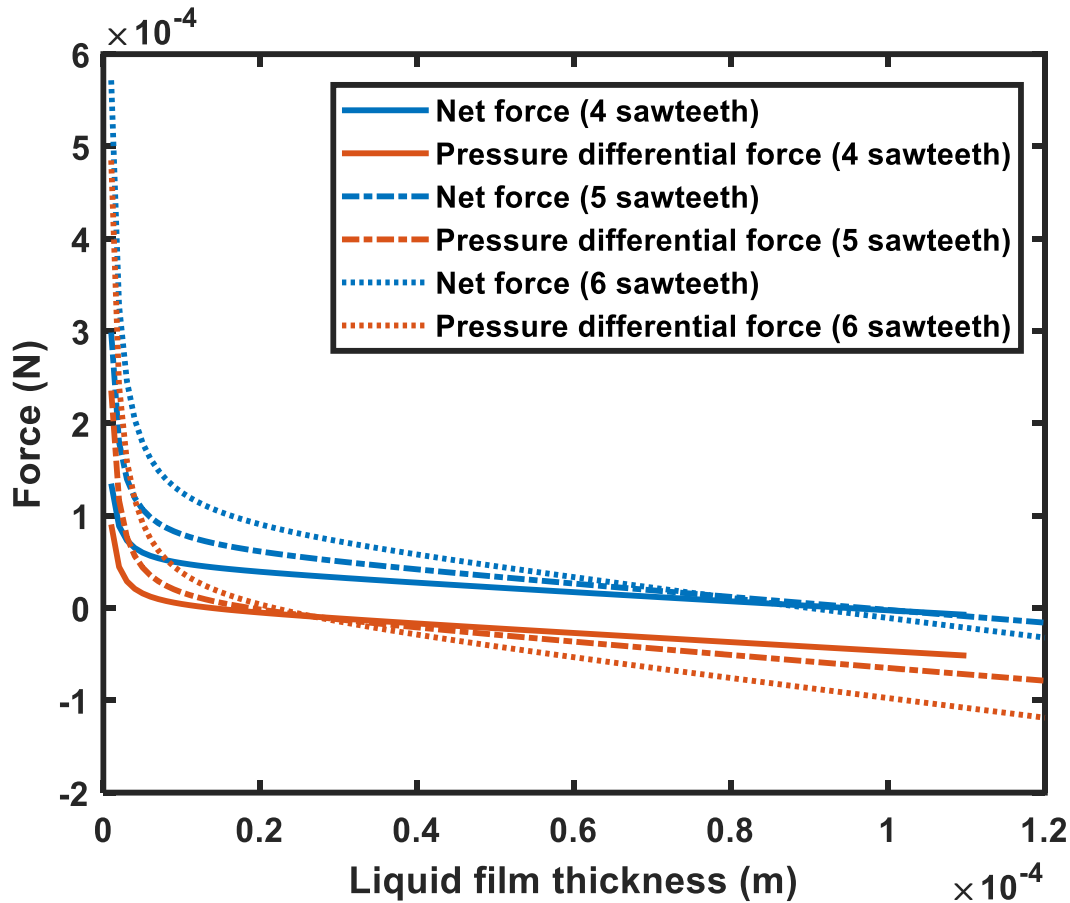


**Figure 3.13 Comparison of the net forces and the differential pressure forces for vapor slugs spanning across four, five, and six sawteeth**

### 3.2 Summary of the Auburn University Experiments

The in-house terrestrial setup fabricated at Auburn University was used to extensively downward-facing vapor bubble dynamics from the  $60^\circ$ - $30^\circ$  sawtooth microstructure. The vapor mobility from the microstructure was quantified using high-speed image processing and compared against a baseline surface. The semi-empirical force balance model was used to study the feasible liquid film thickness range to drive motion across the microstructure, and the driving forces at different vapor bubble sizes and microstructure geometry were explored.

The experimental setup and results also enabled the transfer of information to external stakeholders for the ASCENT project. The organizational structure of ASCENT and the consequent transfer of information to the stakeholders on various features and aspects of the flight experiments are described in the next few sections.

### **3.3 ASCENT – Organizational Chart**

The requirements of the science team were captured in the engineering requirement document (ERD) and the science verification document (SVD). The engineering requirements attempted to capture the progress made in the bi-weekly meetings with Techshot, NASA, and the ISS National Lab.

Over a hundred regular meetings were required to capture the ASCENT project's intricacies, requirements, and science objectives with the space industry personnel. The science requirements and data from the Auburn Terrestrial experimental setup were fed to the NASA implementation partner, Redwire Techshot, under the oversight of the ISS National Lab and NASA. The overall flow of information within the organization chart is illustrated in Figure 3.14.

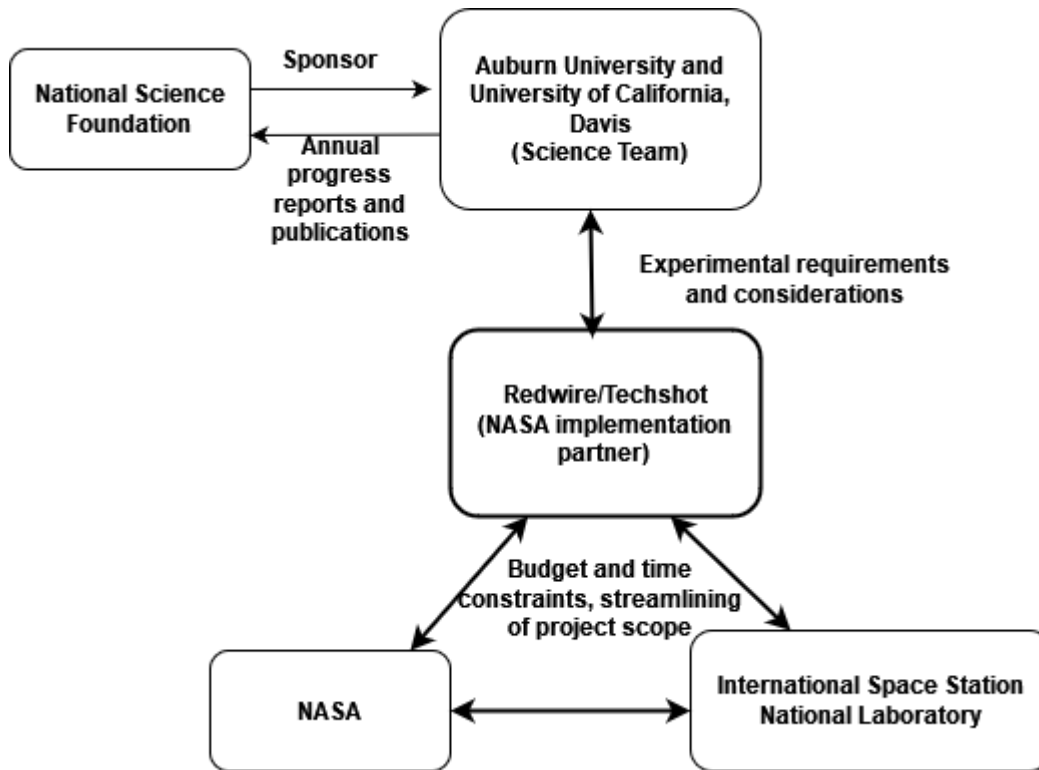


**Figure 3.14 The flow of information between the different agencies involved in the ASCENT investigation**

### **3.4 Transfer of Information from the Science Team to the NASA Implementation Partner**

The next section of this dissertation discusses the transfer of information from the successful Auburn University experimental setup to the NASA implementation partner, Redwire Techshot. The transfer of information included a mix of reproducing elements of the terrestrial experimental setup, discussing alternatives for features incapable of being reproduced for the flight experiment, and brainstorming other procedural and logistical procedures.

Extensive, elaborate experiments were conducted at Auburn University as the flight project worked through delays. In addition to producing reference data, the upward-facing and downward-facing tests conducted in the Auburn University lab also yielded valuable procedural information on the restricted volume available for the flight experiments.

The requirements discussed were eventually captured in a Science Verification Document (SVD), as shown in the Appendix. The main topics of discussion during these bi-weekly meetings included:

#### **3.4.1 Test surface fabrication**

The first few biweekly discussions centered around the fabrication of test surfaces. The options considered were manufacturing the test surfaces in-house using Auburn University's additive manufacturing capabilities or allowing the implementation partner to fabricate the desired test surface using their native paste-based manufacturing technology.

Though a few initial attempts were made using the implementation partner's technology, the precision, and accuracy required for the different features on the surface could not be adequately captured. Therefore, the test surfaces were manufactured at Auburn University's National Center for Additive Manufacturing Excellence (NCAME).

#### **3.4.2 Borosilicate glass ampoule/ test chamber manufacturing**

Auburn University took the head start on the test chamber design and manufacturing the unique test chamber design for the flight experiments. The science team utilized the Auburn glassblowing laboratory services to design several iterations of the unique glass ampoule design, as described in the previous section on the in-house experiments.

The design was deemed successful enough to be adopted by the NASA Implementation partner for the ISS experiments. The flight experiments were completed without any anomalies resulting from the test chamber, even at high heat fluxes. The design process was extensively discussed during the meetings, with a few changes to converge on the final flight design.

### **3.4.3 Filling and charging of the fabricated ampoule**

The lessons learned from the Auburn experimental setup, like using a vacuum to evacuate the test chamber of non-condensable gases and carefully controlling the mass flow rate of the dielectric liquid into the evacuated chamber, were communicated through reports to the implementation partner. An influx of the dielectric liquid at high mass flow rates could potentially damage the confined glass chamber, and a valve was installed to ensure a slow filling process.

### **3.4.4 Degassing the dielectric liquid FC-72**

An external degassing procedure was adopted for the FC-72 liquid in the Auburn University terrestrial setup. The liquid was heated in place with a graham condenser at the highest point to purge the dielectric liquid of non-condensable gases.

This solution was shared with the implementation partner, who adopted a similar approach of maintaining the ampoule at low pressures for several minutes to remove the non-condensable gases.

### **3.4.5 Leak checking**

The dielectric liquid used in the study was highly wetting, able to leak through tiny gaps and crevices. The low contact angle of the liquid, combined with the low boiling point (56°C at 1atm), would result in residue-free evaporation of large volumes of the expensive dielectric liquid. The discussions centered around leak-proofing the eventual flight experimental chamber and identifying possible locations for fluid egress (joints and assembly areas).

### **3.4.6 Characterization of each ground ampoule**

The flight hardware's power control circuit was characterized for each ampoule on the ground before launch. As direct measurement of the heat flux was not feasible for the flight experiments, the input power from the source was calibrated for each ampoule terrestrially. The heat flux



characterization ensured that the team maintained high confidence in the input parameter for the flight experiments.

### **3.4.7 Resistance heater coating in the square ampoule**

The terrestrial experiments at Auburn University utilized an adhesive-based film heater on the outside of the glass face to conduct heat to the test surface. However, a more robust heater was desired for the microgravity experiments.

Initially, a transparent heater coating, like Indium Tin Oxide, was sought to enable imaging through the heated surface. However, the position of the orthogonal mounts precluded imaging from that direction. As the imaging consideration was eliminated, the team converged on utilizing Nichrome as the heater instead.

Nichrome, an alloy of nickel and chromium, has high electrical resistance, thermal stability, and corrosion resistance. In addition, sputtered coating of Nichrome on borosilicate glass is commonly used as a heating element due to the coefficient of thermal expansion between the glass and Nichrome, ensuring a hermetic seal. Due to these advantages, Nichrome was chosen as the resistance heater for ASCENT.

However, some adhesion issues were encountered during the coating process. The implementation partner contacted two external vendors to complete the coating process. The coating failed to adhere properly to borosilicate glass in the inspection articles from the first vendor, the second vendor was contacted, and the coating was successful.

### **3.4.8 Copper coating along the circular section of the ampoule**

The unique design of the ASCENT ampoule to retrofit into the PFMI necessitated two special coatings of the manufactured glass. Though the nichrome coating is the resistance heater, the

power from the PFMI furnace must be delivered to the resistance heater through the ampoule's cross-section.

A highly electrically conductive coating with copper was sputtered on the circular cross-section to deliver power to the nichrome heater. Like the nichrome coating, sputtered copper coating on borosilicate glass is commonly used and well-understood.

### **3.4.9 Placement of thermocouples**

The science team was informed that four thermocouples are available for instrumentation within the ampoule. An additional two thermocouples were utilized for the functioning of the PFMI furnace.

Following the project's objectives, discussions converged on placing the thermocouple at the following locations.

1. A surface thermocouple was placed on the center of the 80 mm long test surface. The thermocouple was epoxied to the side of the test surface.
2. A fluid thermocouple was offset from the surface thermocouple by approximately half of the test surface length. The thermocouple was located on the face opposite to the test surface.
3. The other two thermocouples were placed in the two cold zones. Though control thermistors were already embedded in each cold zones. The fluid thermocouples were located axisymmetrically under the center of each cold zone.

#### **3.4.10 Pressure relief membrane material**

Multiple polymers were explored as possible options as material for the pressure relief membrane. The chief considerations when choosing the pressure relief membrane were the ability of the material to withstand absorptions of the dielectric liquid, FC-72, while being compatible with it.

In particular, the short-to-medium-term effects of the FC-72 liquid and vapor were considered extensively [80]. Based on previous research and the science team's extensive ground experimentation with the dielectric liquid, the science team's top three choices were conveyed to the implementation partner, as listed below.

1. Neoprene/polychloroprene
2. Ethylene Propylene Diene Monomer (EPDM)
3. Fluoroelastomers (e.g., Viton)

The pressure relief membrane was fabricated with Neoprene. Neoprene can be manufactured in various thicknesses and forms, allowing for customization based on specific pressure relief requirements.

#### **3.4.11 Pressure relief testing**

The pressure relief membrane was tested in the final configuration of the fabricated ampoule in the flight furnace. These pre-flight tests, deemed "check out runs," enabled testing the limits of the pressure relief system.

As pressure could not be measured in the ISS experiments, the pressure inside the closed ampoule was measured during these checkout runs.

#### **3.4.12 Thermal interface material**

The thermal interface material used by Auburn's terrestrial experiment, Artic Silver Epoxy, was recommended to the NASA implementation partner. The epoxy was used for all future experiments to reduce thermal resistance between the borosilicate glass surface and the titanium alloy test article.

#### **3.4.13 Thermal interface bonding with constant pressure**

In the Auburn University terrestrial setup, thermal bonding was ensured through the additional ports to locate and cure the test surface in place with the application of pressure. However, the ampoule's constrained volume complicated the pressure application after the test surface was placed within the ampoule.

Consequently, the implementation partner developed a catheter system to apply pressure on the test surface after applying the epoxy. After placing the test surface, the catheter was inserted in a narrow volume and inflated against the test surface. The test surface was allowed to cure in place for 20 minutes.

The application of pressure is crucial to achieve good thermal interface bonding. Pressure helps to eliminate air voids or gaps between the surfaces and the epoxy layer, promoting better thermal conductivity.

#### **3.4.14 Candidate high-speed camera tests**

The candidate camera to be installed in the ISS flight hardware for the microgravity experiments was a Ximea MQ013MG-ON USB3.0 camera. The implementation partner purchased the camera and shipped it to Auburn University for compliance tests. As Auburn University's test setup was fully functional, multiple experimental runs were conducted in the lab.

The camera from the implementation partner was unboxed, as shown in Figure 3.15. The components illustrated are Ximea MQ013MG-ON, USB 3.0 m cable (angled), HonYan Security Lens 1/3" 4mm F1.4 I.R. Fixed Iris CCTV Lens w/ CS-Mount and C/CS Mount adapter.



**Figure 3.15** The unboxed components of the candidate USB 3.0 camera are shown.

As an appropriate lens was unavailable with the camera, the lenses available in the lab were used for imaging. The Ximea camera was mounted with a K2/SC long-distance single micro port main body with a close-focus objective lens (CF-2). The images were backlit with a LED spotlight (Energetic ELY08D-MR5.3S). The lens setup for high-speed camera is shown in Figure 3.16.

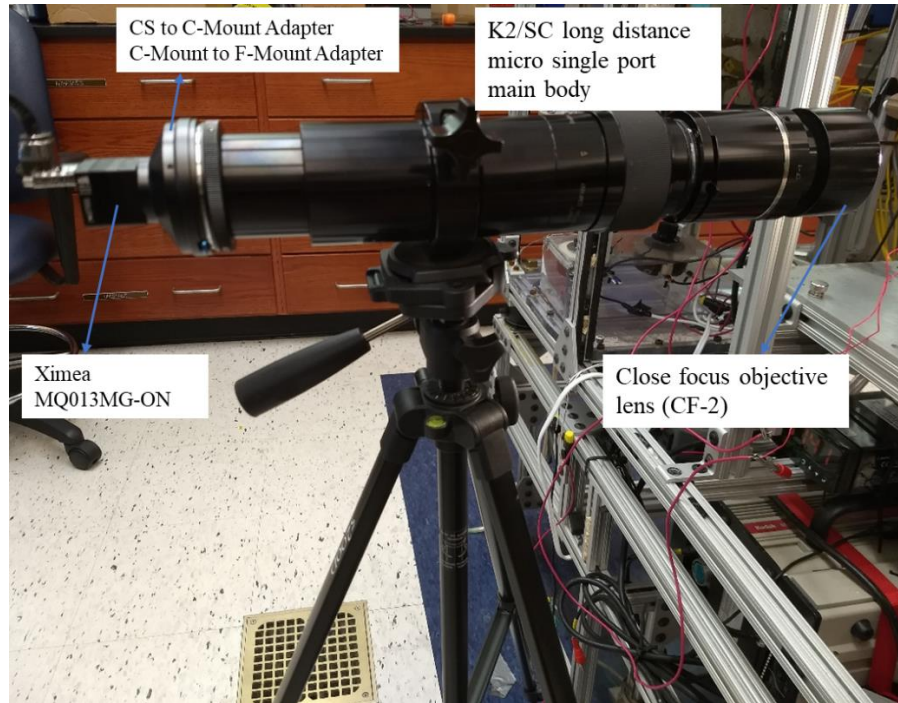
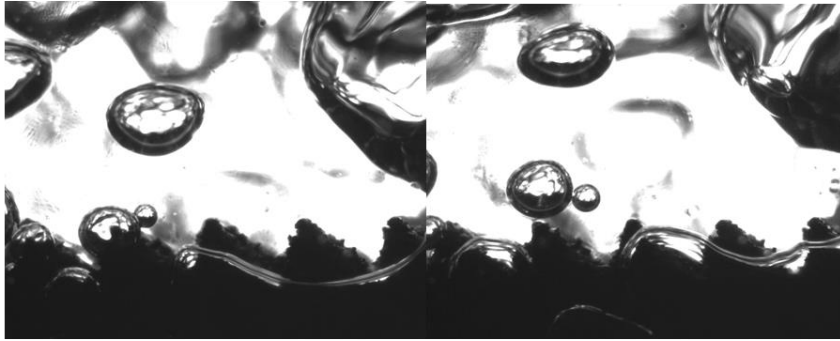


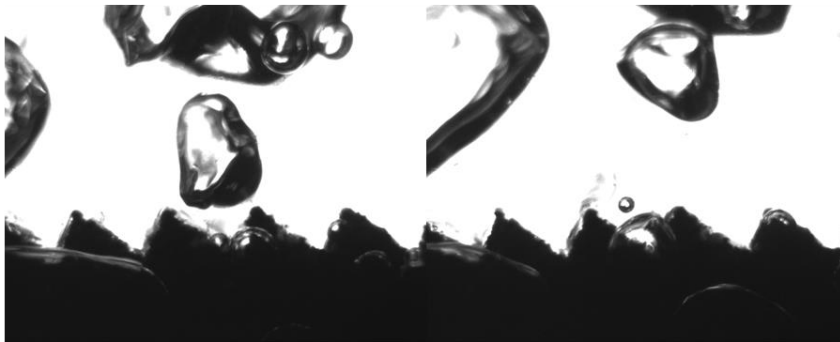
**Figure 3.16 The lens setup at Auburn University for close-range high-speed imaging of the USB3.0 camera**

Two consecutive frames at different fps and resolutions from these preliminary tests are shown in Figure 3.17. Though bubble dynamics were expected to differ in microgravity, the images below showed the number of ratchets covered and bubble tracking possibilities. As explained in the next section, the frame rates listed below are not true.

1280 x 1024, 168 *fps* (*transported\**), 35  $\mu$ s exposure



640 x 512, 537 *fps* (*transported\**), 35  $\mu$ s exposure



320 x 256 (**Region of Interest (ROI)**), 1450 *fps* (*transported\**), 35  $\mu$ s exposure

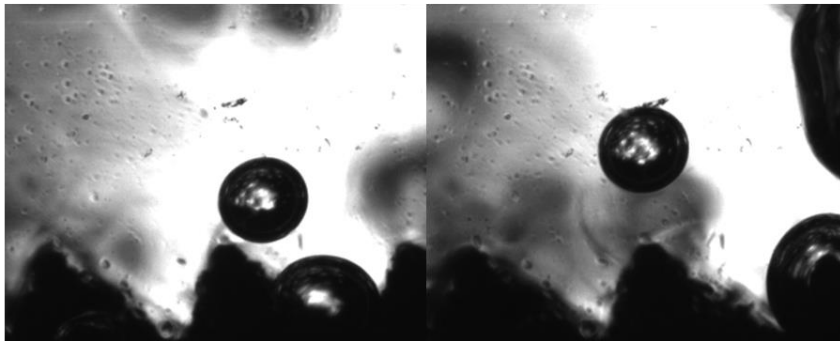


**Figure 3.17** The various framerate and exposures attempted in-house at Auburn University's terrestrial setup.

The true frames per second were limited due to **writing speed and the software**. The true fps and the corresponding file size estimates are listed below. The discrepancy is due to the "Record video to file" setting on the CamTool interface.

**Table 3.3 The raw frames per second from the camera interfacing software due to the default settings**

<b>Video parameters</b>	<b>Recording time (real-time)</b>	<b>Raw fps based on images</b>	<b>File size estimate</b>
1280 x 1024	45.35 seconds	~30.45	1.68 GB
640 x 512	44.93 seconds	~78.75	1.09 GB
320 x 516 (ROI)	47.1 seconds	~112.35	364 MB

The setting "Record Loop" was enabled to obtain the maximum frame rate, and the video was recorded to RAM. The recorded video was subsequently saved to a file. With these settings, the maximum frame rate was 2500 fps @ 320 x 256 (ROI) with 35  $\mu$ s exposure. However, the recorded file size estimate for 12- second (real-time) video was 2.40 GB.

The writing speed to save the recorded video factored into the time between subsequent triggers for the experimental runs.

The following aspects of the camera were investigated satisfactorily:

- Interfacing with the Ximea software
- Lensing using adapters



- Backlighting image field of view with LED spotlight
- Image quality at different resolutions
- Image recording settings to obtain maximum frame rate

These findings were shared with the Redwire Techshot team, and the subsequent experiments from the implementation partner accounted for these findings from these preliminary tests. The lensing requirements were decided based on these observed framerates.

The meetings also included in-depth discussions of possible bottlenecks, delays, and workarounds to get the project closer to launch. Though many flight deadlines were missed, the project's progress was ensured through the pandemic-induced supply chain issues.

The next section of this dissertation discusses the ground experiments conducted at the implementation partner's site in Greenville, Indiana. The objective of the upward-facing ground experiments was to provide reference data for the microgravity experiments while climbing the steep learning curve of the unique experimental setup and procedure.

### **3.5 Terrestrial Experiments at Redwire Techshot**

The following tests were conducted at Techshot (Greenville, Indiana) with the fabricated flight and ground ampoules. The section details tests conducted in the terrestrial mock-up of the PFMI furnace (the ground furnace) and the original flight PFMI furnace before being shipped to the International Space Station.

The implementation partner labeled each unique test surface geometry, as shown in Table 3.4. The flight labels were consequently labeled FLT1, FLT2, FLT3, and FLT4, corresponding to Ampoule #'s 1,2,3, and 4. The ground tests described in this table are discussed in the next few sections.

**Table 3.4 The description of each planned test for the ASCENT project**

<b>Ampoule Type</b>	<b>Ampoule #</b>	<b>Science Material</b>
Development Test 1	6	60-30 / 1mm
Development Test 2	8	60-30 / 2mm
Ground (Checkout Run)	1	Flat
Ground (Checkout Run)	2	60-30 / 1mm
Ground (Checkout Run)	3	60-30 / Slot
Ground (Checkout Run)	4	60-30 / 2mm
Flight	1	Flat
Flight	2	60-30 / 1mm
Flight	3	60-30 / Slot
Flight	4	60-30 / 2mm

### **3.5.1 PFMI Furnace and the ASCENT Ampoule**

The ASCENT investigation was conducted in the Pore Formation and Mobility Investigation Furnace (PFMI) in the International Space Station (ISS) Microgravity Science Glovebox (MSG) [81]. The PFMI furnace was first launched to the ISS in June 2002 [82] for materials science

investigation. It is a Bridgman-type furnace (industrial furnace used for crystal growth) that can support a maximum heater temperature of 130 °C and a maximum thermal gradient of 110 °C/m. It can support a circular sample tube with a maximum diameter of 12.75 mm and 28 cm long. Though initially designed with a single cold zone, an additional cold zone was added for the ASCENT investigation. Each cold zone consists of four thermoelectric devices (TED) capable of achieving a minimum temperature of 5 °C. Six thermocouple ports are available for instrumentation, but two are used for furnace control. The temperature data is recorded at 1 Hz. The legacy cold zone can be translated at 0.5 micrometer/sec to 100 micrometer/sec to  $\pm 5\%$  stability. Two electrode rings provide electrical contact from the furnace to the sample tube. The furnace is equipped with two COHU 3812 CCD cameras (22:1 zoom capability, 25 frames/sec), and one of these cameras was used for the ASCENT investigation. The cameras and electrode rings are mounted on a translation system that allows commands to pan up and down the sample processing frame. A Eurotherm 2408 PID controller provides temperature setpoint input to the heated zone between the two electrode rings.

The PFMI furnace interfaces with a Microgravity Science Glovebox (MSG) laptop computer through a Data Acquisition Pad (DaqPad) and acquires temperature data from the sample using the k-type thermocouples. The process control module allows the control of the setpoint of all available thermocouples. The live feed of the temperature data is overlaid onto the feed of the COHU camera for data transmission.

To support the science requirements for the ASCENT investigation, two high-speed cameras, a light bar, and an additional cold zone were added to the PFMI furnace, as shown in Figure 3.18. The frame rate of legacy COHU cameras at 25 fps was deemed insufficient for the timescale of the ASCENT investigation. Therefore, high-speed cameras captured the vapor dynamics at 900

frames per second. A wide field of view (10cm x 1.5cm) was provided by one high-speed camera, while a narrower, high-speed camera captured a smaller Region of Interest (ROI) (1cm x 1.5cm). The high-speed cameras are in the xiQ compact USB3 series made by Ximea (P.N.: MQ013MG-ON). The high-speed camera was interfaced with a computer through USB 3.0 ports. A Light Bar was added to the PFMI Facility to support this experiment. The process fluid is degassed FC-72.

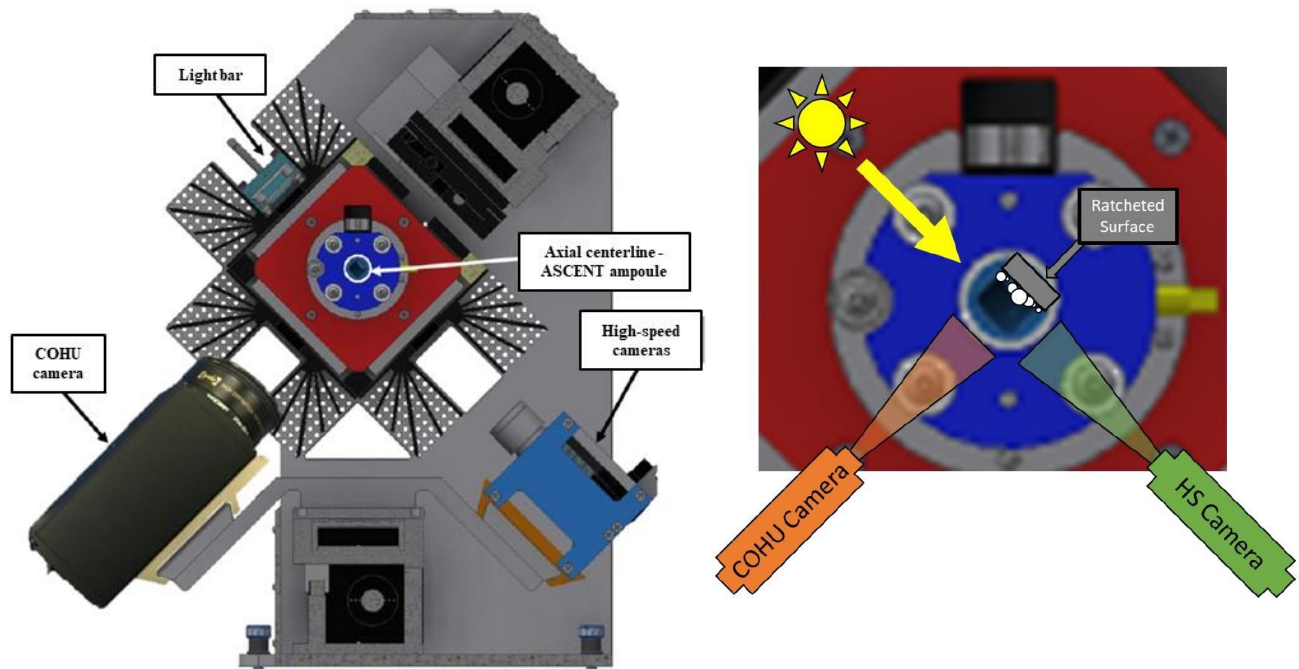


**Figure 3.18** The layout of the imaging system for the PFMI-ASCENT experiment is illustrated. The additional light bar backlights the high-speed camera imaging while the COHU camera captures a top view of the test surface.

All ASCENT ampoules were fabricated to the specifications described in this next section. The test surface (80 mm (length) x 2 mm (base thickness) x 6 mm (width)) was centered in a square borosilicate ampoule with 8mm I.D., 1.2 mm wall thickness, and 90 mm length. One face of the square tube was sputtered with Nichrome, where the resistor film thickness is non-uniform:  $\pm 2.5\%$ .

The area of the resistor coating for all the sample ampoule assemblies was 82 mm (length) x 7 mm (width). The ampoule resistance for the baseline surface and the microstructure were measured at 40.3 and 39.3  $\Omega$ , respectively.

The central square section separated two circular borosilicate glass tube sections with an outer diameter of 12.7 mm and 108 mm in length, as shown in Figure 3.19a. A flame seal merged these three sections into a single ampoule assembly. The ends of the circular cross-section closest to the square face of the borosilicate glass ampoule were sputter coated with copper to a length of 42 mm and a thickness of 15  $\mu\text{m}$  to maintain electrical contact with the resistive nichrome heater, as shown in Figure 3.19b. The circular-to-square transition design was necessary to retrofit the complete ampoule assembly into the forward and aft electrode rings described in the previous section.

The test surface was attached to the borosilicate glass ampoule using Arctic Silver Quick Cure Epoxy. The test surface was located and cured in place using a custom-built carriage. A catheter was inflated, and the pressure was held for 5 minutes to ensure thermal bonding. The epoxied test surface was cured for 20 minutes before inserting thermocouples.

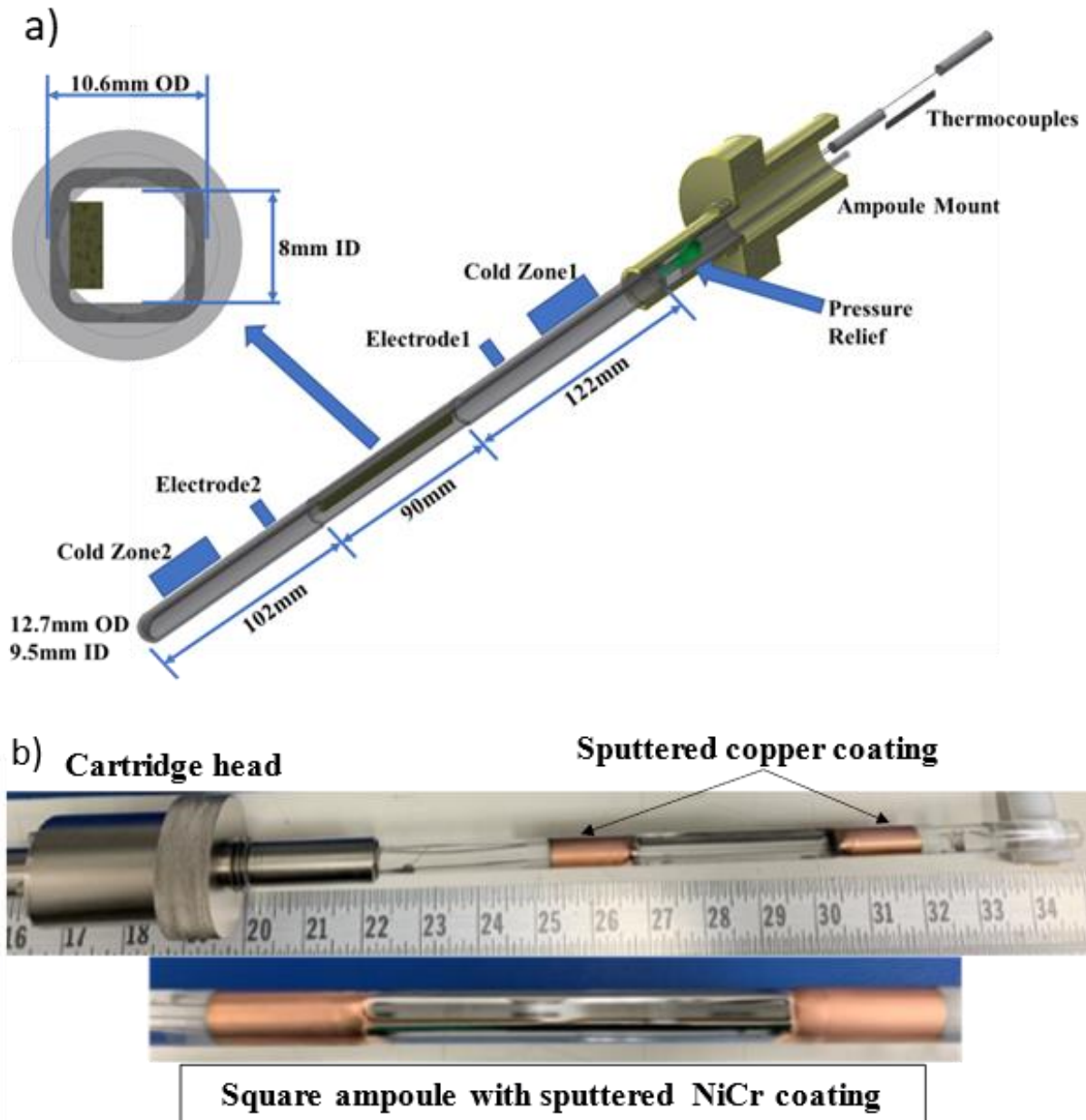
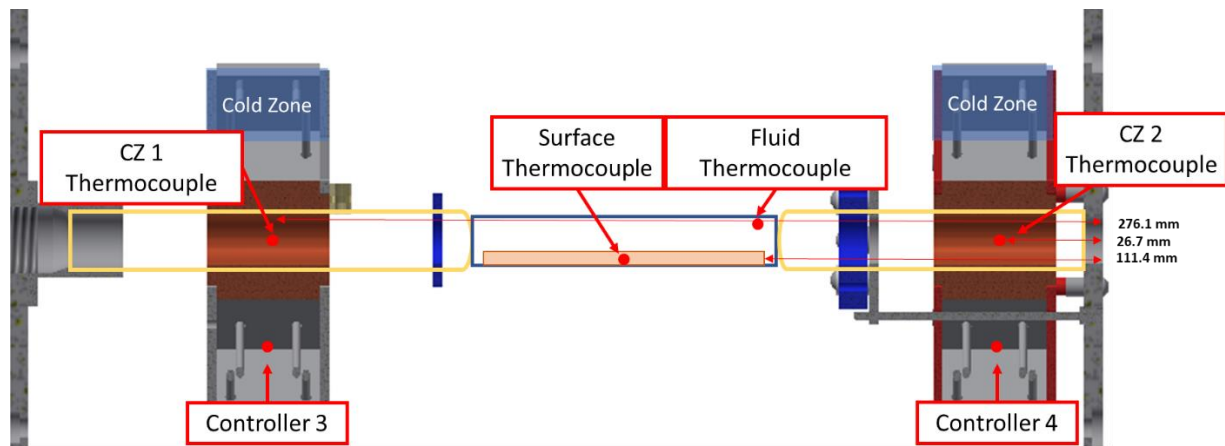


Figure 3.19 a) The layout of the PFMI ASCENT ampoule is shown on the left. b) A fabricated sample ampoule assembly on the right indicates the cartridge head and the sputtered copper and nichrome coating. The nichrome coating is the resistive heater for the ASCENT experiment.

Four internal, sheathed, and compact Omega transition probes were used to measure surface and fluid temperatures with type K thermocouples (0.5 mm diameter) without obstructing the high-speed camera view, as shown in Figure 3.20. The surface thermocouple was affixed to the side of the test surface, centered along its length, using thermal epoxy. The fluid thermocouple was placed in the opposite direction of the surface thermocouple, offset by half the length of the test surface in the sample ampoule assembly. Two thermocouples were also centered radially and axially in the cold zone locations. For the experimental runs described in this article, both cold zone thermocouples (CZ1 and CZ2) were spaced equally apart from the ends of the test surface (84.7 mm away) for symmetry. All thermocouples used for ASCENT were calibrated terrestrially within the temperature range used for the experiment (20-95°C). The leads of the thermocouple wires were wrapped in a PFA sleeve and fed through to a connector with gold-plated contacts to interface with the PFMI furnace.



**Figure 3.20** The position of the surface, fluid, and cold zone thermocouples is illustrated in the PFMI layout. The cold zone thermocouples are centered radially and axially under the cold zone locations.

One of the ampoule ends was sealed to a cartridge head through which instrumentation was fed, the pressure relief system was positioned, and the degassed dielectric fluid was filled into the ampoule. The other end of the ampoule was flame sealed, and the ampoule assembly was designed to be hermetically sealed. A pressure relief system consisting of a compact neoprene membrane was designed to maintain the pressure inside the closed ampoule constant at atmospheric pressure. The experimental flight design did not allow pressure measurement due to space constraints. However, the flight ampoules were tested before launch on the ground to verify the nominal operation of the pressure relief system across the range of desired heat flux values. A vacuum ( $\leq 0.3$  2068 Pa) was pulled from the ampoule, purged from non-condensable gases, and filled with de-aerated FC-72 fluid. The sealed ampoules contained a maximum volume of 35 mL of degassed FC-72 per ampoule and presented no toxicity or O<sub>2</sub> displacement concerns in the transport vehicle in case of a leak.

### **3.5.2 Development Test 1 – Ground Furnace**

The ground furnace differed from the flight furnace: the ability to measure the pressure inside the closed ampoule and a newer version of the thermoelectric devices used to maintain the cold zone temperature. Apart from these two superficial differences, the ground furnace and the PFMI flight furnace were functionally identical.

The test surface for development test 1 was a 60°-30° sawtooth surface with cavities spaced 1-mm apart (ground version). ASCENT's test surfaces require a constant heat flux input (i.e., constant power per unit area) to achieve the expected science outcomes. As the PFMI furnace is configured to provide power to achieve the desired temperature setpoint, multiple science issues were encountered during the test.

- Inability to predict the surface temperature for the onset of nucleate boiling



- During the test, the surface temperature was incremented as many as fifteen times to achieve the start of nucleate boiling and record relevant scientific data, as shown in Figure 3.21.
- The number of attempts and temperature setpoints required for each test surface, cold zone setpoint, and heater temperature might differ significantly and increase the operational time for each of ASCENT's ampoules in the ISS-PFMI furnace.

With heat flux control, the onset of nucleate boiling was expected to fall within a tighter heat-flux range. The control method ampoules were also intended to improve the quality of science outcomes by increasing the time spent at interesting setpoints.

- Inability to compare similar test conditions for the same test surface with multiple runs
  - The ground test produced different nucleation activity from a preliminary run at similar hot and cold zone setpoints. The "expected setpoints" annotated in Figure 1 refer to the data from the preliminary runs.
  - The ability to compare ground tests to flight tests is expected to deteriorate further due to reduced gravity and the control method (temperature-controlled) for ASCENT.
  - The control method and change in buoyancy force for the flight tests will worsen the ability to predict the onset of nucleate boiling from the heater and liquid temperatures.

Though an initial learning curve was expected for the first flight ampoule with heat flux control, the ability to compare test surfaces was expected to improve for subsequent tests. Due to the abovementioned problems, the second development test was conducted with a different control method to mimic the constant heat flux control method.

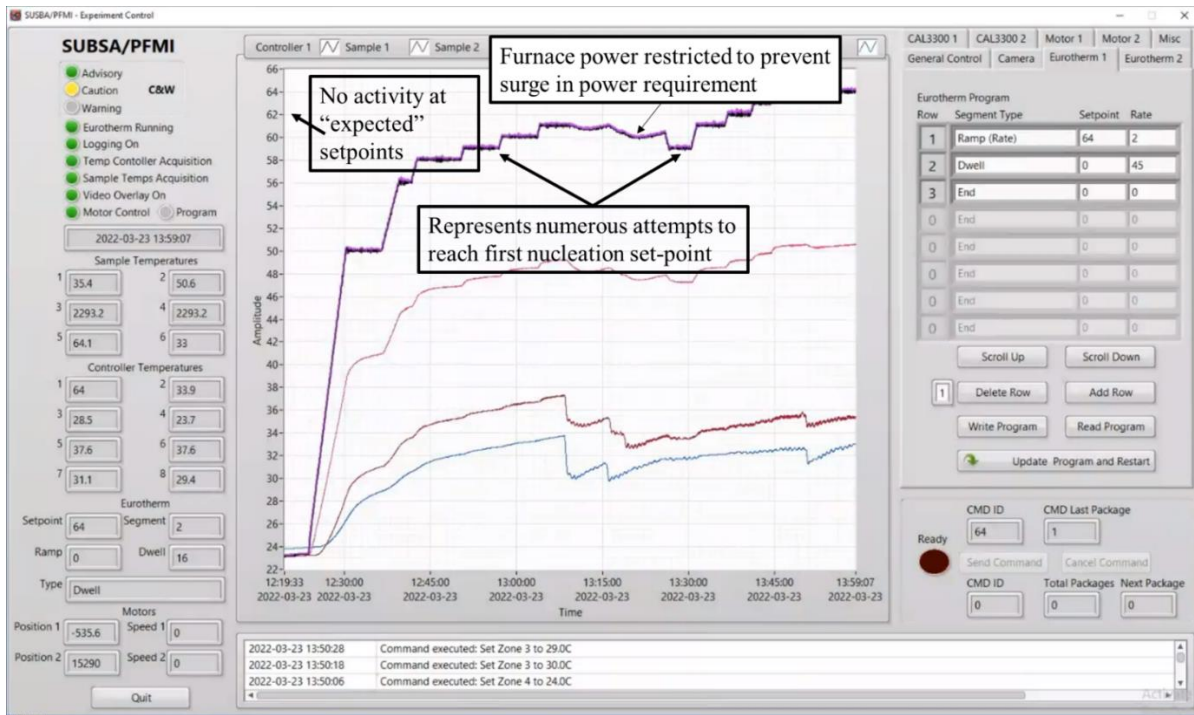


**Figure 3.21 Challenges encountered during the first temperature-controlled ground test for ASCENT. The SUBSA/PFMI control interface is shown.**

### 3.5.3 Development Test 2 – Ground Furnace

Though the PFMI furnace is designed to achieve a temperature setpoint of the test surface, the output voltage was limited to mimic the power-control method. The temperature setpoint was increased to a value higher than expected for the input power in the furnace. However, the output voltage was limited to a predetermined value to achieve a theoretical maximum power through the controller. In effect, the interplay between these parameters converted the temperature control method to the heat flux control method for Development Test 2.

The test surface for development test 1 was a 60°-30° sawtooth surface with cavities spaced 2 mm apart (ground version). The boiling curve for the first cycle (an increase in the heat flux to a maximum, followed by a ramp-down) at the desired temperature setpoint is shown in Figure 3.22.

The x-axis of the plot is the wall superheat, which is the difference in the surface temperature at

the saturation temperature, calculated at the measured pressure in the closed ampoule. The y-axis denoted the heat flux. As the heat flux increases, the surface temperature decreases as the first engineered cavity activates, as denoted by the onset of nucleate boiling (ONB) at  $1.4 \text{ W/cm}^2$  in the figure. With further increases in heat flux, the nucleate boiling regime maintains a steep slope in the boiling curve. At a heat flux of  $2.8 \text{ W/cm}^2$ , the vapor volume covered  $\sim 80\%$  of the ampoule width in the live feed of the high-speed cameras. The neoprene membrane in the ampoule, which acts as the pressure relief mechanism, was almost completely inflated at this heat flux. To safeguard the integrity of the fabricated ampoule, the heat flux was decreased at this vapor volume. The decreasing heat flux section of the boiling curve exhibited hysteresis as expected.

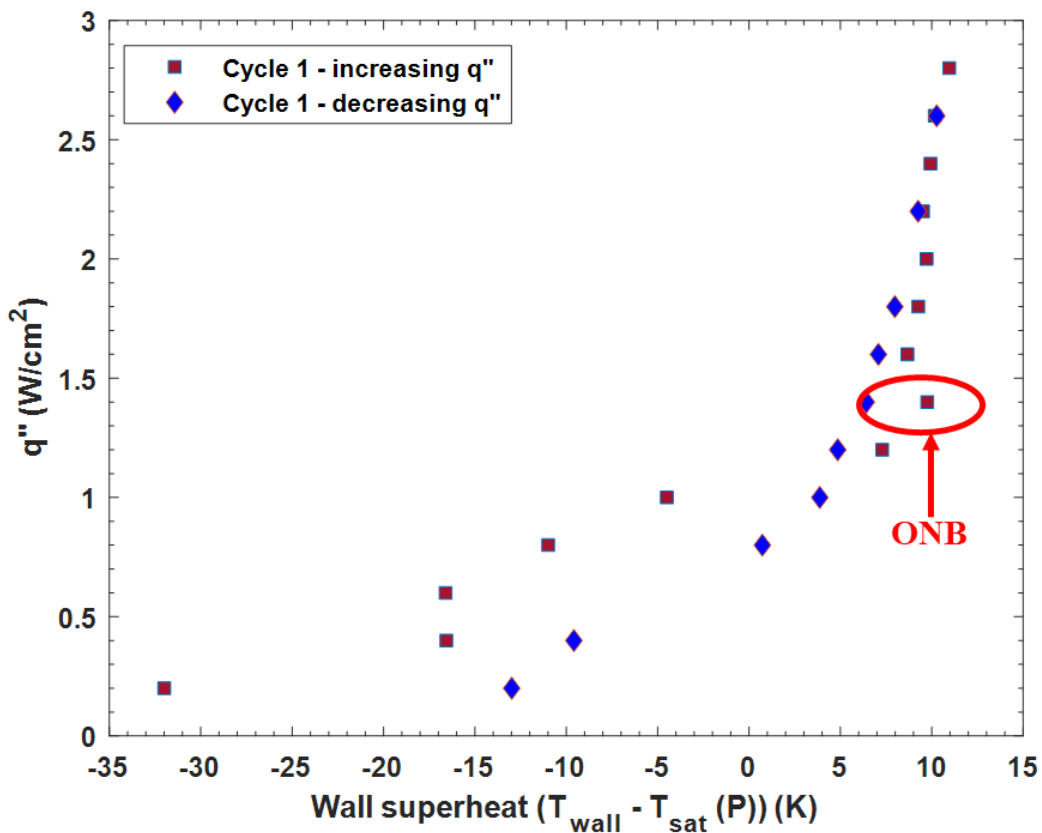


**Figure 3.22 The boiling curve for the first cycle of the heat-flux controlled development test in the PFMI furnace is shown.**

The next cycle was initiated after the test surface reached the ambient temperature, and the boiling curve is shown in Figure 3.23. In contrast to the first cycle, no clear temperature decrease denoted the onset of nucleate boiling as expected. Fewer points were traversed as the heat flux decreased, and no additional imaging outcomes were anticipated from the test.

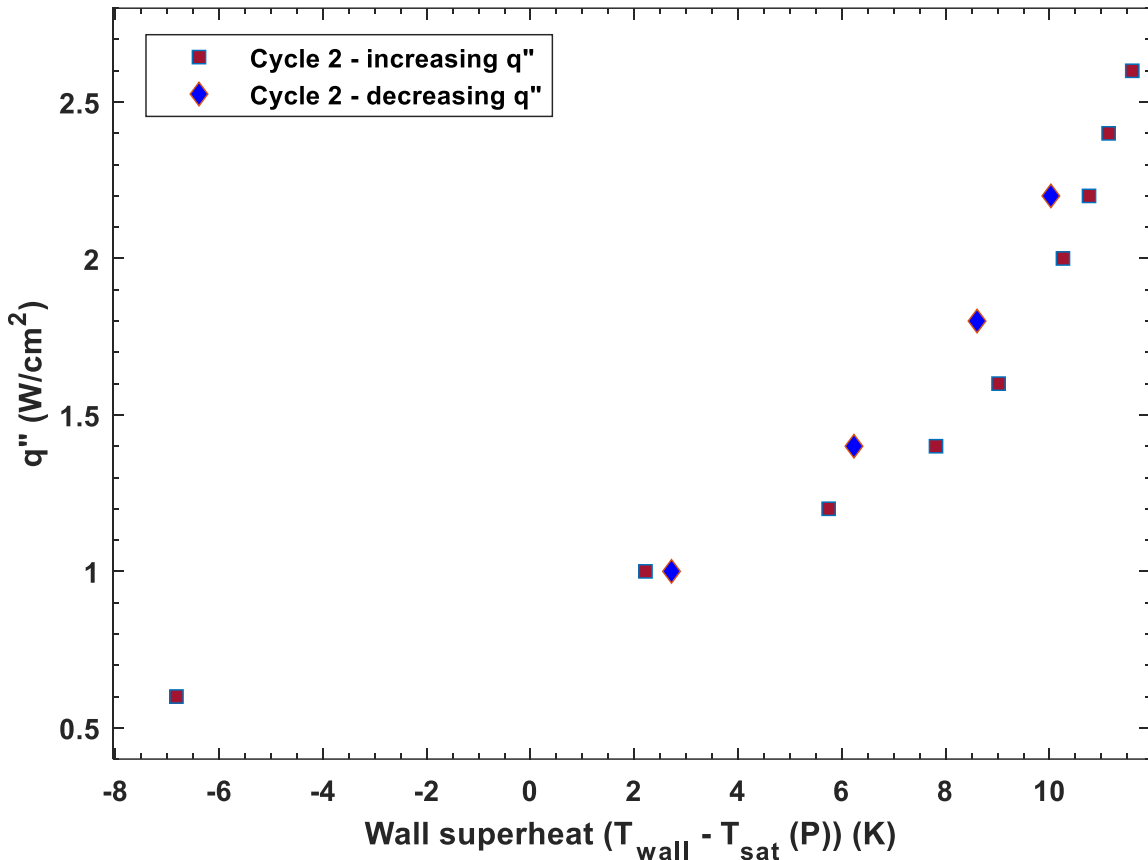


**Figure 3.23 The boiling curve for the second cycle of the heat-flux controlled development test in the PFMI furnace is shown.**

Two high-speed cameras to provide different views of the development test were active during the development test, as shown in Figure 3.24. The narrow high-speed views depicted in Figure 3.24 (a) and (b) were captured during the increasing heat flux section of the curve. Figure 3.24 (a) shows the first engineered cavity nucleating at 1.4 W/cm<sup>2</sup>, triggering a decrease in surface temperature

as expected at ONB. As the heat flux increased further, more engineered cavities were activated. Many cavities were active at a  $2.6 - 2.8 \text{ W/cm}^2$  heat flux, as shown in Figure 3.24 (b). The hysteresis discussed in Figure 3.21 showed that the engineered cavities were active at a heat flux lower than the ONB as the heat flux decreased. The wide view in Figure 3.24 (c) shows multiple cavities still active at  $1.2 \text{ W/cm}^2$ .

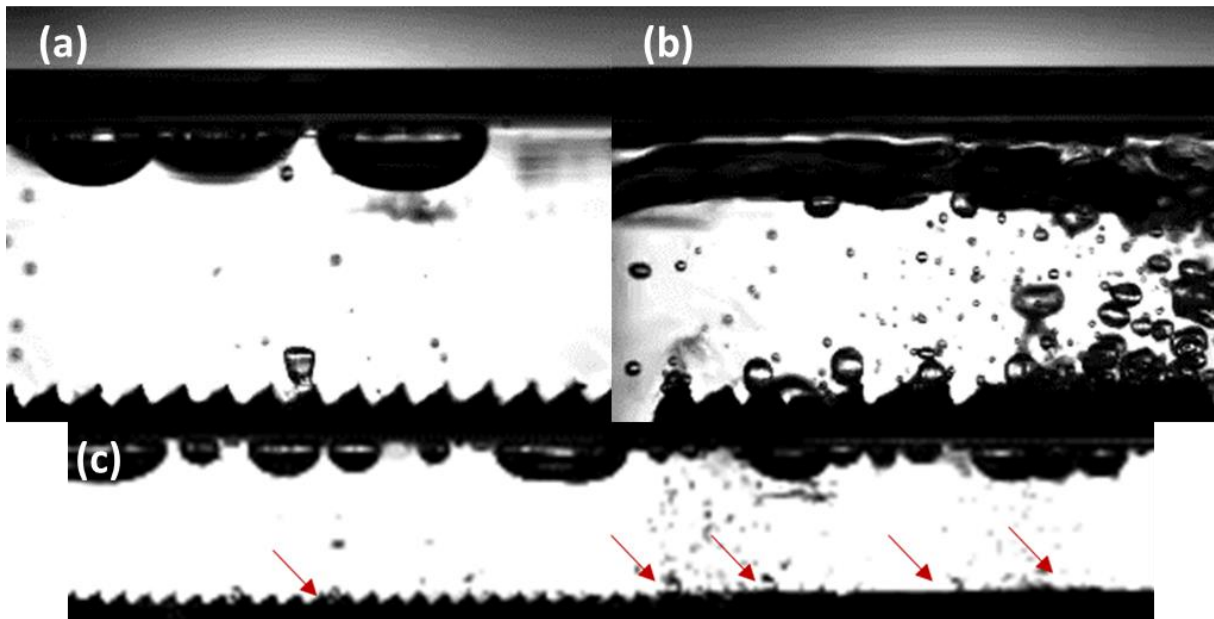


**Figure 3.24** The narrow high-speed view at  $1.4 \text{ W/cm}^2$  and  $2.6 \text{ W/cm}^2$  is shown in (a) and (b) respectively. The wide high-speed view that covers almost the entire test surface at  $1.2 \text{ W/cm}^2$  is shown in (c).

The tests described in the following sections were conducted on flight ampoules in the PFMI furnace before being launched to the ISS.

### 3.5.4 Checkout Runs in Ground Furnace

Before completing the final fabrication of flight ampoules, checkout runs were conducted to ensure that each ampoule's science requirements could be met. In addition, the pressure in the closed ampoule was measured during the runs to ensure the proper functioning of the pressure relief

system. Each checkout run consisted of a short ramp-up and ramp-down cycle to monitor the activation of the engineered nucleation sites in the nucleation boiling regime, as shown in Figure 3.25. High-speed videos were recorded at 2-3 heat fluxes in the nucleate boiling regime, typically at ONB ( $\sim 1.4 \text{ W/cm}^2$  for all test surfaces shown in Figure 3.25) and at the highest heat flux during the cycle. At comparable heat fluxes, the slotted nucleation sites produced more vapor and recorded a higher gauge pressure ( $\sim 0.5 \text{ psi}$ ) than the 60-30 sawtooth with nucleation sites 1-mm apart. The hysteresis during the ramp-down cycle is illustrated in the pressure trace, as active cavities maintained a higher pressure of up to  $1.2 \text{ W/cm}^2$ . Though the baseline test surface is illustrated in the figure, a low number of data points in the nucleate boiling regime precluded meaningful discussion of the trends.

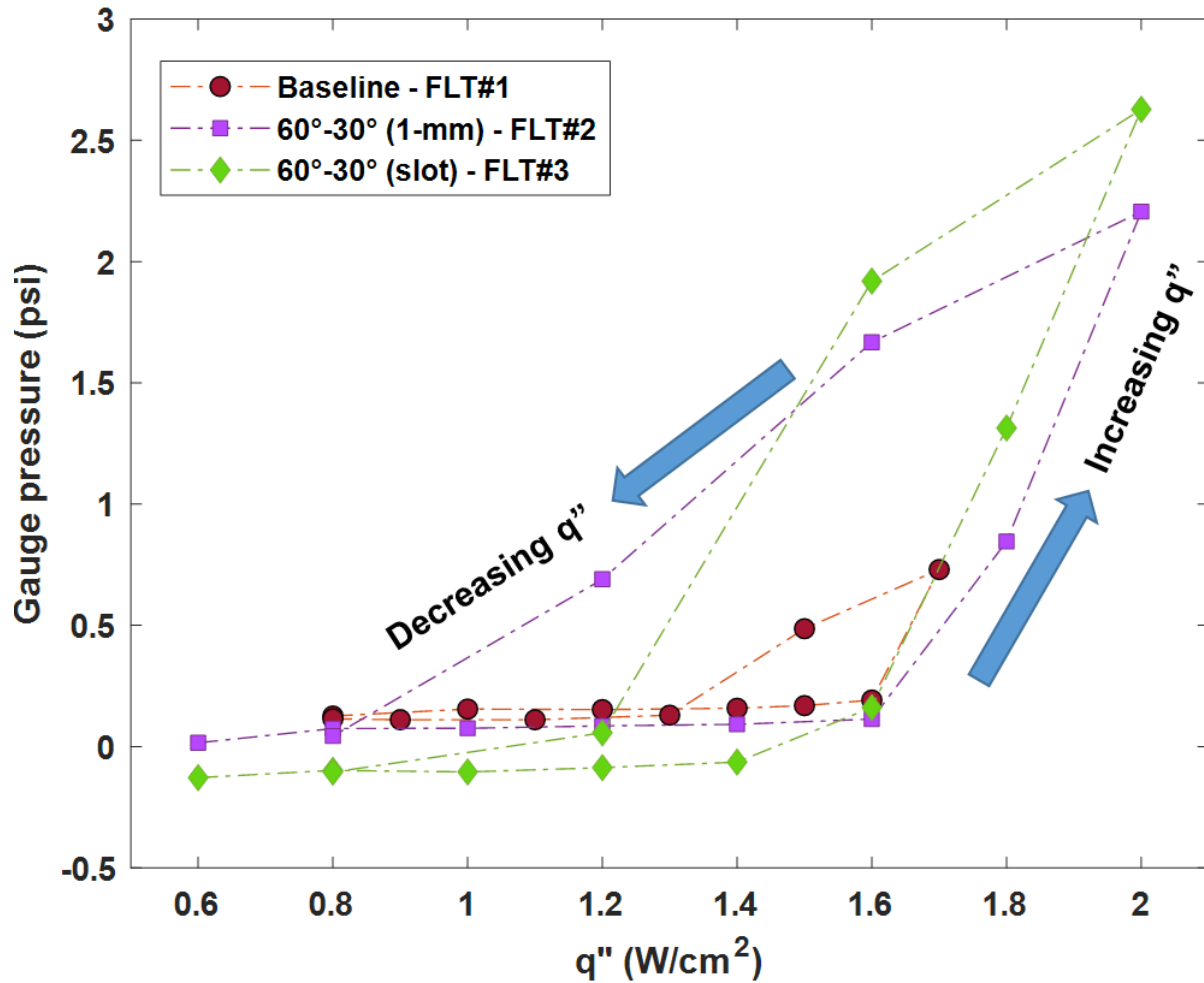


Figure 3.25 The pressure traces of three flight ampoules recorded during the checkout runs are shown.

### 3.5.5 Pre-flight Science Tests – Flight Furnace

All four flight ampoules were processed in the flight PFMI furnace, similar to the planned microgravity runs, with the test surface facing upward in terrestrial gravity. Due to the limited time for these pre-flight science tests, runs were conducted at two cold zone temperatures. Though the tests were conducted at Techshot, the science team monitored the test remotely through web conferencing applications. This proved a good enough practice to replicate for the ISS runs, too, notwithstanding Loss of Signal (LOS) incidents. Due to line-of-sight constraints, there are brief

gaps in communication between the ISS and the ground hardware. Since the LOS incidents can be anticipated in advance; the experiment will be paused for the duration of the event. The SUBSA/PFMI interface produced a live feed of temperatures at the test surface, the fluid temperature, and the two cold zone temperatures.

The tests were initiated at ambient temperatures, and both cold zones were set to the desired temperature. ASCENT will maintain symmetric cold-zone temperatures for all flight and ground tests. The temperature setpoint for the heater was set high enough (80-85°C) to ensure that the output voltage, as described in Development Test 2, limited the heat flux to the test surface. Pre-flight tests were initiated at 0.2-0.4 W/cm<sup>2</sup> and incremented steadily to a maximum heat flux of 2.2 -2.6 W/cm<sup>2</sup>. Next, the heat flux was ramped down to the initial heat flux. A ramp-up in heat flux followed by a ramp-down was a *cycle*. Two consecutive cycles constituted a *run*. All decisions on heat flux, cold zone temperatures, and camera placement were made remotely by the science team at Auburn University.

During these tests, substantial issues were discovered with two flight ampoules.

### **3.5.6 Challenges with the FLT #4 ampoule**

The FLT#4 ampoule, containing the 60°-30° sawtooth with cavities spaced 2 mm apart, did not activate nucleation sites at the desired heat fluxes. Multiple spurious sites were observed with the COHU camera, and the engineered sites did not trigger for the duration of the tests. An improper seal may have led to uneven heat distribution across the test surface as the test surfaces were epoxied to the borosilicate glass ampoule. In addition, the test fluid (FC-72) can flood air gaps in the seal and delay/prevent the triggering of the engineered sites. As the original FLT#4 ampoule would not meet the science outcomes for ASCENT, the corresponding ground ampoule was



converted to the flight ampoule. The corresponding ground ampoule was markedly better for pursuing the project's objectives in microgravity, as observed in Development Test 2.

Two fundamental differences between the ground and flight ampoules challenged the conversion process. The nichrome coating that serves as the resistance heater for the flight and ground ampoules was manufactured in different batches, leading to different resistances of the tube. Consequently, the higher resistance on the ground ampoules would limit the maximum heat flux. However, the limitation of the maximum heat flux is not expected to affect science outcomes, as the operational range of heat fluxes falls significantly below the maximum power afforded by the PFMI furnace.

The ground ampoules were also outfitted with additional hardware to facilitate the pressure measurement system. As this system was not compatible with the cartridge head for the flight furnace, it had to be removed. Removing the fitting's seal with the ampoule could cause irreparable damage. However, the conversion of the ground ampoule to the flight ampoule was completed successfully by Techshot.

### **3.5.7 Challenges with the FLT #1 Ampoule**

One of the cold zone thermocouples (under the translating cold zone) within the ampoule was disrupted during ampoule fabrication and was no longer radially centered in the ampoule housing. As a result, the cold zone temperatures differed by as much as 10°C during pre-flight testing. As minor variations in the location of the cold zone thermocouple could cause notable differences in the temperature readout, a combination of the cold zone temperature in the fluid and the cold zone controller temperature were used to ascertain cold zone functioning. A thermistor measured the cold zone controller temperature, while the fluid cold zone temperature was measured by a thermocouple held in place. The cold zones functioned nominally as the controller temperatures

held steady at the desired setpoints. Due to the additional measurement hardware on the cold zones, the loss of one fluid cold zone temperature readout was not expected to affect the ability to inform decisions during the flight runs or achieve the broader science objectives.

### **3.5.8 Pre-flight test results**

The cold zone temperatures for the pre-flight tests were 40°C and 20°C. A comparison of the first cycle of the runs at each cold zone temperature for the FLT2 ampoule is shown in Figure 3.26. As expected, the surface temperature decreases in the nucleate boiling regime with a decrease in cold zone temperature. Similarly, the test surface could be pushed to a higher input flux (2.6 W/cm<sup>2</sup>) at 20°C compared to 2.2 W/cm<sup>2</sup> at 40°C. A lower cold zone temperature handled a higher vapor load, aiding the pressure relief system in maintaining the pressure inside the closed ampoule within the operational limits. The high-speed videos indicated the lower vapor volume in the closed ampoule at 20°C cold zone temperature at identical heat fluxes.

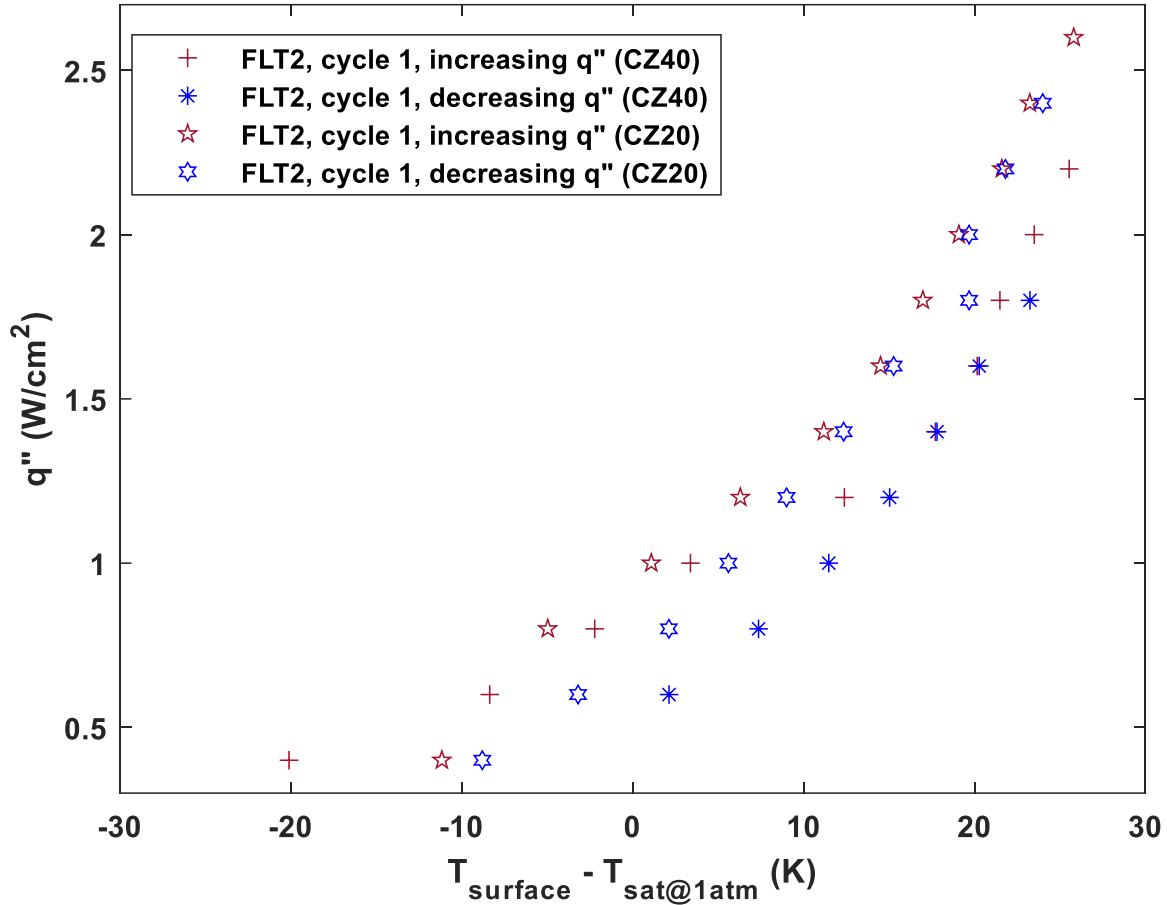


**Figure 3.26** The first cycle (a ramp-up followed by a ramp-down) at each cold zone temperature for the FLT2 ampoule. The test surface is 60-30 sawtooth geometry with cavities spaced 1-mm apart. The boiling curves are generated assuming constant pressure (1 atm) in the closed ampoule.

Consecutive cycles at the same cold zone temperature did not alter the boiling curves, as shown in Figure 3.27. However, it should be noted that the boiling curves obtained from the pre-flight tests did not measure gauge pressure within the ampoule. Any offset in the wall superheat during the onset of nucleate boiling and hysteresis during the heat flux ramp-down in the cycles were not adequately captured by assuming a constant pressure. The surface temperatures were nearly identical across the cycles during the ramp-up and ramp-down sections.

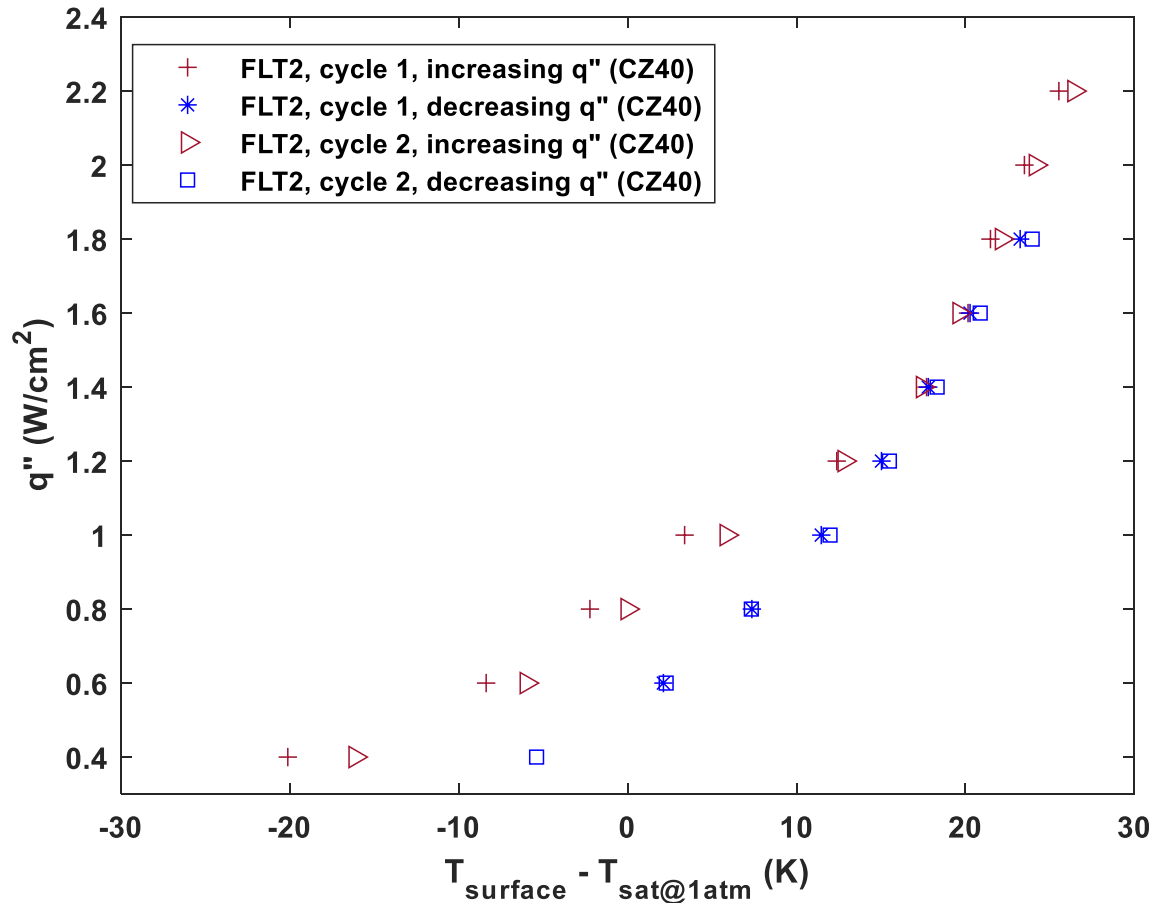


**Figure 3.27** Consecutive cycles at the same cold zone temperature captured during the pre-flight tests for FLT2 at 40°C cold zone temperature. The boiling curves are generated assuming constant pressure (1 atm) in the closed ampoule.

The 60°-30° sawtooth with the slotted cavity (FLT3) produced the lowest surface temperature compared to the 60°-30° sawtooth with engineered cavities spaced 1 mm apart (FLT2) at the same cold zone temperature as shown in Figure 3.28. The baseline, flat surface (FLT1) without the microstructure (but with engineered cavities spaced 1 mm apart) recorded higher surface temperatures in the nucleate boiling compared to the FLT2 and FLT3 ampoules with the microstructure. As the slotted cavity runs along the width of the microstructure, the test surface produced a larger volume of vapor compared to the square-shaped 250 μm engineered cavities. At

the onset of nucleate boiling, triggering just one or two slots produced sizeable jets of vapor that reduced the wall superheat at ONB, as shown in Figure 3.28. Though a pressure-adjusted boiling curve would show a reduction in wall superheat (as shown in Figure 3.22), the slotted cavity reduced the surface temperature by a large enough magnitude to show the decrease with the assumption of constant pressure. The engineered cavities could sustain a higher heat flux (2.6 W/cm<sup>2</sup>), while the large volume of vapor from the slots capped the ramp-up cycle at 2.2 W/cm<sup>2</sup>, as shown in Figure 3.29.

The FLT 2 ampoule exhibited increased bubble departure frequency while the slots ejected large vapor jets from slots spaced 3 mm apart. The vapor levels in both ampoules were comparable at their relative maximum input heat fluxes at the same cold zone temperature. While the COHU camera view did not provide information on the width of the bubbles in the upward-facing configuration in terrestrial gravity, the dimensions of the temporally slowed vapor bubbles in microgravity can be ascertained from the multiple cameras.

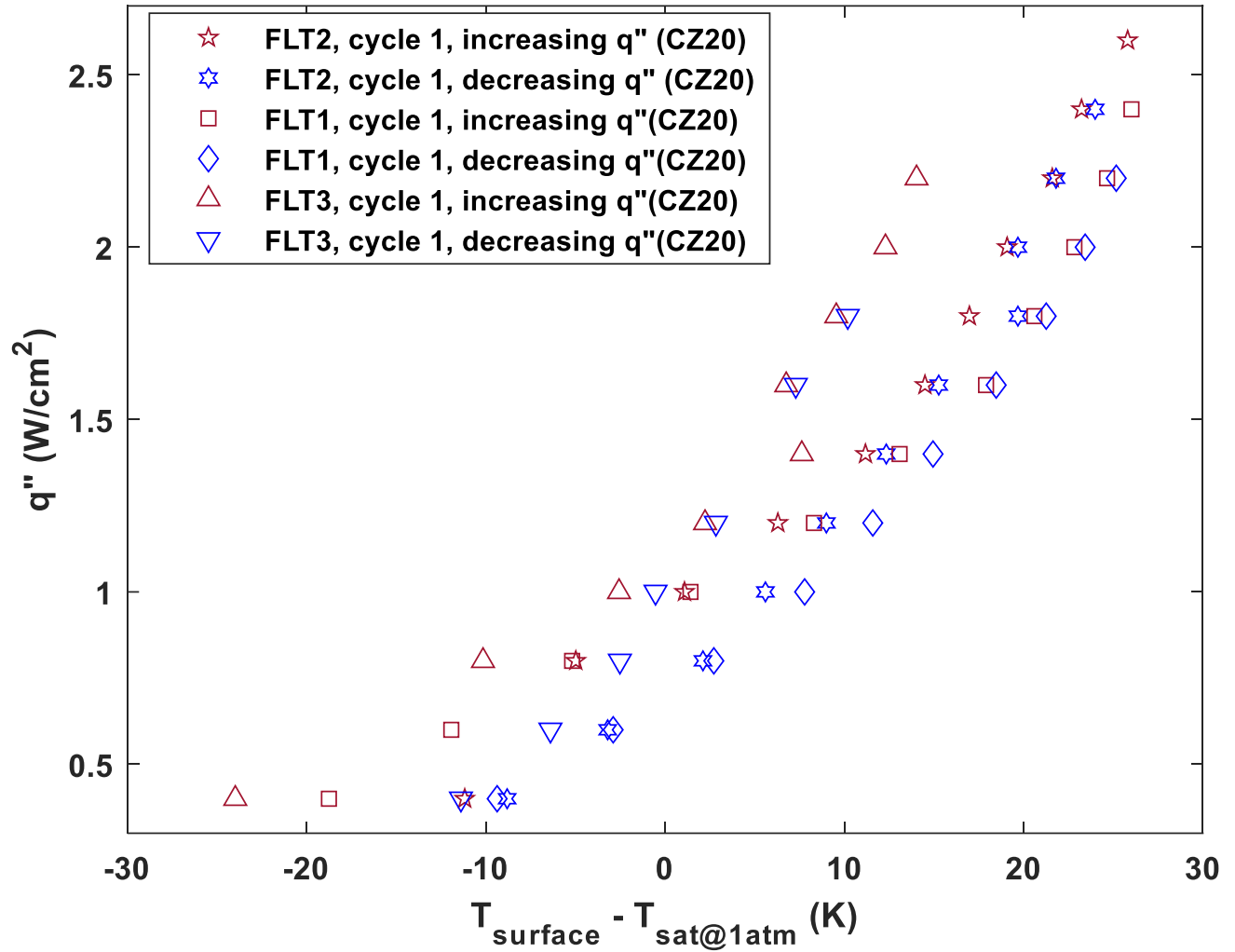


**Figure 3.28** The first cycle of the FLT2, FLT1, and FLT3 ampoules at 20°C cold zone temperature is illustrated in the boiling curve. The boiling curves are generated assuming constant pressure (1 atm) in the closed ampoule.

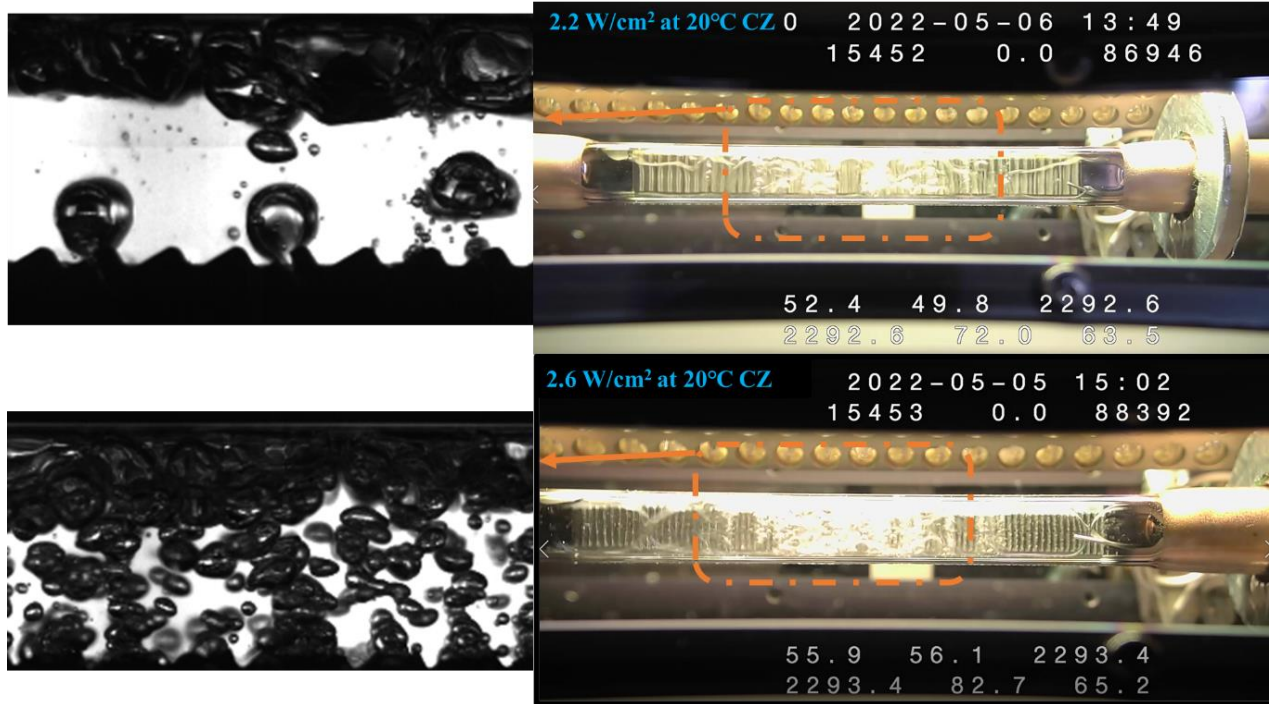


**Figure 3.29** The narrow high-speed (left) and the COHU camera (right) views for the FLT2 and FLT3 flight ampoules captured during the pre-flight science tests.

### 3.5.9 Summary

Through the upward-facing ground tests described in this section, the functioning of the PFMI furnace was streamlined and verified. The syncing of the COHU camera and the high-speed camera was also accomplished through the course of these experiments. Reference terrestrial data from the flight ampoules in the flight furnace were obtained for comparison against the microgravity experiments. The nominal functioning of the pressure relief ampoule across the anticipated heat flux range was verified. The vapor dynamics from the different cavity structures (square vs. slot) were observed, and the boiling curves for each unique test geometry were obtained. The datasets from these tests were considered satisfactory to proceed with the microgravity experiments.

## CHAPTER 4      MICROGRAVITY EXPERIMENTS

### 4.1 Preparation for launch

After completing the various ground-testing sequences, the test surfaces and furnace were prepared for delivery to the ISS. The furnace was shipped to the ISS before ASCENT’s payload to support MSG operations. The ASCENT payload was scheduled for a late load (3 days before the scheduled launch) and early operations aboard the ISS. The important pre-flight milestones are indicated in Table 4.1.

**Table 4.1 The important pre-launch milestones for the ASCENT payload**

Milestone	Date	Activity
L-16days	10/21/2022	FC-72 Degassing completed
L-13days	10/24/2022	Ampoule assembly/filling started
L-12days	10/25/2022	<ul style="list-style-type: none"> <li>• Ampoule assembly/filling completed</li> <li>• Ampoule Inspections, Verifications, and As-Built drawings completed</li> <li>• Ampoule packaged for Transport</li> </ul>
L-5days	11/01/2022	Depart Redwire for Wallops
L-4days	11/02/2022	Badging for Turnover
L-72hours	11/03/2022	Turnover
Launch	11/06/2022	NG-18 Launch



All flight ampoules were re-filled with freshly degassed FC-72 dielectric liquid prior to launch in a condensed timeline. The schedule for the experiments aboard the ISS was subject to crew availability, PFMI furnace readiness, and available processing hours. Therefore, the late load and early operations strategy minimized stowage time aboard the ISS. The re-filled flight-ready ampoules are illustrated in Figure 4.1.

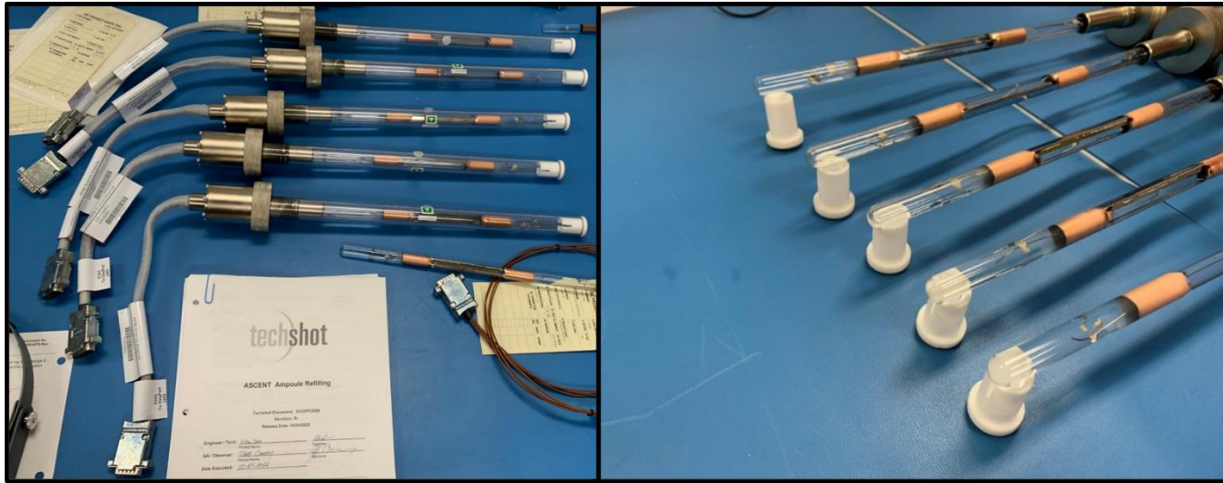


**Figure 4.1 The re-filled flight ampoules for the ASCENT projects are illustrated. Five total flight ampoules were flown to the ISS: A calibration ampoule to verify the functioning of the PFMI furnace and four ampoules with test surfaces provided by the ASCENT science team.**

## 4.2 Experimental anomalies

- Prior to launch, one of the cold zone thermocouples had been disrupted on the FLT 1 ampoule, as described in Chapter 3. The thermocouple was not centered at the desired location. However, this did not affect the flight processing of the ampoule in microgravity conditions. The thermistor located at the cold zone hardware was used to maintain the zone at the desired setpoint of 20°C.
- The FLT 4 ampoule, converted from the ground to the flight version, did not perform nominally during the microgravity experiments. Nucleation was observed from the edge between the test

surface and the borosilicate glass surface. This was most likely due to an imperfect seal between the test surface and the borosilicate glass. It should be noted that this ampoule did not have this issue during a pre-flight terrestrial test (Development Test 2 in Chapter 3). As vapor bubble dynamics from the microstructure also depend on nucleation from the engineered surface, analysis of this ampoule was discarded.

- The FLT 3 ampoule, which contained the test surface with the slot cavities, was found to have a defective thermocouple. Unfortunately, this thermocouple was located at the surface, severely limiting extensive analysis of this ampoule. The loss of the surface temperature thermocouple also complicated operating the ampoule in the PFMI furnace. As the safety setpoint was coupled to the surface thermocouple, providing heat to the ampoule was not feasible.

Extensive discussion between the science team, implementation partner, NASA, and the ISS National Lab converged on the possibility of using the fluid thermocouple as the control thermocouple instead. Consequently, a repair procedure was conducted by a ISS astronaut (Josh Cassada) to rewire the ampoule hardware. The procedure, performed on 16th January 2023, was successful, and the fluid thermocouple setpoint was used to control the surface for subsequent testing.

However, the loss of the surface thermocouple significantly impacted the analysis, leading to curtailed scientific outcomes.

### **4.3 Experimental procedure**

The original PFMI facility was initially designed to maintain the desired setpoint on the heater. However, the ASCENT experiment required a constant heat flux to be maintained across the resistance heater. Therefore, the facility operation method was changed from the constant

temperature method to the constant power input method. The power control method involved setting a user-defined parameter for the maximum voltage, which limits the furnace's power output to a specified percentage of the total power provided by the facility's heating elements. The operator then set an unattainable surface temperature setpoint that the facility continuously operated at the maximum available voltage to try and reach, resulting in constant power output pegged at the user-defined voltage. Nevertheless, the surface temperature still controls the facility, and with updates made to the control software, the temperature never reaches the target setpoint.

ASCENT's unique experimental setup necessitated changes in the constant heat flux application to study vapor bubble dynamics from the constrained test chamber. A typical pool boiling curve is constructed by providing heat input at a desired heat flux, allowing the system to reach a steady state before increasing or decreasing the heat flux to the next setpoint. However, this approach only works with large liquid pools. Constant increments in heat flux eventually produced an extended slug in microgravity conditions due to the ampoule's small volume of FC-72 (~35 mL). Therefore, the heating for ASCENT experiments was executed through on-off cycles to prevent slug formation, which can also be interpreted as extended pulses. The vapor nucleation process from the specially designed sites at the chosen heat flux was observed via orthogonal cameras. Consistent nucleation on the test surface triggered the high-speed video captures. The vapor bubbles combined and merged to form a slug that subsequently diminished in size by turning off the heating. Following the condensation of the vapor into the bulk fluid, the next cycle was initiated. This method effectively prevented slug formation and was observed through orthogonal cameras at each heat flux. An example of an on-off cycle on a baseline surface at  $0.8 \text{ W/cm}^2$  is shown in Figure 4.2.

The cold zones were maintained at 20 °C for all the experimental runs reported in this study. The input parameters for the system are listed in Table 4.2.

**Table 4.2 Test parameters for the ASCENT investigation**

Input heat flux – $q''$ ( $\text{W}/\text{cm}^2$ )	0.5 – 2.3 $\text{W}/\text{cm}^2$
Test surface temperature	20 – 80 °C
Fluid temperature	20 – 80 °C
Pre-determined safety setpoint	80 °C
Cold zone setpoint (symmetrical)	20 °C

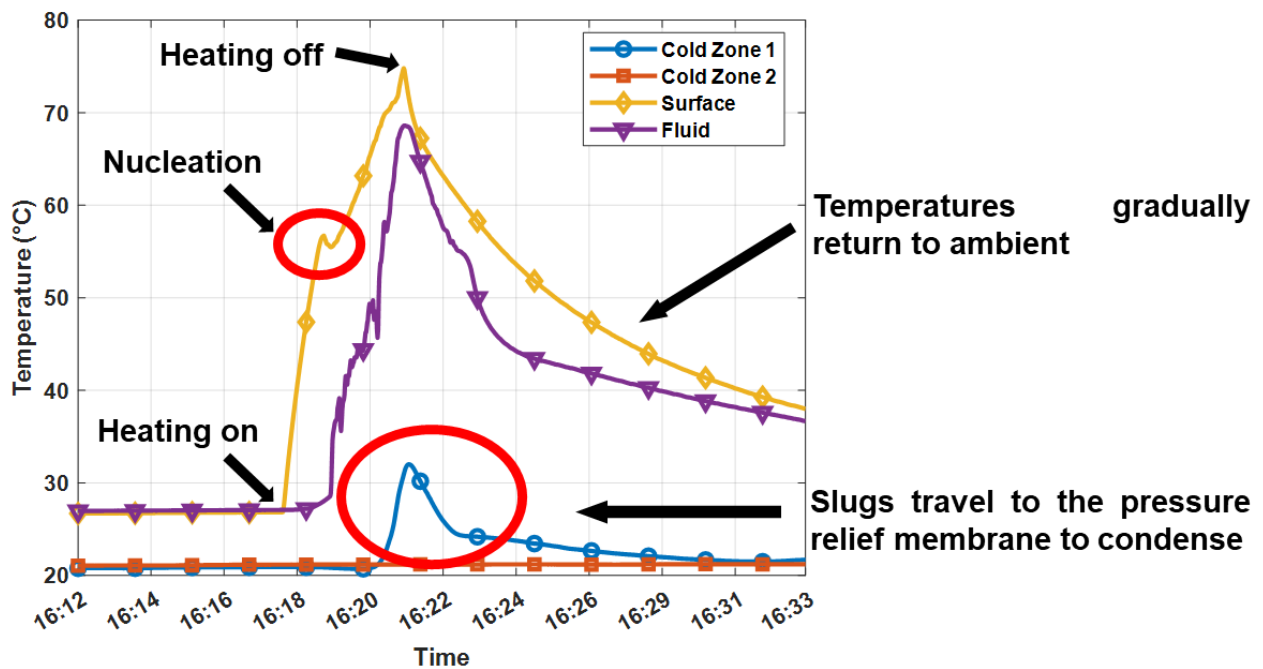


**Figure 4.2** An example run with the on-off cycles is illustrated. At the start of the test, the cold zones are at 20°C, and the sample and fluid temperatures are ambient. A dip in the surface temperature signifies the start of nucleation. As the slugs grow larger and traverse toward the pressure relief system, a temperature spike in the cold zone is recorded. After the

heating is turned off, the temperatures gradually return to ambient conditions. The run illustrated here was recorded on 16th December 2022 at a heat flux of 0.8 W/cm<sup>2</sup> on the baseline surface. The markers in the plot are used to differentiate the different thermocouples. All times are in UTC.

The science team at Auburn University and the University of California, Davis, conducted the ASCENT's investigation remotely through teleconferencing. The downlink from the ISS experiment was streamed through the implementation partner, Redwire Techshot, located in Greenville, Indiana. The science team provided the desired setpoints for each unique experimental run, including heat flux, cold zone temperature, and camera positioning and triggering. Line-of-sight constraints interrupted the downlink from the ISS, leading to brief Loss of Signal (LOS) incidents as shown in Figure 4.3. The duration and timing of these incidents were predicted in advance, and the experiment was paused during these outage periods.



**Figure 4.3** The ISS flight plan indicating loss-of-signal period due to satellite handovers and line-of-sight constraints within the Tracking and Data Relay Satellite System. The orange and green bar indicate the availability of different feeds (video, voice, data etc).

#### 4.4 Data reduction

A 100V DC power supply was used to power the PFMI furnace. A DC-to-DC converter, which can provide a maximum of 43.75V ( $V_{max}$ ) at 30  $\Omega$ , powers the electrode brushes connected to the Nichrome heater, as shown in Figure 4.4. The output of this converter is regulated by the process control module associated with the surface thermocouple within each fabricated ampoule. The

total power delivered to the resistance heater is calculated as a percentage of the maximum voltage ( $V_{\max}=43.75\text{V}$ ) for each increment in heat flux. The thermal power supplied ( $Q$ ) was calculated as,

$$Q = \frac{V^2}{R} \quad 10$$

Where  $V$  is the delivered fractional voltage of  $V_{\max}$  and  $R$  is the resistance of the nichrome heater for each ampoule. The resistance of nichrome does not change significantly over the current study's temperature range ( $20^\circ\text{C}$ - $80^\circ\text{C}$ ) due to its low temperature coefficient of resistance ( $\alpha=1.7 \times 10^{-4} \text{ }^\circ\text{C}^{-1}$ ) [83]. The maximum change in resistance for both ampoules in the study is 1%.

. The heat flux is thus calculated as,

$$q'' = \frac{Q}{A} \quad 11$$

Where  $A$  is the area of the nichrome coating on the borosilicate glass ampoule.

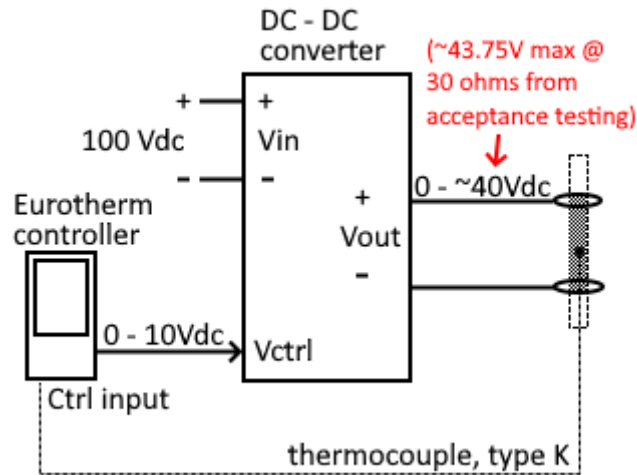


**Figure 4.4** The power supply is connected to a DC-DC converter which steps down the voltage and is controlled by a Eurotherm controller. The surface thermocouple provides feedback to the Eurotherm controller until the desired setpoint is reached.

The experimental heat transfer coefficient was determined as,

$$q'' = h_{experimental} * (T_{surface} - T_{fluid}) \quad 12$$

where  $T_{surface}$  and  $T_{fluid}$  are the surface temperatures and the fluid temperatures, respectively.

## **4.5 Experimental Results and Discussion**

This section contrasts the FLT1 and FLT2 ampoules (the baseline and microstructure with cavities spaced 1-mm apart) for the vapor bubble dynamics. However, the FLT 3 Ampoule (the microstructure with slot cavities) is analyzed separately as the geometry is significantly different. The cold zone temperatures were maintained at 20°C for the reported results.

### **4.5.1 Raw data and analysis approach**

The maximum temperature setpoint was maintained at 80°C at the surface thermocouple for the experimental flight runs. This temperature was a pre-determined safety setpoint to ensure that the closed ampoule would function nominally for the prescribed test duration (five days for each ampoule). The constrained ampoule dimensions (8mm (W) x 8mm (H)), designed to retrofit into the existing Pore Formation and Mobility Investigation (PFMI) hardware, was representative of typical high-heat flux device enclosures and mini channel heat sinks. The constrained width and height of the heated area significantly influenced convective heat transfer and nucleate pool boiling characteristics without gravity. The surface temperature plots for the baseline (left) and microstructure (right) for the duration of the run at a fixed heat flux are shown in Figure 4.5.

Both surfaces display similar trends on the temperature traces. There is a steep increase in the surface temperature after the heating command is issued for all the tested heat fluxes. The start of nucleate boiling is associated with a decrease in the slope of the surface temperature trace and,

sometimes, a decrease in the surface temperature, marked by a "hill" on the traces. The hill is a temperature overshoot to initiate boiling, as shown in Figure 4.2. The onset of nucleate boiling signifies the shift to a more efficient form of heat transfer, dropping the surface temperature momentarily. However, the vapor dynamics continued to increase the temperature of the heated surface towards the safety setpoint for all  $q'' > 1.0 \text{ W/cm}^2$ .

To provide a base of comparison, a quasi-steady temperature analysis was conducted using 20 seconds of data, between 60 and 80 seconds after the initiation of heating, as indicated in Figure 4.5. For the highest heat flux tested ( $2.3 \text{ W/cm}^2$ ), the maximum temperature setpoint was reached at 80 seconds. At 60 seconds, nucleation was observed for all the tested heat fluxes on the baseline surface except  $0.5$  and  $0.6 \text{ W/cm}^2$ , the lowest heat fluxes tested. To capture the bounds of the current experiment, these two limits were chosen by combining high-speed observations and the safety setpoints. Therefore, the analysis in the quasi-steady section of this article is derived from the average of the temperatures recorded between 60 and 80 seconds. Each of the transient tests resulted in one point on the boiling curve.

This quasi-steady state formulation also allows the current study to access comparisons to previous microgravity studies with large pools to study boiling heat transfer. Similar informed decisions on quasi-steady state formulations are common in microgravity boiling studies. For example, Merte et al. [84] used a quasi-steady analysis method to obtain a pool boiling curve for R-113 using a gold film sputtered on a glass substrate. Zhao et al. [85] adopted a quasi-steady heating method in which the input voltage increases exponentially with time. Similarly, a prior study with a transient heating method on thin metallic ribbons in water [86] yielded data well represented by steady-state correlations. In addition, several short-term pool boiling studies that inform current studies were also conducted in parabolic flights and drop towers. Therefore, the quasi-steady state analysis



method described above is adopted for comparison to prior studies due to ASCENT's unique experimental setup.

As slugs formed and continued to grow in the square ampoule, their shape changed from spherical to slug-like due to the walls of the test chamber. ASCENT deviated from extensive liquid pool studies at this transition as the vapor slug extends over the microstructure. While prior pool boiling studies also showed the growth of a large central vapor bubble over the heated surface, the vapor bubble morphology in the current study was significantly influenced by the constrained square walls of the test chamber.

With increased heat flux, the total vapor area for the wide high-speed camera view increased from  $4.5 \text{ mm}^2$  at  $0.5 \text{ W/cm}^2$  to  $200 \text{ mm}^2$  at  $1.2 \text{ W/cm}^2$  for  $\sim 95$  seconds after the heating command was issued, as shown in the inset image in Figure 4.5. As the heat flux increased, more engineered cavities were triggered, and faster bubble growth and coalescence rapidly increased the total vapor area. The COHU and the high-speed cameras captured the nucleating vapor bubbles' activation, growth, and coalescence into a subsequent slug. As expected, increased heat flux triggered nucleation at a higher frequency, as seen in the inset image in Figure 4.5.

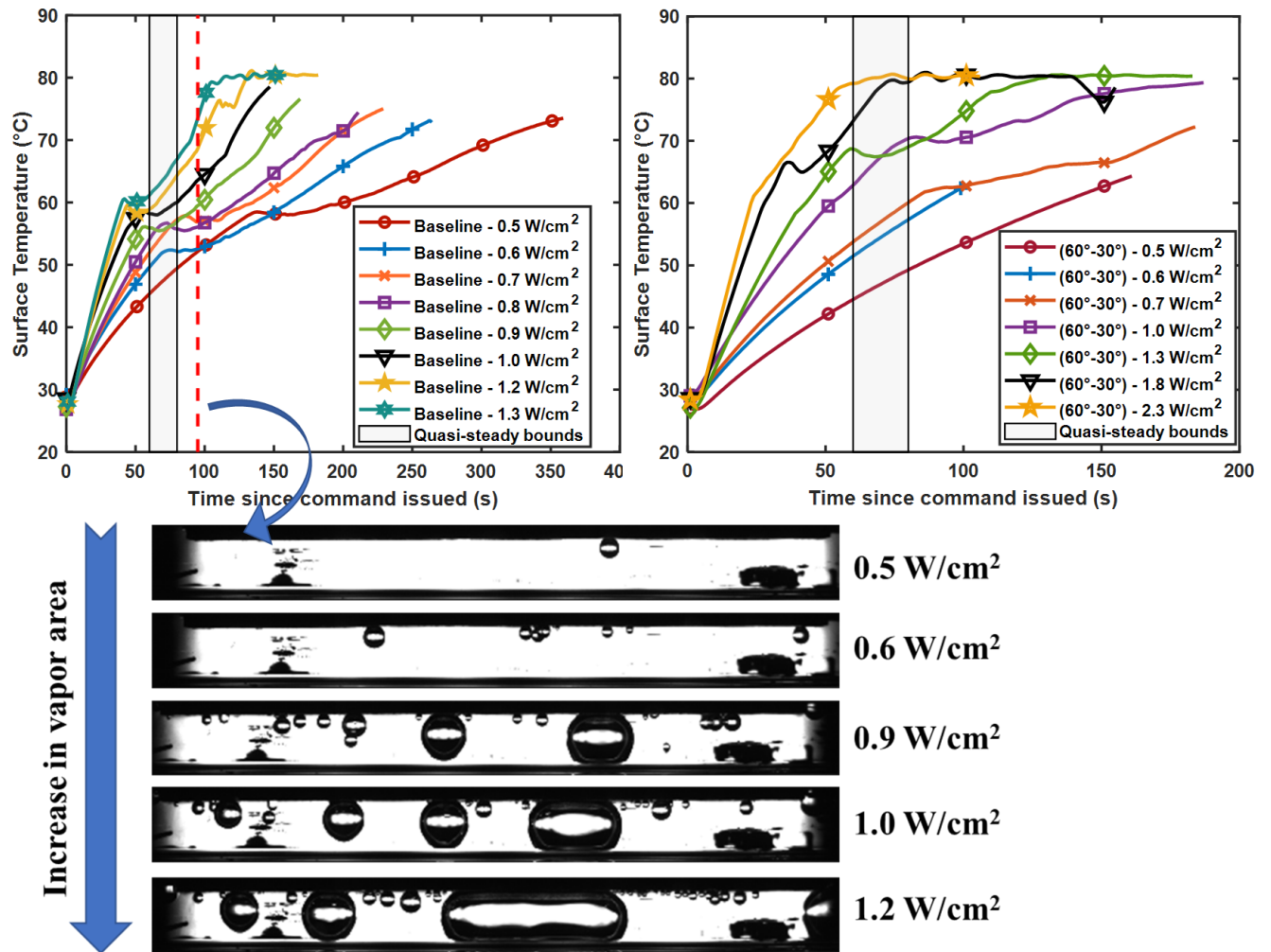
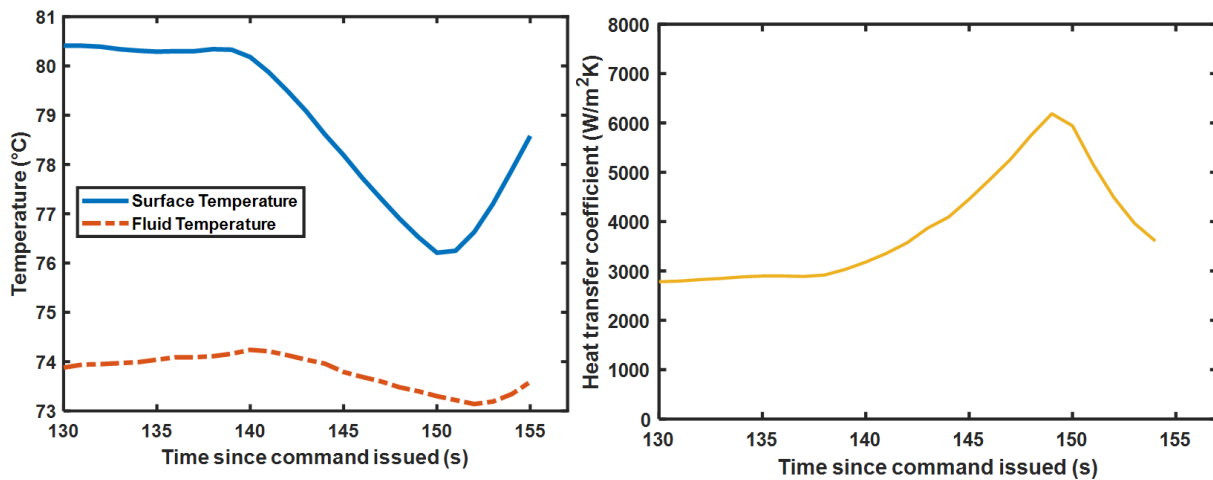


Figure 4.5 The temperature traces at different heat fluxes for the flat baseline surface (left) and the  $60^{\circ}\text{-}30^{\circ}$  microstructure (right). The period between 60 and 80 seconds) was used for the quasi-steady state analysis of the experimental runs from the average between these bounds. The markers in the plot are used to differentiate between the different heat fluxes. The inset image shows the increase in vapor area at  $\sim 95$  seconds after the heating command was issued for different heat fluxes for the baseline surface. The total vapor area increases from  $4.5\text{ mm}^2$  at  $0.5\text{ W/cm}^2$  to  $200\text{ mm}^2$  at  $1.2\text{ W/cm}^2$ .

#### 4.5.2 Nucleation from the liquid film

Perhaps the most unexpected feature across the obtained temperature traces is the dip in surface temperature between 138 seconds and 155 seconds at  $1.8 \text{ W/cm}^2$  for the microstructure. Though the temperature setpoint reached  $80^\circ\text{C}$ , the heater provides constant heat flux to maintain the temperature at the prescribed setpoint. Though minor oscillations occur at other heat fluxes, the magnitude ( $4^\circ\text{C}$ ) of the dip in surface temperature at this heat flux is striking. The heat transfer coefficient increases from about  $2900 \text{ W/m}^2\text{K}$  at 138 seconds to about  $6200 \text{ W/m}^2\text{K}$  at 149 seconds, a jump of more than twice the initial value, as shown in Figure 4.6. This is the highest heat transfer coefficient recorded during the microgravity runs. High-speed imagery (900 fps) and COHU camera images (25 fps) were captured at the prescribed heat flux, elucidating film characteristics at the liquid-vapor interface, as will be described in the next several paragraphs.



**Figure 4.6** The dip in surface and fluid temperatures after the temperature was maintained steadily at  $80^\circ\text{C}$  at  $1.8 \text{ W/cm}^2$  (left). Though minor oscillations were observed at other heat fluxes at the setpoint, the magnitude of this decline was unprecedented. The corresponding jump in the time-dependent experimental heat transfer coefficient is illustrated on the right.

Figure 4.7 illustrates a COHU camera capture at 142 seconds showing vigorous nucleation underneath a growing slug (top) and the narrow, high-speed camera capturing nucleation and coalescence along the liquid film from liquid pockets located along the microstructure (bottom) at  $1.8 \text{ W/cm}^2$ . The process of nucleation and coalescence occurred as rapidly as 8.88 milliseconds from a spot along the liquid film. Liquid pockets separated the growing vapor slug from the engineered microstructure, a phenomenon not observed for the baseline surface.

Though the growth of a slug suppressed nucleation from engineered cavities, the superheated liquid film was observed to create nucleation pockets along the edges and sometimes even along the test surface. However, unlike nucleation from engineered sites, this nucleation was observed at fewer dynamic locations across the entire test surface. Each nucleation and coalescence event was followed by distinct undulations of the liquid-vapor interface along the test surface, as shown in Figure 4.7. The dip in surface temperature is attributed to this highly efficient two-phase heat transfer mechanism, combining the well-known benefits of liquid film evaporation with consistent nucleation. At  $1.8 \text{ W/cm}^2$ , the narrow, high-speed video reveals as many as 41 undulations in a three-second timeframe indicating a cumulative frequency of 13.66 Hz in the 15.20 mm x 8.44 mm observation window.

The surface temperature rises to the setpoint past 150 seconds, giving credence to the theory that this may be a transient effect in constant temperature conditions for a large slug. Another mention of visible bubbles underneath the microlayer in microgravity is the parabolic flight study by Ohta [43], which studied distilled water and ethanol on a smooth surface. The author theorized that the

primary heat transfer mechanism is the nucleation of these tiny vapor bubbles underneath a coalesced vapor slug, as conduction through the liquid film was only assumed to be 30% of the input power.

As the input power was switched off soon after reaching the setpoint for  $2.3 \text{ W/cm}^2$ , a similar dip is not observable at this higher heat flux. At  $1.3 \text{ W/cm}^2$ , though the heating was sustained for up to 180 seconds, the narrow high-speed camera view was not entirely covered by the vapor slug, making a direct comparison infeasible. In addition, the temperature history does not represent a noticeable decline after reaching the setpoint.

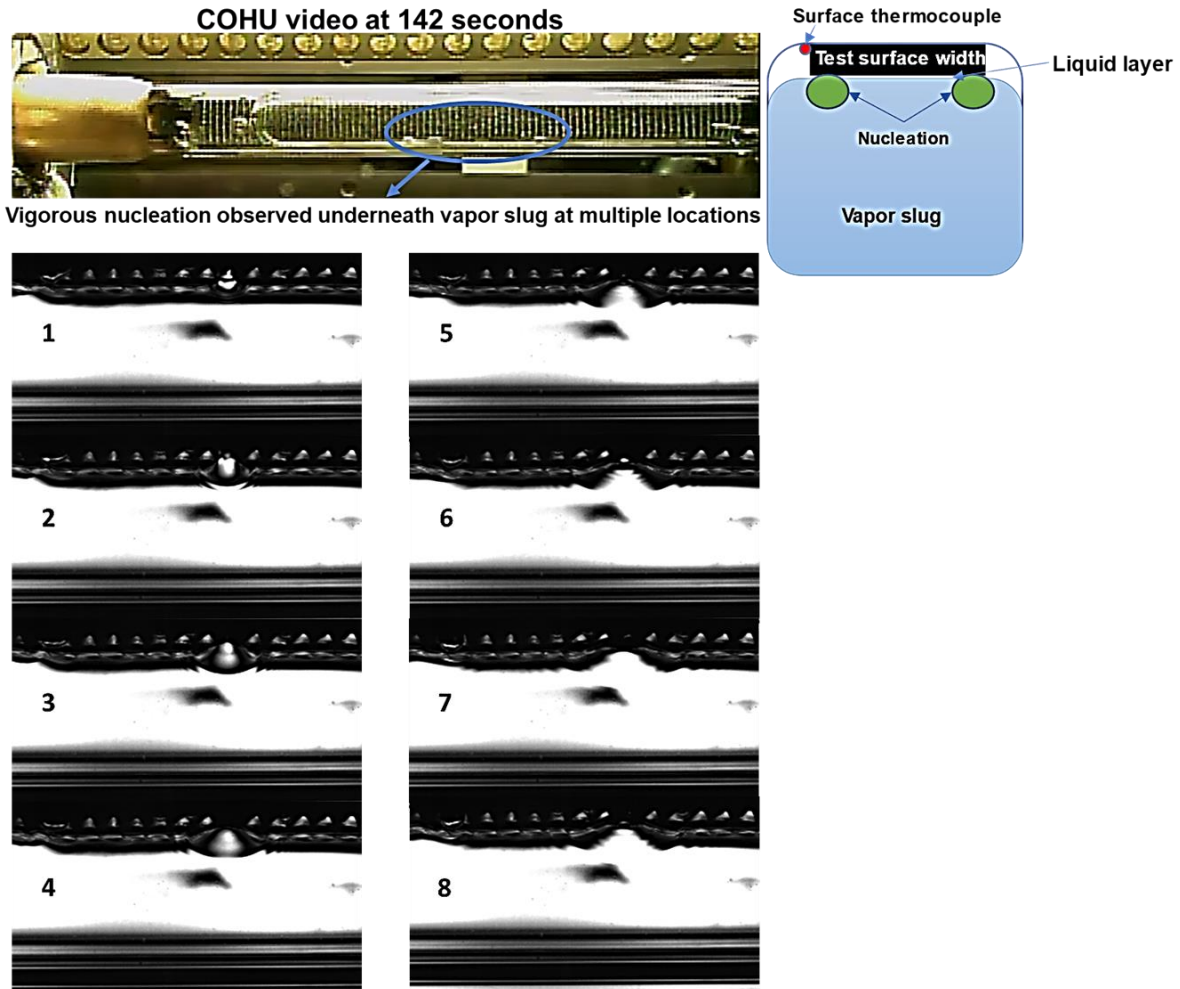


**Figure 4.7 COHU camera capture at 142 seconds after the heating command was issued, capturing consistent, vigorous nucleation at multiple locations along the growing slug in  $\mu\text{g}$  (top). The collage of high-speed images on the bottom (numbered 1-8) depicts detailed nucleation from a spot along the liquid film. The nucleating vapor bubble coalesces into the large slug between frames 4 and 5 as the top of the vapor bubble collapses and creates undulations along the surface. The top left of the collage shows another vapor bubble emerging from the microlayer. Each frame is 1.11 milliseconds apart, and the frame of view is 15.20 mm x 8.44 mm at 900 fps. The schematic on the top right illustrates the location of**

**the surface thermocouple along the test surface relative to the location of the nucleation spot and the vapor slug.**

### **4.5.3 Transient heat transfer analysis**

Figure 4.8 compares the transient heat transfer coefficient from the microstructure against the baseline at three different heat fluxes – 0.7 W/cm<sup>2</sup>, 1.0 W/cm<sup>2</sup>, and 1.3 W/cm<sup>2</sup>. Heat input was not sustained long enough to produce a comparison at the two lower heat fluxes (0.5 and 0.6 W/cm<sup>2</sup>). A clear trend emerges, showing that the heat transfer coefficient from the microstructure increases with time, eventually surpassing the baseline. During initialization, the heat transfer coefficient from the two surfaces is comparable. It can also be seen that the initialization time decreases with increased heat flux for both surfaces.

However, as constant heat flux is applied, the change in vapor bubble dynamics dictates the heat transfer trends inside the closed ampoule. The nucleated vapor bubbles grow and coalesce with neighboring bubbles but continue to access the liquid layer due to the engineered ridges on the microstructure. The variations for the heat transfer coefficient traces arise from the vapor's interaction with the fluid thermocouple, but a clear trend is still discernible. The thermocouple exhibited a temperature fluctuation of approximately 3-5 °C due to the dielectric liquid and vapor interplay on the fluid thermocouple.

The high-speed images show that the vapor slugs get larger with time at all heat fluxes. Therefore, the results show that the microstructure performs better than the baseline as the vapor mass increases. The increase in heat transfer coefficient with time for the baseline surface may be due to the thin film evaporation underneath the vapor slug.

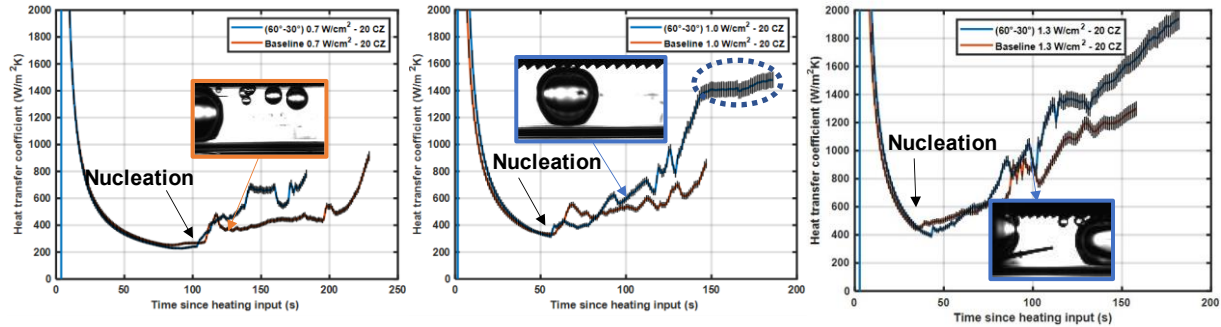


**Figure 4.8 Time-dependent heat transfer coefficient of the microstructure (blue) against the baseline (orange) at different heat fluxes:  $0.7 \text{ W/cm}^2$  (left),  $1.0 \text{ W/cm}^2$  (center), and  $1.3 \text{ W/cm}^2$  (right). The start of vapor nucleation is annotated on the plots. The inset images for  $0.7 \text{ W/cm}^2$  and  $1 \text{ W/cm}^2$  show the narrow high-speed image captures for the baseline and the microstructure surfaces, respectively. The near-constant heat transfer coefficient observed for the microstructure at  $1.0 \text{ W/cm}^2$  from 145 seconds is due to a constant temperature difference being maintained between the surface and fluid. The inset image for  $1.3 \text{ W/cm}^2$  shows a vapor slug departing the frame of view after interacting with the fluid thermocouple (left) at 103 seconds. The error bars on the heat transfer coefficient are  $\pm 4.1\%$  of the derived experimental value, as explained in Appendix D.**

The visible liquid layer on the microstructure is contrasted against the baseline surface at  $1.3 \text{ W/cm}^2$  in Figure 4.9. The slug completely covers the narrow field of view ( $15.20 \text{ mm} \times 8.44 \text{ mm}$ ) on the baseline surface (left), and no microlayer is visible for the baseline surface. However, the asymmetric sawtooth surface (right) interacts with the vapor slug at the crests, but the pockets across the sawtooth discern a transparent visible layer. Similar observations were made in a prior study with a downward-facing surface in terrestrial gravity with the microstructure [69].



Though the objective of this microgravity study was not to explore critical heat flux limits for the surface, the higher heat transfer coefficients from the engineered microstructures due to the liquid film suggest important ramifications for dryout scenarios.

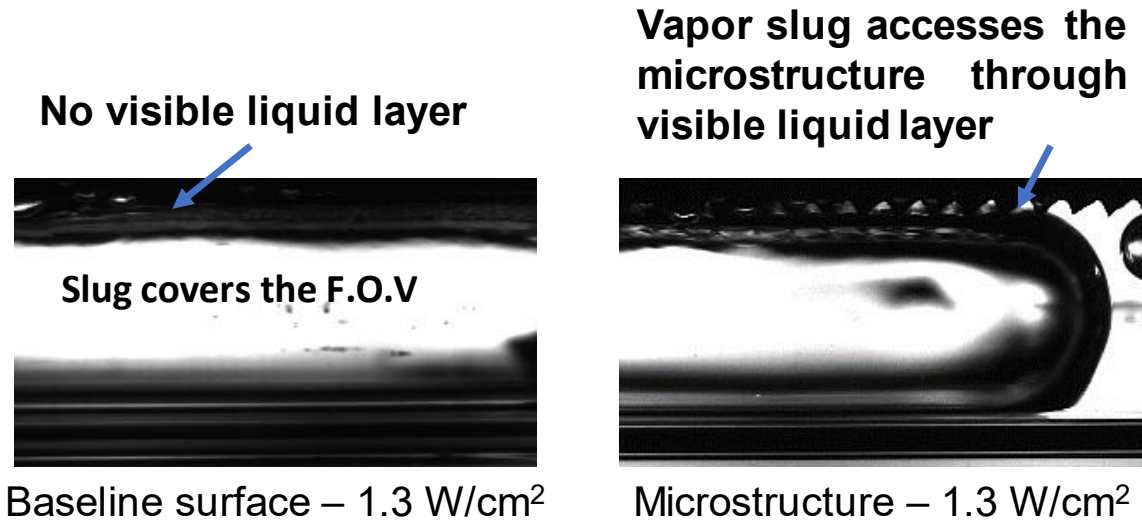


**Figure 4.9** Slug dynamics for the baseline surface (left) and the microstructure (Right) at 1.3 W/cm<sup>2</sup> in microgravity. The vapor slug covers the frame of view (FOV) for the baseline surface, and no microlayer is visible between the vapor slug and the baseline surface. On the right, a growing slug was captured on the microstructure surface with clear visible liquid microlayer film across the crests of the asymmetric sawtooth.

#### 4.5.4 Quasi-steady analysis

The quasi-steady state formulation described in Figure 4.5 is used for the comparison in this section. The analysis reported in this section is derived from the average of the temperatures recorded between 60 and 80 seconds. The comparison shown by Warrier et al. [52] has been extended for ASCENT in Figure 4.10. This comparison falls within the range of ASCENT's

experimental heat fluxes while embodying a good mix of long-term and short-term studies with varying fluids, as shown in Table 4.3. The microgravity data from five previous studies are plotted along with the baseline and the microstructure from ASCENT. As the pressure inside the closed ampoule was not measured during the flight experiments, the pressure was assumed to be constant at atmospheric pressure. A pressure-corrected curve would shift both derived curves to the left, signifying lower wall superheats due to a higher saturation temperature. Figure 4.5 shows that the ASCENT's 250  $\mu\text{m}$  initiate boiling from the engineered cavities at heat fluxes as low as 0.5  $\text{W}/\text{cm}^2$ . However, the quasi-steady analysis method quantifies  $\Delta T_w < 0^\circ\text{C}$  as natural convection in Figure 4.10. Both surfaces show a jump in surface temperature past 0.7  $\text{W}/\text{cm}^2$ , switching from natural convection to nucleate boiling.

**Table 4.3 Test parameters for the microgravity studies in Figure 4.10**

<b>Study</b>	<b>Investigation method</b>	<b><math>\Delta T_{\text{sub}}</math> (<math>^\circ\text{C}</math>)</b>	<b>Fluid</b>	<b>Pressure (kPA)</b>
Merte et al. [84]	Space Shuttle	11	R-113	150
Straub [38]	Drop Tower	17	R-113	102
Kannengeiser et al. [87]	Sounding Rocket	10.5, 11.9	HFE-7000	140,150
Raj et al. [51], [88]	ISS	11	FC-72	101
NPBX [52]	ISS	10.5	FC-72	128
ASCENT	ISS	15	FC-72	101

ASCENT's test surface follows the general trend of the pool boiling curve shown by other microgravity studies in Figure 4.10, except for Warriar et al.'s NPBX study. An increase in heat

flux increases the wall superheat noticeably, unlike the steep slope displayed by the NPBX study for  $\Delta T_w > 0$  °C. However, the authors also remarked that the visual behavior of the vapor mass shown by NPBX is similar to Merte et al., Straub, and Kannengeiser et al.'s study. This is unexpected as the vapor bubble dynamics intricately inform heat transfer in microgravity. The observed may be due to the unique onset of the nucleate boiling methodology adopted by the NPBX study. In their temperature-controlled experiment, the surface temperature was increased until nucleation was observed before the surface temperature was reduced to construct the boiling curve, enabling steady-state measurement.

The trends on both the baseline and the microstructure show the evident influence of the restricted ampoule dimensions with growing vapor slugs and increased heat flux. ASCENT's experimental setup recorded higher surface temperatures in the fully developed nucleate boiling regime than Raj et al. [51] and Warriar et al. [52], who conducted their experiments with perfluoro-n-hexane (3M brand name FC-72). However, the trends show a large variation in wall superheats for data obtained in microgravity. Kannengeiser's two data points, in conjunction with Warriar et al.'s data, demonstrated particularly favorable performance within the fully developed nucleate boiling regime. However, Kannengeiser reported the influx of non-condensable gas (nitrogen) in the sounding rocket study. It should also be noted that the other studies focused on flat plates or very smooth surfaces in large liquid pools.

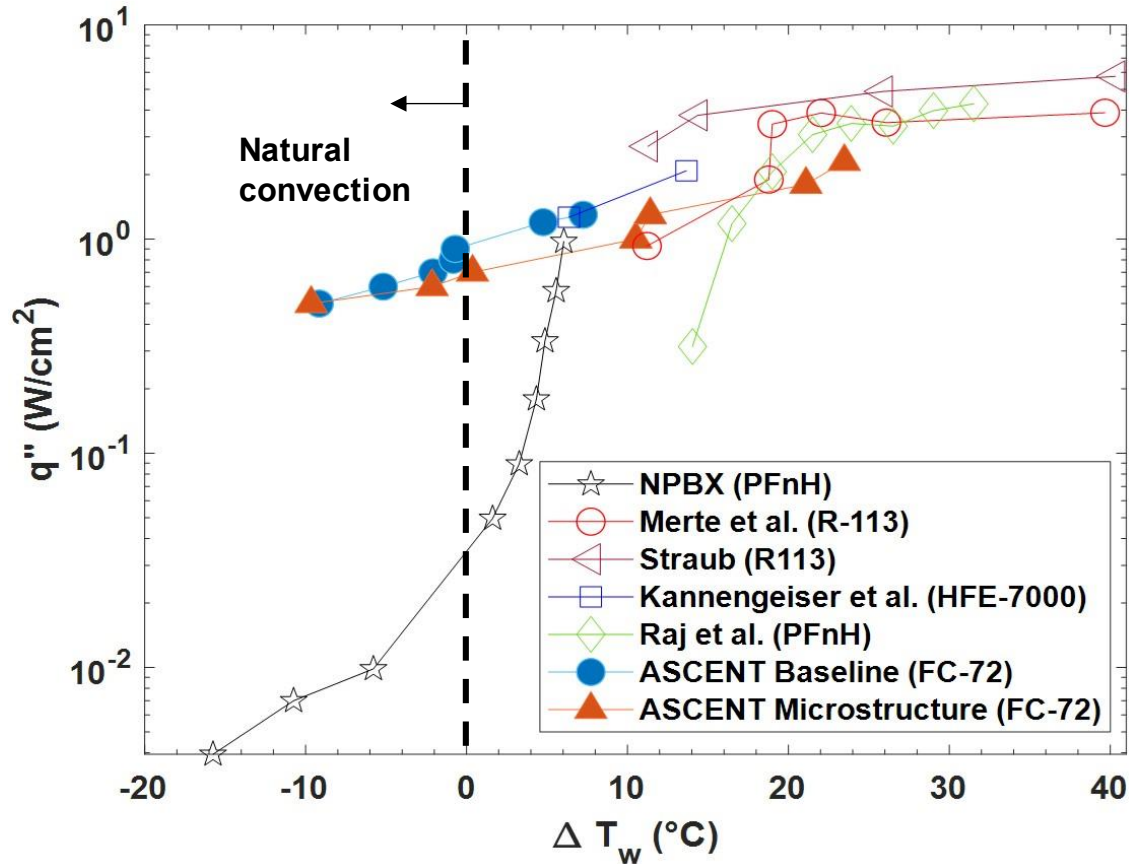


**Figure 4.10 Comparison of nucleate boiling data in previous microgravity studies compared with ASCENT's quasi-steady state data. Adapted from Warriier et al. [52].**

The comparison of 'ASCENT's quasi-steady heat transfer coefficients with previous microgravity studies is shown in Figure 4.11. For  $\Delta T_w < 0$  °C, the baseline and microstructure surfaces provide a low heat transfer coefficient ( $\sim 250$  W/m<sup>2</sup>K). The heat transfer coefficient increased steadily for  $\Delta T_w > 0$  °C on both surfaces as the surface shifted to the more efficient heat transfer mechanism. The highest heat transfer coefficient for the baseline surface was recorded at 1.3 W/cm<sup>2</sup> at  $\Delta T_w = 7.2$ °C at 583 W/m<sup>2</sup>K. Higher heat fluxes were not tested for the baseline surface due to insufficient experimental time. At the highest heat flux tested for the microstructure (2.3 W/cm<sup>2</sup>), the heat transfer coefficient was 2200 W/m<sup>2</sup>K at  $\Delta T_w = 23.5$ °C.

The microgravity data from Warrier et al. showed an apparent increase in heat transfer coefficient with an increase in heat flux, with  $\Delta T_w$  remaining nearly constant. However, the authors described a large vapor slug acting as a heat sink for smaller bubbles that move in and coalesce with it. Raj et al. proposed a framework for nucleate boiling based on the heater length and capillary length ratio. For the current experiments at  $10^{-6}g$ ,  $L_h/L_c=0.11$ . The criteria for transitioning from surface tension-dominated boiling (SDB) to buoyancy-dominated boiling (BDB) for FC-72 was  $L_h/L_c=2.1$ . The current study is in the SDB regime, where boiling heat transfer is independent of gravity level but dependent on heater size. However, the proposed criterion does not account for the square ampoule test chamber in the current study. The comparable vapor bubble descriptions from the other perfluoro-n-hexane studies show that the microstructure can achieve higher heat transfer coefficients for  $\Delta T_w > 20^\circ C$ . The liquid pockets on the microstructure improve heat transfer at higher heat fluxes and wall temperatures as more of the slug contacts the surface.

Kannengeiser et al. argued that the measurement of liquid temperature profiles in the wall vicinity, accomplished using multiple thermocouples, indicates that the thermal boundary layer is tens of microns, much smaller than the capillary length. In the current experiment, the vapor slug was in contact with the baseline surface wall but was separated by a liquid layer for the microstructure surface.

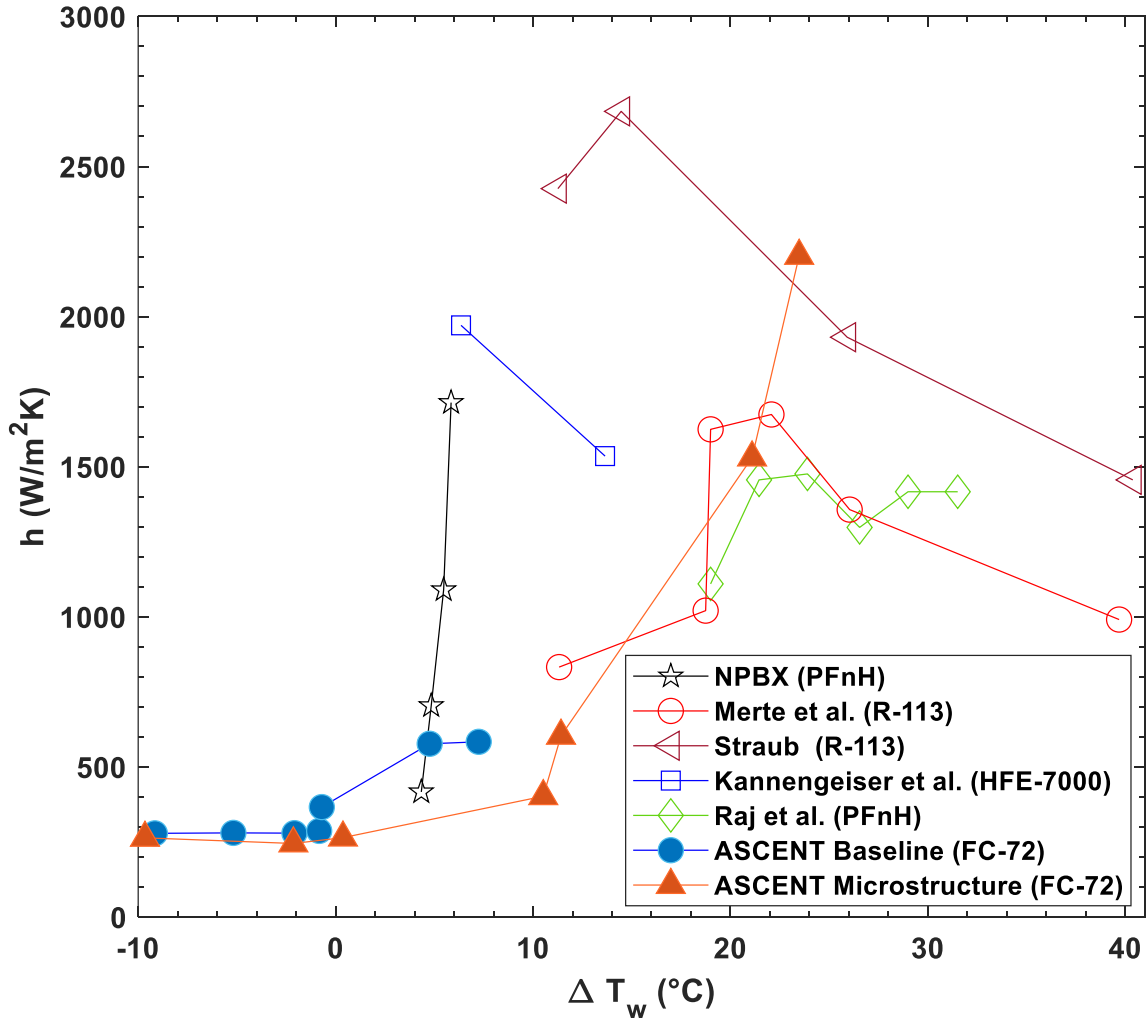


**Figure 4.11 Comparison of ASCENT's derived quasi-steady heat transfer coefficients with other microgravity studies. Adapted from Warriar et al. [52].**

Figure 4.12 compares the quasi-steady boiling curve in microgravity with the terrestrial upward-facing surface for the baseline surface and the microstructure. Before launch, these terrestrial pre-flight tests were conducted with the final flight ampoules in the flight PFMI furnace. The cold zones were maintained at 20°C, identical to the microgravity runs. All curves were constructed assuming constant pressure (1 atm), as internal pressure was not measured during the flight

experiments and the pre-flight terrestrial runs. Without adjusting for internal pressure, the surface temperatures are similar in microgravity and terrestrial gravity for ASCENT's experimental setup.

The plot shows that heat transfer is not severely deteriorated in microgravity conditions, particularly at heat fluxes  $\geq 1.3 \text{ W/cm}^2$ . At lower heat fluxes, the higher surface temperatures at comparable heat fluxes for the microgravity conditions can be attributed to the diminished convective currents that preclude the available cold zones from condensing the vapor bubbles. In addition, the lack of buoyancy forces increases vapor bubble diameters, decreasing subsequent nucleation frequency.

The microstructured surface in microgravity performs similarly to a 1g baseline surface for  $q'' \geq 1.3 \text{ W/cm}^2$ . As mentioned earlier, higher heat fluxes were not explored for the baseline surface during the microgravity runs due to a lack of experimental run-time.

Prior microgravity experiments with perfluoro-n-hexane found conflicting trends. Warriar et al. found that the magnitude of heat flux obtained for a wall superheat decreases as the buoyancy force decreases. However, Raj et al. found that microgravity heat fluxes are larger than those obtained at 1g at  $\Delta T_w < 21.5 \text{ }^\circ\text{C}$ . The current study shows that the surfaces perform very similarly in microgravity compared to terrestrial gravity without adjusting for the internal pressure of the ampoule.

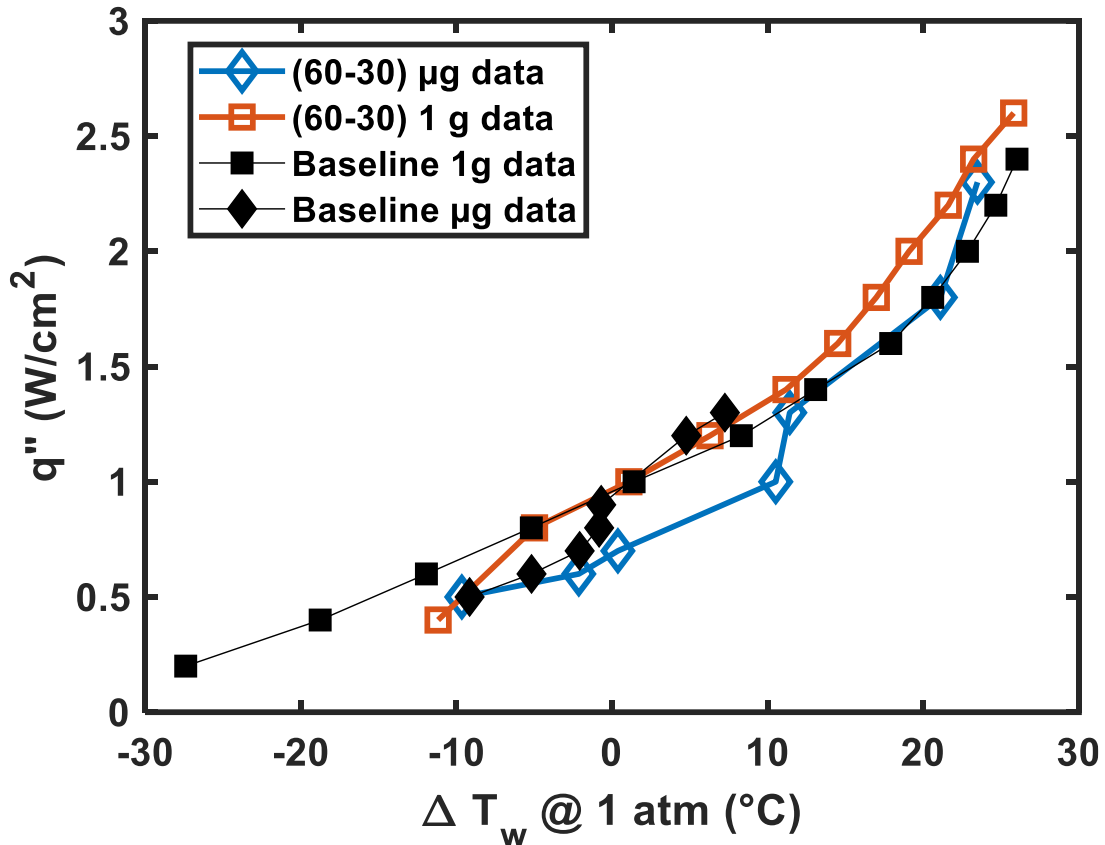


Figure 4.12 Comparison of ASCENT  $\mu\text{g}$  (time-averaged) data with 1g steady-state data assuming constant pressure in the test ampoule.

#### 4.5.5 Nucleation from the engineered cavities

The baseline test surface displayed a trend of triggering more engineered sites with increased heat flux, as shown in Figure 4.13. Significant increases in active cavities were observed beyond 1  $\text{W}/\text{cm}^2$  as vigorous nucleation occurred uniformly across the test surface, rendering it challenging to obtain an accurate count. This observation aligns with Hsu's cavity incipience theory [89] which states that the range of active cavity sizes increases as the wall superheat increases. The engineered sites which activate at lower heat fluxes continue to create vapor as the heat flux increases, supporting the existing framework.



The results indicate that the 250- $\mu\text{m}$  square cavities are effective nucleation sites in microgravity environments, enabling predictable vapor germination on electronic surfaces.

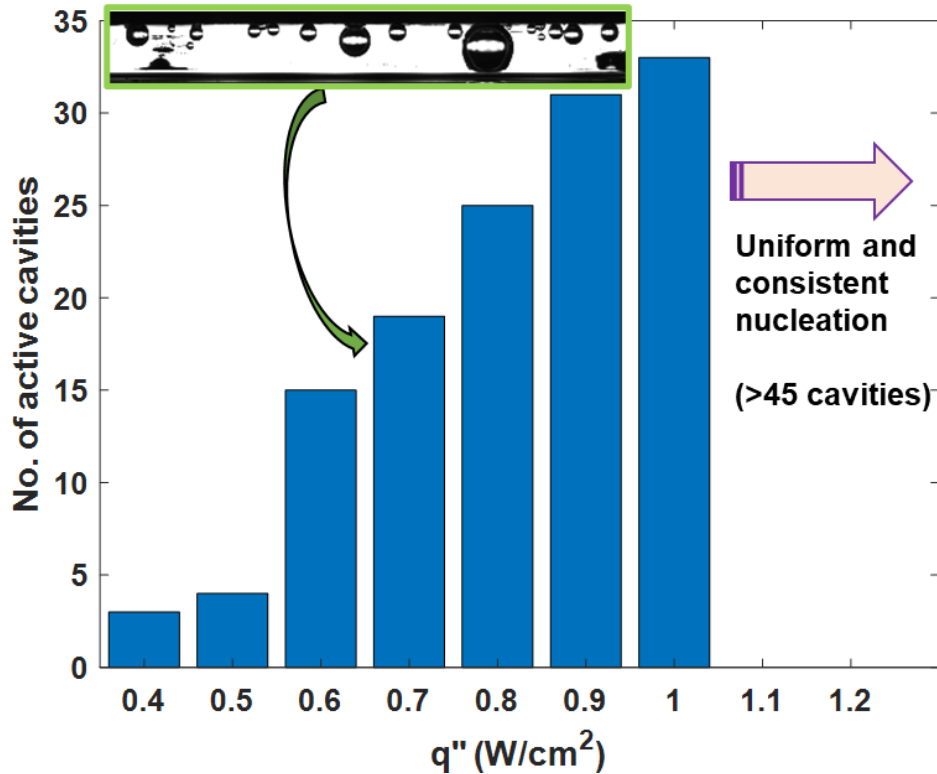


**Figure 4.13** The increase in the number of active cavities with increasing heat flux for the flat test surface is illustrated in the figure. Beyond 1 W/cm<sup>2</sup>, consistent and uniform nucleation was observed across the test surface. The inset image shows a representative high-speed capture at 0.7 W/cm<sup>2</sup>.

As the input heat flux increased, the number of active cavities on the microstructured surface increased similarly to the baseline surface. This is demonstrated in **Figure 4.14**. As the heat flux

increases, more cavities are activated on the test surface, in addition to the initial nucleation sites that occur towards the center of the surface.

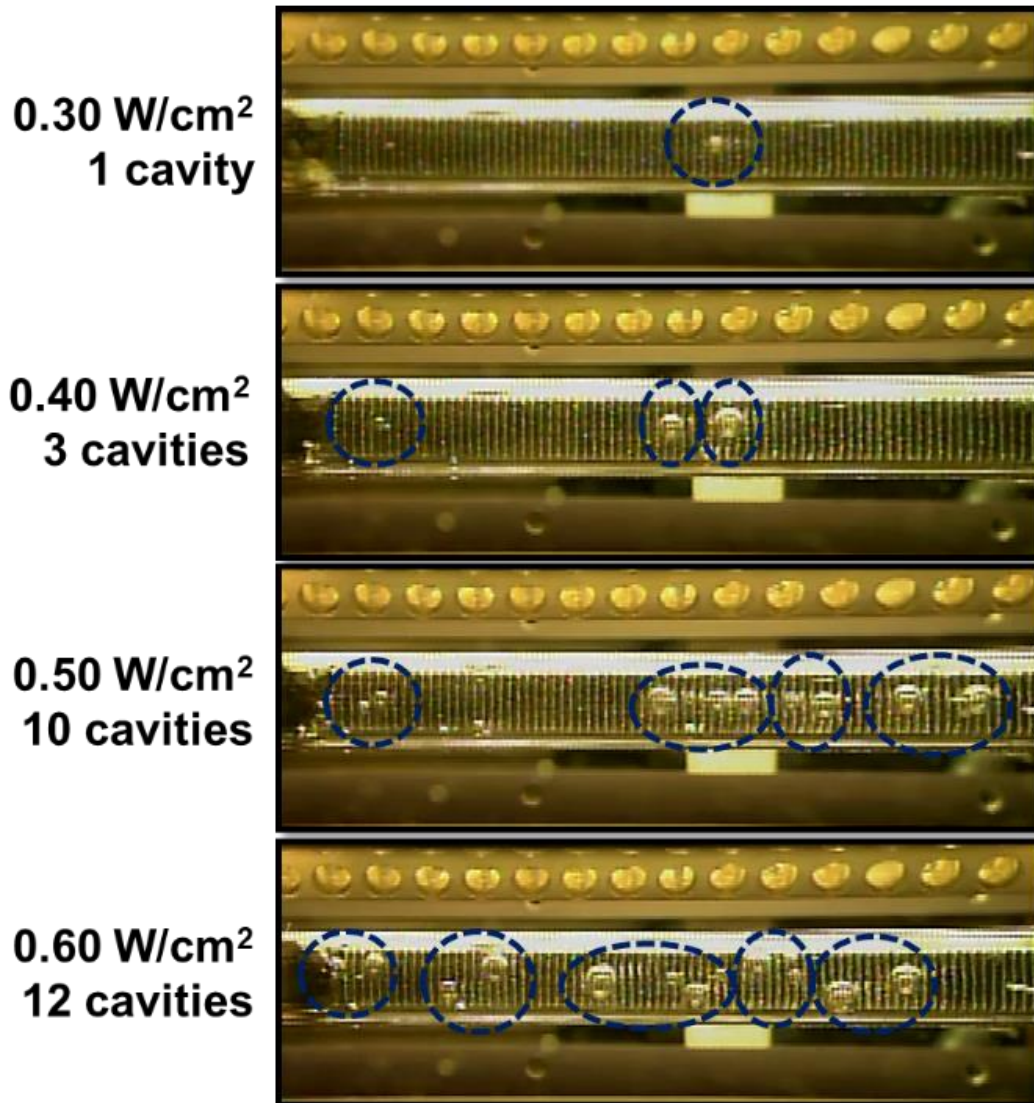


**Figure 4.14** The COHU camera views of the 60°-30° sawtooth structure at multiple heat fluxes in microgravity are illustrated in the figure. The number of triggered active engineered sites increases with input heat flux increment.

#### 4.5.6 Vapor mobility across the microstructure

As the vapor bubbles grow, they remain stationary on the flat surface. However, the microstructure interacts with the vapor bubbles differently, as shown in **Figure 4.15**. The vapor mass remains stationary on the flat surface over 1.45 seconds, but the vapor bubble rides on top of the crests, as shown in the figure. The figure also shows nucleating bubbles growing in place at smaller diameters. The large vapor bubble has detached from the nucleating cavity but remains stagnant on the baseline surface. The bubble is likely driven by heat-transfer-controlled growth, while the smaller bubble is driven by inertia-controlled growth. At the prescribed heat flux ( $0.5 \text{ W/cm}^2$ ), only four cavities are active along the flat surface, preventing bubble growth from active coalescence. When the vapor bubbles reach a specific size on the microstructured surface, they appear to move away from the nucleation site in both lateral directions. The described diameter is termed mobility diameter ( $d_m$ ) by the authors and is defined differently from the conventional departure diameter. The term departure diameter in two-phase heat transfer is defined as vapor detaching from the heated surface. However, in the current study, mobility diameters refer to the bubble diameter at which the vapor bubble starts moving across the microstructure but not detaching. At the low heat fluxes reported in this study, the vapor movement occurred at this size consistently across the sawtooth microstructure. The minimal curvature of the vapor bubbles as it interacts with the microstructure allows access to heated liquid between the troughs of the microstructure, setting up surface tension gradients that enable this motion.

It should be noted that when the vapor mass becomes large enough to contact the walls of the square channel in this study, the slug grows in place without motion. This large slug also induces

motion of the nucleating bubbles towards it for coalescence. The eventual coalescence of comparable bubbles induces vapor motion in the channel but is not the focus of the current article.



**Figure 4.15 Comparison of vapor bubble dynamics from the flat baseline surface (left) and the 60°-30° microstructure (right) at 0.50 W/cm<sup>2</sup>. The 250 μm square cavities produce consistent nucleation activity on both test surfaces, but vapor bubbles ride on the crests of the sawteeth at the departure diameter.**

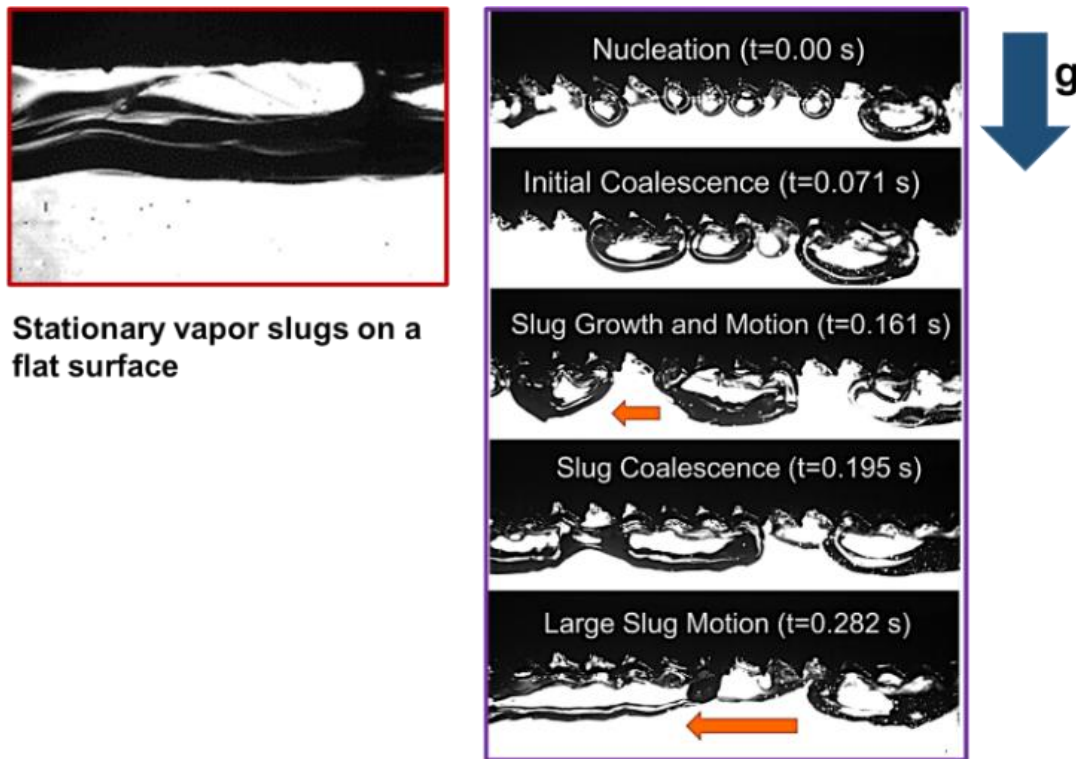
The mobility diameters of the vapor bubbles at different heat fluxes are illustrated in Table 4.4. Background subtraction was performed on the raw high-speed images to isolate the vapor bubbles. The isolated vapor bubbles were converted to binary to measure their areas. The images were calibrated using the pitch of the microstructure to convert the pixel scale to millimeters. Image processing was completed using Fiji [73]. In the low heat flux range, the mobility diameter increases with heat flux increments. However, the upper limit for the mobility diameter is the distance to the opposing wall from the test surface (~6 mm) in the current experimental setup.

Table 4.4 Mobility diameters of the vapor bubbles on the 60°-30°sawtooth microstructure in microgravity

<b>Heat flux (W/cm<sup>2</sup>)</b>	<b>Diameter, d<sub>m</sub>[mm]</b>
0.4	2.88
0.5	3.02
0.6	3.29

In contrast, the surfaces produce large vapor slugs for the adverse-gravity (downward-facing heater) orientation, tested before the ISS experiments. The baseline surface creates stationary vapor slugs that cover the entire heated area, while the microstructure induces vapor mobility in distinct features, as shown in Figure 4.16. Nucleation from the intentional sites produces stationary vapor bubbles that remain pinned to the surface due to buoyancy forces. Coalescence creates slugs

spanning three sawteeth that begin moving across the asymmetric structure. The slugs continue to grow under constant heat input, eventually coalescing to form a large ( $\geq$ six sawteeth) slug that slides away toward the long slope. The observed sliding motion is repeatable, as the cycle repeats on a cleared surface after the departure of the large slug. Changes in the interfacial radius of curvature across the sawteeth, which produces a net pressure difference, have been suggested to cause the observed motion in prior investigations [69].



**Figure 4.16 Comparison in vapor slug movement for the downward-facing surfaces at 1.3 W/cm<sup>2</sup> is illustrated. The baseline surface produces stationary vapor slugs that cover the heated area, while the microstructure produces organized movement of vapor slugs.**

The timescale along which vapor mobility occurs for the downward-facing surface is smaller than in microgravity, though the vapor mass is larger when it moves across the surface. The buoyancy forces, combined with the increased vapor bubble nucleation frequency at the higher heat flux, quicken the overall cycle of vapor mobility in the adverse gravity orientation. Both reduced gravity environments depict liquid pockets underneath the moving slug/bubble on the asymmetric microstructure. As opposed to this, the baseline surface does not indicate the existence of a thin liquid film around the foot of the bubble, indicating a local hotspot leading to dryout. The vapor mobility from the microstructure seen in the investigation could have far-reaching implications in mitigating a long-standing problem in microgravity.

#### **4.5.7 Vapor bubble dynamics from FLT3 Ampoule**

The heat flux was incremented in the described on-off cycles to visualize vapor production from the slot cavities. None of the slot cavities were active below  $0.8 \text{ W/cm}^2$  in microgravity. However, the number of active slots increased with corresponding heat flux increments, as shown in Figure 4.17. The test surface had a total of 17 slots. Beyond  $2.4 \text{ W/cm}^2$ , all slots except two (on the edge of the test surface on either side) were active. In real-time, vigorous nucleation was observed in the center of the test surface and subsequently triggered nucleation across the test surface.

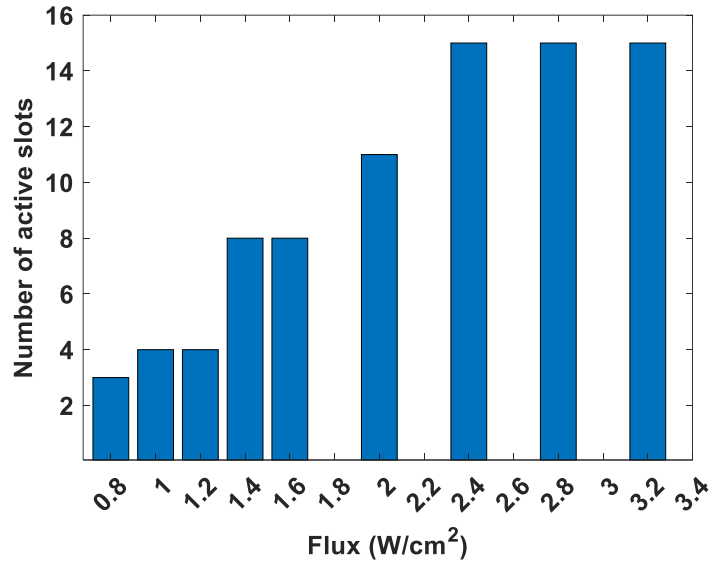


**Figure 4.17** The number of active slots at different heat fluxes in microgravity is represented in the plot.

The slot cavities consisted of multiple active sites along their length, leading to multiple distinct bubbles in the high-speed imagery, as shown in Figure 4.18. A previously ejected bubble is shown at the start of the sequence, and a coalesced mass is visible to the right of the slot in the image sequence. A vapor bubble starts growing from the mouth of the slot (250  $\mu\text{m}$ ) at 5 milliseconds. The bubble grows large and coalesces with a neighboring bubble at 10 milliseconds. The vapor bubble ejects from the slot and moves at an angle between 15 and 20 milliseconds. The vapor generation, growth, and ejection cycle continue with constant heat flux at the active slots. The triggered slots depict consistent nucleation at the prescribed heat flux along their length. The slots were observed to "pulse" with each ejection as fluid moved in and out of the slot.



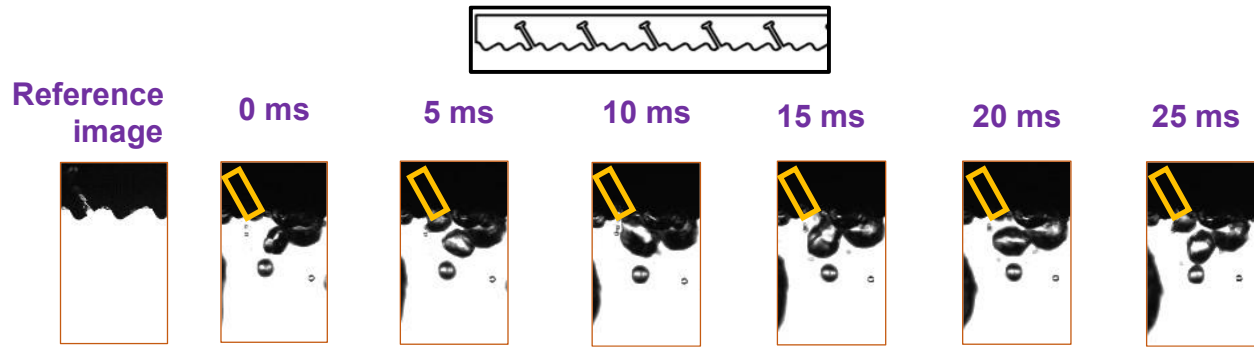


**Figure 4.18 Preferential vapor ejection from a slot in microgravity at  $2.4 \text{ W/cm}^2$  is illustrated in the image sequence. A reference image depicting the location of the slot is appended for ease of viewing. The location of the slot is outlined in the following images to improve clarity.**

The vapor bubble departure frequency at multiple fluxes is summarized in Table 4.5. Two cavities from the narrow frame-of-view camera were selected for observation for 2 seconds in real-time. The trend suggests increasing bubble departure frequency with increasing heat flux up to  $2.0 \text{ W/cm}^2$  and a possible plateau beyond that heat flux. A similar plateau in the number of active slots was observed at  $2.4 \text{ W/cm}^2$ , with consistent nucleation observed across the test surface. It should also be noted that the departure frequency is representative of a single slot but not a nucleation site. Multiple sites activate along the length of the slot, providing a cumulative departure frequency. Therefore, the increase in departure frequency can be attributed to increased departure frequency from the multiple nucleation sites and activation of other sites within the slot. The combination of these mechanisms could explain the plateau suggested by the empirical data.

Table 4.5 Vapor bubble departure frequency ranges with varying heat flux for the slots

<b>Heat Flux (W/cm<sup>2</sup>)</b>	<b>Observed Bubble Departure Frequency Range (Hz)</b>
0.8	20-22
1.0	22-25
1.2	23-25
1.6	28-32
2.0	30-32
2.4	31-35
2.8	30-34

The vapor masses coalesce and grow to move across the microstructure, as shown in Figure 4.19. The active slots create bubbles spanning across 3-5 sawtooth structures. The multiple coalesced bubbles continue to grow as the microstructure provides access to liquid pockets between the crests and troughs. The slugs grow and leave the test surface in the direction of the pressure relief membrane, which expands to account for volume dilation in the two-phase process. The velocity of the individual departing slugs was tracked using the trailing edge, and the maximum departure velocity measured was 20.4 mm/s. It was also observed that the velocity of the departing slug increases with each subsequent departure. When the slugs grow large enough to contact the walls of the ampoule, vapor mobility due to the pressure differences across the microstructure is inhibited by pinning along the walls. Therefore, the slugs require additional forces to overcome the wall forces in the constrained test chamber.

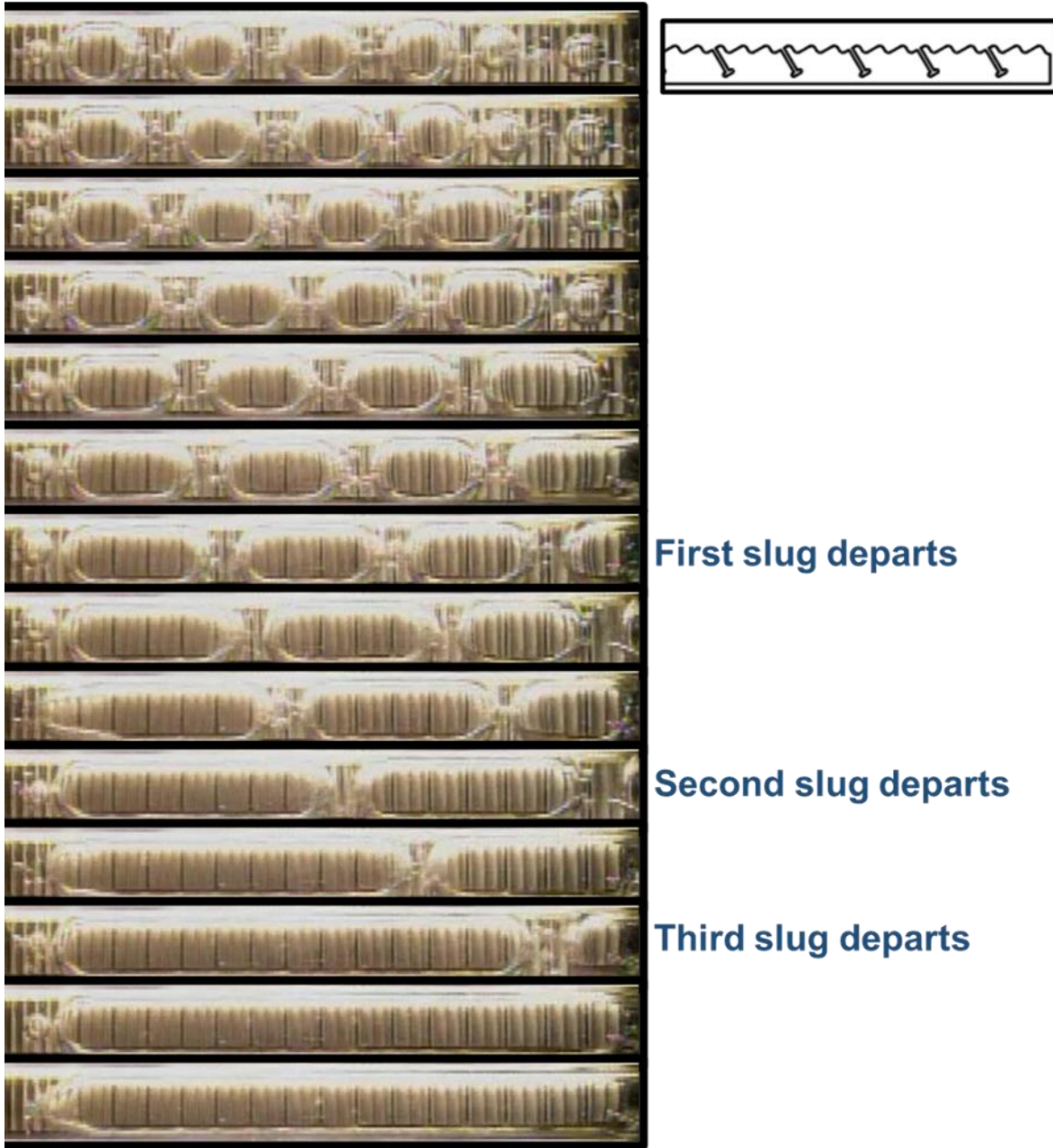


**Figure 4.19** The image sequence shows slug mobility across the sawtooth microstructure at a heat flux of  $2.4 \text{ W/cm}^2$ . The frames are spaced one second apart. Three slugs depart over six seconds by sliding across the microstructure. The side view of the COHU orientation is shown on the top right to improve clarity.

The change in the cold zone temperature as the vapor slugs depart is illustrated in Figure 4.20. The temperature increased by 19°C a minute after the heating command was issued. The cold zone condenses the first slug marking a dip in the temperature trace. The second and third slugs produce a secondary increase from the cold zone setpoint by 17.5 and 17°C, respectively. As constant heat flux is applied across the surface, a vapor slug grows past the test surface before interacting with the cold zone. However, subsequent departures and coalescence do not increase the cold zone temperature to similar magnitudes. The spikes in temperature suggest that vapor mobility across the microstructure produces effective heat dissipation in microgravity.

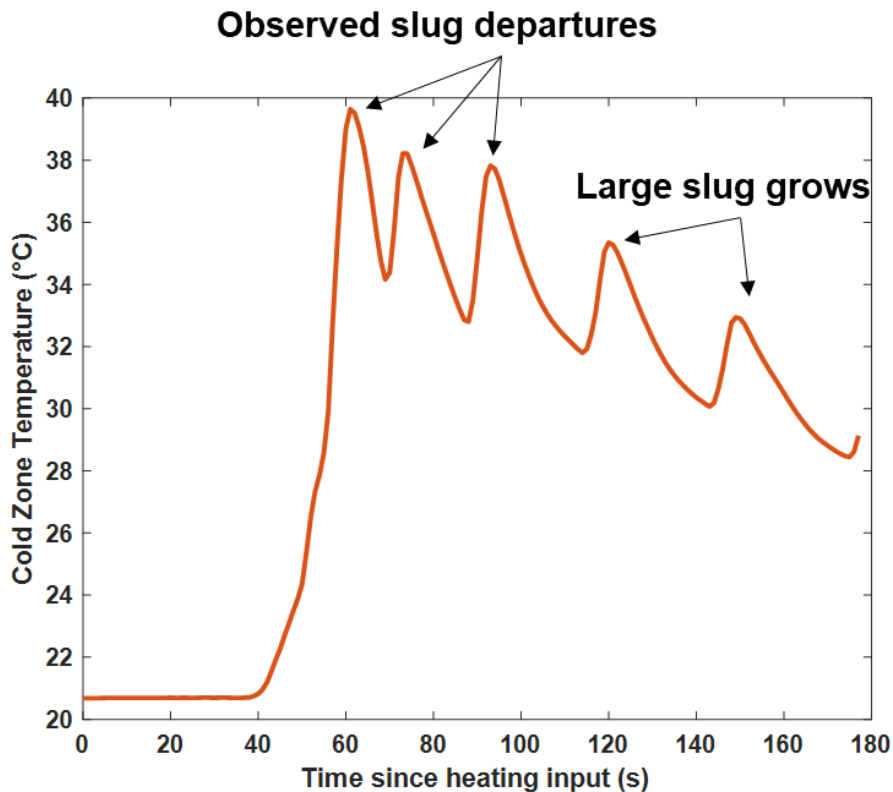


**Figure 4.20** The change in cold zone temperature as vapor slugs move toward the pressure relief membrane is illustrated. The input heat flux is 2.4 W/cm<sup>2</sup>.

The high-speed cameras also depicted pockets of a liquid film beneath the moving vapor slugs across the microstructure, as shown in Figure 4.21. The wide high-speed image shows multiple slugs moving towards the pressure relief membrane, while the narrow, high-speed camera provides improved resolution of the liquid-vapor interface across the microstructure. Vigorous nucleation is observed around the slugs as vapor bubbles eject from the engineered slots. The reported results suggest heat transfer enhancements by the microstructure for bubbles and slugs in microgravity, as the slots induce mobility at departure, and the repeating sawtooth structures prevent local dryout from thin film evaporation.

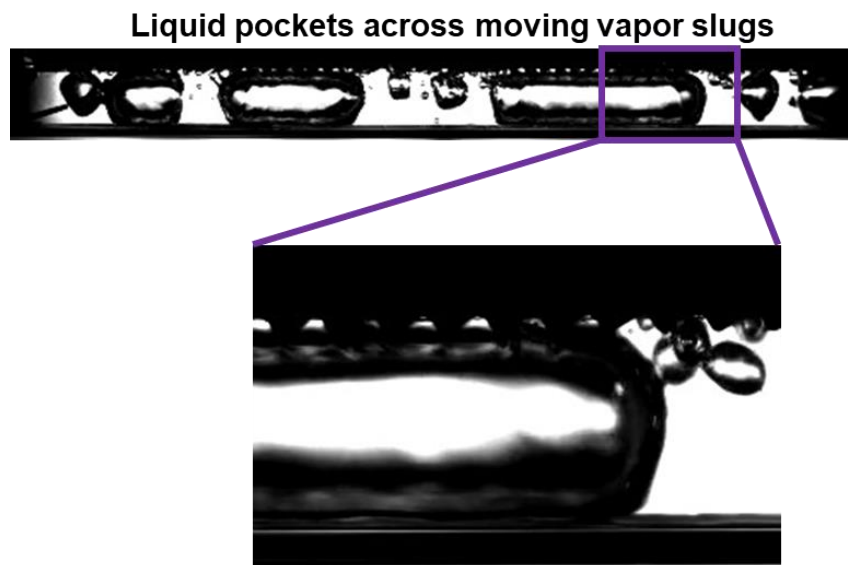


**Figure 4.21** Liquid pockets were observed between the crests and troughs of the microstructure beneath moving vapor slugs. The input heat flux is  $2.8 \text{ W/cm}^2$  for the depicted high-speed images.

#### 4.5.8 Summary

Despite the experimental anomalies encountered during the ASCENT ISS experiment, important pool boiling findings were obtained. The 250 square cavities were effective in microgravity conditions as effective engineered sites for predictable nucleation at heat fluxes as low as  $0.3 \text{ W/cm}^2$ , similar to terrestrial upward-facing and downward-facing surfaces.

The  $60^\circ\text{-}30^\circ$  sawtooth microstructure performed better than the baseline surface as the vapor bubbles grew larger due to the liquid film access afforded by the asymmetric ridges. In contrast, the experimental conditions did not reveal a liquid film beneath the flat heated surface of the baseline.

Vapor mobility was observed across the microstructure for vapor bubbles reaching a certain diameter, termed the mobility diameter. Vapor bubbles and slugs that interacted with the walls of the constrained test chamber were pinned, and further movement was restricted.

Vigorous nucleation and coalescence were observed along the liquid film at  $1.8 \text{ W/cm}^2$ , significantly improving the heat transfer coefficient. Further liquid film assessments are necessary to reproduce this transient phenomenon observed during the ASCENT experiments.

The test surface with the slot cavities produced vigorous nucleation along the length of the slots. The slots ejected vapor bubbles at an angle in microgravity, at heat fluxes as low as  $0.8 \text{ W/cm}^2$ . The number of active slots triggered increased with heat input increase for the heat flux range explored in this investigation. Similarly, the vapor bubble departure increased with increasing heat input, and the slots were observed to consist of multiple active nucleation sites.

## CHAPTER 5 CONCLUSIONS AND RECOMMENDATIONS

The heat transfer characteristics of an asymmetric sawtooth microstructure with specified nucleation sites have been studied for terrestrial adverse gravity and microgravity conditions. The long and short slopes of the 60°-30° microstructure contribute to one aspect of the asymmetry, while 250 μm cavities on the long slope were another aspect. The 250 μm cavities were engineered nucleation sites, enabling predictable vapor nucleation in the nucleate boiling regime. The process fluid used for all-experimental runs was the dielectric fluid FC-72.

Two different microstructure geometries were manufactured in Ti-6Al-4V for the microgravity experiments. Metal additive manufacturing, particularly powder-bed fusion, was used to fabricate a test surface with 1 mm pitch and 250 μm cavities. Another test surface geometry was manufactured using electric discharge machining (EDM) to investigate the effects of vapor nucleation from a slot-based cavity extending across the test surface's width. Slot cavities with a reentrant (hammerhead) design were located in every third ratchet on the shallow slope, and the pitch of the 60°-30° microstructure was 1.5 mm. The vapor bubble dynamics from these engineered surfaces were compared against a baseline surface. The baseline was flat, without the microstructure, but contained the 250 μm cavities spaced 1-mm apart.

Pool boiling experiments were conducted in a constrained test chamber to accommodate the constraints of the ISS hardware within an 8 mm square I.D. ampoule. The subcooling was maintained at 20°C, and the input heat flux range was 0-3.2 W/cm<sup>2</sup> for the terrestrial adverse gravity and microgravity experiments (μg) aboard the International Space Station.

## 5.1 Terrestrial downward-facing experiments

- This study quantified the vapor mobility from the asymmetric sawtooth microstructure using high-speed imagery for the adverse gravity orientation. The total vapor area within each viewing frame shifted in peaks and valleys, contrasting a flat surface that produced nearly stagnant vapor masses. The observed vapor removal pattern was self-regulating, handling higher vapor loads at higher heat fluxes.
- The vapor bubble morphology changed due to variations in the radius curvature ratio between the crest and trough of the sawtooth with an increase in the Bond number, driven by an increase in the sawteeth covered by the vapor slug.
- An empirical force balance model was proposed to calculate the liquid film thickness between the vapor mass and the microstructure and was dependent on the characteristic length scale of the moving slug. The driving forces for vapor motion changed from the crest to the trough of the sawtooth as the liquid film thickness increased.
- The 75°-15° sawtooth structure offered an increased area for buoyancy-driven slug motion at higher film thickness, despite a similar pressure differential force as the 60°-30° sawtooth structure.

## 5.2 Microgravity experiments

- The constrained dimensions of the square chamber were observed to influence vapor bubble dynamics severely, precluding steady-state pool boiling tests.
- The engineered microstructure, consisting of mm-sized 60°-30° sawtooth structures located within a hermetically sealed square ampoule, significantly impacted vapor dynamics and heat transfer compared to a flat baseline surface.



- 250- $\mu\text{m}$  cavities located on the long slope of the microstructure were effective vapor nucleation sites, triggering consistently across both baseline and microstructured surfaces.
- Vapor bubbles were observed riding on the crests of the sawteeth in microgravity, while the baseline surface produced stationary vapor bubbles that grew in place. The microstructure provided access to liquid pockets across the troughs for vapor bubbles reaching a mobility diameter. The mobility diameter increased with increasing heat input in the low heat flux range attempted in this study. Similar mobility was observed for the terrestrial downward-facing surface, as large slugs slid across the microstructure toward the long slope. The study suggests that the microstructure's characteristic length scale for vapor mobility actuated differs in microgravity and the terrestrial adverse-gravity orientation.
- Vigorous nucleation and coalescence were observed from the liquid pockets along the microstructure at  $1.8 \text{ W/cm}^2$  in microgravity, and a significant increase in the heat transfer coefficient was observed at this heat flux. The increase was attributed to the well-known benefits of liquid film evaporation with consistent nucleation.
- The observed equivalent performance of the surfaces under microgravity conditions, in comparison to their behavior in terrestrial environments, augments the overall desirability and applicability of these materials, substantiating their potential for a wide array of practical applications.
- The hammerhead slots ejected vapor bubbles at an angle in microgravity, at heat fluxes as low as  $0.8 \text{ W/cm}^2$ . The number of active slots triggered increased with heat input increase for the heat flux range explored in this investigation. Similarly, the vapor bubble departure

increased with increasing heat input, and the slots were observed to consist of multiple active nucleation sites.

- The investigation results demonstrate that the liquid film dynamics underneath vapor slugs are crucial in enhancing heat transfer in microgravity conditions.

### **5.3 Recommendations**

- Based on the findings of long-term microgravity experiments, it has been observed that microstructures can facilitate mobility across heated surfaces up to a certain diameter. These observations suggest that increasing the number of sawteeth in microgravity experiments in a larger test chamber may be possible to achieve mobility at larger diameters. The results also indicate higher heat transfer coefficients from the microstructure compared to a flat baseline surface. The microstructure could benefit two-phase immersion cooling in microgravity environments in different regimes, namely the isolated vapor bubble regime and the slug regime. By utilizing the motion observed from the microstructure and applying temperature gradients, such as a condenser, it would be possible to implement a cooling system that operates passively without the need for excessive power to maintain it within operational limits.
- In addition, terrestrial downward-facing experiments have shown repeated vapor slug mobility in the same pattern of nucleation and coalescence across both 75°-15° and 60°-30° microstructures. Previous studies by the same group have also demonstrated directional vapor mobility for a terrestrial upward-facing surface and consequent liquid motion around the vapor bubble. The ability of the microstructure to enable vapor mobility in the adverse-gravity orientation has far-reaching implications for constant heat flux components terrestrially. Furthermore, the thin liquid film observed underneath the slug was

contextualized through a force balance model primarily dependent on the size of the slug. These results and analysis enable the development of numerical models for the microstructure, with reference baseline models built on quantitative image processing.

- Future work should focus on manipulating the liquid-vapor interface aggressively as undulations/oscillations along the surface in microgravity conditions, and the thin film nucleation underneath liquid pockets should be investigated further. Manipulating the liquid-vapor interface may require structures of different scales based on the properties of the process fluid for the specific application. Further, the discussed concept can also be combined with pre-existing heat transfer solutions to improve heat transfer in narrow channels for electronic devices.
- Nucleation and coalescence within liquid films in microgravity require further investigation, as the current study indicates significant heat transfer benefits due to this phenomenon. The ability to predictably reproduce this observed phenomenon could enable the development of a thermal management solution for electronics that could replace flow boiling solutions at low to moderate heat fluxes.

## REFERENCES

- [1] “Next Mars Rover Will Have 23 ‘Eyes.’” <https://www.jpl.nasa.gov/news/next-mars-rover-will-have-23-eyes> (accessed May 13, 2023).
- [2] “Nasa Mars rover: Key questions about Perseverance - BBC News.” <https://www.bbc.com/news/science-environment-53129281> (accessed May 13, 2023).
- [3] J. G. Kempenaar, K. S. Novak, M. J. Redmond, E. Farias, K. Singh, and M. F. Wagner, “Detailed Surface Thermal Design of the Mars 2020 Rover,” 2018.
- [4] Z. Zhang, X. Wang, and Y. Yan, “A review of the state-of-the-art in electronic cooling,” *e-Prime - Advances in Electrical Engineering, Electronics and Energy*, vol. 1, p. 100009, Jan. 2021, doi: 10.1016/J.PRIME.2021.100009.
- [5] Z. Guo and M. S. El-Genk, “An experimental study of saturated pool boiling from downward facing and inclined surfaces,” *Int J Heat Mass Transf*, vol. 35, no. 9, pp. 2109–2117, 1992, doi: 10.1016/0017-9310(92)90056-X.
- [6] M. S. El-Genk and H. Bostanci, “Saturation boiling of HFE-7100 from a copper surface, simulating a microelectronic chip,” *Int J Heat Mass Transf*, vol. 46, no. 10, pp. 1841–1854, 2003, doi: 10.1016/S0017-9310(02)00489-1.
- [7] A. H. Howard and I. Mudawar, “Orientation effects on pool boiling critical heat flux (CHF) and modeling of CHF for near-vertical surfaces,” *Int J Heat Mass Transf*, vol. 42, no. 9, pp. 1665–1688, May 1999, doi: 10.1016/S0017-9310(98)00233-6.

- [8] J. Y. Chang and S. M. You, "Heater orientation effects on pool boiling of micro-porous-enhanced surfaces in saturated FC-72," *J Heat Transfer*, vol. 118, no. 4, pp. 937–943, Nov. 1996, doi: 10.1115/1.2822592.
- [9] S. J. Reed and I. Mudawar, "Enhancement of boiling heat transfer using highly wetting liquids with pressed-on fins at low contact forces," *Int J Heat Mass Transf*, vol. 40, no. 10, pp. 2379–2392, Jul. 1997, doi: 10.1016/S0017-9310(96)00286-4.
- [10] M. S. El-Genk and A. F. Ali, "Saturation Boiling Critical Heat Flux of PF-5060 Dielectric Liquid on Microporous Copper Surfaces," *J Heat Transfer*, vol. 137, no. 4, Apr. 2015, doi: 10.1115/1.4029455.
- [11] Y. H. Jeong, "Effect of dimensions and downward-facing angle on CHF under atmospheric condition," *Exp Therm Fluid Sci*, vol. 102, pp. 603–610, Apr. 2019, doi: 10.1016/J.EXPTHERMFLUSCI.2018.10.008.
- [12] Y. Zhang, K. Deng, C. Wang, G. H. Su, W. Tian, and S. Qiu, "Experimental investigation on saturated pool boiling CHF for downward facing heating surface with different sizes and aspect ratio," *International Journal of Thermal Sciences*, vol. 138, pp. 459–466, Apr. 2019, doi: 10.1016/J.IJTHERMALSCI.2019.01.021.
- [13] K. Wang, H. Gong, L. Wang, N. Erkan, and K. Okamoto, "Effects of a porous honeycomb structure on critical heat flux in downward-facing saturated pool boiling," *Appl Therm Eng*, vol. 170, p. 115036, Apr. 2020, doi: 10.1016/j.applthermaleng.2020.115036.
- [14] H. Shi *et al.*, "CHF enhancement of downward-facing saturated pool boiling on the SCGS-modified surfaces with multi-scale conical pin fin structures," *Int J Heat Mass Transf*, vol. 181, Dec. 2021, doi: 10.1016/J.IJHEATMASSTRANSFER.2021.121848.

- [15] D. Zhong, J. Meng, and Z. Li, "Experimental study of saturated pool boiling from downward facing structured surfaces," *International Journal of Thermal Sciences*, vol. 108, pp. 52–61, Oct. 2016, doi: 10.1016/J.IJTHERMALSCI.2016.05.001.
- [16] Z. Zhang, H.-E. Hsieh, Y. Gao, S. Wang, and Z. Zhou, "Heat Transfer Enhancement Using Different SiO<sub>2</sub> Nanofluid Mixing Conditions on a Downward-Facing Heating Surface," *Nucl Technol*, vol. 208, no. 10, pp. 1605–1618, 2022, doi: 10.1080/00295450.2022.2053927.
- [17] Y. Gao, H. E. Hsieh, Z. Zhang, S. Wang, and Z. Zhou, "Experimental study on pool boiling heat transfer characteristics of TiO<sub>2</sub> nanofluids on a downward-facing surface," *Progress in Nuclear Energy*, vol. 153, p. 104402, Nov. 2022, doi: 10.1016/J.PNUCENE.2022.104402.
- [18] Y. Gao, H. E. Hsieh, H. Miao, Z. Zhou, and Z. Zhang, "Investigating the Heat Transfer Characteristics of Impinging Flow on a Downward-Facing Surface," <https://doi.org/10.1080/00295450.2021.1899552>, vol. 208, no. 2, pp. 222–231, 2021, doi: 10.1080/00295450.2021.1899552.
- [19] M. Egbo, M. Borumand, Y. Nasersharifi, and G. Hwang, "Journal Pre-proofs Review: Surface Orientation Effects on Pool-boiling with Plain and Enhanced Surfaces," 2021, doi: 10.1016/j.applthermaleng.2021.117927.
- [20] N. Kumar, M. Q. Raza, D. Seth, and R. Raj, "Aqueous ionic liquid solutions for boiling heat transfer enhancement in the absence of buoyancy induced bubble departure," *Int J Heat Mass Transf*, vol. 122, pp. 354–363, Jul. 2018, doi: 10.1016/j.ijheatmasstransfer.2018.01.101.

- [21] M. Q. Raza, N. Kumar, and R. Raj, “Surfactants for Bubble Removal against Buoyancy,” *Sci Rep*, vol. 6, Jan. 2016, doi: 10.1038/srep19113.
- [22] D.-S. Guo, X.-B. Li, H.-N. Zhang, F.-C. Li, and P.-J. Ming, “Numerical study on the vapor bubble removal by acoustic streaming in downward-facing pool boiling,” *Int J Heat Mass Transf*, vol. 196, p. 123264, Nov. 2022, doi: 10.1016/J.IJHEATMASSTRANSFER.2022.123264.
- [23] I. P. Vishnev, “Effect of orienting the hot surface with respect to the gravitational field on the critical nucleate boiling of a liquid,” *Journal of engineering physics 1975 24:1*, vol. 24, no. 1, pp. 43–48, Jan. 1973, doi: 10.1007/BF00827332.
- [24] M. J. Brusstar and H. Merte, “Effects of heater surface orientation on the critical heat flux - II. A model for pool and forced convection subcooled boiling,” *Int J Heat Mass Transf*, vol. 40, no. 17, pp. 4021–4030, 1997, doi: 10.1016/S0017-9310(97)00077-X.
- [25] I. Mudawar, A. H. Howard, and C. O. Gersey, “An analytical model for near-saturated pool boiling critical heat flux on vertical surfaces,” *Int J Heat Mass Transf*, vol. 40, no. 10, pp. 2327–2339, 1997, doi: 10.1016/S0017-9310(96)00298-0.
- [26] J. Y. Jung, M. S. Lee, H. M. Park, and Y. H. Jeong, “Flow boiling experiments for CHF evaluation under downward-facing heating including flow visualization: Effects of pressure, orientation, mass flux, and local quality,” *Ann Nucl Energy*, vol. 171, Jun. 2022, doi: 10.1016/J.ANUCENE.2022.108994.
- [27] S. Huang, L. Wang, Z. Pan, and Z. Zhou, “Experimental investigation of a new hybrid structured surface for subcooled flow boiling heat transfer enhancement,” *Appl Therm Eng*, vol. 192, p. 116929, Jun. 2021, doi: 10.1016/J.APPLTHERMALENG.2021.116929.

- [28] G. Liang and I. Mudawar, “Pool boiling critical heat flux (CHF) – Part 2: Assessment of models and correlations,” *Int J Heat Mass Transf*, vol. 117, pp. 1368–1383, Feb. 2018, doi: 10.1016/j.ijheatmasstransfer.2017.09.073.
- [29] J. M. Kim, J. H. Kim, and H. S. Ahn, “Hydrodynamics of nucleate boiling on downward surface with various orientation. Part I: Departure diameter, frequency, and escape speed of the slug,” *Int J Heat Mass Transf*, vol. 116, pp. 1341–1351, Jan. 2018, doi: 10.1016/j.ijheatmasstransfer.2017.07.041.
- [30] D. Qiu and V. K. Dhir, “Experimental study of flow pattern and heat transfer associated with a bubble sliding on downward facing inclined surfaces,” *Exp Therm Fluid Sci*, vol. 26, no. 6–7, pp. 605–616, Aug. 2002, doi: 10.1016/S0894-1777(02)00184-X.
- [31] J. S. Kim, Y. N. Kim, and H. K. Cho, “Predicting the sliding bubble velocity on the lower part of a horizontal tube heater under natural convection based on force balance analysis,” *Int J Heat Mass Transf*, vol. 151, p. 119453, Apr. 2020, doi: 10.1016/j.ijheatmasstransfer.2020.119453.
- [32] T. Ren, Z. Zhu, J. Shi, C. Yan, and R. Zhang, “Experimental study on bubble sliding for upward subcooled flow boiling in a narrow rectangular channel,” *Int J Heat Mass Transf*, vol. 152, p. 119489, May 2020, doi: 10.1016/j.ijheatmasstransfer.2020.119489.
- [33] H. Linke *et al.*, “Self-propelled leidenfrost droplets,” *Phys Rev Lett*, vol. 96, no. 15, 2006, doi: 10.1103/PhysRevLett.96.154502.
- [34] F. Kapsenberg, L. Strid, N. Thiagarajan, V. Narayanan, and S. H. Bhavnani, “On the lateral fluid motion during pool boiling via preferentially located cavities,” *Appl Phys Lett*, vol. 104, no. 15, 2014, doi: 10.1063/1.4871863.



- [35] N. Thiagarajan, S. H. Bhavnani, and V. Narayanan, “Self-propelled sliding bubble motion induced by surface microstructure in pool boiling of a dielectric fluid under microgravity,” *Journal of Electronic Packaging, Transactions of the ASME*, vol. 137, no. 2, 2015, doi: 10.1115/1.4029246.
- [36] C. Duron, S. Bhavnani, V. Narayanan, and J. Morris, “Condensate mobility actuated by microsurface topography and wettability modifications,” *Proceedings of the 15th InterSociety Conference on Thermal and Thermomechanical Phenomena in Electronic Systems, ITherm 2016*, pp. 774–780, Jul. 2016, doi: 10.1109/ITHERM.2016.7517625.
- [37] S. Natesh, E. Truong, V. Narayanan, and S. Bhavnani, “Condensation on a horizontal surface with periodic asymmetrical structures – transient film growth,” *Int J Heat Mass Transf*, vol. 108, pp. 1126–1139, May 2017, doi: 10.1016/j.ijheatmasstransfer.2016.12.086.
- [38] J. Straub, “Boiling heat transfer and bubble dynamics in microgravity,” *Adv Heat Transf*, vol. 35, no. C, pp. 57–172, 2001, doi: 10.1016/S0065-2717(01)80020-4.
- [39] H. Merte and J. A. Clark, “Boiling heat transfer with cryogenic fluids at standard, fractional, and near-zero gravity,” *J Heat Transfer*, vol. 86, no. 3, pp. 351–358, Aug. 1964, doi: 10.1115/1.3688689.
- [40] R. Siegel, “Effects of Reduced Gravity on Heat Transfer,” *Adv Heat Transf*, vol. 4, no. C, pp. 143–228, 1967, doi: 10.1016/S0065-2717(08)70274-0.
- [41] M. Zell, J. Straub, and A. Weinzierl, “Nucleate Pool Boiling in Subcooled Liquid Under Microgravity - Results of Texus Experimental Investigations.,” *European Space Agency, (Special Publication) ESA SP*, pp. 327–333, 1984, Accessed: Dec. 28, 2022. [Online]. Available: <https://ui.adsabs.harvard.edu/abs/1984msum.symp..327Z/abstract>

- [42] H. S. Lee, H. Merte, and F. Chiaramonte, "Pool boiling curve in microgravity," *J Thermophys Heat Trans*, vol. 11, no. 2, pp. 216–222, 1997, doi: 10.2514/2.6225.
- [43] H. Ohta, "Experiments on microgravity boiling heat transfer by using transparent heaters," *Nuclear Engineering and Design*, vol. 175, no. 1–2, pp. 167–180, 1997, doi: 10.1016/S0029-5493(97)00172-6.
- [44] T. Oka, Y. Abe, Y. H. Mori, and A. Nagashima, "Pool boiling heat transfer in microgravity (Experiments with CFC-113 and water utilizing a drop shaft facility)," *JSME International Journal, Series B: Fluids and Thermal Engineering*, vol. 39, no. 4, pp. 798–807, 1996, doi: 10.1299/jsmeb.39.798.
- [45] S. Micko, "Hot wire boiling in conditions of reduced gravity; Sieden am Heizdraht unter reduzierter Schwerkraft," 2000.
- [46] M. Steinbichler, *Experimentelle Untersuchung des gesättigten und unterkühlten Siedens an Miniaturheizflächen unter Mikrogravitation*. 2000.
- [47] J. Straub, "Microscale boiling heat transfer under 0g and 1g conditions 1," *International Journal of Thermal Sciences*, vol. 39, no. 4, pp. 490–497, 2000, doi: 10.1016/S1290-0729(00)00204-0.
- [48] C. Kubota *et al.*, "Experiment on nucleate pool boiling in microgravity by using transparent heating surface - Analysis of surface heat transfer coefficients," *J Phys Conf Ser*, vol. 327, no. 1, 2011, doi: 10.1088/1742-6596/327/1/012040.

- [49] J. Kim, J. F. Benton, and D. Wisniewski, "Pool boiling heat transfer on small heaters: Effect of gravity and subcooling," *Int J Heat Mass Transf*, vol. 45, no. 19, pp. 3919–3932, Sep. 2002, doi: 10.1016/S0017-9310(02)00108-4.
- [50] C. D. Henry and J. Kim, "A study of the effects of heater size, subcooling, and gravity level on pool boiling heat transfer," *Int J Heat Fluid Flow*, vol. 25, no. 2, pp. 262–273, Apr. 2004, doi: 10.1016/j.ijheatfluidflow.2003.11.019.
- [51] R. Raj, J. Kim, and J. McQuillen, "Pool boiling heat transfer on the international space station: Experimental results and model verification," *J Heat Transfer*, vol. 134, no. 10, Oct. 2012, doi: 10.1115/1.4006846.
- [52] G. R. Warriar, V. K. Dhir, and D. F. Chao, "Nucleate pool boiling eXperiment (NPBX) in microgravity: International space station," *Int J Heat Mass Transf*, vol. 83, pp. 781–798, 2015, doi: 10.1016/j.ijheatmasstransfer.2014.12.054.
- [53] Y. F. Xue, J. F. Zhao, J. J. Wei, J. Li, D. Guo, and S. X. Wan, "Experimental study of nucleate pool boiling of FC-72 on smooth surface under microgravity," *Microgravity Sci Technol*, vol. 23, no. SUPPL. 1, 2011, doi: 10.1007/s12217-011-9274-5.
- [54] H. Ohta *et al.*, "Tr-1a Rocket Experiment on Nucleate Pool Boiling Heat Transfer Under Microgravity," *ASME International Mechanical Engineering Congress and Exposition, Proceedings (IMECE)*, vol. 1997–X, pp. 249–256, Mar. 1997, doi: 10.1115/IMECE1997-0964.
- [55] O. Kannengieser, C. Colin, and W. Bergez, "Influence of gravity on pool boiling on a flat plate: Results of parabolic flights and ground experiments," *Exp Therm Fluid Sci*, vol. 35, no. 5, pp. 788–796, Jul. 2011, doi: 10.1016/j.expthermflusci.2010.04.010.

- [56] Y. Zhang, J. Wei, Y. Xue, X. Kong, and J. Zhao, “Bubble dynamics in nucleate pool boiling on micro-pin-finned surfaces in microgravity,” *Appl Therm Eng*, vol. 70, no. 1, pp. 172–182, Sep. 2014, doi: 10.1016/j.applthermaleng.2014.04.074.
- [57] P. Di Marco and W. Grassi, “Effect of force fields on pool boiling flow patterns in normal and reduced gravity,” *Heat and Mass Transfer/Waerme- und Stoffuebertragung*, vol. 45, no. 7, pp. 959–966, May 2009, doi: 10.1007/s00231-007-0328-6.
- [58] A. I. Garivalis, G. Manfredini, G. Saccone, P. Di Marco, A. Kossolapov, and M. Bucci, “Critical heat flux enhancement in microgravity conditions coupling microstructured surfaces and electrostatic field,” *NPJ Microgravity*, vol. 7, no. 1, pp. 1–7, Oct. 2021, doi: 10.1038/s41526-021-00167-3.
- [59] N. Zhang, D. F. Chao, and W. J. Yang, “Enhancements of Nucleate Boiling and Critical Heat Flux under Microgravity Conditions,” *J Thermophys Heat Trans*, vol. 15, no. 3, pp. 326–332, 2001, doi: 10.2514/2.6611.
- [60] J. Shi, D. Feng, and Z. Chen, “Experimental investigation on pool boiling heat transfer on untreated/super-hydrophilic metal foam under microgravity,” *Int J Heat Mass Transf*, vol. 151, p. 119289, Apr. 2020, doi: 10.1016/j.ijheatmasstransfer.2019.119289.
- [61] Y. Zhang, J. Zhao, J. Wei, and Y. Xue, “Nucleate Pool Boiling Heat Transfer on a Micro-Pin-Finned Surface in Short-Term Microgravity,” *Heat Transfer Engineering*, vol. 38, no. 6, pp. 594–610, Apr. 2017, doi: 10.1080/01457632.2016.1200377.
- [62] Y. Abe, T. Oka, Y. H. Mori, and A. Nagashima, “Pool boiling of a non-azeotropic binary mixture under microgravity,” *Int J Heat Mass Transf*, vol. 37, no. 16, pp. 2405–2413, Nov. 1994, doi: 10.1016/0017-9310(94)90282-8.

- [63] C. Herman, “Experimental investigation of pool boiling heat transfer enhancement in microgravity in the presence of electric fields,” *NASA Conference Publication*, no. 3338, pp. 195–200, 1996.
- [64] P. Di Marco and W. Grassi, “Effects of external electric field on pool boiling: Comparison of terrestrial and microgravity data in the ARIEL experiment,” *Exp Therm Fluid Sci*, vol. 35, no. 5, pp. 780–787, Jul. 2011, doi: 10.1016/j.expthermflusci.2010.07.011.
- [65] S. Sinha-Ray, W. Zhang, B. Stoltz, R. P. Sahu, S. Sinha-Ray, and A. L. Yarin, “Swing-like pool boiling on nano-textured surfaces for microgravity applications related to cooling of high-power microelectronics,” *NPJ Microgravity*, vol. 3, no. 1, pp. 1–9, Mar. 2017, doi: 10.1038/s41526-017-0014-z.
- [66] J. F. Zhao, J. Li, N. Yan, and S. F. Wang, “Bubble behavior and heat transfer in quasi-steady pool boiling in microgravity,” *Microgravity Sci Technol*, vol. 21, no. SUPPL. 1, Aug. 2009, doi: 10.1007/s12217-009-9151-7.
- [67] A. I. Garivalis and P. Di Marco, “Isolated bubbles growing and detaching within an electric field in microgravity,” *Appl Therm Eng*, vol. 212, p. 118538, Jul. 2022, doi: 10.1016/j.applthermaleng.2022.118538.
- [68] Y. Ma and J. N. Chung, “A study of bubble dynamics in reduced gravity forced-convection boiling,” *Int J Heat Mass Transf*, vol. 44, no. 2, pp. 399–415, Aug. 2001, doi: 10.1016/s0017-9310(00)00106-x.
- [69] K. Sridhar, V. Narayanan, and S. H. Bhavnani, “Asymmetric Sawtooth Microstructure-Induced Vapor Mobility for Suppressed Buoyancy Conditions: Terrestrial Experiment and

- Design for ISS Experiments,” *IEEE Trans Compon Packaging Manuf Technol*, vol. 11, no. 10, pp. 1625–1633, Oct. 2021, doi: 10.1109/TCPMT.2021.3104467.
- [70] S. Bhavnani, V. Narayanan, N. Thiagarajan, and L. Strid, “Passive directional motion of fluid during boiling driven by surface asymmetry in a dielectric fluid,” 2019. doi: 10.1615/JEnhHeatTransf.2019027652.
- [71] F. Kapsenberg, N. Thiagarajan, V. Narayanan, and S. Bhavnani, “Lateral motion of bubbles from surfaces with mini ratchet topography modifications during pool boiling- experiments and preliminary model,” *InterSociety Conference on Thermal and Thermomechanical Phenomena in Electronic Systems, IThERM*, pp. 165–175, 2012, doi: 10.1109/ITHERM.2012.6231427.
- [72] N. Thiagarajan, S. H. Bhavnani, and V. Narayanan, “Self-propelled sliding bubble motion induced by surface microstructure in pool boiling of a dielectric fluid under microgravity,” *Journal of Electronic Packaging, Transactions of the ASME*, vol. 137, no. 2, 2015, doi: 10.1115/1.4029246.
- [73] J. Schindelin *et al.*, “Fiji: An open-source platform for biological-image analysis,” *Nat Methods*, vol. 9, no. 7, pp. 676–682, Jun. 2012, doi: 10.1038/nmeth.2019.
- [74] D. Legland, I. Arganda-Carreras, and P. Andrey, “MorphoLibJ: Integrated library and plugins for mathematical morphology with ImageJ,” *Bioinformatics*, vol. 32, no. 22, pp. 3532–3534, 2016, doi: 10.1093/bioinformatics/btw413.
- [75] J. Y. Tinevez *et al.*, “TrackMate: An open and extensible platform for single-particle tracking,” *Methods*, vol. 115, pp. 80–90, Feb. 2017, doi: 10.1016/j.ymeth.2016.09.016.

- [76] H. Mary and G. J. Brouhard, “Kappa ( $\kappa$ ): Analysis of Curvature in Biological Image Data using B-splines,” *bioRxiv*, no. 852772, pp. 1–14, 2019, doi: 10.1101/852772.
- [77] A. Perron, L. I. Kiss, and S. Poncsák, “An experimental investigation of the motion of single bubbles under a slightly inclined surface,” *International Journal of Multiphase Flow*, vol. 32, no. 5, pp. 606–622, May 2006, doi: 10.1016/j.ijmultiphaseflow.2006.02.001.
- [78] R. Manica, E. Klaseboer, and D. Y. C. Chan, “Force Balance Model for Bubble Rise, Impact, and Bounce from Solid Surfaces,” *Langmuir*, vol. 31, no. 24, pp. 6763–6772, Jun. 2015, doi: 10.1021/acs.langmuir.5b01451.
- [79] D. Legendre, J. Borée, and J. Magnaudet, “Thermal and dynamic evolution of a spherical bubble moving steadily in a superheated or subcooled liquid,” *Physics of Fluids*, vol. 10, no. 6, pp. 1256–1272, May 1998, doi: 10.1063/1.869654.
- [80] J. Aubert and P. Sawyer, “Compatibility of Fluorinert, FC-72, with selected materials.,” 2006, Accessed: Jul. 01, 2023. [Online]. Available: <https://www.osti.gov/biblio/878574>
- [81] R. Spivey and K. B. Morris, “An overview of the Microgravity Science Glovebox (MSG) facility, and the gravity-dependent phenomena research performed in the MSG on the International Space Station (ISS),” *International Astronautical Federation - 59th International Astronautical Congress 2008, IAC 2008*, vol. 2, pp. 779–794, 2008, doi: 10.2514/6.2008-812.
- [82] R. A. Stivey, S. Gilley, A. Ostrogorsky, R. Grugel, G. Smith, and P. Luz, “SUBSA and PFMI transparent furnace systems currently in use in the International Space Station Microgravity Science Glovebox,” 2003. doi: 10.2514/6.2003-1362.

- [83] I. Robertson. Sinclair, “Electronics for electricians and engineers,” p. 270, 1987.
- [84] H. Merte, H. Lee, and R. Keller, “Report on pool boiling experiment prototype model flown on STS-47 (PBE-IA), STS-57 (PBE-IB), STS-60 (PBE-IC),” 1995.
- [85] J.-F. Zhao *et al.*, “Bubble behavior and heat transfer in quasi-steady pool boiling in microgravity,” *Springer*, vol. 21, no. SUPPL. 1, Aug. 2009, doi: 10.1007/s12217-009-9151-7.
- [86] H. A. Johnson, “Transient boiling heat transfer to water,” *Int J Heat Mass Transf*, vol. 14, no. 1, pp. 67–82, Jan. 1971, doi: 10.1016/0017-9310(71)90141-4.
- [87] O. Kannengieser, C. Colin, and W. Bergez, “Pool boiling with non-condensable gas in microgravity: Results of a Sounding Rocket experiment,” *Microgravity Sci Technol*, vol. 22, no. 3, pp. 447–454, Sep. 2010, doi: 10.1007/s12217-010-9211-z.
- [88] R. Raj, J. Kim, and J. McQuillen, “Pool boiling heat transfer on the international space station: Experimental results and model verification,” *J Heat Transfer*, vol. 134, no. 10, 2012, doi: 10.1115/1.4006846.
- [89] Y. Y. Hsu, “On the size range of active nucleation cavities on a heating surface,” *J Heat Transfer*, vol. 84, no. 3, pp. 207–213, 1962, doi: 10.1115/1.3684339.
- [90] T. G. Beckwith, N. L. Buck, and R. D. Marangoni, *Mechanical measurements*. 1982. [Online]. Available: <https://diversidade.acessibilidade.ufpa.br/cmb9ithg9vij/19-dr-isabelle-gerhold-ii/0201847655-mechanical-measurements-6th-ed-r6G736tl8Ws.pdf>



## APPENDIX A: THERMOPHYSICAL PROPERTIES OF FC-72

**Table A.1 The thermophysical properties of FC-72 at 1 atm**

<b>Properties</b>	<b>FC-72</b>
Saturation temperature, $T_{\text{sat}}$ ( $^{\circ}\text{C}$ )	56.6
Specific heat, $C_p$ (J/kg-K)	1097.41
Latent heat of vaporization, $h_{\text{fg}}$ (J/kg)	84510.9
Liquid density, $\rho_l$ ( $\text{kg}/\text{m}^3$ )	1619.73
Vapor density, $\rho_v$ ( $\text{kg}/\text{m}^3$ )	13.396
Thermal conductivity, $k$ (W/m-K)	0.05216
Dynamic viscosity, (Ns/m <sup>2</sup> )	0.000454
Prandtl number, Pr	9.555
Surface tension, $\sigma$ (N/m)	0.008273

## APPENDIX B: SAMPLE MODEL CALCULATIONS

Sample calculation for the slug across four sawteeth (calculated in Wolfram Mathematica)

### Input

```
t = 0.02; (*//time of observation for slugs (s) *)
m = 4; (*no of long and short slopes*)
l1 = 0.00086; (*//length of long slope L1
(m) *) l2 = 0.0005; (*//length of short
slope L2(m) *) h = 0.001; (*//height of
the slug (m) *)
μ = 0.00045; (*//viscosity of saturated FC-72 (Ns/m2) *)
r1 = 0.00016;
(*//statically measured radius of curvature at crest (m) *)
r2 = 0.000268;
(*//statically measured radius of curvature at trough (m) *)
V = 0.026; (*//experimental velocity (M/s) *)
σ = 0.008273; (*surface tension of saturated FC-72 σ (N/m) *)
ρl = 1619.3; (*density of saturated liquid
(kg/m3) *)
ρg = 13.396; (*density of saturated vapor
(kg/m3) *)
g = 9.81; (*gravitational acceleration
(m/s2) *)
d = m / 1000; (*diameter of vapor bubble (m) *)
θ = 30 Degree; (*angle of microstructure °*)
```

### Calculations

$$Bo = g * (\rho_l - \rho_g) * d * d / \sigma = 30.4681$$

$$\Delta P = 2 * \sigma * (1/r_1 + 1/r_2) = 165.151 \text{ N/m}^2$$

$$\frac{\partial P}{\partial x} (\text{longslope}) = \delta P_{(\text{longslope})} = -\Delta P / l_1 = -192036 \text{ N/m}^3$$

$$\frac{\partial P}{\partial x} (\text{shortslope}) = \delta P_{(\text{shortslope})} = -\Delta P / l_2 = -330303 \text{ N/m}^3$$

$$F_{\Delta P, \text{longslope}} = \left\{ m \left[ \left( \frac{\mu V}{H} + \frac{H}{2} \frac{\partial P}{\partial x} \right) LD \cos \theta \right]_{\text{long slope}} \right\} =$$

$$0.0000119165 \left( \frac{0.000017}{H} - 96\,018.2 \text{ H} \right) \text{ N}$$

$$F_{\Delta P, \text{shortslope}} = -n \left[ \left( \frac{\mu V}{H} + \frac{H}{2} \frac{\partial P}{\partial x} \right) LD \sin \theta \right]_{\text{short slope}} =$$

$$4 * 10^{-6} \left( \frac{0.000017}{H} - 96\,018.2 \text{ H} \right) \text{ N}$$

The drag coefficient on the vapor bubble from the correlation is calculated by

$$C_d = 0.0683 * B o^{(0.45)} = 0.317798$$

$$F_d = 0.5 * A * C_d * \rho_l * U^2 = 1.09289 \times 10^{-6} \text{ N}$$

$$F_{b1} = \rho_l * g * V_{\text{half ellipsoid}} * \cos \theta * \frac{l_1}{l_1 + l_2} = 0.0000761223 \text{ N}$$

$$F_{b2} = \rho_l * g * V_{\text{half ellipsoid}} * \cos \theta * \frac{l_1}{l_1 + l_2} = 0.0000219746 \text{ N}$$

$$F_{am(\text{spherical})} = \frac{\pi}{6} D^3 [(\rho_l) C_m + \rho_v] \left( \frac{dU}{dt} \right) = 8.81778 \times 10^{-6} \text{ N}$$

Plug the above values into the overall energy balance:

$$F_{\Delta P, \text{tot}} - F_d + F_{b1} - F_{b2} - F_{am} = F_{\Delta P, \text{longslope}} - F_{\Delta P, \text{shortslope}} - F_d + F_{b1} - F_{b2} - F_{am} = 0$$

H (liquid film thickness is the only unknown)

Solve for  $H > 0 \in \text{Real numbers}$

$$H \rightarrow 0.000093523 = 93.5 \mu\text{m}$$

## APPENDIX C: UNCERTAINTY ANALYSIS

### Experimental Uncertainty for the Microgravity Experiments

The experimental uncertainty on the heat flux is calculated using the propagation of source errors [90]. The sources of error from the DC-DC converter are the voltage and current. The non-uniformity of the sputtered coating also introduces uncertainties in the length and width of the resistive heater. Errors in the efficiency of the DC-DC converter were negligible as the flight PFMI furnace characterized each flight ampoule before launch terrestrially.

$$(U_{q/q})^2 = \left(\frac{U_v}{V}\right)^2 + \left(\frac{U_I}{I}\right)^2 + \left(\frac{U_w}{W}\right)^2 + \left(\frac{U_L}{L}\right)^2$$

The uncertainties on the voltage ( $U_v/V$ ), current ( $U_I/I$ ), heated length ( $U_L/L$ ), and width ( $U_w/W$ ) were less than 0.2%, 0.2%, 2.5%, and 2.5%, respectively.

$$(U_{q/q})^2 = (0.002)^2 + (0.002)^2 + (0.025)^2 + (0.025)^2$$

The resulting uncertainty on the heat flux is calculated to be  $\pm 3.54\%$ .

$$U_{q/q} = 0.0354$$

The maximum uncertainty values were calculated to be  $\pm 1.45\%$  for the thermocouples used in the flight experiment, using the methods of Beckwith et al. [90]

Similarly, the uncertainty in the experimental heat transfer coefficient is calculated from the uncertainties on the surface temperature, fluid temperature, and input heat flux, as shown below.

$$\left(\frac{U_h}{h}\right)^2 = (U_{q/q})^2 + \left(\frac{U_{T_s}}{T_s}\right)^2 + \left(\frac{U_{T_f}}{T_f}\right)^2$$

The uncertainties on the heat flux ( $U_{q''/q''}$ ), surface temperature ( $\frac{U_{T_s}}{T_s}$ ), and fluid temperature ( $\frac{U_{T_f}}{T_f}$ ), and width ( $U_w/W$ ) were less than 3.54%, 1.45%, and 1.45%, respectively. The resulting uncertainty on the experimental heat transfer coefficient is  $\pm 4.1\%$ .

## **APPENDIX D: SCIENCE VERIFICATION DOCUMENT**

The science verification document was created to capture the requirements of the ASCENT experiment including design files for all components, protocol documents and data files including sensor calibration information.

The document was created by the implementation partner as a result of the 100+ biweekly meetings with the science team at Auburn University and University of California, Davis.

A curated sub-section of the science verification document with the following sections is attached in this appendix.

**Science Verification Checklist**

**ASCENT Success Criteria**


**Sample Flight Ampoule Processing Protocol**


**Flight Ampoule Thermocouple Calibration Data**

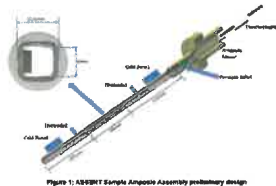
*Table 1: Summary of the Science Requirements*

Item	Component	Science Requirement	Verification/Explanation
1.	<b>PFMI</b>	The experiment will be completed using the PFMI facility.	The experiment was designed to be conducted in the PFMI facility as defined in the Experiment Requirements Document (ERD) for the PFMI- ASCENT investigation (G102DS4291; Item 1.1).
2.		The experiment will need two cold zones on the PFMI.	<p>The PFMI facility (Techshot PN: 112304-1) was modified to support two Cold Zones. The Cold Zones have been utilized in multiple rounds of testing. The Cold Zones are shown in Figure 7 of the ERD (G102DS4291; Item 1.1). That image was generated from the current CAD model of the PFMI facility, even though both Cold Zones are not explicitly shown in the assembly drawing (Drawing 112304; Item 2.1).</p> <p>This modification was authorized by Task Order MOD #4, Requirement 6, which states <i>“The contractor shall modify the flight and ground unit to provide the capability to support a second Cold Zone to support science requirements.”</i> The contract modification is not included as an attachment to this document because it contains privileged information that exceeds the scope of this experiment.</p>
3.		The experiment will require an additional source of illumination to backlight the bubbles during imaging.	A Light Bar is Techshot PN: 112850-1 (Drawing 112850; Item 3.1) was added to the PFMI Facility to support this experiment. The Light Bar is shown installed in the PFMI facility in Figure 2 of the ERD (G102DS4291; Item 1.1). The light bar’s functionality was tested and approved by the PI team.



Item	Component	Science Requirement	Verification/Explanation
4.	Ampoule	<p>A total of 8 ampoules (2x of each type) are required for the experiment. Four of the ampoules will be fabricated as flight hardware. The remaining four ampoules will be fabricated for use in ground-based experiments, and will include a mechanism to measure pressure inside the ampoule.</p>	<p>There are four unique part numbers (Techshot PNs: 112346-1, -2, -3, -4) for the PFMI Ascent Ampoules that are used for science experiments and one (Techshot PN: 112346-5) for the Calibration Ampoule. All of these parts are described on a single drawing (Drawing 112346; Item 4.1). Two of each part number were fabricated to flight specifications. One of each part number was fabricated for Flight and one for Ground.</p> <p>The As-Built drawing for each flight ampoule is attached (Items 4.2 – 4.6).</p> <p>NOTE: The As-Built drawings that are attached and provided to the PI at the time that this document will be signed are those completed prior to refurbishment of the science solution (FC-72) that is planned for immediately prior to late-load turnover. After the flight ampoules have been reloaded with FC-72, the As-Built drawings will be updated in accordance with Techshot policy and with QA oversight. Once those drawings have been completed and scanned, they will be provided to the PI.</p> <p>The Ground -4 ampoule was converted to a Flight -4 ampoule as requested by the PI and agreed to by NASA. The subtle differences between and flight and ground ampoule are accepted by the PI.</p> <p>PI acknowledges receipt of this information and accepts the demonstrated performance of this ampoule as sufficient to achieve science objectives.</p> <p>PI Initials: </p>

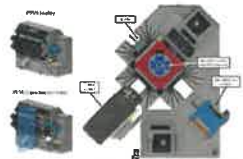
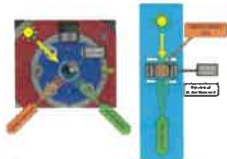
Item	Component	Science Requirement	Verification/Explanation
5.		<p>There will be 4 types of ampoules. The geometry of the ratcheted surface will be the only variable between each ampoule type.</p>	<p>Note 19 on Drawing 112346 states:            “-1 THRU -4 ASSEMBLIES ARE IDENTICAL EXCEPT FOR RATCHET SAW TOOTH SAMPLE.            -5 ASSEMBLY IS FOR CALIBRATION CONTAINING NO RATCHET SAW TOOTH SAMPLE.”</p> <p>During assembly the ERD is referenced to verify that the correct surface is installed in the correct ampoule according to <i>Table 5: Test Matrix</i>. When a surface is installed in an ampoule, it is noted on the As-Built drawings (Items 4.2 – 4.6).</p> <p>The Flight -1 ampoule had a thermocouple (TC) become dislodged and is no longer on the centerline of the ampoule.</p> <hr/> <p>PI acknowledges receipt of this information, understands that the identified ampoule does not meet this requirement, and accepts the demonstrated performance of all ampoules as sufficient to achieve science objectives.</p> <p>PI Initials: </p>
6.		<p>The geometry of the square-profile section of the ampoule will be:</p> <p style="margin-left: 40px;">Length<sup>‡</sup>: 90 mm ± 0.13 mm</p> <p style="margin-left: 40px;">Outer Dimension*: 10.4 mm ± 0.25 mm</p> <p style="margin-left: 40px;">Inner Dimension: 8 mm ± 0.13 mm</p> <p style="margin-left: 40px;">Wall Thickness: 1.2 mm ± 0.13 mm</p> <p><sup>‡</sup> Includes transition zone between square and round cross sections</p> <p>* Driven dimension</p>	<p>The square profile of the ampoule is made from the PFMI ASCENT Ampoule, Square (Techshot PN: 112342-1) and is described by Drawing 112342 (Item 6.1). Note 5 on the drawing states “MAKE FROM FRIEDRICH &amp; DIMMOCK, INC. PN BST-8-120.” The Part Number “BST-8-120” codes for an 8.0mm ID and a 1.2mm Wall (Product Specifications for BST-8-120; Item 6.2). The 90mm length is specified in Drawing 112342. It should be noted that the dimensions in 112342 that describe the square profile are reference dimensions, as noted by being in parentheses; this means that the dimensions of the profile are driven by the “make from” specification.</p>

Item	Component	Science Requirement	Verification/Explanation
7.		<p>The ampoules will be made from borosilicate glass.</p>	<p>The PFMI ASCENT Ampoule Tube Assembly (Techshot PN: 112344-1) and is described by Drawing 112344 (Item 7.1). The assembly consists of three parts which are (1) PFMI ASCENT Ampoule, Closed End (Techshot PN: 112341-1) which is described by Drawing 112341 (Item 7.2), (2) PFMI ASCENT Ampoule, Square (Techshot PN: 112342-1) which is described by Drawing 112342 (Item 6.2), and (3) PFMI ASCENT Ampoule, Open End (Techshot PN: 112343-1) which is described by Drawing 112343 (Item 7.3).</p> <p>Note 5 on Drawing 112341 specifies "MAKE FROM MCMMASTER PN 8729K37." The specifications for McMaster-Carr PN 8729K37 (Item 7.4) defines the material as "Borosilicate Glass".</p> <p>Note 5 on Drawing 112342 states "MAKE FROM FRIEDRICH &amp; DIMMOCK, INC. PN BST-8-120." The manufacturer describes this part as "Borosilicate Square Tubing" (Product Specifications for BST-8-120; Item 6.2).</p> <p>Notes 5 – 7 on Drawing 112343 (Item 7.3) define how 112343-1 is fabricated. It is made from two sections tubing of different sizes that are flame sealed together to create a single part, as defined by Note 7 which states "JOIN NOTES 5 AND 6 TOGETHER AND OVERLAP PER SPECIFIED DISTANCE. FLAME SEAL."</p> <p>Note 5 on Drawing 112343 (Item 7.3) specifies "MAKE FROM MCMMASTER 8729K37." The specifications for McMaster-Carr PN 8729K37 (Item 7.4) defines the material as "Borosilicate Glass".</p> <p>Note 6 on Drawing 112343 (Item 7.3) specifies "MAKE FROM MCMMASTER 8729K41". The specifications for McMaster-Carr PN 8729K41 (Item 7.5) defines the material as "Borosilicate Glass".</p>
8.		<p>The general geometry of the ampoule shall be as shown in <a href="#">Figure 1</a>.</p> 	<p>Figure 1 from the ERD is attached for reference (Item 8.1). The released drawing of the ampoule (Item 4.1) shows that the design of the ampoule is consistent with the general form of Figure 1. The drawing of the PFMI ASCENT Ampoule, Tube Assembly (Item 6.1) also shows the general geometry of the ampoule. Some of the final dimensions have changed since Figure 1 was generated, but the general geometry of the ampoule is consistent with the figure.</p>


Item	Component	Science Requirement	Verification/Explanation
9.		The middle section of the ampoule shall have a square profile.	<p>The PFMI ASCENT Ampoule Tube Assembly (Techshot PN: 112344-1) and is described by Drawing 112344 (Item 7.1). The assembly consists of three parts which are (1) PFMI ASCENT Ampoule, Closed End (Techshot PN: 112341-1) which is described by Drawing 112341 (Item 7.2), (2) PFMI ASCENT Ampoule, Square (Techshot PN: 112342-1) which is described by Drawing 112342 (Item 6.2), and (3) PFMI ASCENT Ampoule, Open End (Techshot PN: 112343-1) which is described by Drawing 112343 (Item 7.3).</p> <p>The drawing shows that the center section of the ampoule is the portion that contains the square profile.</p>
10.		One face of the square profile section of the ampoule (on the interior of which the ratcheted surface is mounted) will be coated with Nichrome (NiCr) and serve as the heat source.	Note 6 on Drawing 112344 (Item 7.1) specifies application of NiCr to the ampoule.
11.		The ampoules must be sealed and provide one Level of Containment for the process fluid.	<p>Drawing 112346 (Item 4.1) specifies the design of the ampoule. Images from a CAD rendering of the assembly are attached for reference (Item 11.1). The LOC-1 for the science materials is obtained by using epoxy to bond the Pressure Relief Assembly (Techshot PN: 112676-1) to the Ampoule Tube Assembly (Techshot PN: 112344-1).</p> <p>The Ampoule Tube Assembly (Drawing 112344; Item 7.1) is an inseparable part formed by flame sealing three sections of tubing together. One end is a solid, round bottom section of sealed tubing, and the other end is open.</p> <p>The Pressure Relief Assembly is described by Drawing 112676 (Item 11.2). The assembly consists of a Main Plug (Techshot PN: 112420-1; FN 2), an inflatable Membrane (Techshot PN: 112669-1; FN1), and a set of tubing and fittings that terminate in a dry break QD fitting (FN7).</p> <p>During assembly at the 112346 part-level, the Pressure Relief Assembly is bonded to the Ampoule Tube Assembly using epoxy to create a seal. This process is defined by Note 9 on Drawing 112346 (Item 4.1). Once this process is done, LOC-1 for the science material has been created.</p> <p>Each ampoule is leak tested during assembly according to Section 5.3, Steps 21 &amp; 23 of the Ampoule Assembly Instructions (G102AI4866; Item 11.3).</p>

Item	Component	Science Requirement	Verification/Explanation										
12.		The ampoules must be capable of being degassed and then filled with the process fluid.	The degassing and filling of the ampoule is described by Section 5.3, Step 22 of the Ampoule Assembly Instructions (G102AI4866; Item 11.3).										
13.	<b>Specimen</b>	The experiment will use FC-72 as the process fluid.	The process fluid was designated as FC-72. The material was submitted to JSC toxicology and was rated HRL-0 (V2 Verified PFMI HMST; Item 13.1).										
14.	<b>Specimen (continued)</b>	<p>There will be four variations of the ratcheted surface. The first type of surface will be a flat surface without ratchets. The second will include a 60°-30° asymmetric ratchet with preferential cavities spaced 1mm apart. The third ampoule will contain a 60°-30° ratchet with preferential slot cavities. The fourth ampoule will consist of a 60°-30° asymmetric ratchet with preferential cavities spaced 2mm apart.</p> <p>The correlation between ampoule and ratchet geometry shall be:</p> <table border="1" style="margin-left: 20px;"> <thead> <tr> <th>Ampoule #</th> <th>Ratchet Geometry</th> </tr> </thead> <tbody> <tr> <td>-1</td> <td>Flat</td> </tr> <tr> <td>-2</td> <td>60-30 / 1mm</td> </tr> <tr> <td>-3</td> <td>60-30 / Slot</td> </tr> <tr> <td>-4</td> <td>60-30 / 2mm</td> </tr> </tbody> </table>	Ampoule #	Ratchet Geometry	-1	Flat	-2	60-30 / 1mm	-3	60-30 / Slot	-4	60-30 / 2mm	<p>The ratcheted surfaces were fabricated by the PI and sent to Techshot in a flight-ready condition.</p> <p>During assembly the ERD is referenced to verify that the correct surface is installed in the correct ampoule according to Table 5: Test Matrix. When a surface is installed in an ampoule, it is noted on the As-Built drawings (Items 4.2 – 4.6).</p>
Ampoule #	Ratchet Geometry												
-1	Flat												
-2	60-30 / 1mm												
-3	60-30 / Slot												
-4	60-30 / 2mm												
15.		The ampoule shall be designed such that all internal instrumentation is symmetrical with respect to the centerline of the ratcheted-surface test specimen.	<p>Drawing 112346 (Item 4.1) specifies the design of the ampoule. All items were designed to be symmetric as defined by Requirement 15.</p> <p>The Flight -1 ampoule had a thermocouple (TC) become dislodged. That TC is no longer on the centerline of the ampoule, and therefore that ampoule is not symmetric.</p> <p>PI acknowledges receipt of this information and accepts the demonstrated performance of this ampoule as sufficient to achieve science objectives.</p> <p>PI Initials: <span style="border: 1px solid green; padding: 2px;">HAB</span></p>										


Item	Component	Science Requirement	Verification/Explanation
16.		The ratcheted surfaces shall be made of titanium alloy (Ti-6Al-4V).	The ratcheted surfaces were fabricated by the PI and sent to Techshot in a flight-ready condition.
17.		The ratcheted surfaces shall be fabricated by the PI and provided to Techshot no later than 16-weeks prior to launch.	The ratcheted surfaces were fabricated by the PI and sent to Techshot in a flight-ready condition.
18.		The overall geometry of the ratcheted surfaces shall be:  Length: 80 mm ± 0.13 mm Height: 6 mm ± 0.13 mm Thick: 2.3 mm ± 0.13 mm	The ratcheted surfaces were fabricated by the PI and sent to Techshot in a flight-ready condition.
19.		The flat side of the ratcheted surfaces must be attached to the inside of the glass ampoule with Arctic Silver MCSE (Medium Cure Silver Epoxy) or QCSE (Quick Cure Silver Epoxy).	Installation of the ratcheted surface into the ampoule is defined in Drawing 112346 (Item 4.1). Pages 2 – 3 detail the installation of the ratcheted surface (FN7) onto the Tube Assembly (FN2; 112344-1). Note 6 states “place FN7 (RATCHET) in the ASSEMBLY CARRIAGE as shown. Apply a thin layer of FN21 (EPOXY).”. Referring to the Parts List, FN21 is described as “ARCTIC SILVER THERMAL EPOXY, QUICK CURE SILVER EPOXY, 8G” with the associated Part Number of “QCSE-8G” and the Manufacturer as “Arctic Silver”.
20.		<b>Pressure Relief System</b>	The ampoule must include a pressure relief system that allows for expansion of the process fluid during the experiment.


Item	Component	Science Requirement	Verification/Explanation
21.		The pressure relief system should be capable of maintaining near constant pressure over the full range of Heat Flux (0 – 3.5 W/cm <sup>2</sup> ).	<p>This requirement was verified by conducting <i>Acceptance Test A-5 (Constant Pressure Verification)</i> of the PFMI – ASCENT Test Plan (G102DS5199; Item 21.1) according to the test protocol defined in Techshot Document G102PC5214 (Item 20.1).</p> <p>PI acknowledges receipt of data from ground-based tests on Ground and/or Flight ampoules and accepts the demonstrated performance of the pressure relief system as demonstrated with the Ground ampoule(s) as sufficient to achieve science objectives with the Flight ampoules.</p> <p>PI Initials: <span style="border: 1px solid green; padding: 2px;">HAB</span></p>
22.		The pressure within the development ampoules must be measured (ground experiments only).	<p>The ground ampoules were designed to be outfitted with a pressure measurement device. Multiple tests were conducted using the ground ampoules and the data was delivered to the PI prior to turnover of the flight ampoules.</p> <p>This requirement was verified by conducting <i>Acceptance Test A-5 (Constant Pressure Verification)</i> of the PFMI – ASCENT Test Plan (G102DS5199; Item 21.1) according to the test protocol defined in Techshot Document G102PC5214 (Item 20.1).</p>
23.	Imaging System	<p>Orthogonal cameras will be used to view the ratcheted surface inside the ampoule from different perspectives, as shown in <a href="#">Figure 2</a> and <a href="#">Figure 3</a>.</p> <div style="display: flex; justify-content: space-around; align-items: center;">   </div> <p><small>Figure 2: An exploded CAD rendering that shows the basic form of the ratcheted surface. Figure 3: Diagram detailing the light path and camera perspective for this experiment.</small></p>	<p>Figures 2 &amp; 3 from G102DS4291 are attached for reference (Item 23.1). Drawing 112304 (Item 2.1) describes the PFMI Facility. On Page 2, the location of the Light Bar can be identified by referencing FN3; this location is consistent with Figures 2 &amp; 3. On Page 2 the location of the camera mount is visible in the Right View, though not called out specifically. On the same page, FN9 identifies the label that indicates where the ampoule is installed. These are both consistent with Figures 2 &amp; 3. The location of the second camera mount is obscured in all views, but is -90° off-set from the front mount shown in the Right View on Page 3.</p> <p>Additionally, during ampoule fabrication measures are taken to ensure that when the ampoule is installed in the PFMI facility, the ampoules are properly oriented according to Figures 2 &amp; 3. This process is defined by Section 5.3, Steps 24 – 26 of the Ampoule Assembly Instructions (Item 11.3).</p>





Item	Component	Science Requirement	Verification/Explanation
24.	Imaging System (continued)	The existing front PFMI camera system can be used for one perspective.	One perspective is observed using a COHU camera, as shown in Figures 2 & 3 of G102DS4291 (Item 23.1). The function of the video system was verified according to <i>Test D-2.5 &amp; D-2.6 Test Protocol (Video System)</i> , Techshot Document G102PC5218 (Item 24.1) and was accepted by the PI.
25.		A set of two, high-speed cameras will be used for the second perspective.	The second perspective is provided by two high speed cameras. The cameras are mounted in the HIGH SPEED CAMERA ASSEMBLY, Techshot PN: 112844-1 (Drawing 112844; Item 25.1).  The function of the video system was verified according to <i>Test D-2.5 &amp; D-2.6 Test Protocol (Video System)</i> , Techshot Document G102PC5218 (Item 24.1) and was accepted by the PI.
26.		At each timepoint where a video is captured, all three cameras should be triggered simultaneously. If triggering of the low-speed COHU camera cannot be controlled by the same software as the high-speed cameras, the video recorded from the COHU should start before the high-speed cameras are triggered and should be stopped after the high-speed video capture has ended. This will ensure that low-speed camera footage exists for the entire duration that is recorded on the high-speed cameras.  NOTE: In this context “triggering” refers to starting each video capture event.	The function of the video system, including simultaneous capture of video from all cameras was verified according to <i>Test D-2.5 &amp; D-2.6 Test Protocol (Video System)</i> , Techshot Document G102PC5218 (Item 24.1) and was accepted by the PI.  Techshot’s software engineer performs the synchronization manually after the completion of the experiment. This manual synchronization has been completed on tests F-1 through F-4. This data has been delivered to the PI team.  PI acknowledges receipt of data from ground-based tests on Ground and/or Flight ampoules and accepts the demonstrated performance of the video capture system as sufficient to achieve science objectives.  PI Initials: 





Item	Component	Science Requirement	Verification/Explanation
27.		<p>The high-speed cameras will have a frame rate of at least 900fps.</p>	<p>The cameras (FN16 on Drawing 112844, Item 25.1) are in the xiQ compact USB3 series made by Ximea (PN: MQ013MG-ON). The product line brochure (Item 27.1) provides product specifications. This document identifies the maximum frame rate as 172/210 fps, however this as at the maximum resolution. The document also states that the device is capable of being used as a "VGA sensor at &gt; 500 fps." The product page on the manufacturer website (Item 27.2) also states "Can reach 1000+ fps at 640x400 resolution ROI."</p> <p>The function of the video system was verified according to <i>Test D-2.5 &amp; D-2.6 Test Protocol (Video System)</i>, Techshot Document G102PC5218 (Item 24.1) and was accepted by the PI.</p> <p>PI acknowledges receipt of data from ground-based tests on Ground and/or Flight ampoules and accepts the demonstrated performance of the video capture system as sufficient to achieve science objectives.</p> <p>PI Initials: </p>

Item	Component	Science Requirement	Verification/Explanation
28.		<p>One high-speed cameras will provide a wide field of view with a Region of Interest of 10cm wide by 1.5cm tall.</p> <p>The other high-speed cameras will provide a narrow field of view with a Region of Interest of 1cm wide by 1.5cm tall.</p>	<p>The field of view of the cameras is controlled by their position on the mount and the attached lenses. The high-speed cameras are mounted in the HIGH SPEED CAMERA ASSEMBLY, Techshot PN: 112844-1 (Drawing 112844; Item 25.1). The lenses used on the cameras are a 25mm, f/1.8 Cr Series Fixed Focal Length Lens (FN10; Edmund Optics; PN 35-173) and an 8.5mm, f/1.8 Cr Series Fixed Focal Length Lens (FN11; Edmund Optics; PN 36839).</p> <p>The function of the video system was verified according to <i>Test D-2.5 &amp; D-2.6 Test Protocol (Video System)</i>, Techshot Document G102PC5218 (Item 24.1) and was accepted by the PI.</p> <p>Techshot has not explicitly measured the implemented dimensions to be exactly as described in the requirements. However, the system has been tested in both development tests and flight ampoule check out tests (F-1 through F-4).</p> <p>PI acknowledges receipt of data from ground-based tests on Ground and/or Flight ampoules and accepts the demonstrated performance of the video capture system as sufficient to achieve science objectives.</p> <p>PI Initials: </p>
29.		<p>Two high-speed cameras will be physically constrained to each other and the set will be capable of linear translation along the longitudinal axis of the specimen (ratcheted surface).</p>	<p>The high-speed cameras are mounted in the HIGH SPEED CAMERA ASSEMBLY, Techshot PN: 112844-1 (Drawing 112844; Item 25.1). The cameras are physically constrained in a single assembly, which is later installed in the PFMI prior to operations on the ISS.</p> <p>The function of the video system was verified according to <i>Test D-2.5 &amp; D-2.6 Test Protocol (Video System)</i>, Techshot Document G102PC5218 (Item 24.1) and was accepted by the PI.</p>
30.		<p>One high-speed camera shall be viewable during the live feed. If possible, both high-speed cameras will be viewable during the live feed.</p>	<p>The PI has been present during multiple ground tests that simulate on-orbit operations. The information that was available to the PI during these operations was accepted as sufficient for processing the ampoules. It is expected that the on-orbit processing will be completed in the same manner as these ground tests.</p>

Item	Component	Science Requirement	Verification/Explanation
31.		The nominal video duration is between 1-5s. The maximum video duration is 10s.	Ground tests were conducted according to the Ampoule Processing Protocol (Techshot document G102PC5219; Item 31.1). The data (including video) was provided to the PI for evaluation. The PI has acknowledged that processing of the ampoules on the ISS using similar procedures will provide desired data.
32.		The computer controlling the imaging system shall have sufficient storage to complete the experiment (3 GB / Run). The data can be deleted from the computer once it has been downloaded and accepted by the PI.	<p>The computer used for ISS operations will be specially formatted for use in this experiment. NASA is loaning an identical laptop to Techshot for ground testing. According to the provided NASA Form 893, Loan of NASA Equipment, (Item 32.1) the computer is a HP ZBook 15 G2 (SN: MXL5411W5M).</p> <p>According to HP Support (via chat; Item 32.2) the device was configured with a 256GB SSD.</p> <p>Assuming two Runs per CZ temperature (6GB) and five CZ temperatures (30GB), a total of 120GB would be required for the experiment. That leaves 136GB for the OS and control software, which is more than reasonable. This also assumes that no data is downloaded and deleted between Tests. Based on previous experience, the video data from each run should be able to be downloaded daily. This is not guaranteed, as NASA manages available bandwidth for data downloads.</p>

Item	Component	Science Requirement	Verification/Explanation
33.		<p>The video feed can be converted to a compressed format (*.avi) for rapid review and analysis. The original images shall be saved in their original, uncompressed format (*.tif), downloaded, and provided to the PI.</p>	<p>Ground tests were conducted according to the Ampoule Processing Protocol (Techshot document G102PC5219; Item 31.1). The data (including video) was provided to the PI for evaluation. The PI has acknowledged that processing of the ampoules on the ISS using similar procedures will provide desired data.</p> <p>Techshot's software engineer performs the conversion manually after the completion of the experiment. This manual conversion has been completed on tests F-1 through F-4. This data has been delivered to the PI team.</p> <p>PI acknowledges receipt of data from ground-based tests on Ground and/or Flight ampoules and accepts the data provided as sufficient to achieve science objectives.</p> <p>PI Initials: </p>
34.	Lighting System	<p>The lighting system shall be designed to backlight (from the perspective of the high-speed cameras) the bubbles that form and escape from the ratcheted surface.</p> <p>Prior to flight operations, the ground (or flight) PFMI facility will be used to capture video of a ground ampoule using the high-speed cameras. The PI will use those images to verify that there is sufficient illumination and accept the design of the lighting system.</p>	<p>The ampoules have been designed to be processed according to Figures 2 &amp; 3 of the ERD (Item 23.1).</p> <p>The function of the video and light systems was verified according to <i>Test D-2.5 &amp; D-2.6 Test Protocol (Video System)</i>, Techshot Document G102PC5218 (Item 24.1).</p> <p>PI acknowledges receipt of data from ground-based tests on Ground and/or Flight ampoules and accepts the demonstrated illumination of the video system as sufficient to achieve science objectives.</p> <p>PI Initials: </p>
35.		<p>Control of the lighting system is binary (on/off) and will be controlled by MSG on the ground during flight operations (not controlled by ISS crewmember). The parameters of the lighting system will not be adjustable on the ISS.</p>	<p>All ground ampoules have been processed using the same constraints.</p> <p>The function of the video system was verified according to <i>Test D-2.5 &amp; D-2.6 Test Protocol (Video System)</i>, Techshot Document G102PC5218 (Item 24.1) and was accepted by the PI.</p>


Item	Component	Science Requirement	Verification/Explanation
36.	Temperature	The maximum temperature in the Hot Zone will be between 50°C & 100°C.	The maximum temperature achievable in the ASCENT ampoules when processed in the PFMI facility was characterized according to <i>Test A-2 Test Protocol (Max Temp Characterization)</i> , Techshot Document G102PC5220 (Item 36.1). The maximum temperature achieved during that test was between 50°C & 100°C.
37.	Temperature (continued)	<p>The temperature setpoints for the Cold Zones shall be between 20°C &amp; 40°C.</p> <p>The tolerance for the Cold Zone temperature is defined by the subcooling values for the experiment. The subcooling values are not directly measured, but will be determined experimentally during preflight, ground tests. In order to maintain proper subcooling, the Cold Zone temperatures (as measured by the PFMI facility control TCs) must be maintained within 0.5°C of the setpoint.</p>	<p>Tests will be executed according to <i>Table 5: Test Matrix</i> from the ERD (Item 1.1). All values for the Cold Zone Setpoints were between 20°C &amp; 40°C.</p> <p>PI acknowledges receipt of data from ground-based tests on Ground and/or Flight ampoules and accepts the performance of the Cold Zones as sufficient to achieve science objectives.</p> <p>PI Initials: </p>

Item	Component	Science Requirement	Verification/Explanation
38.		<p>Four internal thermocouples will be required to measure:</p> <ul style="list-style-type: none"> <li>• Surface temperature of the ratcheted surface (TC-5)</li> <li>• Fluid Temperature (TC-6)</li> <li>• Temperature in Cold Zone 1 (TC-1)</li> <li>• Temperature in Cold Zone 2 (TC-2)</li> </ul> <p>The thermocouple on the test surface (TC-5) shall be used as the control for temperature setpoint.</p>	<p>The location of the four thermocouples is defined by the drawing for the PFMI ASCENT Ampoule Assembly (Item 4.1). Each ampoule was assembled per drawings and tested.</p> <p>The Flight -1 ampoule had a thermocouple (TC) become dislodged. That TC is no longer in the exact position as defined by the assembly drawing.</p> <p>The Power Control Method (PCM) used to process the ampoules does not change how the PFMI facility fundamentally operates. The PCM utilizes a user definable parameter (maximum voltage) in the software to limit the power output of the furnace to a specified percentage of the total power that the facility is capable of providing to the heating elements. The operator then enters a temperature setpoint (TC-5) for the facility that unattainable given the power output limitation previously entered in the control software. The result is that the facility will continuously operate at the maximum available voltage in a vain attempt to reach the temperature setpoint, which effectively results in a constant power output. The facility is still controlled by TC-5, however clever manipulation of the control software prevents the temperature at TC-5 from ever reaching the target setpoint.</p> <p>PI acknowledges receipt of the drawing and accepts the actual assembled location of the four thermocouples in the ampoules as sufficient to achieve science objectives.</p> <p>PI Initials: </p>
39.		<p>The thermocouple wire will be no greater than 0.5 mm OD to minimize obstruction in videos.</p>	<p>The thermocouples used in the for the PFMI ASCENT Ampoule Assembly are defined by drawing 112346 (Item 4.1). The thermocouples used are FN8, FN9, &amp; FN10. All the thermocouples used are from the same series by OMEGA Engineering, the only difference is the length.</p> <p>The product specification document (Item 39.1) can be used to decode the part numbers. The "020" in the PNs codes of a sheath diameter of 0.50mm.</p>



Item	Component	Science Requirement	Verification/Explanation
40.		The ampoule will be designed such that the Cold Zones are located symmetrically on each side of the sample.	<p>Drawing 112346 (Item 4.1) specifies the design of the ampoule. All items were designed to be symmetric to the centerline of the Test Surface, as defined by Requirement 15.</p> <p>The position of the translating Cold Zone was measured for the Flight PFMI during ground tests. Section 5.1, Step 8 of the <i>Ampoule Processing Protocol</i> (Techshot Document G102PC5219; Item 31.1) directs the operator to set the position of the CZ. The encoder position for each ampoule was measured on the Ground and Flight PFMI facilities.</p> <p>The position for the translating Cold Zone for the Ground PFMI facility will be measured prior to future ground tests.</p> <p>This requirement does not have a mathematical tolerance on “symmetric”. Therefore, Techshot proceeded with due diligence to make sure the system was as symmetric as reasonably possible.</p> <hr/> <p>PI acknowledges receipt of data from ground-based tests on Ground and/or Flight ampoules and accepts the demonstrated symmetry of the Cold Zones as sufficient to achieve science objectives.</p> <p>PI Initials: <span style="border: 1px solid green; padding: 2px;">HAB</span></p>
41.	Process Parameters and Controls	Each ampoule shall be processed according to the Power and Cold Zone Temperature Profile as defined in the Test Matrix (Section 4).	The procedure to process ampoules in the PFMI facility is defined by the <i>Ampoule Processing Protocol</i> (Techshot Document G102PC5219; Item 31.1). Under Section 1, Related Documentation, there is a note that states “Refer to the most recent revision of the PFMI – ASCENT ERD (G102DS4291) to verify that this test is conducted in a manner consistent with the Test Matrix (Table 5) in that document.”

Item	Component	Science Requirement	Verification/Explanation
42.		<p>The following parameters should be capable of being adjusted from the ground as the experiment is conducted:</p> <ul style="list-style-type: none"> <li>• Power Input to Heated Section (Heat Flux)</li> <li>• Cold Zone Temperature</li> </ul>	<p>The Cold Zone Temperatures and the Power Input to the Heated Section (Heat Flux) were established as controllable parameters through manipulation of the PFMI system. The PFMI facility is designed to operate with temperature as a controlling parameter. The facility also has adjustable parameters in the control software to regulate (limit) the power that the facility can use when attempting to increase the temperature of an ampoule.</p> <p>Techshot's engineers devised a method to configure the software to limit the power available to the temperature controller and then use an unachievable temperature as the controller setpoint, thus generating a constant power output from the device. The PFMI facility was not designed to be operated in this manner, but ground tests have shown that the method is effective at generating a constant power output from the PFMI temperature controller.</p> <p>Control of heating with the Power Control Method and control of the Cold Zones were both demonstrated via processing of ampoules on the ground as documented by <i>G102PC5219 R- Ampoule Processing Protocol (Test F1, Run 1, -2 Ampoule)</i> - (PFD 2.02). Additional ampoules were processed, and those executed protocols are included with Pre-Flight Deliverables.</p> <p>PI acknowledges receipt of data from ground-based tests on Ground and/or Flight ampoules and accepts the performance of the power control method as sufficient to achieve science objectives.</p> <p>PI Initials: <span style="border: 1px solid green; padding: 2px;">KFB</span></p>




Item	Component	Science Requirement	Verification/Explanation
43.		<p>The maximum Power Input to Heated Section shall be 3.5 W/cm<sup>2</sup>.</p> <p>Ground tests to characterize the relationship between specimen temperature (at TC-5 per Requirement 38) and heater power (by measuring voltage and current) must be completed prior to flight operations.</p>	<p>Characterization of the thermal control of the furnace via the power control method was demonstrated by execution of <i>Test A-2 Test Protocol (Max Temp Characterization)</i> which was defined by Techshot Document G102PC5220 (Item 36.1). The PI has reviewed the executed protocol and acknowledged that the facility and ampoules are capable of meeting the science objectives.</p> <p>This requirement was changed after Revision D of the ERD. This change is to mitigate any dangers with the ground -4 ampoule being converted to a flight -4 ampoule. The ground runs to date have not exceed 2.8 W/cm<sup>2</sup>.</p> <p>PI acknowledges receipt of data from ground-based tests on Ground and/or Flight ampoules and accepts the performance of the power distribution system as sufficient to achieve science objectives.</p> <p>PI Initials: </p>
44.		Both Cold Zones will have the same temperature setpoint during an experiment.	The procedure to process ampoules in the PFMI facility is defined by the Ampoule Processing Protocol (Techshot Document G102PC5219; Item 31.1). Section 5.2, Step 2 of that document directs the test administrator to “Set Cold Zone Temperatures (TCZ) to one of the values identified in the ERD Test Matrix (Table 5 of G102DS4291).”
45.	ISS Control PC	The cameras shall interface with and be controlled by an existing ISS laptop computer.	Techshot is in the process of negotiating Payload Integration Agreement PIA-30059 Revision A for the PFMI ASCENT investigation. That agreement states that the OD will provide a pantry laptop configured for the ASCENT investigation for the duration of the science, approximately 3-months. A draft of that PIA is on-hand at Techshot, but is not included as an attachment because it is a controlled release document.
46.		The computer used for ISS imaging operations shall have sufficient RAM to conduct the experiment.	The computer that is being made available is a HP ZBook 15 G2 (SN: MXL5411W5M). HP support was contacted to determine the build configuration of that specific unit. According to HP Support (via chat; Item 32.2) the device was configured with 8GB of RAM.

Item	Component	Science Requirement	Verification/Explanation
47.	Operations	The computer used for ISS imaging operations shall have a USB3.0 interface available for use by the cameras.	The computer that is being made available is a HP ZBook 15 G2 (SN: MXL5411W5M). According to the laptop specifications (Item 47.1) the device has two USB 3.0 ports and a USB 3.0 Charging Port.
48.		Video feeds from cameras during operations will be downloaded and provided to the PI in a standard video format (*.avi).	Techshot's software engineer performs the conversion manually after the completion of the experiment. This manual conversion has been completed on tests F-1 through F-4. This data has been delivered to the PI team.  The PI has received video data from ground tests, and has approved of the format in which it was delivered.
49.		Techshot's Payload Operations Control Center (POCC) will have a data link to the PFMI facility and provide ground support during crew interactions. Techshot personnel will routinely monitor experiment progress, monitor hardware status, and provide data to researchers. All data is recorded at the Techshot POCC. Data will be downloaded by Techshot (as permitted by bandwidth and communication to the ISS) will be provided to the PI in a timely manner.	The PFMI facility will be monitored at all times while in operation by a Techshot team member.  Data will be downloaded and transferred to the PI in a timely manner.
50.	Operations	The experiment will be controlled by Techshot personnel from their POCC. Control of process parameters can be either automated (controlled via Thermal Profile) or manual (controlled by facility operator in the POCC).	The PFMI facility will be monitored at all times while in operation by a Techshot team member. This oversight will be similar to that which was used to control the facility during ground tests, within the constraints of ISS operations. Similarly to how the ground experiments were conducted, Techshot will have the PI team explicitly give directions to change the power setting at each data point during the flight experiment.
51.		Video conferencing (via Zoom or similar) between the POCC and the PI shall be made available.	This process has been vetted through multiple ground runs with the PI. The process used during those tests will be similar to the process used during flight operations. The PI has indicated that they are very pleased with the process.

Item	Component	Science Requirement	Verification/Explanation
52.	Transport and Stowage	The ampoules will be stowed and transported to and from the ISS under ambient conditions.	The MR Loader excel document is used to submit manifest inputs to NASA. That document (Item 52.1) indicates that the ampoules will be stowed / transported under ambient conditions during all mission phases.
53.		Upon completion of ISS operations, and acceptance of the flight data by the PI, the flight ampoules will be disposed in the trash (not returned to the ground).	Disposition of the ampoules (disposal in trash) has been coordinated with NASA CMC personnel.  PI acknowledges that the Flight ampoules will not be returned to the ground after operations on the ISS.  PI Initials: 
54.	Data Acquisition	Data from the furnace and the sample thermocouples shall be acquired at a minimum rate of 1Hz from start to finish of the experiment.	Data from multiple ground runs has been provided to the PI for analysis. Completed Ampoule Processing Protocols for the Flight ampoules have been delivered to the PI for analysis (for example: <i>Executed G102PC5219 R-Ampoule Processing Protocol (Test F1, Run 1, -2 Ampoule)</i> ; Item PFD 2.02). Data capture frequency has been demonstrated and accepted.
55.		Video data from the PFMI Imaging System COHU camera should be made available to the PI within 7-days of the conclusion of each experiment run.	Data download from the ISS is determined by available bandwidth. Current estimations indicate that there should be little to no difficulty transmitting data to the PI in the specified time.  PI acknowledges that download of data from the ISS is limited by downlink bandwidth, which is controlled by NASA, and understands that Techshot cannot guarantee the timetable for data delivery.  PI Initials: 

Item	Component	Science Requirement	Verification/Explanation
56.		Video data from the PFMI Imaging System high-speed cameras should be made available to the PI within 7-days of the conclusion of each experiment run.	<p>Data download from the ISS is determined by available bandwidth. Current estimations indicate that there should be little to no difficulty transmitting data to the PI in the specified time.</p> <p>PI acknowledges that download of data from the ISS is limited by downlink bandwidth, which is controlled by NASA, and understands that Techshot cannot guarantee the timetable for data delivery.</p> <p>PI Initials: <span style="border: 1px solid green; padding: 2px;">JAB</span></p>
57.		Video recorded at the POCC during operations should be made available to the PI within 14-days of the conclusion of all flight operations.	Current estimations indicate that there should be little to no difficulty transmitting data to the PI in the specified time.
58.	Ground Test	The ground test must be run with the ratcheted surface facing away from the ground and parallel to the ground.	<p>Preliminary tests were completed with the ratcheted surface facing downward (toward the ground). Accumulation of bubbles at the top of the ampoule made it nearly impossible to get quality video data in that configuration. The orientation of the specimens on the ground has been updated to have the ratcheted surface facing up, away from the ground. The PI has witnessed several of these tests live and has reviewed video data from those events. The PI approved changing the requirement to have the specimen facing up.</p> <p>PI acknowledges this change to the requirement during tested as described above.</p> <p>PI Initials: <span style="border: 1px solid green; padding: 2px;">JAB</span></p>

Item	Component	Science Requirement	Verification/Explanation
59.	ISS Operations	<p>All ISS Operations must be observed by the PI (as defined in this document), as input from the PI is critical to science objectives. The PI can either (1) be physically present in the POCC at the Techshot facility in Greenville, IN, or (2) observe the operations via video conference (Teams meeting hosted by Techshot). This includes installation (and swap out) of the ampoules in the PFMI Facility.</p> <p>NOTE: Scheduling of ISS operations will be completed months in advance of when the operations take place. Scheduling of ISS operations is driven by NASA with input from Techshot. Once the ISS operations schedule has been finalized, it will not be changed without extreme extenuating circumstances.</p>	<p>Remote monitoring of the experiment by the PI was practiced during ground runs on the PFMI facility. Similar operations will be used for ISS operations.</p> <p>PI acknowledges that they must be available as described in this requirement during ISS operations. The PI understands that once operations are scheduled, that schedule will not change except for in extreme circumstances as allowed by NASA.</p> <p>PI Initials: </p>
60.		<p>In the event of a LOS event during ISS operations, the experiment will be paused (remain in the configuration immediately prior to the LOS) and will remain in that configuration until AOS.</p>	<p>Anticipated LOS event timing will be available to Techshot personnel once logged onto the Console each day for POCC operations. A designated person will track upcoming LOS events and give the project team member controlling the PFMI facility at least a 10-minute warning prior to each event.</p>

**Pre-Flight Deliverables (ERD Section 5.1)**

The following data must be provided to the PI prior to flight operations.

Item	Description	Units	Data Type	Data Frequency	Verification/Explanation
1.	Pressure inside development ampoule	kPa	Numeric	N/A	The Pressure was characterized by completion of Test D-2.2 & A-5 Test Protocol (PRS Verification) as defined in Techshot Document G102PC5214 (Item 20.1). The data was provided to and accepted by the PI.

Item	Description	Units	Data Type	Data Frequency	Verification/Explanation																														
2.	Results from preflight testing	N/A	Report	Delivered within 14-days of test completion.	<p>Testing of the PFMI facility and ASCENT ampoules was defined by the PFMI – ASCENT Testing Plan, Techshot Document G102DS5199 (Item 21.1). All tests were conducted according to protocols.</p> <p>The following executed protocols a were provided to the PI:</p> <table border="0"> <tr> <td>G102PC5214 R- (PRS Verification)</td> <td>Item 20.1</td> </tr> <tr> <td>G102PC5215 R- (Ampoule Leveling)*</td> <td>Item PFD 2.01</td> </tr> <tr> <td>G102PC5218 R- (Video System)</td> <td>Item 24.1</td> </tr> <tr> <td>G102PC5219 R- (-1 Ampoule, Run 1)</td> <td>Item PFD 2.06</td> </tr> <tr> <td>G102PC5219 R- (-1 Ampoule, Run 2)</td> <td>Item PFD 2.07</td> </tr> <tr> <td>G102PC5219 R- (-2 Ampoule, Run 1)</td> <td>Item PFD 2.02</td> </tr> <tr> <td>G102PC5219 R- (-2 Ampoule, Run 2)</td> <td>Item PFD 2.03</td> </tr> <tr> <td>G102PC5219 R- (-3 Ampoule, Run 1)</td> <td>Item PFD 2.04</td> </tr> <tr> <td>G102PC5219 R- (-3 Ampoule, Run 2)</td> <td>Item PFD 2.05</td> </tr> <tr> <td>G102PC5219 R- (-4 Ampoule, Run 1)</td> <td>Item PFD 2.08</td> </tr> <tr> <td>G102PC5219 R- (-4 Ampoule, Run 2)</td> <td>Item PFD 2.09</td> </tr> <tr> <td>G102PC5220 R- (Max Temp Charact.)</td> <td>Item 36.1</td> </tr> <tr> <td>G102PC5221 R- (Thermal Epoxy Insp.)</td> <td>Item PFD 2.10</td> </tr> <tr> <td>(Inspection Video Files)</td> <td>Item PFD 2.11</td> </tr> <tr> <td>G102PC5222 R- (Degassing FC-72)</td> <td>Item PFD 2.12</td> </tr> </table> <p>No other additional testing is required.</p> <p>*A copy of the ampoule leveling protocol was not filled out for each run. The process was executed under direction of the PI prior to each run.</p> <p>PI acknowledges that they accepted that the ampoules were level prior to starting all ground tests.</p> <p>PI Initials: </p>	G102PC5214 R- (PRS Verification)	Item 20.1	G102PC5215 R- (Ampoule Leveling)*	Item PFD 2.01	G102PC5218 R- (Video System)	Item 24.1	G102PC5219 R- (-1 Ampoule, Run 1)	Item PFD 2.06	G102PC5219 R- (-1 Ampoule, Run 2)	Item PFD 2.07	G102PC5219 R- (-2 Ampoule, Run 1)	Item PFD 2.02	G102PC5219 R- (-2 Ampoule, Run 2)	Item PFD 2.03	G102PC5219 R- (-3 Ampoule, Run 1)	Item PFD 2.04	G102PC5219 R- (-3 Ampoule, Run 2)	Item PFD 2.05	G102PC5219 R- (-4 Ampoule, Run 1)	Item PFD 2.08	G102PC5219 R- (-4 Ampoule, Run 2)	Item PFD 2.09	G102PC5220 R- (Max Temp Charact.)	Item 36.1	G102PC5221 R- (Thermal Epoxy Insp.)	Item PFD 2.10	(Inspection Video Files)	Item PFD 2.11	G102PC5222 R- (Degassing FC-72)	Item PFD 2.12
G102PC5214 R- (PRS Verification)	Item 20.1																																		
G102PC5215 R- (Ampoule Leveling)*	Item PFD 2.01																																		
G102PC5218 R- (Video System)	Item 24.1																																		
G102PC5219 R- (-1 Ampoule, Run 1)	Item PFD 2.06																																		
G102PC5219 R- (-1 Ampoule, Run 2)	Item PFD 2.07																																		
G102PC5219 R- (-2 Ampoule, Run 1)	Item PFD 2.02																																		
G102PC5219 R- (-2 Ampoule, Run 2)	Item PFD 2.03																																		
G102PC5219 R- (-3 Ampoule, Run 1)	Item PFD 2.04																																		
G102PC5219 R- (-3 Ampoule, Run 2)	Item PFD 2.05																																		
G102PC5219 R- (-4 Ampoule, Run 1)	Item PFD 2.08																																		
G102PC5219 R- (-4 Ampoule, Run 2)	Item PFD 2.09																																		
G102PC5220 R- (Max Temp Charact.)	Item 36.1																																		
G102PC5221 R- (Thermal Epoxy Insp.)	Item PFD 2.10																																		
(Inspection Video Files)	Item PFD 2.11																																		
G102PC5222 R- (Degassing FC-72)	Item PFD 2.12																																		

Item	Description	Units	Data Type	Data Frequency	Verification/Explanation
3.	Calibration curve for Heater Power vs Specimen Temperature	Power vs. Temperature	Numeric	One per ampoule (eight total)	<p>G102PC5216 R- (Flight PFMI Char.) -1 FLT    Item PFD 3.01            G102PC5216 R- (Flight PFMI Char.) -2 FLT    Item PFD 3.02            G102PC5216 R- (Flight PFMI Char.) -3 FLT    Item PFD 3.03            G102PC5216 R- (Flight PFMI Char.) -4 FLT    Item PFD 3.04</p> <p>Testing of the Ground ampoules will occur after nominal turnover. The executed protocols for those tests will be submitted to the PI once completed. It is anticipated that those tests will happen before the flight ampoules are processed on the ISS, but it is not guaranteed or required to meet science objectives.</p>
4.	Characterization test data for each thermocouple based on calibrated thermocouple	C	Numeric	One per Thermocouple at 5 temperatures between 40C and 90C including 40C and 90C.	<p>The thermocouples are characterized as part of the assembly process. That data is recorded in the assembly documentation (Items 4.2, 4.3, 4.4, and 4.5).</p> <p>A summary of the thermocouple characterization is provided in the presentation <i>PFMI – ASCENT Flight TC Calibration Overview</i> (PFD 4.01).</p> <p>The complete data for the Thermocouple Characterization is included in the excel document <i>PFMI- ASCENT - Flight TC Characterization Data</i> (PFD 4.02), which was sent to the PI in a Zip file.</p>



Table 2: Success Criteria for the ISS Experiment

Criteria	ACCEPTABLE		MINIMUM	UNACCEPTABLE	
	Excellent	Good	Minimum	Poor	Failure
<b>Science Success Criteria</b>	1. Consistent vapor nucleation from most of the cavities. (≥90%) <sup>1</sup>	1. Consistent vapor nucleation from many of the cavities. (≥50%) <sup>1</sup>	1. Consistent vapor nucleation from some of the cavities. (≥25%) <sup>1</sup>	1. Inconsistent vapor nucleation or nucleation from few of the cavities. (<25%) <sup>1</sup>	1. No clear vapor nucleation from any of the cavities. <sup>1</sup>
<b>Per Run</b>	1. Able to visibly identify bubbles in all cameras.  2. Able to capture 1-2 second video from all cameras.  3. Able to determine direction of travel of moving bubbles and track that movement (or lack of movement) from all cameras.	1. Able to visibly identify bubbles in HS <sub>NARROW</sub> camera & the COHU camera.  2. Able to capture 1-2 second video from HS <sub>NARROW</sub> camera & the COHU camera.  3. Able to determine direction of travel of moving bubbles and track that movement (or lack of movement) from the HS <sub>NARROW</sub> camera & the COHU camera.	1. Able to clearly identify bubbles from either HS camera.  2. Able to capture 1-2 second video from either HS camera.  3. Able to determine direction of travel of moving bubbles and track that movement (or lack of movement) from either HS camera.	1. Unable to clearly identify bubbles in neither HS camera.  2. Unable to capture videos from both HS <sub>NARROW</sub> and COHU cameras.  3. Unable to determine that bubbles are moving, but cannot track the movement.	1. Camera system is not operational.  2. Unable to capture videos.  3. Unable to determine if bubbles are moving.
<b>Overall Success</b>	1. Excellent or Good rating for ALL runs on ALL Ampoules.	1. Excellent or Good rating for ≥80% of Runs on ALL Ampoules.  2. Minimum rating (or better) for 100% of Runs on ALL Ampoules.	1. Minimum rating (or better) for ≥80% of Runs for: -1 Ampoule (Flat), -3 Ampoule (Slot),  AND  -2 Ampoule (1mm) or -4 Ampoule (2mm).	1. Minimum rating (or better) for <80% of Runs for -1, -3, & -2 / -4 Ampoules.	1. Poor or Failure rating for >70% of ALL Runs.
<sup>1</sup> As evaluated at maximum Heat Flux setpoint.			HS <sub>NARROW</sub> = Narrow Field of View High-Speed Camera HS <sub>WIDE</sub> = Wide Field of View High-Speed Camera		

The PI acknowledges that data from ground tests on Flight and/or Ground ampoules has been delivered to their team. The PI has evaluated (or has had the opportunity to evaluate) that data against the Success Criteria as shown in Table 2. The PI accepts that Techshot / Redwire has faithfully executed reasonable due diligence in preparing the hardware for operations on the ISS. The PI has stated that there are unknown factors governing the physics of their investigation that could prevent some of the Success Criteria (bubbles forming at the engineered nucleation sites, for example) from being met once the system is operated in microgravity on the ISS, and such failures could be no fault of the engineering, manufacture, assembly, or operation of the hardware. The PI acknowledges that the ground tests are sufficient to meet the minimum success criteria in Table 2.

PI Initials: 

The PI acknowledges that bubbles that were found in the -1, -2 and -3 flight ampoules as disclosed on July 18, 2022 by Rachel Ormsby via email. The bubbles formed months after the ampoules were assembled. The ampoules were leak tested according to protocol during assembly, and no leaks were found. The process fluid (FC-72) was degassed multiple times during the assembly process according to approved protocols. The PI team has provided Techshot with information on prior experience with degassing.

PI Initials: 

The PI acknowledges that the cause of the bubbles has not been positively identified. Potential sources of the bubble may be (1) dissolved gas in the FC-72 that might not be extracted through the approved degassing protocols, (2) a chemical interaction between the FC-72 and the Ratcheted Surface, the Artic Silver that is used to bind the test surface to the ampoule, the Epoxy that is used to fill gaps on the sides of the test surface, or a combination of these (and other) sources, or (3) a pinhole leak in the system at the expansion bladder or where items are bonded together. These sources are not meant to represent a complete list of all potential causes of the bubbles, but merely those that have been thus far identified and discussed. The PI has indicated that they believe the most probable cause is a leak in the system. Techshot does not believe that there is a leak in the system and is confident in the engineering, manufacture, assembly, and operation of the ampoules. The devices have been leak tested at multiple stages of assembly and operation, and no evidence of leaking has ever been identified. Since the cause of the bubbles has not been positively identified, there is significant risk in launching the ampoule under nominal load conditions, and the PI accepts this risk and will not ask for a reflight.

PI Initials: 

The PI acknowledges the corrective action, approved by NASA, CASIS, and the PI, in response to the bubbles that were found in the -1, -2 and -3 flight ampoules. The fluid will be drained and the ampoules refilled as close to launch as possible. The degassing duration will be increased from 5 minutes to 10 minutes for each instance at which it is executed. Given that the cause of the bubbles has not been identified, there is no guarantee that the corrective actions will ensure the success of the experiment on the ISS, and the PI accepts this risk and will not ask for a reflight.

PI Initials: 



## PFMI – ASCENT: Flight Ampoule Processing Report

Techshot Document: G102TD5460

Revision: -

Release Date: 02/01/2023

Engineer / Tech: Tony Hammond

Printed Name

*Tony Hammond*

Signature

QA / Observer: Jeff Canary

Printed Name

*Jeff Canary*

Signature

Date: 12/12/2022

Execution Note:	<b>F2-SP2</b>
-----------------	---------------

## Approval



02 FEB 2023

Prepared By: **Chris Scherzer**  
 Title: **PFMI Deputy Program Manager**

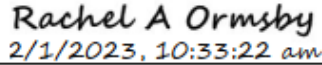
Date:



02 FEB 2023

Approved By: **Tony Hammond**  
 Title: **Software Engineer**

Date:



2/1/2023, 10:33:22 am

Approved By: **Rachel Ormsby**  
 Title: **PFMI Program Manager**

Date:

## i. Revision History

REVISION NUMBER	DATE	PAGES AFFECTED	INSTRUCTIONS/REMARKS
-	02/01/2023	All	Baseline Release

## TABLE OF CONTENTS

<b>1.0 REPORT SUMMARY</b> .....	<b>3</b>
<b>2.0 OVERVIEW OF PROCESSING DAY</b> .....	<b>4</b>
<b>3.0 DATA GUIDE</b> .....	<b>5</b>
<b>4.0 ANNOTATED GRAPH</b> .....	<b>6</b>
<b>5.0 SUMMARY OF RUNS</b> .....	<b>7</b>
HS/COHU VIDEO SETS .....	7
VIDEO-GROUND SETS .....	7
<b>6.0 CONTROL ADJUSTMENTS LOGS</b> .....	<b>8</b>
<b>7.0 POWER SETTINGS SPREADSHEET</b> .....	<b>10</b>
<b>8.0 DATA / OBSERVATION / CONCLUSIONS</b> .....	<b>13</b>
<b>9.0 TERMS</b> .....	<b>14</b>

## 1.0 REPORT SUMMARY

### PURPOSE

The purpose of this report is to document the processing of a PFMI – ASCENT Ampoule in the PFMI facility on the ISS. This document can be used in lieu of completion of Techshot document G102PC5219 R- (PFMI - ASCENT - Ampoule Processing Protocol). That protocol was intended to provide a repeatable process by which each ASCENT ampoule could be processed. However, system did not behave as anticipated, and new methods were implemented in order to obtain useful science from the ampoules that were on the ISS. The procedures used to process the ampoules were completed under direct supervision of the ASCENT PI team. Each instance of this report will document the flight activities and processing of an ampoule through one complete session (day).

### INTRODUCTION

Per the project's ERD, each flight ampoule (1-4) was to be processed at 5 different cold zone setpoints over 5 days. However, on-orbit behavior of the fluid in these ampoules made it not possible to simply repeat the ground processing plan at different setpoints. Vapor generated from the heated sample surface during ground tests circulated to the cooled ends where it was condensed to some degree. In  $\mu$ -gravity, vapor generated from the heated surface tended to remain above the surface and collect into large slugs, eventually filling the part of the ampoule containing the sample surface.

The science team had to modify their testing plans to the point where the original test protocol could not very well represent what was done on a given day. Information that follows captures the various actions taken during this day's sample processing. The bulk of it comes from documents previously generated for and supplied to the science team.

Techshot had a data collection plan in place that used the notation "F4-SP2" to represent Flight ampoule 4 at cold zone setpoint 2; that convention was kept intact, but the "SP2" part now indicates which day of processing instead of which cold zone setpoint.


### VARIATIONS FROM THE ERD and Test Plan

The order that the ampoules were processed varied between the ERD (RE, released 06/17/2022) and the Test Plan (RC, released 06/28/2022). The designations in the Test Plan were created after the ERD, so it was expected that would be the processing order, However, immediately prior to flight operations the order was changed. To remove any ambiguity, those differences are clarified below.

Test Designation	Ampoule		
	ERD	Test Plan	Flight
F1	-1	-2	-1
F2	-2	-3	-2
F3	-3	-1	-3
F4	-4	-4	-4

The meaning of the term “RUN” was defined consistently in the ERD and Test Plan. However, since the Flight experiments were not able to be executed strictly to the plan outlined in the protocol, the term “RUN” took on a slightly different meaning. Regarding the processing of the Flight ampoules the term “RUN” refers to the small set of control adjustments made before having to stop and wait for the generated vapor to condense; This includes short applications of a known amount of heat flux (power control), sequences of temperature setpoints (temperature control), or other combinations of heating-related actions.

## 2.0 OVERVIEW OF PROCESSING DAY

DATE:	12/12/2022
Processing Day:	2 of 6
Ampoule Designation:	F2
Ampoule PN:	112428-2
Session Designation:	F2-SP2
Cold Zone SP (°C):	20°C
Number of Runs completed:	8
Root folder for Data Collected:	
Processing Notes:	<p>The PI team had us run a series of power-on to some level, then off (or to a lower level) once nucleations were observed. From that point, high speed video sets were requested of available nucleation sites, and then some number of the generated vapor slug as the system cooled down. Powers attempted were 11%, 14.5%, 17%, 20%, 20% again, then 23%-to-14.5% once bubbles began to form.</p> <p>As for COHU video requests for each of those trials, they would like to have the duration of each transition to bubbling until the remaining center bubble disappeared - there were 1 or 2 where that disappearance was interrupted or deemed taking too long by the PI team to bother with the entire COHU period.</p>

### 3.0 DATA GUIDE

The spreadsheet in this folder **Control-Adjustment-and-Video-Capture-log.xlsx** contains a log of control adjustments and video sets collected at various points of processing.

For each high-speed set of videos referenced in the spreadsheet mentioned above, named “001”, “002”, etc.,

- The raw TIFF format files (both narrow and wide views) can be found in in the folder:

**.\\Video-HS-Raw\\**

- A version converted for quick viewing can be found in in the folder:

**.\\Video-HS-Converted\\**

- Video from PFMI’s camera that covers that time can be found in in the folder:

**.\\Video-COHU\\**

Any video recorded from PFMI’s COHU camera that were not associated with a set of high-speed videos can be found in the folder:

**.\\Video-Ground\\**

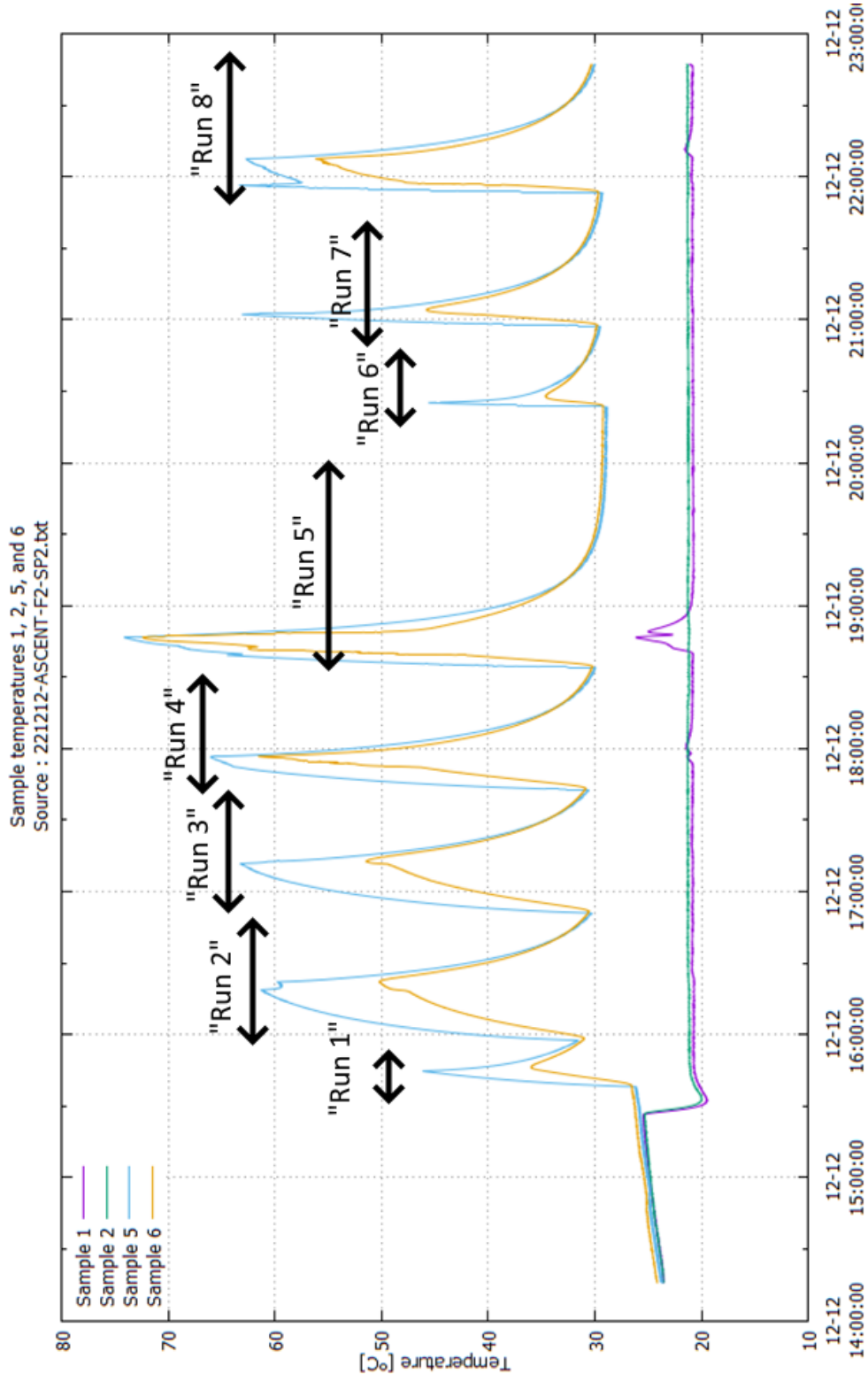
Those would include segments requested in real time by the PI team, or any that were planned to be recorded such as times when a crew member is handling an ampoule, or any anomalies observed during run time.

Log files with temperature and other PFMI data can be found in the folder:

**.\\LogData\\**

### 4.0 ANNOTATED GRAPH

The annotated graph below is provided to help locate which videos are associated with each portion of processing.





## 5.0 SUMMARY OF RUNS

The following test procedure is valid for processing a PFMI – ASCENT Ampoule in the PFMI facility.

RUN	HS/COHU VIDEO SETS	VIDEO-GROUND SETS
1.	None	None
2.	001, 002	1615-1650-cooldown-cohu
3.	003,004	1710-1742-cooldown-cohu
4.	005	1752-1833-cooldown-cohu
5.	006 through 016	1835-1942-cooldown-cohu
6.	017, 018	None
7.	019, 020	2102-2152-cooldown-cohu
8.	021 through 026	2151-2245-cooldown-cohu
9.		
10.		

## 6.0 CONTROL ADJUSTMENTS LOGS

File Location:	
----------------	--

The spreadsheet below shows the control adjustments made during processing as well as the time each set of high-speed videos was captured. This is how the information has been conveyed to the PI team since the early days of ground testing. Column headers in the spreadsheet represent the following :

### Temperature setpoints [°C] :

- Zone 1 - main heater controller setpoint.
- Zone 3 - translating cold zone setpoint.
- Zone 4 - stationary cold zone setpoint.
- Zone 2 - over-temperature watchdog controller for the main heater system.

### Max Output [%] :

The maximum allowed output of the main heater controller.

### Desired Flux [W/cm<sup>2</sup>] :

This is the heat flux corresponding to the Max Output setting when operating in power-control mode.

### Zone Setpoints:

Zone	Set Point (°C)
1	80
2	75
3	20
4	20

### Data Notes:

NOTE #1:	[NONE]
NOTE #2:	[NONE]
NOTE #3:	[NONE]
NOTE #4:	[NONE]

Content of the log is shown in the image below:

Computer Timestamp when command was issued	Temperature setpoints [°C]			Max Output [%]	Estimated Heat Flux [W/cm <sup>2</sup> ]	HS Camera File set	Laptop time of video capture
	Zone 1	Zone 3	Zone 4				
<u>FLT04 -- run 1</u>							
00:00:00	cycle 1						00:00:00
	80	20	20	0	0		
15:38:05				11	0.142		
15:44:39				0	0		
15:57:35				11	0.142		
						<b>001</b>	16:19:15
						<b>002</b>	16:30:05
16:22:05				0	0		
16:51:02				14.5	0.152		
						<b>003</b>	17:10:10
17:12:35				0	0		
						<b>004</b>	17:34:50
17:42:43				17	0.209		
						<b>005</b>	17:52:08
17:56:42				0	0		
18:34:01				20	0.289		
						<b>006</b>	18:36:30
						<b>007</b>	18:40:45
						<b>008</b>	18:41:55
						<b>009</b>	18:45:15
18:46:50				0	0		
						<b>010</b>	18:48:15
						<b>011</b>	18:49:25
						<b>012</b>	18:51:01
						<b>013</b>	18:52:58
						<b>014</b>	19:59:58
						<b>015</b>	20:01:34
						<b>016</b>	20:02:20
20:23:28				20	0.289		
20:25:10				0	0		
						<b>017</b>	20:31:25
						<b>018</b>	20:33:00
20:57:20				20	0.289		
21:02:29				0	0	<b>019</b>	21:02:15
						<b>020</b>	21:03:45
21:53:13				23	0.383		
21:56:47				14.5	0.152	<b>021</b>	21:56:30
						<b>022</b>	21:57:50
						<b>023</b>	22:01:05
22:07:28				0	0		
						<b>024</b>	22:08:06
						<b>025</b>	22:09:20
						<b>026</b>	22:12:45

## 7.0 POWER SETTINGS SPREADSHEET

The document “**G102RF5227 - ASCENT Ampoule Power Tables.xlsx**” was re-worked to include an expanded range of power settings than it initially had for each ampoule.

Ampoule Parameters		Desired Flux (W/cm <sup>2</sup> )	Power Required (W)	Tube Resistance (Ω)	Voltage (V)	Current(I)	Percentage
Width (cm)	0.8	0.01	0.066	39.3	1.61	0.04	3.7%
Length (cm)	8.29	0.02	0.133	39.3	2.28	0.06	5.3%
Area (cm <sup>2</sup> )	6.632	0.03	0.199	39.3	2.80	0.07	6.4%
Resistance	39.3	0.04	0.265	39.3	3.23	0.08	7.4%
		0.05	0.332	39.3	3.61	0.09	8.3%
Furnace		0.06	0.398	39.3	3.95	0.10	9.1%
Max Voltage	43.43	0.07	0.464	39.3	4.27	0.11	9.8%
		0.08	0.531	39.3	4.57	0.12	10.5%
		0.09	0.597	39.3	4.84	0.12	11.2%
		0.10	0.663	39.3	5.11	0.13	11.8%
		0.11	0.730	39.3	5.35	0.14	12.3%
		0.12	0.796	39.3	5.59	0.14	12.9%
		0.13	0.862	39.3	5.82	0.15	13.4%
		0.14	0.928	39.3	6.04	0.15	13.9%
		0.15	0.995	39.3	6.25	0.16	14.4%
		0.16	1.061	39.3	6.46	0.16	14.9%
		0.17	1.127	39.3	6.66	0.17	15.3%
		0.18	1.194	39.3	6.85	0.17	15.8%
		0.19	1.260	39.3	7.04	0.18	16.2%
		0.20	1.326	39.3	7.22	0.18	16.6%
		0.22	1.459	39.3	7.57	0.19	17.4%
		0.24	1.592	39.3	7.91	0.20	18.2%
		0.26	1.724	39.3	8.23	0.21	19.0%
		0.28	1.857	39.3	8.54	0.22	19.7%
		0.30	1.990	39.3	8.84	0.23	20.4%
		0.32	2.122	39.3	9.13	0.23	21.0%
		0.34	2.255	39.3	9.41	0.24	21.7%
		0.36	2.388	39.3	9.69	0.25	22.3%
		0.38	2.520	39.3	9.95	0.25	22.9%
		0.40	2.653	39.3	10.21	0.26	23.5%
		0.42	2.785	39.3	10.46	0.27	24.1%
		0.44	2.918	39.3	10.71	0.27	24.7%
		0.46	3.051	39.3	10.95	0.28	25.2%
		0.48	3.183	39.3	11.19	0.28	25.8%
		0.50	3.316	39.3	11.42	0.29	26.3%
		0.52	3.449	39.3	11.64	0.30	26.8%
		0.54	3.581	39.3	11.86	0.30	27.3%
		0.56	3.714	39.3	12.08	0.31	27.8%
		0.58	3.847	39.3	12.30	0.31	28.3%
		0.60	3.979	39.3	12.51	0.32	28.8%
		0.62	4.112	39.3	12.71	0.32	29.3%

<u>Pct Command</u>	<u>Approx. Resulting Flux</u>		
14	0.142	19.1	0.264
14.5	0.152	19.2	0.267
14.6	0.154	19.3	0.270
14.7	0.156	19.4	0.272
14.8	0.159	19.5	0.275
14.9	0.161	19.6	0.278
15	0.163	19.7	0.281
15.1	0.165	19.8	0.284
15.2	0.167	19.9	0.287
15.3	0.169	20	0.289
15.4	0.172	20.1	0.292
15.5	0.174	20.2	0.295
15.6	0.176	20.3	0.298
15.7	0.178	20.4	0.301
15.8	0.181	20.5	0.304
15.9	0.183	20.6	0.307
16	0.185	20.7	0.310
16.1	0.188	20.8	0.313
16.2	0.190	20.9	0.316
16.3	0.192	21	0.319
16.4	0.195	21.1	0.322
16.5	0.197	21.2	0.325
16.6	0.199	21.3	0.328
16.7	0.202	21.4	0.331
16.8	0.204	21.5	0.335
16.9	0.207	21.6	0.338
17	0.209	21.7	0.341
17.1	0.212	21.8	0.344
17.2	0.214	21.9	0.347
17.3	0.217	22	0.350
17.4	0.219	22.1	0.353
17.5	0.222	22.2	0.357
17.6	0.224	22.3	0.360
17.7	0.227	22.4	0.363
17.8	0.229	22.5	0.366
17.9	0.232	22.6	0.370
18	0.234	22.7	0.373
18.1	0.237	22.8	0.376
18.2	0.240	22.9	0.380
18.3	0.242	23	0.383
18.4	0.245	23.1	0.386
18.5	0.248	23.2	0.390
18.6	0.250	23.3	0.393
18.7	0.253	23.4	0.396
18.8	0.256		
18.9	0.259		
19	0.261		

23.5	0.400	27.6	0.551
23.6	0.403	27.7	0.555
23.7	0.406	27.8	0.559
23.8	0.410	27.9	0.563
23.9	0.413	28	0.567
24	0.417	28.1	0.571
24.1	0.420	28.2	0.575
24.2	0.424	28.3	0.580
24.3	0.427	28.4	0.584
24.4	0.431	28.5	0.588
24.5	0.434	28.6	0.592
24.6	0.438	28.7	0.596
24.7	0.442	28.8	0.600
24.8	0.445	28.9	0.604
24.9	0.449	29	0.609
25	0.452	29.1	0.613
25.1	0.456	29.2	0.617
25.2	0.460	29.3	0.621
25.3	0.463	29.4	0.626
25.4	0.467	29.5	0.630
25.5	0.471	29.6	0.634
25.6	0.474	29.7	0.638
25.7	0.478	29.8	0.643
25.8	0.482	29.9	0.647
25.9	0.485	30	0.651
26	0.489	30.1	0.656
26.1	0.493	30.2	0.660
26.2	0.497	30.3	0.664
26.3	0.501	30.4	0.669
26.4	0.504	30.5	0.673
26.5	0.508	30.6	0.678
26.6	0.512	30.7	0.682
26.7	0.516	30.8	0.687
26.8	0.520	30.9	0.691
26.9	0.524	31	0.695
27	0.528	31.1	0.700
27.1	0.531	31.2	0.704
27.2	0.535	31.3	0.709
27.3	0.539	31.4	0.714
27.4	0.543	31.5	0.718
27.5	0.547	31.6	0.723



## 9.0 TERMS

The following table defines several terms used in the PFMI – ASCENT experiment. This table is comparable to Table 1 in the PFMI – ASCENT ERD (G102DS4291).

Term	Definition
$q''_{MIN}$	The lowest Heat Flux at which a video might be captured
$q''_{MAX}$	The highest Heat Flux at which a video might be captured
$T_{MIN}$	The lowest temperature at which a video might be captured
$T_{MAX}$	The highest temperature at which a video might be captured
$T_s$	The temperature of the Test Surface (ratcheted surface) as measured by TC-5
$T_{FLUID}$	The temperature of the Process Fluid (FC-72) as measured by TC-6
$T_{CZ-1}$	The temperature in of the Process Fluid in Cold Zone 1 as measured by TC-1
$T_{CZ-2}$	The temperature in of the Process Fluid in Cold Zone 2 as measured by TC-2
$T_{CZ}$	The temperature setpoint for the Cold Zones
Pre-Heat	Increasing the surface temperature ( $T_s$ ) from ambient to $T_{MIN}$ by increasing the Heat Flux ( $q''$ ) from null to $q''_{MIN}$ .
Ramp-Up	Increasing the surface temperature ( $T_s$ ) from $T_{MIN}$ to $T_{MAX}$ by increasing the Heat Flux ( $q''$ ) from $q''_{MIN}$ to $q''_{MAX}$ .
Ramp-Down	Subsequent decreasing of temperature ( $T_s$ ) from $T_{MAX}$ to $T_{MIN}$ by decreasing the Heat Flux ( $q''$ ) from $q''_{MAX}$ to $q''_{MIN}$ (or to null).
Cycle	A single Ramp-Up followed by a Ramp-Down
Run (ground)	Two Cycles conducted in immediate succession
Run (flight)	Combinations of heat flux or temperature commands issued between periods of waiting for vapor to condense.
Test	All consecutive Runs at the same $T_{CZ}$
Ampoule Test Group	Five Tests on the same Ampoule at different Cold Zone temperature setpoints
Experiment	Four Ampoule Test Groups, one for each Ampoule Type
Ampoule Type	One of four Ampoules that are distinguished by the geometry of the Test Surface (ratcheted surface)



# PFMI – ASCENT

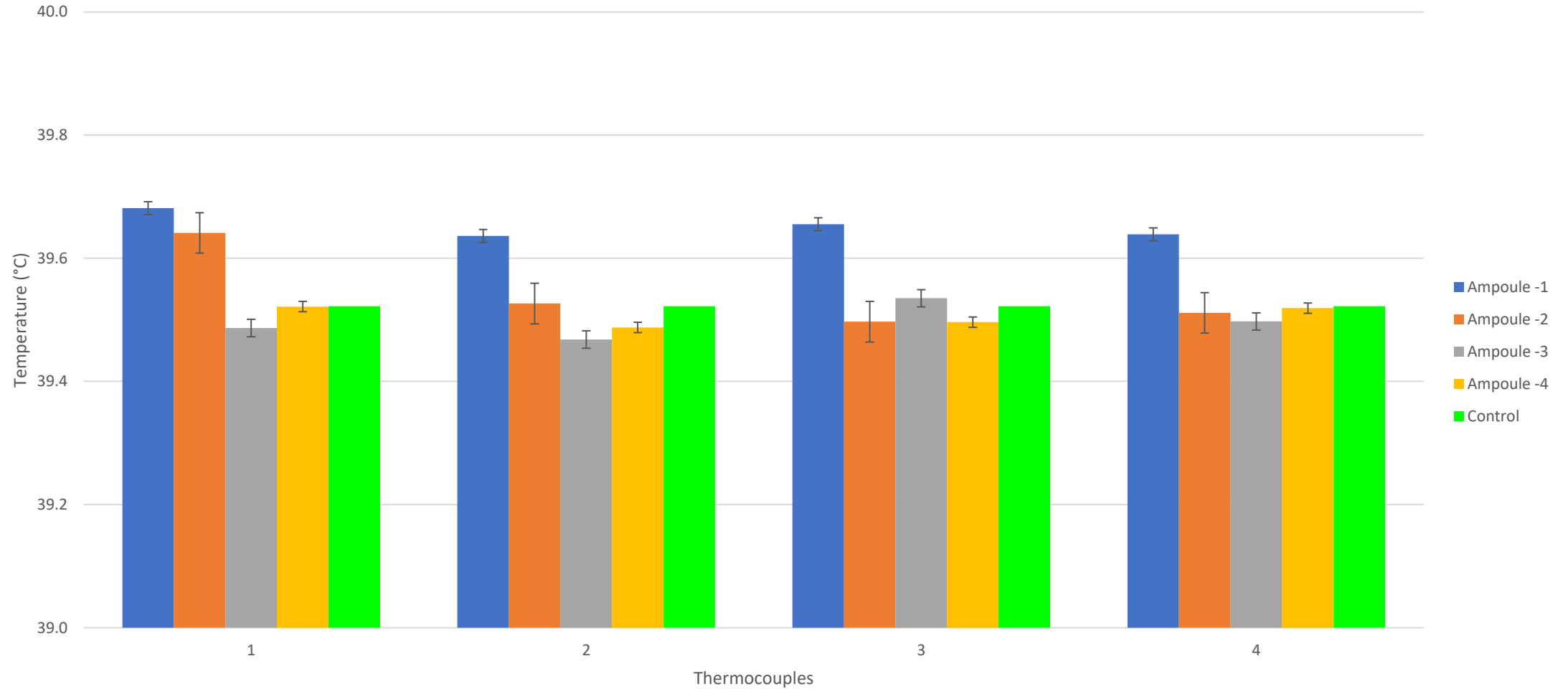
FLIGHT THERMOCOUPLE CALIBRATION DATA

# OVERVIEW

- THERMOCOUPLE MEASUREMENTS WERE VERIFIED AT 5 DIFFERENT TEMPERATURES
  - 40°C, 55°C, 65°C, 75°C, & 90°C
- TC MEASUREMENTS WERE VERIFIED AGAINST AN INDEPENDENT MEASUREMENT DEVICE (DIGI-SENSE) AS A CONTROL
- DATA WAS COLLECTED FOR APPROXIMATELY 10SECONDS AT EACH TEMPERATURE
  - AFTER TEMPERATURE STABILIZED
- THERMOCOUPLE NUMBERING FOR THIS TEST DOES NOT NECESSARILY CORRELATE TO THE EXACT SAME NUMBER FOR THE FLIGHT AMPOULE, BUT THE AMPOULE NUMBERS ARE CORRECT
  - EXAMPLE: TC 3.3 IN THIS TEST WAS USED IN AMPOULE 3, BUT MIGHT NOT BE TC-3 ACCORDING TO THE ERD
- ALL TCS MEASURED WITHIN  $\pm 0.2^{\circ}\text{C}$  OF THE CONTROL MEASUREMENT

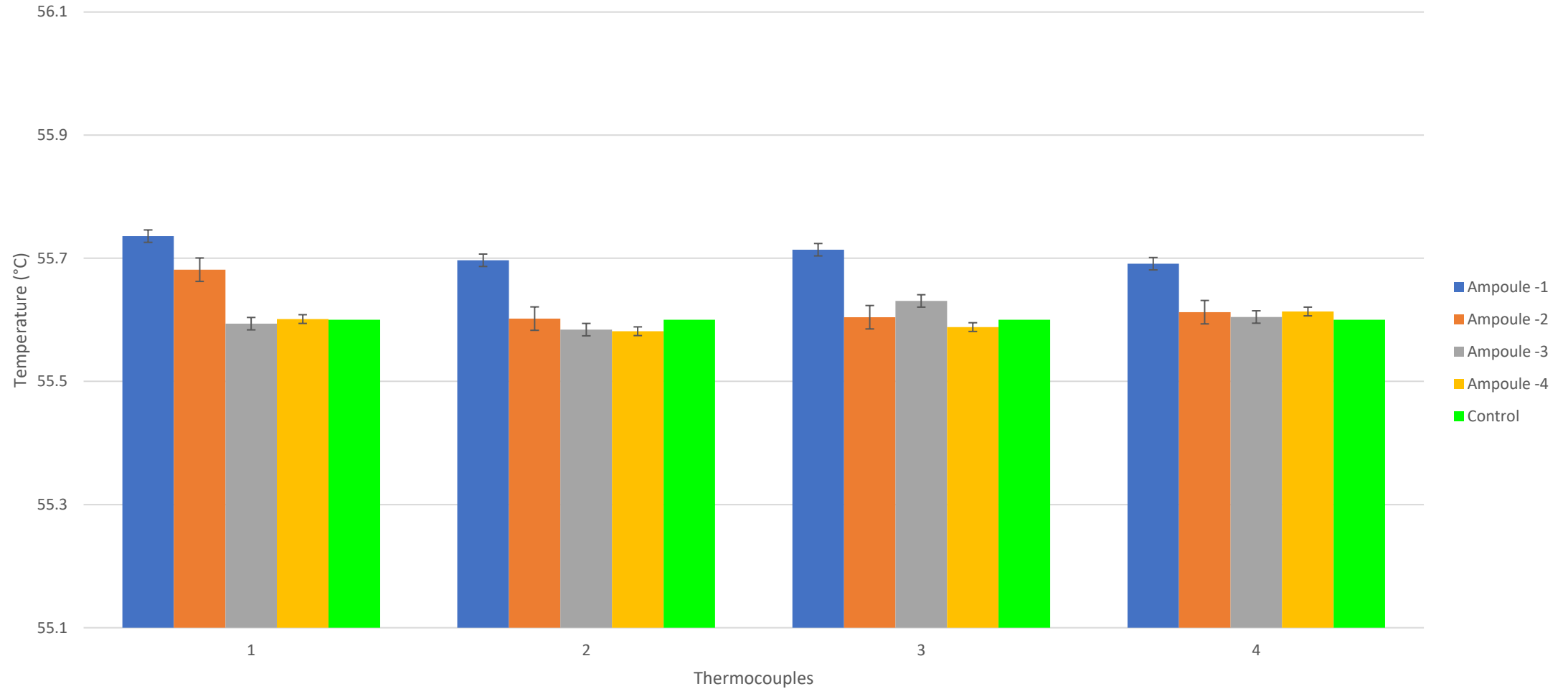
# FLIGHT AMPOULES - 40°C (39.5°C)

Thermocouple Characterization (40°C)



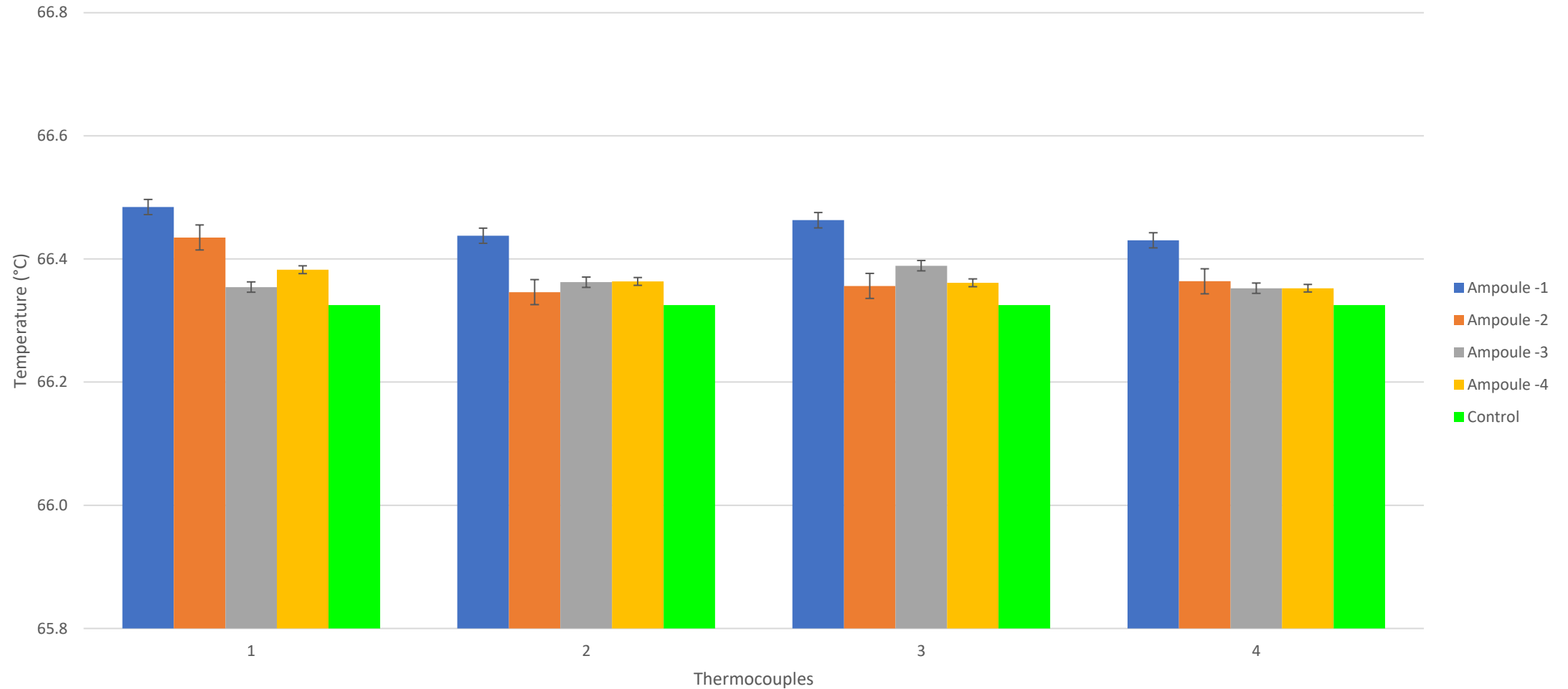
# FLIGHT AMPOULES - 55°C (55.6°C)

Thermocouple Characterization (55°C)



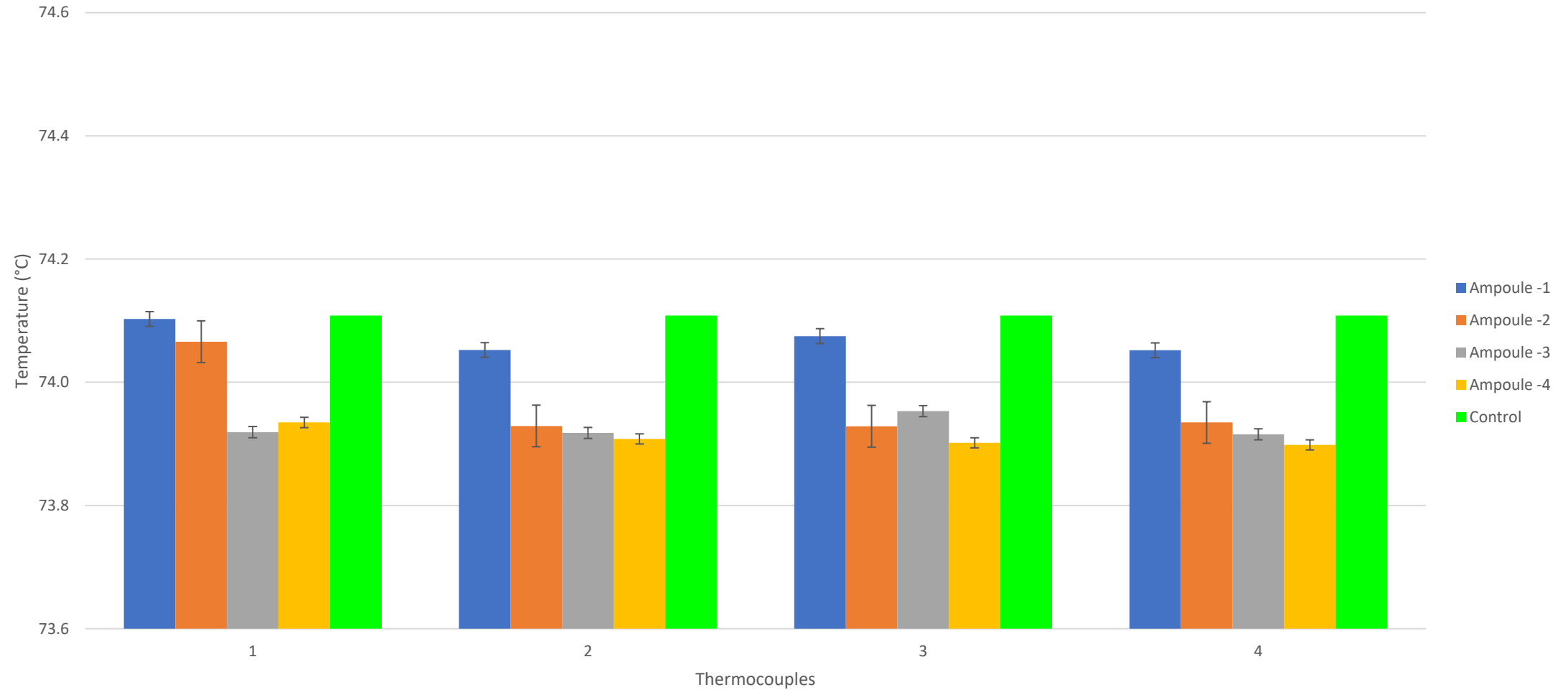
# FLIGHT AMPOULES - 65°C (66.3°C)

Thermocouple Characterization (65°C)



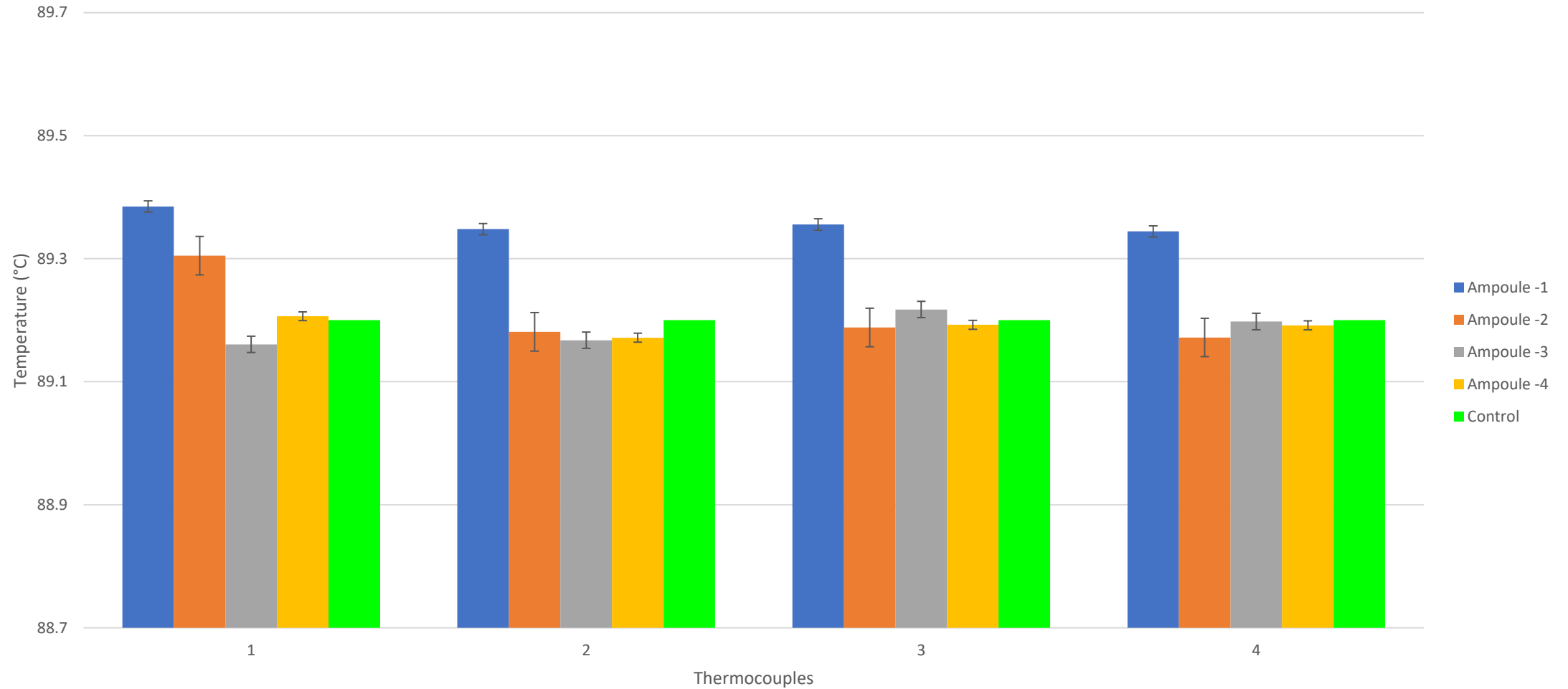
# FLIGHT AMPOULES - 75°C (74.1°C)

Thermocouple Characterization (75°C)



# FLIGHT AMPOULES - 90°C (89.2°C)

Thermocouple Characterization (90°C)



# FLIGHT AMPOULES – AVERAGE DATA



<b>40°C</b>																			
TC Number	1.1	1.2	1.3	1.4	2.1	2.2	2.3	2.4	3.1	3.2	3.3	3.4	4.1	4.2	4.3	4.4	All TCs	DigiSense (Control)	
Average	39.7	39.6	39.7	39.6	39.6	39.5	39.5	39.5	39.5	39.5	39.5	39.5	39.5	39.5	39.5	39.5	39.5	39.5	39.5
SD	0.0148	0.0190	0.0112	0.0166	0.0176	0.0134	0.0124	0.0251	0.0041	0.0109	0.0127	0.0259	0.0098	0.0147	0.0166	0.0111	0.0726	0.0441	

<b>55°C</b>																			
TC Number	1.1	1.2	1.3	1.4	2.1	2.2	2.3	2.4	3.1	3.2	3.3	3.4	4.1	4.2	4.3	4.4	All TCs	DigiSense (Control)	
Average	55.7	55.7	55.7	55.7	55.7	55.6	55.6	55.6	55.6	55.6	55.6	55.6	55.6	55.6	55.6	55.6	55.6	55.6	55.6
SD	0.0118	0.0054	0.0165	0.0195	0.0177	0.0162	0.0134	0.0075	0.0148	0.0133	0.0105	0.0114	0.0195	0.0086	0.0199	0.0124	0.0516	7.54E-15	

<b>65°C</b>																			
TC Number	1.1	1.2	1.3	1.4	2.1	2.2	2.3	2.4	3.1	3.2	3.3	3.4	4.1	4.2	4.3	4.4	All TCs	DigiSense (Control)	
Average	66.5	66.4	66.5	66.4	66.4	66.3	66.4	66.4	66.4	66.4	66.4	66.4	66.4	66.4	66.4	66.4	66.4	66.4	66.3
SD	0.0716	0.0721	0.0615	0.0668	0.0692	0.0571	0.0565	0.0633	0.0713	0.0606	0.0637	0.0600	0.0817	0.0815	0.0826	0.0673	0.0450	0.0452	

<b>75°C</b>																			
TC Number	1.1	1.2	1.3	1.4	2.1	2.2	2.3	2.4	3.1	3.2	3.3	3.4	4.1	4.2	4.3	4.4	All TCs	DigiSense (Control)	
Average	74.1	74.1	74.1	74.1	74.1	73.9	73.9	73.9	73.9	73.9	74.0	73.9	73.9	73.9	73.9	73.9	74.0	74.1	74.1
SD	0.0718	0.0582	0.0672	0.0648	0.0656	0.0726	0.0633	0.0654	0.0589	0.0650	0.0639	0.0629	0.0568	0.0610	0.0645	0.0709	0.0727	0.0669	

<b>90°C</b>																			
TC Number	1.1	1.2	1.3	1.4	2.1	2.2	2.3	2.4	3.1	3.2	3.3	3.4	4.1	4.2	4.3	4.4	All TCs	DigiSense (Control)	
Average	89.4	89.3	89.4	89.3	89.3	89.2	89.2	89.2	89.2	89.2	89.2	89.2	89.2	89.2	89.2	89.2	89.2	89.2	89.2
SD	0.0250	0.0307	0.0233	0.0249	0.0398	0.0385	0.0262	0.0289	0.0221	0.0283	0.0288	0.0350	0.0277	0.0231	0.0215	0.0219	0.0800	2.97E-14	